

Fabrication and Reactivity of Iron Carbide Films on Copper Substrates as Model Catalysts for Fischer-Tropsch Synthesis

PROEFSCHRIFT

ter verkrijging van de graad van doctor aan de Technische
Universiteit Eindhoven, op gezag van de rector magnificus
prof.dr. S.K. Lenaerts,

voor een commissie aangewezen door het College voor
Promoties, in het openbaar te verdedigen op woensdag 28
februari 2024 om 11:00 uur

door

Daniel Garcia Rodriguez

geboren te Barcelona, Spanje

Dit proefschrift is goedgekeurd door de promotoren en de samenstelling van de promotiecommissie is als volgt:

Voorzitter:	prof.dr. C. Storm
Promotor:	prof.dr.ir. M.C.M. van de Sanden
Copromotor:	Dr. C.J. Weststrate
Promotiecommissieleden:	prof.dr. M. Creatore
	prof.dr. G. Mul (Universiteit Twente)
	prof. dr. J. Lauritsen (Aarhus University)
	prof.dr.ir. M.G.D. Geers
	Dr. L.B.F. Juurlink (Universiteit Leiden)

Onderzoek of ontwerp dat in dit proefschrift wordt beschreven is uitgevoerd in overeenstemming met de TU/e Gedragscode Wetenschapsbeoefening.

A mi familia



This work was carried out in the context of the SynCat@DIFFER programme between the Dutch Institute For Fundamental Energy Research (DIFFER), Eindhoven University of Technology (TU/e) and Syngaschem BV and is funded jointly by the Netherlands Organization for Scientific Research (NWO) and Syngaschem BV. The research was conducted at DIFFER, Eindhoven, The Netherlands. DIFFER is part of the institutes organization of NWO.

A catalogue record is available from the Eindhoven University of Technology Library

ISBN: 978-90-386-5952-7

Cover design by Naghieli Amarista Ruiz

Printed by: ProefschriftMaken

Copyright @ 2024 Daniel Garcia Rodriguez

Summary

Iron-based catalysts are extensively used in the chemical industry to convert syngas (a mixture of carbon monoxide and hydrogen) into valuable chemicals and fuels via the Fischer-Tropsch synthesis (FTS). Iron-based FTS catalysts have been the subject of intense research for several years. As a result of the reduction and carburization of iron oxide precursors, metallic iron and iron carbides are formed, which are thought to be the active species responsible for the catalytic reaction in FTS. The high complexity of the catalyst makes it impossible to elucidate the molecular details of the catalytic reaction. The main inspiration behind the research in this dissertation is to explain how the FTS precursors interact with the surface of a model catalyst of iron carbide. To create this model catalyst, we used an electron beam evaporator to evaporate iron on top of two copper single crystal substrates with a (100) and (111) surface, respectively.

Ethylene was used as a carbon precursor in a post-treatment step to synthesize iron carbide.

The structure of the surface was studied by means of LEED (Low-energy electron diffraction), AES (Auger spectroscopy) and CO TPD titration (Temperature programmed desorption), and the reactivity of these films was studied with SR-XPS (Synchrotron radiation X-ray photoelectron spectroscopy), AES, LEED and RAIRS (Reflective absorption infrared spectroscopy).

Chapter 3 describes the structure and growth mode of the evaporated iron and iron carbide films where LEED, AES and CO titration was used to characterize the film. In the initial stages of growth, the iron films follow the FCC(100) crystallographic directions, as evidenced by the lack of superstructure spots in LEED from 0.5 ML to 2 ML of Fe. Different superstructure spots appear in LEED from 2 ML to 12 ML, confirming the coexistence of FCC(100) and BCC(110) iron. Synchrotron X-ray photoelectron spectroscopy (SR-XPS) and Auger electron spectroscopy (AES) confirm that a pure surface carbide is formed after ethylene dissociation from 0.5 ML to 12 ML of iron, showing a single peak at 282.6 eV in the C1s spectrum, and three characteristic Auger transitions in the C_{KLL} Auger spectrum. Carbon atoms enforce a tetracoordinate square planar arrangement of the surrounding iron atoms creating a

p4g(2x2) clock reconstruction with coverage of 0.5 ML, forming a Fe₂C surface composition. The electron diffraction does not show any spots related to BCC-Fe(110), indicating that the structure of the underlying Fe layers transforms into the FCC structure when the outermost layer reconstructs into the p4g(2x2) clock reconstruction. Introducing carbon into the subsurface layers through post-treatment with ethylene was unsuccessful. However, experiments involving the evaporation of Fe in an ethylene atmosphere resulted in the population of subsurface layers exhibiting a p4g(2x2) surface structure.

After characterizing the iron and iron carbide films, their interaction with CO and H₂ was explored, as described in *Chapter 4*. On iron, it was found that CO and H₂ dissociate independent of the thickness of the film, and the carbon found after CO dissociation also shows carbidic nature. Contrary to what happens on non-carburized films, CO and H₂ do not dissociate on a fully saturated Fe₂C film (p4g(2x2)). The interaction with molecular CO is also weaker since the CO and H₂ desorption temperature decreases by 100 K with respect to the non-carburized film. To adsorb H₂ on Fe₂C films, a W filament was used to transfer energy to the H₂ molecules and thus overcome the dissociative barrier of adsorption.

In *Chapter 5*, the growth mode and structure of different iron and iron carbide film thicknesses on Cu(111) were studied using the same techniques described in Chapter 3. The first part describes the iron film thickness regime below 2.6 ML, where the iron film consists of multilayer islands with an FCC-Fe structure before ethylene exposure. After dissociating ethylene on such islands, the shape of the C_{KLL} peak in AES corresponds to graphitic rather than carbidic carbon. Between 2.6 and 16 ML, Fe forms a mixed BCC-FCC film. AES after ethylene decomposition indicates that a pure carbide is formed after ethylene dissociation, while a complex LEED pattern suggests the formation of a mixture of structures, where the FCC-Fe parts appear to form a clock-reconstructed surface (p4g(2x2)). The behaviour changes for films thicker than 16 ML: the LEED pattern shows that the BCC(110) surface is formed, but after dissociating ethylene on this surface, the presence of both on-surface and bulk carbide are identified from quantification of the carbon content and spectroscopically by means of AES.

Chapter 6 shows that forming a closed iron film on Cu(111) requires ~8.6 ML of Fe, and on such pure iron films, the maximum amount of CO that can be dissociated is 0.2 ML, leaving a maximum of 0.4 ML of dissociated products on the surface. A pure BCC(110)-Fe phase is formed for films above ~16 ML, where a maximum of 0.3 ML of CO can dissociate. Like Fe₂C/Cu(100) described in Chapter 4, carbon monoxide cannot dissociate on a fully saturated iron carbide film. The desorption temperature of carbon monoxide on the iron carbide film decreases by 50 K with respect to the desorption from the non-carburized iron film, which is attributed to the weaker bonding of CO in the presence of surface carbon. The carbon monoxide dissociation reaction has been examined on an 8 ML iron film surface with different concentrations of pre-adsorbed carbon. The dissociated amount decreases linearly with increasing carbon coverage, and the sum of dissociation products (C_{ad}+O_{ad}) remains constant at 0.4 ML. After saturating the surface with carbon and oxygen, the surface becomes unreactive toward any dissociation reaction.

The primary aim of this research was to create an iron carbide model catalyst for FTS. Throughout the investigations, a Fe₂C surface carbide with a p4g(2x2) structure was found, which is remarkably stable and inert. We found that a carbon-saturated iron surface exhibited no reactivity towards CO and H₂ dissociation, but a non-saturated surface did show dissociative reactivity.

In real-life iron catalysts, different carbide and oxide phases can be found after exposing the catalysts to FT conditions (~230 °C and 20 bar total pressure); even though these conditions are far from our experimental conditions, we found that the thick iron films, where only BCC(110) is present, and the substrate does not play a role in the structure anymore, could be used as a model catalyst, mainly because there is no formation of p4g(2x2) due to carbon diffusion; hence a reactive iron carbide structure could be studied. Furthermore, we also learnt how to create bulk iron carbide, the closest structure to real-life catalysts someone can get at UHV.

Samenvatting

IJzergebaseerde katalysatoren worden uitgebreid gebruikt in de chemische industrie om syngas (een mengsel van koolmonoxide en waterstof) om te zetten in waardevolle chemicaliën en brandstoffen via de Fischer-Tropsch-synthese (FTS). IJzergebaseerde FTS-katalysatoren zijn al enkele jaren onderwerp van intensief onderzoek. Als gevolg van de reductie en carburisatie van ijzeroxideprecursoren worden metallisch ijzer en ijzercarbiden gevormd, die naar verluidt de actieve soorten zijn die verantwoordelijk zijn voor de katalytische reactie in FTS. De complexiteit van de katalysator maakt het onmogelijk om de moleculaire details van de katalytische reactie te achterhalen. De belangrijkste inspiratie achter het onderzoek in deze dissertatie is om uit te leggen hoe de FTS-precursoren interageren met het oppervlak van een modelkatalysator van ijzercarbide. Om deze modelkatalysator te creëren, hebben we een elektronenstraalverdamer gebruikt om ijzer te verdampen op twee koperen enkelkristallijne substraten met respectievelijk een (100) en (111) oppervlak. Ethyleen werd gebruikt als koolstofprecursor in een nabehandelingsstap om ijzercarbide te synthetiseren. De structuur van het oppervlak werd bestudeerd met behulp van LEED (Low-energy electron diffraction), AES (Auger spectroscopy) en CO TPD-titratie (Temperature programmed desorption), en de reactiviteit van deze films werd bestudeerd met SR-XPS (Synchrotron radiation X-ray photoelectron spectroscopy), AES, LEED en RAIRS (Reflective absorption infrared spectroscopy). Hoofdstuk 3 beschrijft de structuur en groeimodus van de verdampte ijzer- en ijzercarbide-films, waarbij LEED, AES en CO-titratie werden gebruikt om de film te karakteriseren. In de beginstadiën van de groei volgen de ijzeren films de kristallografische richtingen FCC(100), zoals blijkt uit het ontbreken van superstructuurpunten in LEED van 0.5 ML tot 2 ML Fe. Verschillende superstructuurpunten verschijnen in LEED van 2 ML tot 12 ML, wat de gelijktijdige aanwezigheid van FCC(100) en BCC(110) ijzer bevestigt. Synchrotron X-ray photoelectron spectroscopy (SR-XPS) en Auger electron spectroscopy (AES) bevestigen dat er een puur oppervlaktecarbide wordt gevormd na ethyleendissociatie van 0.5 ML tot 12 ML ijzer, wat zich uit in een enkele piek bij 282.6 eV in het C1s-spectrum, en drie karakteristieke Auger-overgangen in het CKLL Auger-spectrum. Koolstofatomen dwingen een tetracoördinatie-vierkant-vlakke rangschikking van de omringende ijzeratomen af, waardoor een p4g(2x2) klokreconstructie met een dekking van 0.5 ML wordt gevormd, resulterend in een Fe₂C oppervlaktesamenstelling. De

elektronendiffractie toont geen punten die verband houden met BCC-Fe(110), wat aangeeft dat de structuur van de onderliggende Fe-lagen transformeert naar de FCC-structuur wanneer de buitenste laag zich hervormt tot de $p4g(2 \times 2)$ klokreconstructie. Het introduceren van koolstof in de subsurface lagen via nabehandeling met ethyleen was onsuccesvol. Echter, experimenten waarbij Fe werd verdampt in een ethyleenatmosfeer resulteerden in de populatie van subsurface lagen die een $p4g(2 \times 2)$ oppervlaktestructuur vertonen.

Na het karakteriseren van de ijzer- en ijzercarbide-films werd hun interactie met CO en H₂ onderzocht, zoals beschreven in Hoofdstuk 4. Bij ijzer werd vastgesteld dat CO en H₂ dissociëren onafhankelijk van de dikte van de film, en de koolstof die wordt aangetroffen na CO-dissociatie vertoont ook een carbide-achtige aard. In tegenstelling tot wat er gebeurt op niet-gecarbureerde films, dissociëren CO en H₂ niet op een volledig verzadigde Fe₂C-film ($p4g(2 \times 2)$). De interactie met moleculair CO is ook zwakker, aangezien de desorptietemperatuur van CO en H₂ met 100 K daalt ten opzichte van de niet-gecarbureerde film. Om H₂ op Fe₂C-films te adsorberen, werd een W-filament gebruikt om energie over te dragen aan de H₂-moleculen en zo de dissociatiebarrière van adsorptie te overwinnen. In Hoofdstuk 5 werd de groeimodus en structuur van verschillende diktes van ijzer- en ijzercarbide-films op Cu(111) bestudeerd met behulp van dezelfde technieken als beschreven in Hoofdstuk 3. Het eerste deel beschrijft het ijzerfilm-diktegebied onder 2.6 ML, waarbij de ijzerfilm bestaat uit meerlaagse eilanden met een FCC-Fe structuur vóór blootstelling aan ethyleen. Na het dissociëren van ethyleen op dergelijke eilanden komt de vorm van de C_{KLL}-piek in AES overeen met grafietachtige koolstof in plaats van carbidische koolstof. Tussen 2.6 en 16 ML vormt Fe een gemengde BCC-FCC-film. AES na ethyleenontleding geeft aan dat er een puur carbide wordt gevormd na ethyleendissociatie, terwijl een complex LEED-patroon wijst op de vorming van een mengsel van structuren, waarbij de FCC-Fe-delen een oppervlak met een klokreconstructie ($p4g(2 \times 2)$) lijken te vormen. Het gedrag verandert voor films dikker dan 16 ML: het LEED-patroon toont aan dat het BCC(110)-oppervlak wordt gevormd, maar na het dissociëren van ethyleen op dit oppervlak wordt de aanwezigheid van zowel oppervlakte- als bulkcarbide geïdentificeerd aan de hand van kwantificatie van het koolstofgehalte en spectroscopisch met behulp van AES.

Hoofdstuk 6 toont aan dat het vormen van een gesloten ijzerfilm op Cu(111) ~8.6 ML Fe vereist, en op dergelijke zuivere ijzerfilms kan de maximale hoeveelheid CO die kan dissociëren 0.2 ML zijn, waarbij maximaal 0.4 ML gedissocieerde producten op het

oppervlak achterblijven. Voor films boven ~16 ML wordt een zuivere BCC(110)-Fe-fase gevormd, waarbij maximaal 0.3 ML CO kan dissociëren. Net als Fe₂C/Cu(100) beschreven in Hoofdstuk 4 kan koolmonoxide niet dissociëren op een volledig verzadigde ijzercarbide-film. De desorptietemperatuur van koolmonoxide op de ijzercarbide-film daalt met 50 K ten opzichte van de desorptie vanaf de niet-gecarbureerde ijzerfilm, wat wordt toegeschreven aan de zwakkere binding van CO in aanwezigheid van oppervlaktekoolstof. De dissociatiereactie van koolmonoxide is onderzocht op een ijzerfilmoppervlak van 8 ML met verschillende concentraties voorgeadsorbeerde koolstof. De gedissocieerde hoeveelheid neemt lineair af met toenemende koolstofbedekking, en de som van dissociatieproducten (CO+O₂) blijft constant op 0.4 ML. Na verzadiging van het oppervlak met koolstof en zuurstof wordt het oppervlak niet-reactief ten opzichte van enige dissociatiereactie. Het primaire doel van dit onderzoek was het creëren van een ijzer carbide modelkatalysator voor FTS. Gedurende de onderzoeken werd een Fe₂C oppervlaktecarbide met een p4g(2x2) structuur gevonden, die opmerkelijk stabiel en inert is. We ontdekten dat een koolstofsaturatie van het ijzeroppervlak geen reactiviteit vertoonde ten opzichte van CO- en H₂-dissociatie, maar een niet-gesatureerd oppervlak vertoonde wel dissociatieve reactiviteit. In echte ijzerkatalysatoren kunnen verschillende carbide- en oxidefasen worden gevonden na blootstelling aan FT-condities (~230 °C en 20 bar totale druk); hoewel deze omstandigheden ver verwijderd zijn van onze experimentele omstandigheden, ontdekten we dat de dikke ijzerfilms, waar alleen BCC(110) aanwezig is en het substraat geen rol meer speelt in de structuur, kunnen worden gebruikt als een modelkatalysator, voornamelijk omdat er geen vorming van p4g(2x2) is als gevolg van koolstofdifusie; hierdoor kon een reactieve ijzercarbide-structuur worden bestudeerd. Bovendien hebben we ook geleerd hoe bulkijzercarbide kan worden gecreëerd, de structuur die het dichtst in de buurt komt van katalysatoren in het echte leven die men kan bereiken bij UHV.

Contents

Summary	VI
Samenvatting	IX
Chapter 1: Introduction	1
1.1 Greenhouse gases	2
1.2 Heterogeneous catalysis	4
1.3 Fischer-Tropsch synthesis.....	5
1.4 Fe catalysts for FTS.....	8
1.4.1 Iron carbides	9
1.5 The Surface Science Approach.....	15
1.6 Scope of the thesis	16
1.7 References.....	17
Chapter 2: Experimental techniques and methodology	23
2.1 Description of the vacuum system.....	24
2.2 Low Energy Electron Diffraction (LEED)	26
2.3 Synchrotron radiation X-ray photoelectron spectroscopy (SR-XPS).....	31
2.3.1 XPS quantification analysis	33
2.4 Auger electron spectroscopy (AES)	35
2.4.1 Auger quantification	37
2.4.2 Auger as a qualitative technique to identify carbidic species.	39
2.4.3 O _{KLL} + LEED to determine the amount of dissociated CO.....	40
2.5 Temperature-programmed desorption (TPD).....	41
2.5.1 TPD+LEED References and Quantification	42
2.6 Thermal electron beam evaporation.....	44
2.7 Reflection Absorption InfraRed Spectroscopy (RAIRS)	45
2.8 References.....	46
Chapter 3: Fabrication of iron carbide films on Cu(100)	51
3.1 Introduction	52
3.2 Experimental.....	54
3.3 Iron thin film structure and morphology	55
3.4 Ethylene dissociation on a 4 ML iron film	59

3.5	Carbon-induced “clock” reconstruction on iron thin films	62
3.6	Film-thickness dependence	64
3.7	Iron carbide thermal stability	65
3.8	Bulk carbide formation and decomposition.....	66
3.9	Iron carbide thick films (>12ML)	69
3.10	General discussion	71
3.11	Summary and conclusions.....	72
3.12	References.....	74
Chapter 4: CO and H₂ reactivity on iron and iron carbide films on Cu(100)		79
4.1	Introduction	80
4.2	Experimental.....	82
4.3	Results and discussion	83
4.3.1	Reactivity of CO on 4 ML of Fe/Cu(100)	83
4.3.2	CO reactivity: influence of Fe film thickness.....	88
4.3.3	CO on Fe _x C: molecular adsorption, desorption and dissociation	92
4.4	Conclusions	102
4.5	References.....	104
Chapter 5: Iron carbide fabrication on Cu(111)		109
5.1	Introduction	110
5.2	Experimental.....	111
5.3	Iron thin film structure and morphology	113
5.4	Ethylene dissociation for Fe coverages below 2.6 ML	116
5.5	Ethylene dissociation on iron for film thicknesses between 2.6 ML and 16 ML. Carburization on BCC Fe(110) + FCC(111) mixtures.	118
5.6	Ethylene dissociation on a thick iron film on Cu(111), with ~16 ML of iron 121	
5.7	General discussion	124
5.8	References.....	127
Chapter 6: CO reactivity on iron and iron carbide films on Cu(111) 131		
6.1	Introduction	132
6.2	Experimental.....	134

6.3	Results	135
6.3.1	CO dissociation on different iron thicknesses on Cu(111)	135
6.3.1.1	CO dissociation on (~16 ML) Fe BCC(110) films	137
6.3.1.2	Morphological changes upon CO dissociation	139
6.3.1.3	CO desorption from iron carbide films	141
6.3.1.4	Carbon influence on CO dissociation Fe FCC(111)+BCC(110)	142
6.4	Discussion.....	143
6.4.1	CO desorption and dissociation on Fe/Cu(111) and comparison with Fe/Cu(100).....	144
6.4.2	CO desorption and dissociation on Fe _x C _y /Cu(111) and comparison with Fe ₂ C/Cu(100).....	147
6.5	Summary and Conclusions.....	148
6.6	References.....	149
	Chapter 7: Conclusions and Outlook.....	153
7.1	Chapter 3: Iron and iron carbide films on Cu(100)	154
7.2	Chapter 5 and Chapter 6: Iron and iron carbide films on Cu(111). Structure versatility and usefulness as a model catalyst.....	157
7.3	Outlook.....	158
7.3.1	Other characterization techniques.....	158
7.3.2	Improved measurements with present techniques	159
7.3.3	Fe(110) single crystal comparison.....	160
7.4	Final Remarks.....	160
	Acknowledgements	163
	List of publications	166
	Curriculum Vitae	167



1.1 Greenhouse gases

The increase in anthropogenic carbon dioxide (CO₂) emissions has been a topic of significant concern in recent years. Human activities, such as burning fossil fuels, deforestation, and the cement industry (limestone- CaCO₃ is heated in a kiln to produce lime-CaO and CO₂) have rapidly increased atmospheric CO₂ concentrations [1]. These emissions are considered the leading cause of the increase in global temperature and Earth's climate changes by enhancing the greenhouse effect [2]. The impact of climate change on ecosystems, health, and global economies may be evident today, but it is anticipated that the effects will worsen significantly if no action is taken to mitigate them.

With the alarming consequences of climate change, it is crucial to augment the share of energy supply from renewable resources, such as wind and solar, that produce significantly lower CO₂ emissions. Despite the pressing need to reduce carbon emissions, some projections estimate that natural gas, coal, and petroleum may still constitute more than 70% of energy demand by 2040. This phenomenon can be attributed to the relatively low cost of fossil resources like coal in certain parts of the world, unconventional natural gas resources such as shale gas, and advanced oil recovery technologies that facilitate the extraction of previously inaccessible reserves. [3]

Countries worldwide are setting ambitious targets to reduce their greenhouse gas emissions and increase their use of renewable energy. The European Union, for instance, has set a goal of reaching net-zero emissions by 2050 and has implemented policies and regulations to promote the use of renewable energy. Similarly, the United States has rejoined the Paris Agreement and set a goal of reaching net-zero emissions by 2050. China, the world's largest emitter of greenhouse gases, has pledged to peak its emissions by 2030 and achieve carbon neutrality by 2060. The energy transition has become a priority in the Netherlands in recent years. The country aims to reduce its CO₂ emissions by 49% by 2030 and achieve carbon neutrality by 2050. Various policy measures, such as subsidies for renewable energy projects and a carbon tax on fossil fuels, have facilitated the transition to renewable energy sources. The Netherlands has invested heavily in

renewable energy sources such as wind and solar and has become a world leader in offshore wind power. [4]

The adoption of renewable energy sources has the potential to significantly reduce CO₂ emissions and mitigate the impact of climate change. However, using renewable energy sources also presents challenges, such as intermittency, which can affect the stability and reliability of the power supply. Therefore, integrating renewable energy sources with energy storage technologies and smart grid systems is crucial to overcome these challenges and ensuring a sustainable and reliable energy supply.

Synthesis gas, a mixture of carbon monoxide (CO) and hydrogen gas (H₂), can be produced from various feedstocks, such as coal, natural gas, and biomass, and has wide-ranging applications in producing fuels, chemicals, and materials. It is also expected to play an important role in the sustainable chemical industry since synthesis gas can be produced from CO₂ and green hydrogen [5,6]. This reaction is the so-called "reverse water gas shift" reaction (RWGS→Eq 1.1) in which CO₂ and H₂ over a suitable catalyst, typically a mixture of metal oxides such as FeO_x, CeO₂, Mn₂O₃, CrO₃ or TiO₂ between 500 °C and 600 °C to produce CO and H₂O [7]. Metal carbides, like iron carbide, are also active towards RWGS [8]. The reaction is slightly endothermic and requires energy input to proceed:



Synthesis gas can be converted into various products, such as olefins, paraffins, and oxygenated compounds, as well as long-chain hydrocarbons via Fischer-Tropsch synthesis (FTS).

1.2 Heterogeneous catalysis

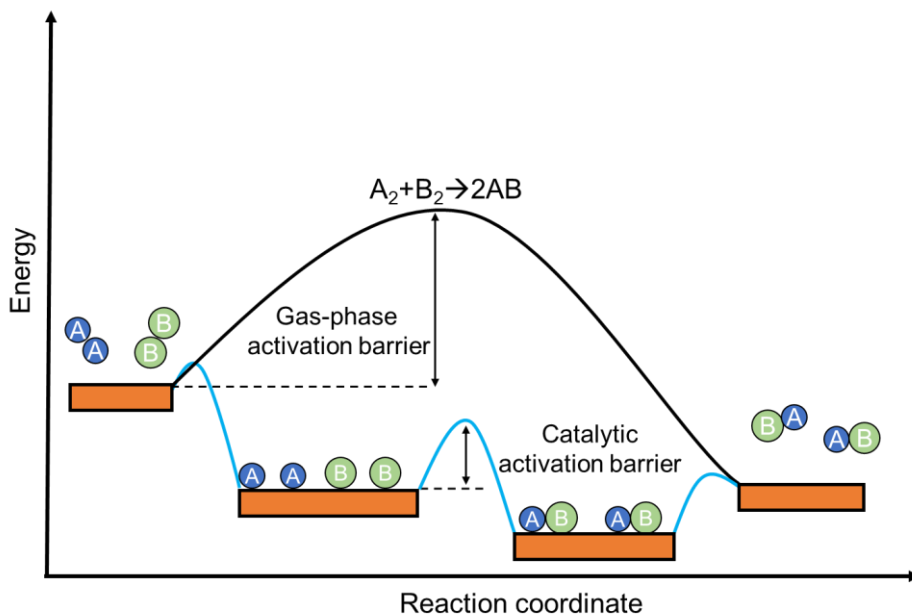


Figure 1.1. The diagram illustrates the potential energy difference between the catalytic and non-catalytic pathways of the reaction $A_2 + B_2 \rightarrow 2AB$. The reaction without a catalyst requires more energy to overcome the barrier than the catalytic pathway. Adapted from [9].

A catalyst is a substance that speeds up the rate of a chemical reaction by offering an alternative pathway with lower activation energy without being consumed in the reaction. This allows the reaction to occur more quickly, making the process more efficient (depending on the reaction conditions, some catalysts can be used for several years).

Heterogeneous catalysts, frequently employed in the chemical industry, consist of solid materials that interact with gaseous or liquid reactants. Figure 1.1 shows a simplified model of the main reaction sequence for a heterogeneous cycle. The catalytic cycle consists of the adsorption of the reactant on the catalyst surface, bond breaking, diffusion of the reactants, product formation, and desorption. The Haber-Bosch reaction is an example of a catalytic process, where a solid material (the catalyst) is used to increase the reaction rate between N_2 and H_2 to produce

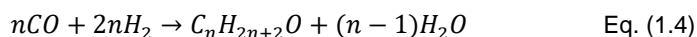
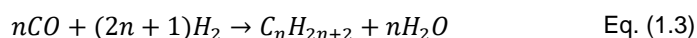
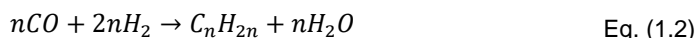
ammonia (NH₃). In the case of the Haber-Bosch reaction, iron is used as a catalyst to lower the activation energy required for the reaction to occur, allowing nitrogen (N₂ bond energy is ~ 945 kJ/mol, making it one of the strongest bonds found in diatomic molecules) and hydrogen to react and form ammonia more readily. Using a catalyst in the Haber-Bosch process is crucial for achieving high reaction rates and energy efficiency. Without the catalyst, the reaction would occur much more slowly and at higher temperatures and pressures, making the process impractical and uneconomical [10].

1.3 Fischer-Tropsch synthesis

Basics

In 1902, Sabatier published the first results of syngas conversion, demonstrating that a mixture of carbon monoxide and hydrogen could be transformed into methane using nickel and cobalt catalysts. In the 1920s, Franz Fischer and Hans Tropsch advanced this process by showing that synthesis gas could be converted into a mixture of hydrocarbons (1-olefine, paraffin, and oxygenated products), which could serve as gasoline or diesel fuel through the FTS.

The following equations summarize the overall reactions to the various products:



Equations 1.2, 1.3 and 1.4 show the formation of olefins, paraffin, and oxygenates, respectively. Reaction 1.5 is the water-gas shift, which mainly occurs in Fe-based catalysts, and through this reaction, the products can be reused to minimize H₂ use in feedstock at the same time that the H₂/CO ratio is adjusted to the formation of

hydrocarbons in situations where the amount of H_2/CO is low, like when the syngas is derived from coal. Several transition metals, such as Fe, Co, Ni, Ru, and Rh, show FT activity [11,12]. Iron- and cobalt-based catalysts are mainly used in industry [13,14] as the best trade-off between catalyst cost, lifetime, and product selectivity. On the fundamental level, the process is a surface polymerization reaction with an initiation step to start a chain, propagation steps to make it grow, and a termination step where the product leaves the surface. As a result, a distribution of chain lengths is produced that typically follows an Anderson-Schultz-Flory distribution: α is the chain growth probability, $(1 - \alpha)$ is the probability that specific chain terminates, w_i is the weight fraction of chain length, and i the number of carbon atoms.

$$w_i = i(1 - \alpha)^2 \alpha^{i-1} \quad \text{Eq. (1.6)}$$

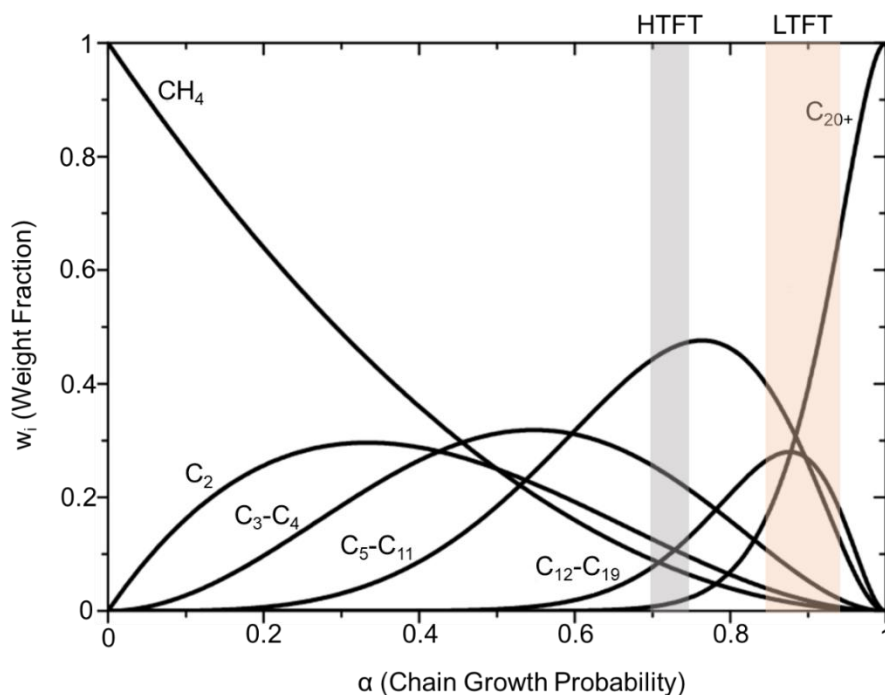


Figure 1.2 Anderson-Schultz-Flory distribution for different α values. High-temperature Fischer-Tropsch technology (HTFT) corresponds approximately to $0.70 < \alpha < 0.75$, and low-temperature Fischer-Tropsch (LTFT) to about $0.85 < \alpha < 0.95$ [16].

Figure 1.2. illustrates the product distribution (Eq. 1.6) for various α values. Iron catalysts typically exhibit α values ranging from 0.70 to 0.75, resulting in gasoline production (C_5 - C_{11}) at high-temperature Fischer-Tropsch, and lower temperatures will increase the chain growth probability (0.85 to 0.95) forming larger hydrocarbons. Whereas cobalt catalysts have α values of 0.75 to 0.90, leading to larger hydrocarbon generation [15]. The α value may also vary based on operating conditions, such as lowering the temperature, reducing the H_2/CO ratio, and increasing pressure, which results in a higher α value and longer chain production. Additionally, using promoters in the reaction tends to increase the chain length. [11] The FTS reaction has been a topic of study for nearly a century, but a definitive mechanism has yet to be established. Three different mechanisms have been proposed throughout history, each one of them with different initiation, propagation and termination steps:

The carbide mechanism proposed by Fischer and Tropsch in 1926 says that CO dissociates before the carbon atom is partially hydrogenated into CH_x species. These CH_x species combine by adding one monomer at a time to produce hydrocarbon chains. Before leaving the catalyst surface, the intermediate can terminate in various ways, resulting in an alkane, alkene, or oxygenate. Many variations have been considered within the basic carbide mechanism, such as whether CO dissociation occurs unassisted or through hydrogen interaction and whether there are two or more hydrogen atoms per monomer (CH or CH_2). [16]

The enol mechanism describes the initiation step as an H-assisted CO dissociation forming CHOH species (oxymethylene), which acts as a monomer, and the propagation step occurs via condensation with H_2O elimination. Different products can be obtained depending on the termination route.

The CO insertion mechanism involves inserting a CO molecule into a C_xH_y molecule, followed by the cleavage of the C-O bond to form a $C_{x+1}H_z$ intermediate that can accommodate another CO molecule.

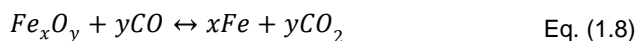
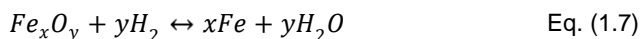
These mechanisms produce surface oxygen atoms, which must be removed for the reaction to proceed. This can be achieved by hydrogenating oxygen to form water or coupling it with CO to produce CO_2 . [17]

In summary, the main difference between these mechanisms are the monomers of the propagation steps. These monomers are CH_x , $CHOH$ and CO for the carbide, enol and CO insertion mechanisms.

1.4 Fe catalysts for FTS

As a catalyst for FTS, Fe presents a notable advantage over Ru and Co in terms of its abundance and affordability [10]. The Fe catalyst exhibits a broader temperature range for operation compared to the Co catalyst, and it can endure lower H_2/CO ratios in the synthesis gas feedstock. This can be attributed to the fact that Fe-based FT catalysts actively participate in the WGS, which converts CO and H_2O into H_2 and CO_2 , elevating the H_2/CO ratio during the process. Furthermore, it is believed that Fe displays higher selectivity towards lower olefins when compared to Co, which has contributed to the advancement of catalysts for FT to olefins technology. [17,18]

The most commonly used iron catalyst precursor for FTS is iron oxide (Fe_2O_3) [19,20]. Iron oxide is reduced to metallic iron in the presence of hydrogen (H_2) and CO at elevated temperatures, typically between $200-350^\circ C$, to form the active catalyst for FTS, as shown in Equations 1.7 and 1.8 [20]. Metallic iron can subsequently adsorb CO on one of the active sites ($*$ in Eq 1.9) and dissociate it. The dissociated products can react with the iron atoms to form, i.e., iron carbides (Eq 1.10). This will be discussed further in the next section.



1.4.1 Iron carbides

Structures

Iron carbides are interstitial compounds where carbon atoms are located in the spaces between the iron atoms without significantly disrupting the crystal structure. This arrangement of carbon atoms within the iron lattice gives rise to unique properties. The presence of carbon atoms can affect the mechanical, thermal, and catalytic properties of the material. Typically, two classes of iron carbides are distinguished depending on the carbon location: carbon atoms can occupy trigonal-prismatic interstices (Fe_7C_3 , $\chi\text{-Fe}_5\text{C}_2$, $\theta\text{-Fe}_3\text{C}$) or octahedral interstices ($\epsilon\text{-Fe}_2\text{C}$, $\epsilon'\text{-Fe}_2\text{C}$), Figure 1.3 [21].

	Formula	Atomic ratio C:Fe	Crystal lattice	Interstitial occupation of carbon atoms	Wt% carbon
Hexagonal carbide	ϵ	Fe_2C	hcp to monoclinic	Octahedral	9.7
	ϵ'	$\text{Fe}_{2.2}\text{C}$	hcp	Octahedral	8.9
Eckstrom and Adcock carbide		Fe_7C_3	Orthorhombic	Trigonal prismatic	8.4
Hägg carbide	χ	Fe_5C_2	Monoclinic	Trigonal prismatic	7.9
Cementite	θ	Fe_3C	Orthorhombic	Trigonal prismatic	6.7
		Fe_xC			

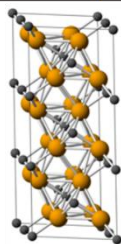
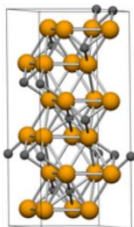
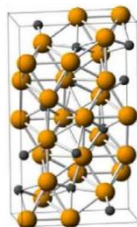
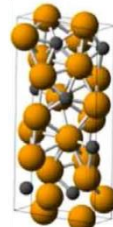
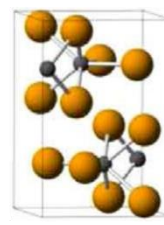
 $\epsilon\text{-Fe}_2\text{C}$  $\epsilon'\text{-Fe}_{2.2}\text{C}$  Fe_7C_3  $\chi\text{-Fe}_5\text{C}_2$  $\theta\text{-Fe}_3\text{C}$

Figure 1.3 Top: Iron carbide phase characteristics. The table was taken and modified from [13]. Bottom: Ball diagram of the crystal structures of iron carbide. Models adapted from Liu et al. [22].

The Fe_3C phase, known as cementite, is the most important iron carbide phase in metallurgy. It is commonly found in the pearlite ($\text{Fe}_3\text{C}+\alpha\text{-Fe}$) microstructure of steel. It acts as a hardening phase and determines the properties of the steel produced. A low carbon content, for example, leads to softer and more ductile steel, while a high carbon content leads to harder and more brittle steel.

During Fischer-Tropsch synthesis, the iron oxide, hydroxide, or oxy-hydroxide precursors are pre-treated with CO-containing gas, and carburization occurs at a low temperature [16]. As a result, a complex mixture of phases is formed, which evolves with catalyst age. In-situ studies during catalyst pretreatment and under FTS operating conditions indicate that the active phase contains a mixture of various coexisting phases, including $\alpha\text{-Fe}$, iron oxides, and various iron carbides [13,23]. Hägg carbide, $\chi\text{-Fe}_5\text{C}_2$, is always found under FT conditions and is often regarded as the active phase for FT [23–25]. Because of this, extensive research has been performed to understand its properties, reactivity, and phase structures [8,17,20,26–28]. The $\theta\text{-Fe}_3\text{C}$ phase, an intermediate in the transition from pure $\alpha\text{-Fe}$ to the carbon-rich χ -phase, becomes the dominant phase at high temperatures and low CO pressure. X-ray, electron, and neutron diffraction measurements experimentally determined its structure [29–31]. The Eckstrom-Adcock iron carbide (Fe_7C_3) has been identified in FTS by means of X-ray diffraction (XRD), X-ray absorption fine structure (XAFS), Mössbauer spectroscopy (MES) and Transmission electron microscopy (TEM) [28]. It is a trigonal prismatic carbide, where the carbon is found in the trigonal prismatic sites of distorted hcp structures of iron atoms. The formation of Fe_7C_3 occurs from the Fe_3C phase at high temperatures [32]. The $\epsilon\text{-Fe}_2\text{C}$ is formed directly from $\alpha\text{-Fe}$ at $<200\text{ }^\circ\text{C}$ [32]; a mixture of phases is obtained at higher temperatures. This phase has been identified by means of XRD and MES after FT conditions. [33]

Reactivity on single and multiple phases of iron carbide

Industrial iron-based catalysts are complex because they contain not only the catalytic material but also supporting materials, additives, and promoters. Adding structural and chemical promoters can improve unmodified and unpromoted iron

catalyst's selectivity, activity, and sintering in FTS processes. It is possible to suppress sintering using structural promoters such as Si, Al, and Mg, stabilize the active phase, and improve mechanical strength using chemical promoters such as Cu or Ag. Using alkali metals such as potassium can help promote chain growth, reduce the formation of methane, and inhibit the formation of secondary hydrogenation reactions, which results in a higher olefin-to-paraffin ratio. [16]

These additional components in the industrial catalysts and the fact that the active phase only represents a small fraction of the entire system make it challenging to investigate the system at a molecular level. Considerable efforts have been made to optimize the selectivity, activity, and efficiency of real catalysts using an empirical approach. However, without a fundamental understanding, developing new catalysts in the past was based on an inefficient and expensive trial-and-error approach.

Researchers have tried to prepare and study single-phase iron carbide structures under FT conditions for decades to understand which phase shows the best performance for FTS. The iron carbide phases most commonly investigated for FTS are χ -Fe₅C₂, θ -Fe₃C, and ϵ -Fe₂C. Some studies have associated the FTS activity of iron carbide catalysts with the presence of χ -Fe₅C₂ on the catalyst surface [34,35]. Others have focused on exploring the activity and selectivity of individual carbide phases.

Lyu et al. [36] successfully synthesized and isolated nanoparticles of ϵ -Fe₂C and found that the intrinsic activity of ϵ -Fe₂C ($\sim 1258 \mu\text{molCO g}_{\text{Fe}}^{-1} \text{s}^{-1}$) surpasses the activity of χ -Fe₅C₂ by a factor of 2 and θ -Fe₃C by 6-10 times. They achieved this by confining the nanoparticles within graphene layers. However, the challenge lies in the fact that ϵ -Fe₂C is unstable under FTS conditions, which complicates the experimental investigation. This confirmed the superior activity of ϵ -Fe₂C as the most active phase for FTS and opened a promising route to create single-phase iron carbide nanocrystals.

In another research on ϵ (')-Fe₂C by Wang et al. [37], where they research the fabrication and reactivity in FTS conditions of ϵ (')-carbides (ϵ (')-Fe₂C + ϵ -Fe₂C \rightarrow same space group p6m/mmc and cell dimensions, these two phases show similar chemical properties and are considered as one). This phase was identified by means of MES and XRD after FT conditions. The results show the high stability of the

structure and the lowest CO₂ selectivity (<5%) compared to conventional Fe-based catalysts.

Wezendonk et al. [28] report the reactivity towards CO and H₂ on iron carbide nanoparticles. They report that the ϵ' -Fe₂C and χ -Fe₅C₂ phases have the same activity but different selectivity depending on the size of the nanoparticle (3.6 nm to 6 nm). The ϵ' -Fe₂C phase shows higher CH₄ selectivity, meaning higher hydrogenation ability and low C₅₊ conversion. Moreover, the χ -Fe₅C₂ phase shows a higher C₅₊ conversion. The exact reason for this behaviour is still unknown, but their hypothesis is related to the different active site configurations on the surface or C_{ad} and H_{ad} surface coverage dependence.

Zhao et al. [38] synthesized phase-pure nanoparticles of Fe₂C, Fe₇C₃, and Fe₅C₂, all displaying activity in the FT reaction, and Fe₅C₂ was the most active. They used XPS, XRD, and TEM to determine the phase composition, structure, and morphology of the nanoparticles. Furthermore, a novel technique named transient high-pressure stepwise temperature programmed surface reaction (STPSR) was used to calculate the reaction mechanisms and kinetics by exploring syngas activation, hydrocarbon, and methane formation. Note: The activity value calculated for Fe₅C₂ is ~230 $\mu\text{molCO g}_{\text{Fe}}^{-1} \text{s}^{-1}$ (270°C), almost 5 times lower than the value (~1258 $\mu\text{molCO g}_{\text{Fe}}^{-1} \text{s}^{-1}$ -- 340°C) reported by Lyu et al. [36]

Chang et al. [28] compared a number of silica-supported iron carbides and found that Fe₇C₃ has the highest intrinsic activity (TOF= 4.59×10⁻² s⁻¹) compared to χ -Fe₅C₂ and ϵ -Fe₂C in the Fe/SiO₂ system. They also show that ϵ -Fe₂C produced lower CH₄ and higher C₅₊ selectivity than χ -Fe₅C₂ and Fe₇C₃, suggesting that ϵ -Fe₂C has outstanding C-C coupling ability.

This brief overview of experimental findings shows that assessing the activity and selectivity of iron carbides in applied catalysis is difficult because of the experimental complexity in the fabrication process, as different preparation methods yield different results. For this reason, DFT has gained importance in the last decades in the systematic study of well-defined single-phase iron carbide surfaces.

DFT studies

Density Functional Theory (DFT) has been used by others to gain detailed electronic and structural information on well-defined systems, analyze surface reactions, and ultimately predict catalytic properties, facilitating rational design and optimization of efficient catalysts.

Fe₅C₂ and others. Structural studies

A study by Steynberg et al. [39] used DFT to investigate χ -Fe₅C₂ surfaces with different carbon contents and crystallographic directions. The surfaces studied have similar surface energy, making it difficult to predict which surface will be predominantly exposed under reaction conditions. This was explored in more detail using ab initio atomistic thermodynamics by Zhao et al. [40], where they explored the effects of CO and syngas pretreatment on the surface morphology of nine different χ -Fe₅C₂ surfaces. They found that CO pretreatment favours C-rich terminations, whereas syngas pretreatments favour C-poor terminations.

Zhao et al. [41] studied the properties and reactivity of different iron carbide phases (ϵ -Fe₂C, χ -Fe₅C₂, θ -Fe₃C, and Fe₄C), where they found that ϵ -Fe₂C-(1-21)-2.00, χ -Fe₅C₂-(100)-2.25, θ -Fe₃C-(010)-2.33 and Fe₄C-(100)-3.00 are the most thermodynamically stable surfaces due to their low surface free energy. These surfaces have a similar atomic arrangement, where "[...] each surface carbon atom coordinates with four surface iron atoms, and each surface iron atom coordinates with two surface carbon atoms". As a result, their reactivity is expected to be similar. The authors indeed report that the adsorption energy of CO and the activation energy of C-O are the same between surfaces if the same coverage is used, except for the Fe₄C-(100)-3.00, which shows the weakest ability to activate the C-O bond.

DFT mechanisms + reactivity

DFT has also been used for mechanistic studies, where the CO dissociation reaction has been an important topic of study. DFT calculations have been used to investigate two types of reaction mechanisms on iron carbide surfaces, the Langmuir-

Hinshelwood (LH) and Mars-van Krevelen (MvK) mechanisms. According to the LH mechanism, the iron carbide surface offers a favourable substrate where two surface species react together from their adsorbed states to form a new species, while in the MvK mechanism, the catalyst material plays an active role in the reaction as the carbon atoms that form part of the iron carbide lattice take part in the reaction.

Work by Gracia et al. [42] on CO hydrogenation on carbon-terminated $\text{Fe}_5\text{C}_2(100)$ shows how the adsorption and dissociation of CO on fully saturated iron carbide surface via the LH mechanism is less favourable than adsorption and dissociation at carbon vacancies, illustrating that the MvK mechanism is feasible. In a more recent study by Ozbek and Niemantsverdriet. [26], a $\chi\text{-Fe}_5\text{C}_2(001)_{-0.05}$ with varying carbon vacancy concentration was used to investigate the different steps of the mechanism. It was found that CO dissociation is not feasible at a high carbon content. Vacancies created by reacting surface carbon with hydrogen to CH_x create vacancies in the iron carbide structure where CO dissociation becomes feasible.

Broos et al. [27] and also shown in his PhD thesis [17], performed a comprehensive study of direct and H-assisted CO dissociation pathways on different surface terminations of the Hägg Carbide with the lowest surface energies ($\chi\text{-Fe}_5\text{C}_2(010)_{0.25}$, $(11-1)_{0.0}$, $(100)_{0.0}$, $(11-1)_{0.5}$ and $(100)_{0.287}$). As a general trend, they found that CO adsorption energy depends on the presence of interstitial carbon atoms in the first subsurface layer. Also, they found that there is competition between direct and H-assisted pathways for CO dissociation on the surfaces mentioned above. They show that due to the presence of interstitial carbon atoms, the H-assisted mechanism contributes more to the CO dissociation rate than the direct pathway. Furthermore, the direct CO dissociation mechanism becomes easier with increasing the adsorption strength of CO.

Deng et al. [43] studied the adsorption of CO and $\text{H}_{(\text{ad})}$ as well as CO dissociation and the formation of C_xH_y on $\text{Fe}_3\text{C}(100)$. They found that the direct dissociation energy of CO and H-assisted dissociation is endothermic, but the hydrogenation of surface carbon is exothermic and, thus, the lowest required energy for chain growth. These authors also show that surface vacancies lower the CO dissociation barrier considerably. Broos et al. [44] studied CO dissociation on several Fe_3C surface terminations. These authors do not consider the role of carbon vacancies in detail

and find that dissociation barriers on terrace-like facets are high, while on the corrugated $\text{Fe}_3\text{C}(111)$ surface, a barrier as low as 40 kJ mol^{-1} was found, even lower than on $\text{Fe}(111)$.

Zhang et al. [45] investigated the Fe_7C_3 phase using DFT, where they refer to the experimental study by Chang et al. [28], who showed a high activity of Fe_7C_3 for FTS. They studied the hcp- Fe_7C_3 (211) surface termination and found that the effective barrier energy of the CO activation mechanism on the hcp- Fe_7C_3 (211) is lower than those on the $\chi\text{-Fe}_5\text{C}_2$ (510) and $\theta\text{-Fe}_3\text{C}$ (100). The influence of carbon vacancies was not considered in this work.

The carbon-rich $\text{Fe}_2\text{C}(001)$ surface was investigated in a study by Yu et al. [46]. They found that the CO dissociation and coupling reactions are not thermodynamically favourable compared to the CO adsorption. CO can react with the lattice carbon forming C-CO, which is an important stage for the FTS reaction. These findings will also be important when we discuss the reactivity of our iron carbide films on $\text{Cu}(100)$ and $\text{Cu}(111)$.

1.5 The Surface Science Approach

Thanks to the development of modern characterization techniques, it is now possible to study catalysis at the atomic level and gain fundamental insights into catalytic phenomena. Such insights into active sites, poisoning mechanisms, and reaction pathways are crucial for developing catalysts [11,19]. Surface science presents a unique opportunity to simplify the complexity of real-life catalysts used in the industry by investigating their structures, morphology and reactivity under controlled conditions at the atomic level. Thanks to the advancements in ultrahigh vacuum (UHV) systems, with pressures ranging from 10^{-8} to 10^{-10} mbar, and surface-sensitive techniques such as X-ray photoelectron spectroscopy (XPS), it is possible to create and study simple model systems at the molecular level. These systems comprise nanoparticles on clean single-crystal substrates called flat model catalysts. Most of the time, this system consists of a flat substrate covered with a thin layer of support material on which the active catalyst material is placed. The high exposed surface area of the active material makes it suitable for applying spectroscopic techniques.

However unlike the single-crystal approach, catalyst particles on a flat surface model are often undefined in size and shape and exhibit multiple surface facets, making single crystals the more accurate and well-defined method of conducting surface chemistry. [11,19]

As shown before iron carbide has attracted significant theoretical interest in the context of the FTS process. However, the availability of experimental data in this area remains scarce. One of the primary reasons for this scarcity is the inherent complexity associated with working on iron-single crystals. One of the reasons not to work with iron single crystals is that iron is highly reactive and susceptible to oxidation. Even small exposures to air or moisture can lead to the formation of oxide layers on the crystal surface, which can interfere with experiments. For this reason, some people have started working on their iron carbide surfaces without using iron single-crystals but instead evaporating iron onto a well-defined substrate (novel single crystals, i.e., Cu or Au).

Li et al. [12] investigated CO reactivity on iron carbide films supported on Au(111). They claim that the carbide phase is responsible for the CO dissociation reaction (seen by increased C1s and O1s intensity in XPS). They also studied the O₂ reactivity on these saturated iron carbide films, where they found that after dosing O₂, the C1s peak decreased considerably, forming iron oxides.

1.6 Scope of the thesis

This thesis aims to create an iron carbide model catalyst to study the interaction (adsorption, desorption and dissociation) of the FT reactants (CO and H₂) with the surface. To fabricate these model iron catalysts, we evaporated iron onto single crystals of copper with a (100) and (111) crystallographic direction and used ethylene as a carbon source to create iron carbide. The structure of the iron and iron carbide films and their reactivity were investigated under ultra-high vacuum (UHV) conditions using different surface-sensitive techniques such as Auger spectroscopy (AES), Temperature-programmed desorption (TPD), Low Energy Electron Diffraction (LEED), X-ray photoelectron spectroscopy (XPS), and Reflection-Absorption Infrared Spectroscopy (RAIRS).

In *Chapter 2*, the UHV system is described, the background theory of the techniques mentioned above and the quantification references used to determine atomic percentages of the dissociation products, i.e. total adsorbed carbon after ethylene or CO dissociation, are also detailed.

The fabrication and characterization of different iron and iron carbide model catalysts on Cu(100) and Cu(111) with different thicknesses are discussed in *Chapters 3 and 5*. In these chapters, LEED and TPD are used to determine the structure, growth mode and thickness of the deposited films, AES to determine the chemical composition and thickness, and finally, H₂ TPD to determine the amount of deposited carbon. These chapters aimed to characterize and understand the structure used to create our iron carbide model catalysts.

The interaction of H₂ and CO with iron and iron carbide films is described in *Chapters 4 and 6*. In *Chapter 4*, Synchrotron X-ray photoelectron spectroscopy was used to follow in situ the dissociation reaction of CO and ethylene on non-carburized iron films and in carburized iron films. *Chapter 6* shows the reactivity of CO with TPD on iron and iron carbide films supported on Cu(111). The chemical composition after CO adsorption and desorption was studied using AES.

In *Chapter 7*, a general discussion is provided where the results are considered in the context of applied catalysis, along with suggested directions for future research.

1.7 References


- [1] G. Ortega-Ruiz, A. Mena-Nieto, AA Golpe, J.E. García-Ramos, CO₂ emissions and causal relationships in the six largest world emitters, *Renew. Sustain. Energy Rev.* 162 (2022) 112435. <https://doi.org/10.1016/J.RSER.2022.112435>.
- [2] D. Lüthi, M. Le Floch, B. Bereiter, T. Blunier, J.M. Barnola, U. Siegenthaler, D. Raynaud, J. Jouzel, H. Fischer, K. Kawamura, T.F. Stocker, High-resolution carbon dioxide concentration record 650,000-800,000 years before present, *Nature.* 453 (2008) 379–382. <https://doi.org/10.1038/nature06949>.
- [3] A. Shah, R. Fishwick, J. Wood, G. Leeke, S. Rigby, M. Greaves, A review of novel techniques for heavy oil and bitumen extraction and upgrading, *Energy Environ. Sci.* 3 (2010) 700–714. <https://doi.org/10.1039/b918960b>.
- [4] EE Agency, Greenhouse gas emissions - country profile, (2021). <https://www.eea.europa.eu/themes/climate/ghg-country-profiles>.

- [5] W. Hong, A techno-economic review on carbon capture, utilization and storage systems for achieving a net-zero CO₂ emissions future, *Carbon Capture Sci. Technol.* 3 (2022) 100044. <https://doi.org/10.1016/j.ccst.2022.100044>.
- [6] R.M. Cuéllar-Franca, A. Azapagic, Carbon capture, storage and utilization technologies: A critical analysis and comparison of their life cycle environmental impacts, *J. CO₂ Util.* 9 (2015) 82–102. <https://doi.org/10.1016/j.jcou.2014.12.001>.
- [7] M. González-Castaño, B. Dorneanu, H. Arellano-García, The reverse water gas shift reaction: A process systems engineering perspective, *React. Chem. Eng.* 6 (2021) 954–976. <https://doi.org/10.1039/d0re00478b>.
- [8] Q. Zhang, L. Pastor-Pérez, Q. Wang, T. Ramirez Reina, Conversion of CO₂ to added value products via rWGS using Fe-promoted catalysts: Carbide, metallic Fe or a mixture?, *J. Energy Chem.* 66 (2022) 635–646. <https://doi.org/10.1016/J.JECHEM.2021.09.015>.
- [9] I. Chorkendorff, J.W. Niemantsverdriet, *Concepts of Modern Catalysis and Kinetics*, WILEY-VCH, Weinheim, 2003. <https://doi.org/https://doi.org/10.1002/3527602658>.
- [10] W.M. Haynes, *CRC Handbook of Chemistry and Physics*, 95th ed., CRC Press, Boca Raton, 2016. <https://doi.org/https://doi.org/10.1201/9781315380476>.
- [11] F.J.E. Scheijen, *The surface chemistry of CO on iron and other bcc metals*, Technische Universiteit Eindhoven, 2010. <https://doi.org/10.6100/IR657952>.
- [12] Y. Li, Z. Li, A. Ahsen, L. Lammich, G.J.A. Mannie, J.W. Niemantsverdriet, J. V. Lauritsen, Atomically Defined Iron Carbide Surface for Fischer-Tropsch Synthesis Catalysis, *ACS Catal.* 9 (2019) 1264–1273. <https://doi.org/10.1021/acscatal.8b03684>.
- [13] E. De Smit, B.M. Weckhuysen, The renaissance of iron-based Fischer-Tropsch synthesis: On the multifaceted catalyst deactivation behaviour, *Chem. Soc. Rev.* 37 (2008) 2758–2781. <https://doi.org/10.1039/b805427d>.
- [14] S. Abelló, D. Montané, Exploring iron-based multifunctional catalysts for Fischer-Tropsch synthesis: A review, *ChemSusChem.* 4 (2011) 1538–1556. <https://doi.org/10.1002/cssc.201100189>.
- [15] I. Chokendorff, J.W. Niemantsverdriet, *Concepts of Modern Catalysis and Kinetics*, Wiley- VCH, Weinheim, 2003.
- [16] J. van de Loosdrecht, F.G. Botes, I.M. Ciobica, A. Ferreira, P. Gibson, D.J. Moodley, A.M. Saib, J.L. Visagie, C.J. Weststrate, J.W. Niemantsverdriet, *Fischer-Tropsch Synthesis: Catalysts and Chemistry*, 2nd ed., Elsevier Ltd., 2013. <https://doi.org/10.1016/B978-0-08-097774-4.00729-4>.
- [17] RJP Broos, *Computational modelling of the Fischer-Tropsch reaction on Iron Carbides*, Technische Universiteit Eindhoven, 2020.
- [18] H. Schulz, Comparing Fischer-Tropsch synthesis on iron- and cobalt catalysts. The dynamics of structure and function, in: *Stud. Surf. Sci. Catal.*, 2007: pp. 177–199. [https://doi.org/10.1016/S0167-2991\(07\)80479-4](https://doi.org/10.1016/S0167-2991(07)80479-4).
- [19] Y. Li, *Atomic-scale study of iron-based Fischer-Tropsch catalysts. A combined STM and XPS study*, iNANO (Interdisciplinary Nanoscience Center), 2018.

- [20] M. Ding, Y. Yang, B. Wu, Y. Li, T. Wang, L. Ma, Study on reduction and carburization behaviors of iron phases for iron-based Fischer-Tropsch synthesis catalyst, *Appl. Energy*. 160 (2015) 982–989. <https://doi.org/10.1016/j.apenergy.2014.12.042>.
- [21] X. Cui, J. Xu, C. Zhang, Y. Yang, P. Gao, B. Wu, Y. Li, Effect of pretreatment on precipitated Fe-Mo Fischer-Tropsch catalysts: Morphology, carburization, and catalytic performance, *J. Catal.* 282 (2011) 35–46. <https://doi.org/10.1016/j.jcat.2011.05.020>.
- [22] X.W. Liu, S. Zhao, Y. Meng, Q. Peng, A.K. Dearden, C.F. Huo, Y. Yang, Y.W. Li, X.D. Wen, Mössbauer Spectroscopy of Iron Carbides: From Prediction to Experimental Confirmation, *Sci. Rep.* 6 (2016). <https://doi.org/10.1038/srep26184>.
- [23] J.W. Niemantsverdriet, A.M. van der Kraan, W.L. van Dijk, HS van der Baan, Behavior of Metallic Iron Catalysts during Fischer-Tropsch Synthesis Studied with Mössbauer Spectroscopy, X-ray Diffraction, Carbon Content Determination, and Reaction Kinetic Measurements, *J. Phys. Chem.* 25 (1980) 3363–3370. <https://doi.org/10.1021/j100462a011>.
- [24] F.J.E. Scheijen, D. Curella-Ferré, J.W. Niemantsverdriet, Adsorption and dissociation of CO on body-centered cubic transition metals and alloys: effect of coverage and scaling relations, *J. Phys. Chem. C*. 113 (2009) 11041–11049. <https://doi.org/10.1021/jp811130k>.
- [25] D.B. Cao, F.Q. Zhang, Y.W. Li, J. Wang, H. Jiao, Structures and energies of coadsorbed CO and H₂ on Fe₅C₂ (001), Fe₅C₂(110), and Fe₅C₂(100), *J. Phys. Chem. B*. 109 (2005) 10922–10935. <https://doi.org/10.1021/jp050940b>.
- [26] M.O. Ozbek, J.W. Niemantsverdriet, Elementary reactions of CO and H₂ on C-terminated χ -Fe₅C₂(001) surfaces, *J. Catal.* 317 (2014) 158–166. <https://doi.org/10.1016/j.jcat.2014.06.009>.
- [27] RJP Broos, B. Zijlstra, I.A.W. Filot, E.J.M. Hensen, Quantum-Chemical DFT Study of Direct and H- and C-Assisted CO Dissociation on the χ -Fe₅C₂ Hägg Carbide, *J. Phys. Chem. C*. 122 (2018) 9929–9938. <https://doi.org/10.1021/acs.jpcc.8b01064>.
- [28] Q. Chang, C. Zhang, C. Liu, Y. Wei, A. V. Cheruvathur, A.I. Dugulan, J.W. Niemantsverdriet, X. Liu, Y. He, M. Qing, L. Zheng, Y. Yun, Y. Yang, Y. Li, Relationship between Iron Carbide Phases (ϵ -Fe₂C, Fe₇C₃, and χ -Fe₅C₂) and Catalytic Performances of Fe/SiO₂ Fischer-Tropsch Catalysts, *ACS Catal.* 8 (2018) 3304–3316. <https://doi.org/10.1021/acscatal.7b04085>.
- [29] HKDH Bhadeshia, Cementite, *Int. Mater. Rev.* 65 (2019) 1–27. <https://doi.org/10.1080/09506608.2018.1560984>.
- [30] A.I. Gardin, An electron-diffraction study of the structure of cementite, *Sov. Phys. - Crystallography*. 7 (1963) 694–700.
- [31] IG Wood, L. Vočadlo, K.S. Knight, D.P. Dobson, W.G. Marshall, G.D. Price, J. Brodholt, Thermal expansion and crystal structure of cementite, Fe₃C, between 4 and 600 K determined by time-of-flight neutron powder diffraction, *J. Appl. Crystallogr.* 37 (2004) 82–90. <https://doi.org/10.1107/S0021889803024695>.
- [32] K. Opeyemi Otun, Y. Yao, X. Liu, D. Hildebrandt, Synthesis, structure, and performance of carbide phases in Fischer-Tropsch synthesis: A critical review, *Fuel*. 296 (2021) 120689. <https://doi.org/10.1016/j.fuel.2021.120689>.

- [33] X.W. Liu, Z. Cao, S. Zhao, R. Gao, Y. Meng, J.X. Zhu, C. Rogers, C.F. Huo, Y. Yang, Y.W. Li, X.D. Wen, Iron carbides in Fischer-Tropsch synthesis: Theoretical and experimental understanding in epsilon-iron carbide phase assignment, *J. Phys. Chem. C*. 121 (2017) 21390–21396. <https://doi.org/10.1021/acs.jpcc.7b06104>.
- [34] T. Riedel, H. Schulz, G. Schaub, K.W. Jun, J.S. Hwang, K.W. Lee, Fischer-Tropsch on iron with H₂/CO and H₂/CO₂ as synthesis gases: The episodes of formation of the Fischer-Tropsch regime and construction of the catalyst, *Top. Catal.* 26 (2003) 41–54. <https://doi.org/10.1023/B:TOCA.0000012986.46680.28>.
- [35] E. de Smit, A.M. Beale, S. Nikitenko, B.M. Weckhuysen, Local and long range order in promoted iron-based Fischer-Tropsch catalysts: A combined in situ X-ray absorption spectroscopy/wide angle X-ray scattering study, *J. Catal.* 262 (2009) 244–256. <https://doi.org/10.1016/j.jcat.2008.12.021>.
- [36] S. Lyu, L. Wang, Z. Li, S. Yin, J. Chen, Y. Zhang, J. Li, Y. Wang, Stabilization of ε-iron carbide as high-temperature catalyst under realistic Fischer–Tropsch synthesis conditions, *Nat. Commun.* 11 (2020) 1–8. <https://doi.org/10.1038/s41467-020-20068-5>.
- [37] P. Wang, W. Chen, F.K. Chiang, A. Iulian Dugulan, Y. Song, R. Pestman, K. Zhang, J. Yao, B. Feng, P. Miao, W. Xu, E.J.M. Hensen, Synthesis of stable and low-CO₂ selective ε-iron carbide Fischer-Tropsch catalysts, *Sci. Adv.* 4 (2018) 1–7. <https://doi.org/10.1126/sciadv.aau2947>.
- [38] H. Zhao, J.X. Liu, C. Yang, S. Yao, H.Y. Su, Z. Gao, M. Dong, J. Wang, A.I. Rykov, J. Wang, Y. Hou, W.X. Li, D. Ma, Synthesis of iron-carbide nanoparticles: Identification of the active phase and mechanism of Fe-based Fischer-Tropsch synthesis, *CCS Chem.* 3 (2021) 2712–2724. <https://doi.org/10.31635/ccschem.020.202000555>.
- [39] P.J. Steynberg, J.A. Van Den Berg, W.J. Van Rensburg, Bulk and surface analysis of Hägg Fe carbide (Fe₅C₂): A density functional theory study, *J. Phys. Condens. Matter.* 20 (2008). <https://doi.org/10.1088/0953-8984/20/6/064238>.
- [40] S. Zhao, X.W. Liu, C.F. Huo, Y.W. Li, J. Wang, H. Jiao, Surface morphology of Hägg iron carbide (χ-Fe₅C₂) from ab initio atomistic thermodynamics, *J. Catal.* 294 (2012) 47–53. <https://doi.org/10.1016/j.jcat.2012.07.003>.
- [41] S. Zhao, X.W. Liu, C.F. Huo, Y.W. Li, J. Wang, H. Jiao, Determining surface structure and stability of ε-Fe₂C, χ-Fe₅C₂, θ-Fe₃C and Fe₄C phases under carburization environment from combined DFT and atomistic thermodynamic studies, *Catal. Struct. React.* 1 (2015) 44–60. <https://doi.org/10.1179/2055075814Y.0000000007>.
- [42] J.M. Gracia, F.F. Prinsloo, J.W. Niemantsverdriet, Mars-van krevelen-like mechanism of CO hydrogenation on an iron carbide surface, *Catal. Letters.* 133 (2009) 257–261. <https://doi.org/10.1007/s10562-009-0179-5>.
- [43] L.J. Deng, C.F. Huo, X.W. Liu, X.H. Zhao, Y.W. Li, J. Wang, H. Jiao, Density functional theory study on surface C_xH_y formation from CO activation on Fe₃C(100), *J. Phys. Chem. C*. 114 (2010) 21585–21592. <https://doi.org/10.1021/jp108480e>.
- [44] RJP Broos, B. Klumpers, B. Zijlstra, I.A.W. Filot, E.J.M. Hensen, A quantum-chemical study of the CO dissociation mechanism on low-index Miller planes of θ-Fe₃C, *Catal. Today.* 342 (2020) 152–160. <https://doi.org/10.1016/j.cattod.2019.02.015>.

- [45] M. Zhang, J. Ren, Y. Yu, Investigating the CO activation mechanism on hcp-Fe₇C₃(211) via density functional theory, *Mol. Catal.* 505 (2021) 111506. <https://doi.org/10.1016/j.mcat.2021.111506>.
- [46] X. Yu, X. Zhang, Y. Meng, Y. Zhao, Y. Li, W. Xu, Z. Liu, CO adsorption, dissociation and coupling formation mechanisms on Fe₂C(001) surface, *Appl. Surf. Sci.* 434 (2018) 464–472. <https://doi.org/10.1016/j.apsusc.2017.10.225>.



02

EXPERIMENTAL TECHNIQUES AND METHODOLOGY

ABSTRACT: This chapter overviews the experimental techniques used to study the adsorption, desorption, and dissociation of CO, H₂ and ethylene and the structure, morphology and composition of evaporated iron and iron carbide film surfaces on Cu(100) and Cu(111). The employed techniques are Auger spectroscopy (AES), Low Energy Electron Diffraction (LEED), Synchrotron Radiation X-ray photoelectron spectroscopy (SR-XPS), temperature-programmed desorption with a mass spectrometer (TPD), and Reflection absorption infrared spectroscopy (RAIRS). An overview of the Ultra-High Vacuum system (UHV) and cleaning procedures will also be presented.

2.1 Description of the vacuum system

Most of the results described in this thesis were obtained using a home-built UHV system which consists of a single vacuum chamber with a base pressure of 1×10^{-10} mbar. The pressure is maintained by a combination of a Leybold Turbomolecular pump (Turbovac 90 i(x)) backed by a Leybold rough pump (Ecodyr 65 Plus) and a titanium sublimation pump. The system is equipped with combined Auger electron spectroscopy (AES) and Low Energy Electron Diffraction (LEED) optics (Vacuum Microengineering Model LPS300-D), a quadrupole mass spectrometer (QMG 250 PrismaPro), and a dual pocket electron beam evaporator (e-flux2 Dual Evaporator from Tectra) which was used for Fe deposition. Furthermore, it has four leak valves for high-purity gas dosage (Linde and Messer). The IPS3 sputter gun and a power supply from Vacuum Microengineering were used to clean the surface.

In the present work, a Cu(100) and a Cu(111) single crystal were used as substrates for iron deposition. The disc-shaped single crystals are 8 mm in diameter and have a thickness of 1.2 mm. The sample is held by a U-shaped 0.5 mm (diameter) Tungsten wire placed in the 0.51 mm wide slits at the side of the samples, as shown in Figure 2.1 (a). The schematic drawing of the single crystal in Figure 2.1 (a) shows a small hole (depth of 3 mm and diameter of 0.7 mm) in the side of the crystal that is used to insert a type K (chromel-alumel) thermocouple to measure the sample temperature. Temperatures can be reached from 80K to 1000 K without temperature fluctuation. The lower temperature limit is due to the liquid nitrogen inserted in the hollow manipulator and the thermal conductivity from the liquid container to the

sample. The upper limit is to avoid copper melting. The Cu substrates are cleaned by sputtering cycles with 2 keV Ar⁺ bombardment at 300 K, followed by a flash anneal to 1000 K for both substrates. The sample manipulator allows both samples to be mounted simultaneously, which makes it possible to switch between the samples within a minute and without breaking the vacuum.

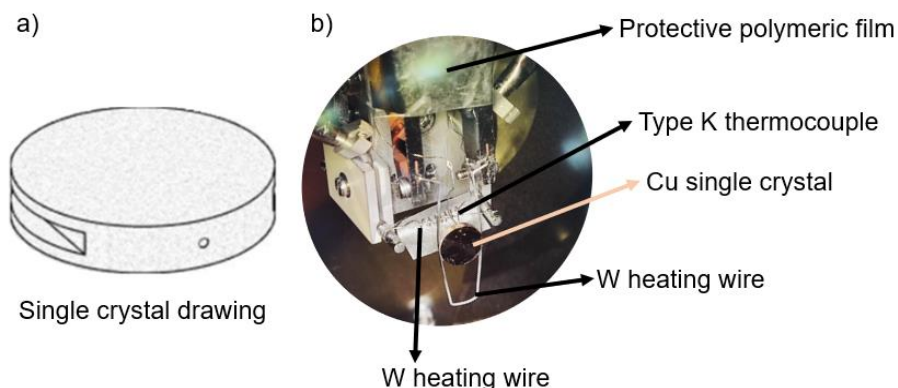


Figure 2.1 (a) Diagram of the single crystal (image taken from Surface preparation laboratory webpage). (b) A picture from inside of the UHV chamber. The crystal is mounted using a W wire which holds and heats the sample at the same time.

Some additional experiments were performed in a second home-built UHV system (base pressure 2×10^{-10} mbar), where the sample mounting and the heating is identical to that in the UHV set-up described before. In addition to LEED/AES (same brand as the last one), a QMS (and QMG 220 PrismaPlus) and a sputter gun, this system is equipped with Reflection Absorption Infra-Red Spectroscopy (RAIRS) (Nicolet iS10 spectrometer equipped with a liquid nitrogen-cooled MCT detector), and a second shielded quadrupole mass spectrometer (Hiden Analytical) located in a separately pumped compartment which is connected to the main chamber by a 5 mm aperture. During desorption experiments, the sample is placed at a distance of around 2 mm from this aperture. In this way, molecules that desorb from other parts of the sample holder do not reach the mass spectrometer; only the desorbing molecules from the sample are measured.

Synchrotron radiation X-Ray photoelectron spectroscopy (SR-XPS) was performed at the Matline beamline of the ASTRID2 synchrotron light source (Aarhus, Denmark). Normal emission was employed to record the Fe3p/Cu3p, C1s, and O1s spectral regions using photon energies of 150 eV, 380 eV, and 650 eV, respectively. The binding energy (BE) scale was calibrated using the Fermi edge measurement for each photon energy.

2.2 Low Energy Electron Diffraction (LEED)

In 1927, Davisson and Germer fired electrons with energies between 15 and 200 eV at a polycrystalline nickel crystal and discovered that the angular variations in the reflected flux were consistent with electron diffraction. They had a fortuitous sample overheating accident that caused the coalescence of many small crystallites into a few larger ones, which considerably helped observe the diffraction phenomena. Although it was Thomson in the same year who reported the observation of transmission electron diffraction patterns from a film of Pt using a beam of 'cathode rays' (electrons) between 30-60 kV (confirming De Broglie's PhD hypothesis of the duality wave/ particle of the electron), Davisson and Thomson were the ones that were awarded Nobel prize in Physics for these findings [1–4]. Electrons with 100 eV have a wavelength of approximately 1 Å; such low-energy electrons diffract from a grating with periodicity on the order of atomic dimensions and thus give atomic scale information [5]. The diffraction of low-energy electrons has developed into a valuable surface-sensitive analysis technique used to obtain information on the long-range order of the single crystal surface and of ordered adsorbate overlayers.

Figure 2.2. shows a schematic structure of the LEED/AES optics used to measure the diffraction patterns shown in this thesis. The electron gun, which consists of a heated cathode (1% Thoriated tungsten) and a set of focusing lenses, creates a mono-energetic beam of electrons, the energy of which can be varied between 40 eV to 270 eV. The electron beam has a diameter of about 1 mm, which is a relatively small area of the single crystal (8 mm); even so, it makes LEED an averaging technique since the size of domains on the surface is in the nm range.

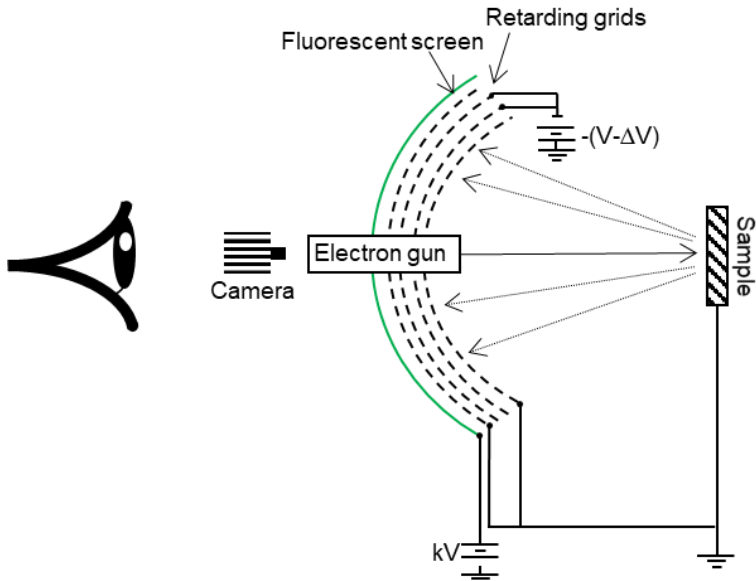


Figure 2.2 Simplified LEED optics with an observer looking at the fluorescent screen where a diffraction pattern of backscattered electrons occurs.

LEED operates the following way: The electron gun produces a mono-energetic, collimated electron beam. These electrons strike the sample. Some of these electrons are elastically diffracted from the surface towards the optics. A large fraction of the incident electrons is also inelastically scattered, but the LEED optics are used as a high pass energy filter to select out only the elastically backscattered electrons, where the first grid closest to the sample is grounded to screen the potentials of the other grids. Energy selection is done by grids 2 and 3. A retarding voltage is applied to these grids so that only electrons with energies higher than the applied voltage are passed through the filter. Two grids instead of one are used to improve the energy resolution of the high-pass filter. The fourth grid is grounded and filters out the potential of the screen, which is held between 3 and 5 kV and accelerates electrons towards the fluorescent screen to produce a diffraction pattern. The pattern is recorded using a digital camera mounted behind the fluorescent screen [5–8]. Since the scattering cross-section is large for electrons with a kinetic energy of around 100 eV, the penetration depth of the electron beam is in the order of a few atomic layers, as can be seen from the so-called universal electron mean

free path curve in Figure 2.3. This results in a high surface sensitivity, and the technique is very suitable for determining periodic surface structures.

Bragg's law states that the diffraction of X-rays or electrons occurs when the spacing of the atoms in a crystal lattice is such that the reflected beams interfere constructively. Mathematically, this can be expressed as $2d \sin \theta = n\lambda$, where d is the spacing between the atomic planes, θ is the angle of incidence of the X-rays or electrons, n is an integer, and λ is the wavelength of the incident radiation.

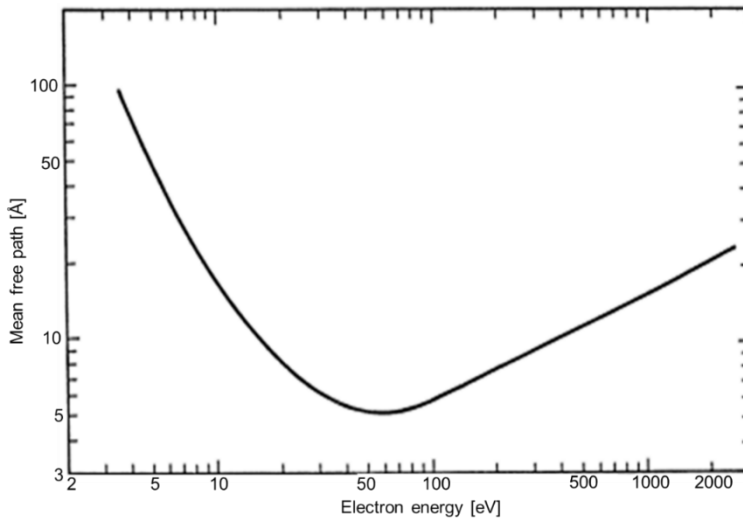


Figure 2.3. "Universal curve" of the electron mean free path as a function of electron kinetic energy. The graph was taken and modified from [5].

The diffraction condition of Bragg's law can be understood in terms of Ewald's sphere (Figure 2.4), which visually represents Bragg's law in reciprocal space. The sphere represents the momentum transfer between the incident and scattered waves, and its radius corresponds to the magnitude of the wave vector. The points where the Ewald sphere intersects with the diffraction rod mark the point where the corresponding atomic planes reflect the incident waves constructively, leading to a diffraction spot at this position. The position of the diffraction spot depends on the angle of incidence and the spacing between the atomic planes, as given by Bragg's law [9].

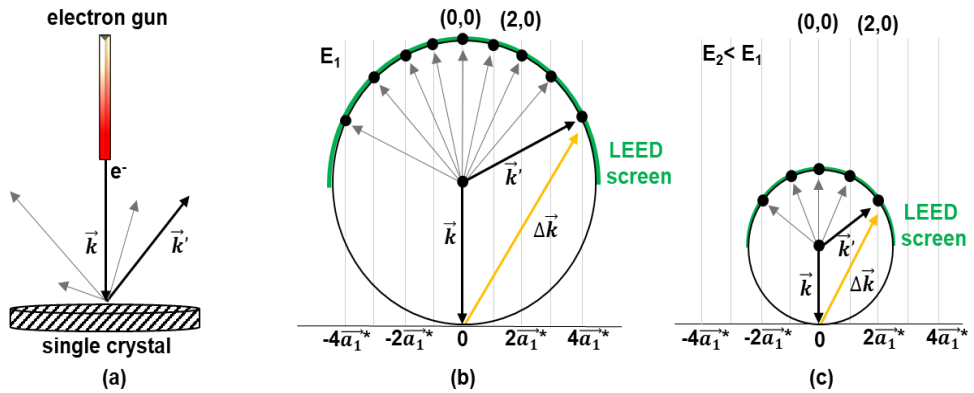


Figure 2.4. Schematic drawing of the Ewald sphere. Electrons are emitted (a) by the electron gun normal to the surface with \vec{k} before are elastically scattered. The representation of the LEED spots based on the electron energy is represented in (b) and (c).

Thus, the diffraction pattern is the magnified version of the reciprocal surface lattice and the spots/beams we observe give information on the size and symmetry of the substrate unit cell. More importantly, the size and symmetry of the overlayer unit cell relative to that of the substrate can be deduced from the diffraction pattern [10,11]. As an example, Figure 2.5. shows the experimentally obtained diffraction patterns for clean Cu(100) left and Cu(111) right, respectively, for electron energy of 100 eV. The LEED pattern from the right shows different beam intensities in (0,1) and (1,0) spots. This effect is due to layer stacking, {111}, in the Cu(111), FCC cubic structure (ABCABC...), as is represented in the centre ball diagram. In Cu(100), the stacking of {100} planes is ABAB the reciprocal space lattice does not show differences in the beam intensities in this case [12,13].

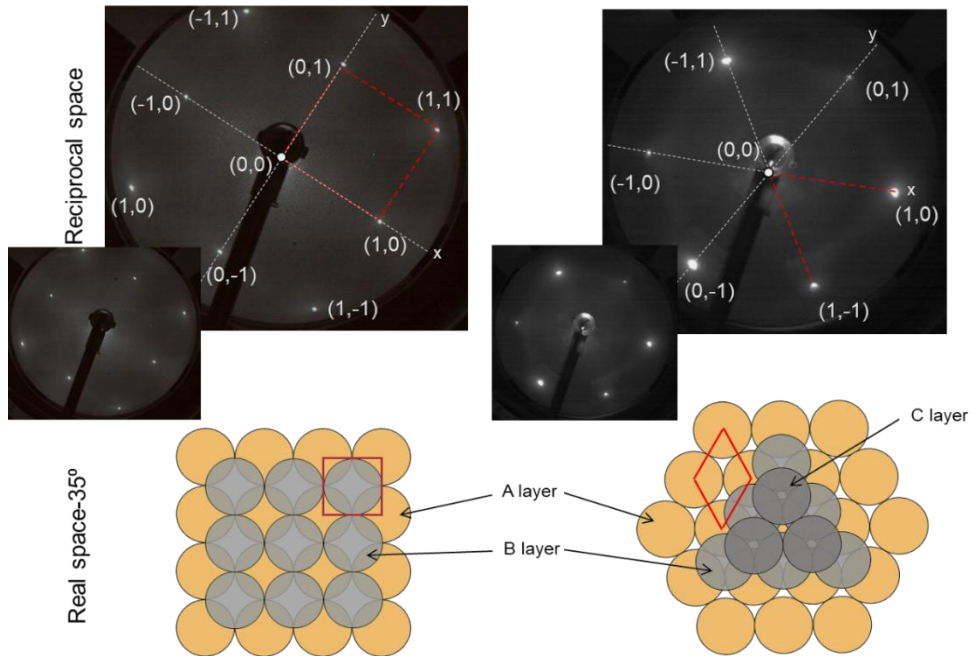


Figure 2.5. Left and right are LEED patterns from Cu(100) and Cu(111) after Ar⁺ sputtering and annealing to 1000 K, respectively. Both images were taken at 100eV. The red lines are the unit cells, and ball diagrams show the layer stacking.

Adatoms, or adsorbed molecules, often form ordered adsorbate layers on single-crystal surfaces, giving rise to additional diffraction spots in the LEED pattern. In this way, information about the size and symmetry of the unit cell of the adsorbate overlayer relative to the substrate can be obtained from the relative positions of the adsorbate-related diffraction spots [5,14]. Figure 2.6. shows an example of the diffraction pattern obtained after 0.5 monolayer (ML) of CO was adsorbed at 100 K on Cu(100). In addition to the (1x1) from the substrate, new spots ($\{1/2, 1/2\}$) form an additional overall $c(2 \times 2)$ array. A simple model of the real space lattice can be obtained using simple vector geometry. The ball diagram corresponds to CO molecules adsorbed on top sites in the Cu(100).

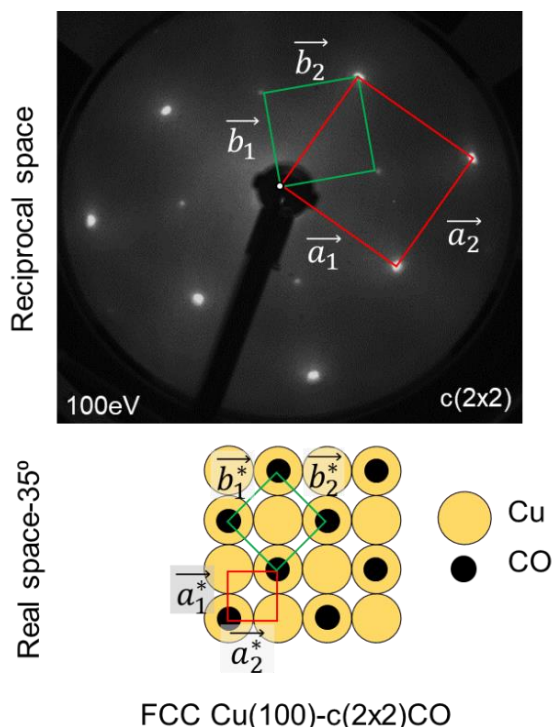


Figure 2.6. Comparison between reciprocal space measurements of the LEED (top) and the derived ball models in the real space (bottom). The red square represents the unit cell of the substrate, and the green square is the unit cell of the adsorbed CO molecule.

2.3 Synchrotron radiation X-ray photoelectron spectroscopy (SR-XPS)

XPS is a quantitative chemical analysis technique with high surface sensitivity. It was developed by Kai Siegbahn and his group in Uppsala and was honoured with the Nobel Prize in 1981 [15]. The physical principle of XPS is based on the photoelectric effect (Figure 2.7 (a)), which was first observed by Hertz in 1887 and theoretically explained by Einstein in 1905. Figure 2.7 (a) shows a schematic depiction of the photoemission process.

In XPS, absorption of an X-ray photon leads to a photoelectron emission. The kinetic energy of the emitted photoelectrons is measured, and this energy is directly related to the energy of the photon, the binding energy of the electron within the original atom and is typically associated with a particular element and its chemical state.

Since soft X-rays are typically used, the photoelectrons have energies in the 50-1000 eV energy range, which strongly interact with matter. As a result, only electrons generated near the surface can escape without losing additional energy, and the information depth of XPS corresponds to the outermost nanometers of the sample, which makes XPS a surface-sensitive analysis technique.

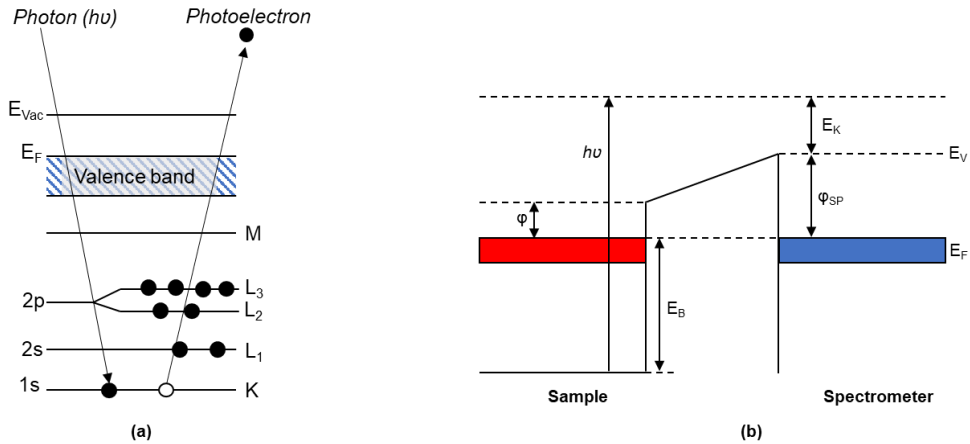


Figure 2.7. (a) Schematic illustration of the core-level photoemission by the photoelectric effect in a metal. (b) Energy-level diagram of the sample and the spectrometer in a core-level photoemission experiment on a metallic sample.

The basic equation (Eq. 2.1) that describes this effect is [16] :

$$E_K = h\nu - E_B - \phi \quad \text{Eq. (2.1)}$$

E_K = Kinetic energy of the emitted photoelectron

$h\nu$ = energy of the incident photon

E_B = Binding energy that the emitted electron had in the solid relative to the Fermi level of the sample

ϕ = Work function spectrometer (Fig. 2.7 (b))

The value ϕ remains constant, and the photon energy is known. We can reduce, therefore, the previous equation to:

$$E_B = h\nu - E_K \quad \text{Eq. (2.2)}$$

A mono-energetic source of X-rays is necessary to produce photoelectrons with discrete kinetic energy. In this thesis, XPS measurements were performed with ASTRID2, a synchrotron beamline at the Physics Department at Aarhus University. The photon flux per unit area (brilliance) at such facility is easily ten orders of magnitude larger than a typical laboratory source. Another advantage of using a Synchrotron source is the tunability of the photon energy so that the surface sensitivity and photoemission cross-section can be optimized for each element. Combined with the high flux, this means that high-resolution measurements can be performed at a much faster rate than using a laboratory source, this allows fast measurements even in low-density systems, i.e. the sub-monolayer adsorbate layers studied in this work so that surface reactions such as CO desorption, CO dissociation or ethylene dissociation can be monitored real-time [17–19].

In the present thesis, XPS was mainly used to analyze surface carbon species, and small shifts in the binding energy of photoelectrons were used to detect differences in the chemical nature of the surface carbon. Different carbon species show variations in binding energies and can be easily detected using SR-XPS. Table 2.1. shows some reference values obtained from the literature that help to assign the surface carbon species encountered in the experiments discussed here.

sp^3 [eV]	sp^2 [eV]	Carbide	Reference
	284.5	283.1	[20]
	284.6	283.5	[21]
285.8	284.8		[22]
		282.8	[23]
		283.2	[24]
		283.0	[25]

Table 2.1 Carbon binding energies for different carbon species on iron samples.

2.3.1 XPS quantification analysis

The number of photoelectrons collected from the surface is proportional to the concentration of the elements present. In order to determine the concentration, the peak area is analyzed. There are, however, different factors that can affect

quantitative analysis, such as the energy of photons, the cross-section of the core level, the type of analyzer and the angle of incidence and angle of emission [26–28]. These factors can largely be eliminated by using a known reference state. In the present work, we used a known reference to evaluate the Fe3p and C1s signal intensities. For Fe3p quantification, we exploited the fact that different Fe film thicknesses on Cu(100) give rise to distinctly different LEED patterns. Figure 2.8 shows the (5x1) LEED pattern obtained in the UHV chamber of the beamline, with its corresponding XPS spectrum. The literature shows this (5x1) corresponds to approximately 4 ML of iron [29]. We used this spectrum as a reference to quantify the amount of evaporated iron.

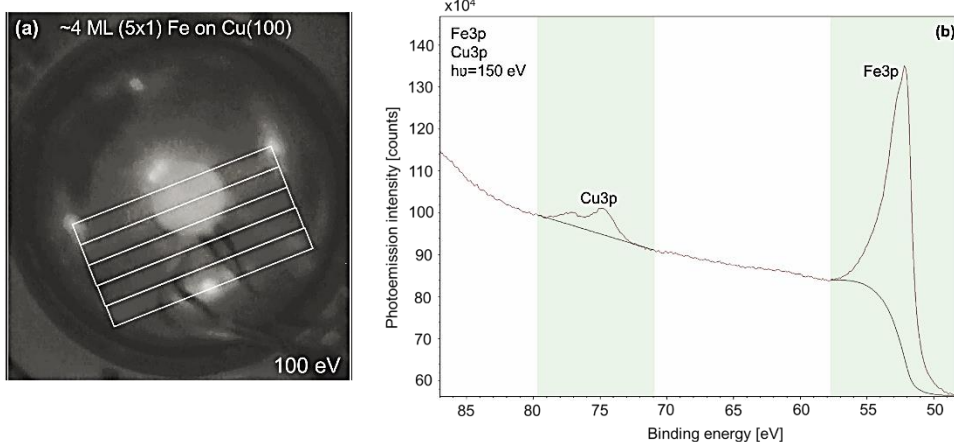


Figure 2.8 (a) (5x1) LEED pattern taken at 100 K after evaporating ~4 ML of iron on Cu(100) at room temperature. (b) XPS spectrum after recording the LEED pattern in (a) using 150 eV photon energy.

Figure 2.9 shows a C1s spectrum after saturating the Fe surface with carbon from ethylene dissociation, producing a single peak at 282.5 eV. Through in-house TPD-based quantification (see here-after), the carbon quantity deposited in this manner was determined to be 0.5 ML. This carbon peak was used as a reference to quantify the amount of deposited carbon. A Shirley background (BG) (black line) was used for quantitative evaluation. The BG represents the estimate for the inelastic scattered electrons moving through the solid state in the Shirley approximation [30–32].

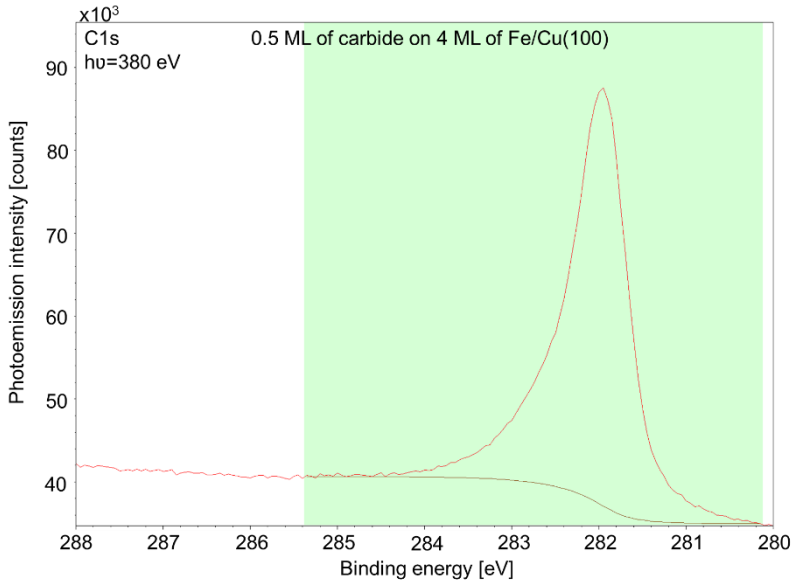


Figure 2.9. C1s spectra acquired in the ASTRID2, Synchrotron, using 380 eV photon energy.

2.4 Auger electron spectroscopy (AES)

Figure. 2.10. shows a schematic diagram of the core hole decay process that generates an Auger electron. Initially, ionizing radiation causes the ejection of an electron from the inner shell of the atom. Subsequently, the resulting hole is filled by an electron from a higher energy level.

The energy released by the electron relaxation from a higher to lower energy is transferred to a third electron, which is ejected as an Auger electron. The kinetic energy of the Auger electrons is given by:

$$E_{kin} = E_K - E_{L_1} - E_{L_{2,3}} - \varphi \quad \text{Eq. (2.3)}$$

Where E_{kin} is the kinetic energy of the Auger electron, E_K , E_{L_1} , E_{L_2} , and E_{L_3} are the binding energies of the K, L₁, L₂ and L₃ electron orbits of the atom, φ is the work function of the spectrometer [33,34]. In the present work, electrons with a typical

energy of 2 keV were used to create the core holes. The grids of the LEED optics are used as a retarding field analyzer to record an electron energy spectrum.

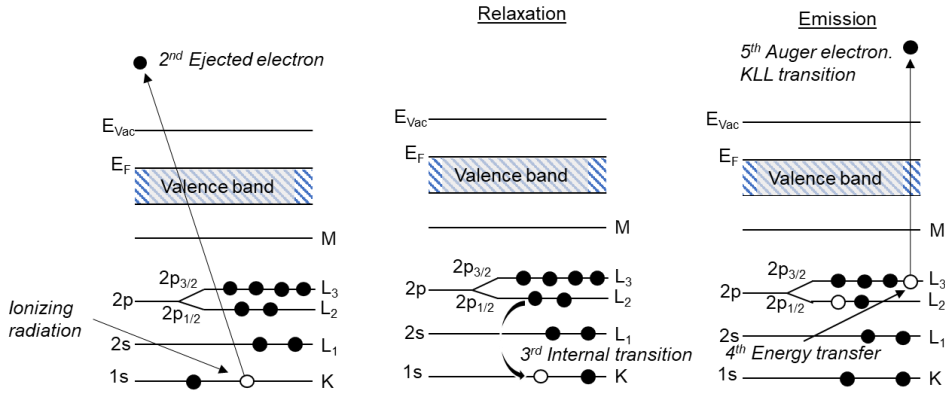


Figure 2.10. Diagrammatic steps in the Auger process for an isolated atom.

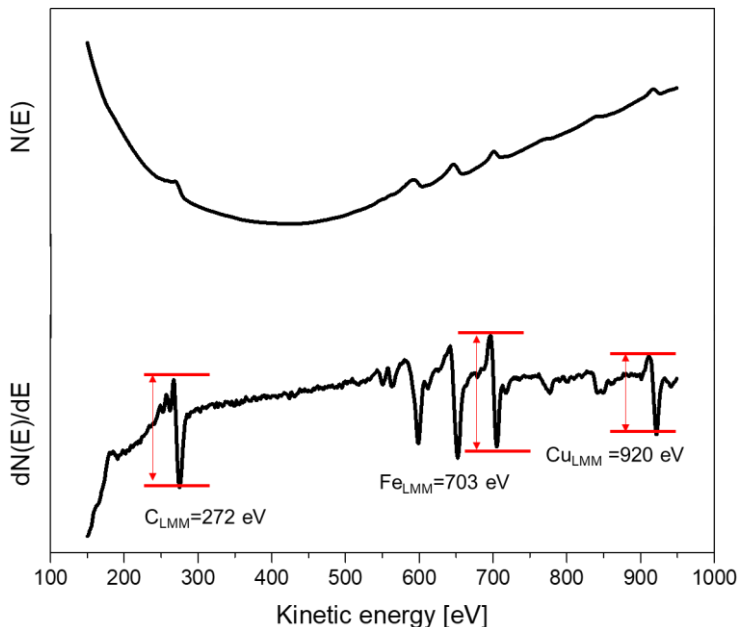


Figure 2.11. Upper curve: energy distribution $N(E)$ of backscattered electrons from an iron carbide film surface at a primary energy of 2000 eV. Lower curve: Differential distribution of the upper curve $dN(E)/dE$, demonstrating the improved resolution of the peaks. The red lines show the peak-to-peak intensities of the peaks.

In Figure. 2.11. a spectrum obtained after evaporating iron on Cu(100) followed by carburization of the film with ethylene is shown as an example. The signal consists of a large background signal on top of which the Auger electrons form small peaks. By using a lock-in amplifier, the derivative of the spectrum can be measured with a much better signal-to-noise ratio, as shown in the lower panel, and this is the typical manner in which Auger electron spectra are presented.

2.4.1 Auger quantification

Similar to XPS, AES offers a quantitative analysis of the chemical composition of the sample's outermost atomic layers. The peak area in the Auger spectrum presented in the $N(E)$ form is directly proportional to the elemental concentration. The large background of secondary electrons makes it difficult to determine the peak area accurately; instead, the peak-to-peak height in the derivative of the spectrum is typically used as a quantitative measure [35].

For light elements such as C or O, only the KLL Auger transition exists, but for heavier elements such as Cu and Fe, both the LMM transitions at high kinetic energy, and the MNN transitions at low kinetic energy (47 eV) are detectable. Many previous works prefer to use the low kinetic energy peaks due to higher surface sensitivity since the inelastic mean free path of these electrons (with KE of ~300 eV) is only about two monolayers. However, these low-energy Auger electrons are more susceptible to distortion by magnetic effects and localized specimen charging. The lack of reproducibility combined with a large secondary electron background in the low kinetic energy region makes it difficult to accurately determine the peak-to-peak ratio of the MNN transitions of Cu and Fe. Instead, the high kinetic energy peaks shown in Figure 2.11 were used as their peak heights could be determined more accurately [36].

When different elements are present in the sample, determining their relative concentrations in terms of atomic concentration is of interest. The elemental concentration can be expressed as:

$$C_x = \frac{I_x}{S_x d_x} / \sum_{\alpha} \frac{I_{\alpha}}{S_{\alpha} d_{\alpha}} \quad \text{Eq. (2.4)}$$

$$d_x = L_x E_{m,x} I_{p,x} \quad \text{Eq. (2.5)}$$

I_x = peak-to-peak amplitude of the element X from the test specimen

S_x = Relative sensitivity

d_x = Relative scale factor (detector and Lock-in amplifier)

L_x = Lock-in amplifier sensitivity

$E_{m,x}$ = Modulation energy

$I_{p,x}$ Primary beam current

The calculation of the sensitivity factors usually requires a pure silver target or a pure element inside the UHV chamber. Assuming a constant relative scale factor, we find these sensitivity factors to be tabulated elsewhere. The margin of error between tabulated values is lower than 1% for 3 keV and 5 keV beam energy [35,37,38]. In summary, we can calculate the atomic concentration using the peak height, measured as shown in Figure 2.11, and sensitivity factor of 0.2 for Fe, Cu and C, and 0.5 for O. Furthermore, well-known references like 0.5 ML of pure carbide, or 0.5 ML of oxygen were used to confirm these concentrations.

2.4.2 Auger as a qualitative technique to identify carbidic species.

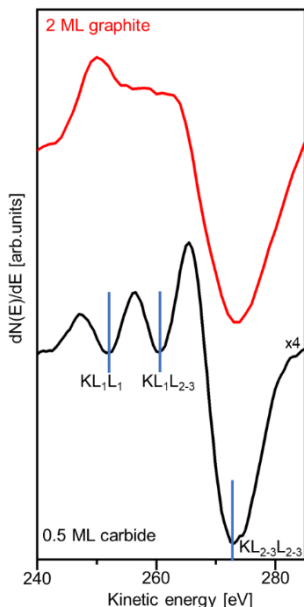


Figure 2.12. Comparison of two different C_{KLL} Auger spectra of iron carbide (black) and graphite (red) supported on $Cu(100)$ after ethylene dissociation and heating to 500 K and 900 K, respectively. Taken at 300 K and 2000 eV.

Like in XPS, the Auger signal contains information about the chemical nature of the element. However, since the Auger peak shape is usually complex, it is often difficult to extract useful information easily. For the present work, the peak shape of the C_{KLL} transition is of particular interest. Literature reports indicate that the peak shape of carbidic carbon is distinctly different from that of graphitic carbon. In Figure 2.12, two different spectra, from carbide and graphite, can be seen. Carbides present three distinguishable features. These features are at kinetic energies of 253 eV (KL_1L_1), 261 eV ($KL_1L_{2,3}$) and 272 eV ($KL_{2,3}L_{2,3}$) [21], and this was routinely used to evaluate the quality of the carbide prepared. Because of the overlap of graphitic and carbidic carbon peaks, AES is less suitable for determining relative concentrations of a carbide and graphite mixture; in these cases, XPS provides more detailed information.

2.4.3 O_{KLL} + LEED to determine the amount of dissociated CO

A well-defined O-covered Cu(100) surface was used as a reference to quantitatively evaluate the O_{KLL} surface oxygen coverage.

250 L of O_2 were dosed at 500 K on Cu(100) to create a 0.5 ML of O_{ad} . The oxygen adsorption forms a $(\sqrt{2} \times \sqrt{2})R45^\circ$ LEED pattern characteristic for this system and is well-known in the literature [39–41]. After adsorbing the oxygen, an AES measurement was performed to determine the intensity of 0.5 ML of oxygen (O_{KLL}). In Figure 2.13, a summary of the beforementioned pattern and the Auger spectrum can be seen. The oxygen signal was used as a reference to cross-check XPS and TPD data of the amount of dissociated CO on iron and iron carbide layers.

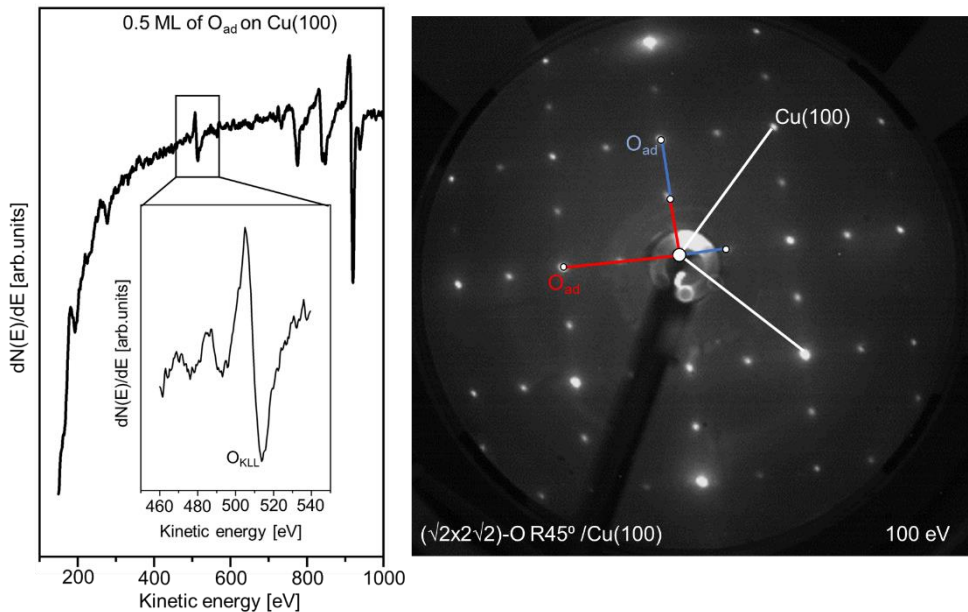


Figure 2.13. Auger spectrum after depositing 0.5 ML of oxygen on Cu(100). LEED pattern shows two different O_{ad} domains. LEED taken at 100 K and Auger at 300 K and 2000 eV

2.5 Temperature-programmed desorption (TPD)

Temperature-programmed techniques are used to examine the desorption of adsorbates and reaction products while linearly increasing the surface temperature [42]. These techniques have the advantage of being applicable to all areas of catalysis, such as single crystals, model catalysts, and industrial catalysts.

The temperature-programmed desorption method is particularly useful in surface science studies to examine the desorption of gases (dosed at low temperatures) from single crystals and polycrystalline foils and to examine desorption kinetics which provides information on adsorption strengths and reaction barriers.

The rate at which adsorbates desorb from the surface is given by the Arrhenius or Polanyi-Wigner equation.[43]

$$r_{des} = -\frac{d\theta}{dt} = v_n e^{\left(\frac{-\Delta E_{des}}{RT}\right)} * \theta^n \quad \text{Eq. (2.6)}$$

r_{des} = rate of desorption

θ = coverage in monolayers

t = time (s) ; T =temperature [K]

v_n = pre-exponential factor of desorption [s^{-1}]

ΔE_{des} = activation energy [J/mol]

R = gas constant [J/mol*K]

The TPD measurement is typically performed by adsorbing a molecule or atom onto a surface at a low temperature, typically 100 K in the present study. The sample is heated at a constant temperature (2 K/s in our case) after the gas is absorbed, and the desorbing species are identified and quantified using a quadrupole mass spectrometer.

When the pumping speeds are high, gas re-adsorption can be disregarded, and the desorption rate is linearly correlated with the mass spectrometer signal. This leads to the area under the TPD spectrum being proportional to the total quantity of desorbed species and, therefore, the initial relative coverage. The exposure of an

adsorbate is measured in Langmuir (where $1 \text{ L} = 1.33 \times 10^{-6} \text{ mbar}\cdot\text{s}$). The Langmuir unit is frequently used in surface science to measure the quantity of a substance adsorbed onto a surface. This unit is based on the "Langmuir pressure," defined as the pressure necessary to deposit a single layer of atoms or molecules onto the surface. The Langmuir unit is designed such that the number of atoms or molecules that strike the surface per unit of time should be comparable to the number of atoms or molecules present in a single atomic layer.

2.5.1 TPD+LEED References and Quantification

CO adsorption on Cu(100) and Cu(111). CO titration+coverage reference

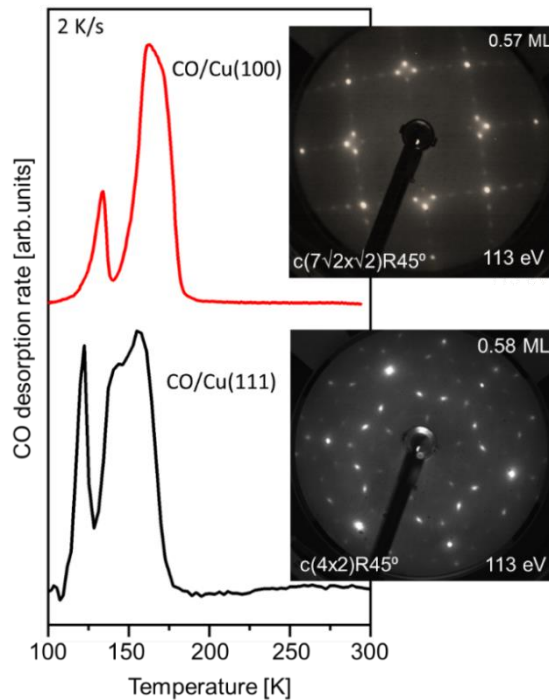


Figure 2.14. TPD spectra of CO from Cu(100) and Cu(111). The CO saturated (3 L) ad-layers form a $c(7\sqrt{2}\times 2)R45^\circ$ on Cu(100), and a $c(4\times 2)$ on Cu(111). LEED were taken at 100 K after saturating the surface with CO and 113 eV.

TPD can be used to derive the absolute surface coverage by using a well-known reference state. For quantitative CO coverage analysis, well-known CO structures on Cu(100) and Cu(111) were used. Figure 2.14 shows a relevant reference experiment of CO desorption from Cu(100) and Cu(111) single crystals. CO from Cu(100) (red-line) shows two desorption peaks at 135 K and 175 K. Literature proposes that the $c(7\sqrt{2} \times \sqrt{2})\text{-}45^\circ$ LEED pattern observed at 100 K corresponds to a CO coverage of 0.57 ML. The 135 K peak corresponds to desorption of 0.07 ML, leaving 0.5 ML that gives rise to a $c(2 \times 2)$ LEED pattern after heating to 140 K. This insight allows CO desorption peaks from the Fe and Fe_xCy-covered samples to be analyzed quantitatively. For the system, CO/Cu(111), similar coverage CO/Cu(100) was found [44].

H₂ adsorption on Cu(100). Carbon quantification

A well-defined adsorbate structure of hydrogen on Cu(100) was used as a reference for quantification of the hydrogen concentration desorption. H₂ dissociation on Cu(100) is an activated process, and a hot tungsten filament (~1600 K) was placed close to the sample during H₂ dosing to increase the dissociative sticking probability [45]. Figure 2.15 shows the H₂ desorption spectrum from the Cu(100) substrate, which served as a reference to determine the quantity of carbon deposited via ethylene decomposition. The total desorption area corresponds to 1 ML of adsorbed hydrogen atoms, with two different desorption states, one below 200 K forming a $p4g(2 \times 2)\text{-H}$ structure [45–47], and for temperatures higher than 200 K, the H_{ad} desorbs and the surface goes back to the original state, a (1×1). By quantifying the amount of desorbed H₂ from the Cu(100), we can determine the amount of desorbed H₂ from ethylene dissociation and, thus, the carbon left after dissociation.

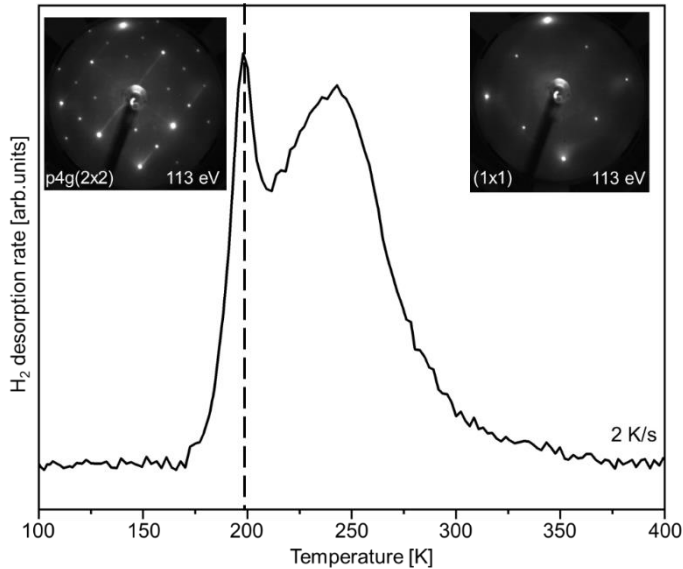


Figure 2.15. TPD spectrum from Cu(100) 2Ks^{-1} saturated with atomic hydrogen. The change in structure from $p4g(2\times 2)$ to (1×1) is shown in the inset. LEED patterns were taken at 100 K.

The peak shape of the H₂ desorption spectrum from Cu(100) is identical to that reported in the literature, while the desorption peak temperatures are somewhat lower than those found in ref. [45]. These authors state that the H₂ desorption peak temperatures are susceptible to small quantities of impurities, catalyzing recombinative H₂ desorption and causing a downward shift of the H₂ desorption [48]. Due to the frequent deposition of Fe in our experiments, a small amount of Fe typically persisted on the surface after cleaning, below the detection limit of AES but visible by SR-XPS, and we attribute the lower H₂ desorption from Cu(100) to the influence of residual Fe.

2.6 Thermal electron beam evaporation

The fabrication of iron carbide thin films discussed in this thesis involves the deposition of metallic iron onto a Cu substrate single-crystals via physical vapour deposition. To this end, the UHV set-up is equipped with a dual pocket electron beam evaporator (Tectra GmbH e-flux2). The shield around the evaporation source is

water-cooled and prevents excessive degassing of the source during operation at high temperatures.

For Fe deposition, an iron rod (99.997% GoodFellow) is biased by a high positive voltage of up to 2 kV. As a result, electrons from the surrounding filament are accelerated and bombard the tip of the rod, causing it to become heated so that iron starts to evaporate. The evaporated iron is partly ionized, and the evaporation rate can be measured by measuring the flux of positive ions [16]. These high-energy ions should not reach the surface as they may lead to sputtering damage. Thus, an ion trap is placed at the very tip of the evaporator to deflect the Fe ions so that they do not reach the sample surface and only neutral species arrive. To ensure reproducibility, we used a constant power to the Fe rod to obtain a flux of 20 nA for all the experiments in this thesis. Different Fe thicknesses were achieved by changing the evaporation time [49]. The Fe films are typically grown at 300 K at a typical pressure of 1×10^{-9} mbar during evaporation and a deposition rate of ~ 0.5 ML per minute.

2.7 Reflection Absorption InfraRed Spectroscopy (RAIRS)

Infrared absorption spectra were recorded using a Perkin Elmer Frontier spectrometer. After leaving the spectrometer, the (p-polarized) light travels through a compartment with custom-made optics that focus the beam onto the 8 mm disc-shaped sample. The light enters the vacuum chamber through a KBr window and is reflected off the sample surface, and the angle of incidence is 15° with respect to the surface plane. After reflection, the light leaves the vacuum chamber through another KBr window, after which it is focused onto a liquid nitrogen-cooled MCT detector. All parts of the beam path at atmospheric pressure are flushed with dry N_2 to eliminate signals from CO_2 (g) and H_2O (g) from the spectra. The spectrum obtained by reflection from a clean Cu(100) sample was subtracted from the spectra, and in addition, a spline background was used to eliminate changes in the background resulting from sample heating. All spectra were measured with a resolution of 4 cm^{-1} and a step size of 0.5 cm.

2.8 References

- [1] L.J. Clarke, *An Introduction to Low Energy Electron Diffraction*, JOHN WILEY & SONS, 1985.
- [2] G. Thomson, A. Reid, *Diffraction of Cathode Rays by a Thin Film*, *Nature*. 119 (1927) 890.
- [3] G. Thomson, *The Diffraction of Cathode Rays by Thin Films of Platinum*, *Nature*. 120 (1927) 802.
- [4] L.H. Davisson, C Hermer, *The Diffraction of Electrons by a Crystal of Nickel*, *Phys. Rev.* 30 (1927) 705–740. <https://doi.org/10.1002/j.1538-7305.1928.tb00342.x>.
- [5] M.A. Van Hove, W.H. Weinberg, C.-M. Chan, *Low-Energy Electron Diffraction*, in: *Low-Energy Electron Diffraction. Exp. Theory Surf. Struct. Determ.*, 1st ed., Springer Berlin, Heidelberg, 1986. <https://doi.org/10.1017/CBO9781107415324.004>.
- [6] M.S. Altman, *Trends in low energy electron microscopy*, *Condens. Matter*. 22 (2010) 084017. <https://doi.org/10.1088/0953-8984/22/8/084017>.
- [7] J.J. Lander, J. Morrison, F. Unterwird, *Improved Design and Method of Operation of Low Energy Electron Diffraction Equipment*, *Rev. Sci. Instrum.* 33 (1962) 782–783. <https://doi.org/10.1063/1.1717975>.
- [8] A.U. MacRae, *Low-Energy Electron Diffraction*, *Science* (80-.). 139 (1963) 379–388.
- [9] C. Kittel, *Introduction to solid state physics*, 8th ed., John Wiley & Sons, Inc, 2005. [https://doi.org/10.1016/0022-5096\(57\)90051-0](https://doi.org/10.1016/0022-5096(57)90051-0).
- [10] T. Urano, T. Kanaji, *Structures of iron films deposited on Si(111)7x7 surface studied by LEED*, *Appl. Surf. Sci.* 33–34 (1988) 68–74. [https://doi.org/https://doi.org/10.1016/0169-4332\(88\)90289-9](https://doi.org/https://doi.org/10.1016/0169-4332(88)90289-9).
- [11] T. Urano, M. Kaburagi, S. Hongo, T. Kanaji, *LEED I-V curve analysis for the structure of iron films on Si(111) surfaces*, *Appl. Surf. Sci.* 41–42 (1989) 103–106. [https://doi.org/https://doi.org/10.1016/0169-4332\(89\)90040-8](https://doi.org/https://doi.org/10.1016/0169-4332(89)90040-8).
- [12] Y. Darici, J. Marciano, H. Min, *LEED measurements of one monolayer of iron epitaxially grown on Cu(111)*, *Surf. Sci.* 195 (1988) 566–578. [https://doi.org/https://doi.org/10.1016/0039-6028\(88\)90360-3](https://doi.org/https://doi.org/10.1016/0039-6028(88)90360-3).
- [13] L.H. Jenkins, M.F. Chung, *LEED and Auger investigations of Cu (111) surface*, *Surf. Sci.* 24 (1971) 125–139. [https://doi.org/10.1016/0039-6028\(71\)90223-8](https://doi.org/10.1016/0039-6028(71)90223-8).
- [14] J.C. Tracy, *Structural influences on adsorption energy. III. CO on Cu(100)*, *J. Chem. Phys.* 56 (1972) 2748–2754. <https://doi.org/10.1063/1.1677603>.
- [15] K. Siegbahn, *Electron spectroscopy for atoms, molecules and condensed matter - an overview*, *J. Electron Spectros. Relat. Phenomena.* 36 (1985) 113–129. [https://doi.org/10.1016/0368-2048\(85\)80013-X](https://doi.org/10.1016/0368-2048(85)80013-X).

- [16] A. Einstein, B. Podolsky, N. Rosen, Can quantum-mechanical description of physical reality be considered complete?, *Phys. Rev.* 47 (1935) 777–780. <https://doi.org/10.1007/s10701-010-9411-9>.
- [17] J. Tersoff, D.R. Hamann, Theory of the scanning tunneling microscope, *Phys.Rev.B.* 31 (1985) 805–813. <https://doi.org/10.1103/PhysRevB.31.805>.
- [18] B. Hammer, J.K. Norskov, Electronic factors determining the reactivity of metal surfaces, *Surf. Sci.* 343 (1995) 211–220. [https://doi.org/10.1016/0039-6028\(96\)80007-0](https://doi.org/10.1016/0039-6028(96)80007-0).
- [19] H. Wolfschmidt, C. Baier, S. Gsell, M. Fischer, M. Schreck, U. Stimming, STM, SECPM, AFM and electrochemistry on single crystalline surfaces, *Materials (Basel)*. 3 (2010) 4196–4213. <https://doi.org/10.3390/ma3084196>.
- [20] J.C. Lascovich, R. Giorgi, S. Scaglione, Evaluation of the sp² / sp³ ratio in amorphous carbon structure by XPS and XAES, *Appl. Surf. Sci.* 47 (1991) 17–21. [https://doi.org/https://doi.org/10.1016/0169-4332\(91\)90098-5](https://doi.org/https://doi.org/10.1016/0169-4332(91)90098-5).
- [21] G. Panzner, W. Diekmann, The bonding state of carbon segregated to α -iron surfaces and on iron carbide surfaces studied by electron spectroscopy, *Surf. Sci.* 160 (1985) 253–270. [https://doi.org/10.1016/0039-6028\(85\)91040-4](https://doi.org/10.1016/0039-6028(85)91040-4).
- [22] S.T. Jackson, G.R. Nuzzo, Determining hybridization differences for amorphous carbon from the XPS C1s envelope, *Appl. Surf. Sci.* 90 (1995) 195–203. [https://doi.org/10.1016/0169-4332\(95\)00079-8](https://doi.org/10.1016/0169-4332(95)00079-8).
- [23] H.P. Bonzel, H.J. Krebs, On the chemical nature of the carbonaceous deposits on iron after CO hydrogenation, *Surf. Sci.* 91 (1980) 499–513. [https://doi.org/10.1016/0039-6028\(80\)90347-7](https://doi.org/10.1016/0039-6028(80)90347-7).
- [24] JB Butt, Carbide phases on iron-based Fischer-Tropsch synthesis catalysts part I: Characterization studies, *Catal. Letters*. 7 (1990) 61–81. <https://doi.org/10.1007/BF00764492>.
- [25] A. Wiltner, C. Linsmeier, Formation of endothermic carbides on iron and nickel, *Phys.Stat.Sol.* 201 (2004) 881–887. <https://doi.org/10.1002/psaa.200304362>.
- [26] S. Tougaard, A. Jablonski, Quantitative XPS: Influence of Elastic Electron Scattering in Quantification by Peak Shape Analysis, *Surf. Interface Anal.* 25 (1997) 404–408. [https://doi.org/https://doi.org/10.1002/\(SICI\)1096-9918\(199706\)25:6<404::AID-SIA250>3.0.CO;2-A](https://doi.org/https://doi.org/10.1002/(SICI)1096-9918(199706)25:6<404::AID-SIA250>3.0.CO;2-A).
- [27] MP Seah, The Quantitative Analysis of Surfaces by XPS: A review, *Surf. Interface Anal.* 2 (1980) 222–239. <https://doi.org/https://10.1002/SIA.740020607>.
- [28] S. Tougaard, Accuracy of the Non-destructive Surface Nanostructure Quantification Technique Based on Analysis of the XPS or AES Peak Shape, *Surf. Interface Anal.* 26 (1998) 249–269. [https://doi.org/https://doi.org/10.1002/\(SICI\)1096-9918\(199804\)26:4<249::AID-SIA368>3.0.CO;2-A](https://doi.org/https://doi.org/10.1002/(SICI)1096-9918(199804)26:4<249::AID-SIA368>3.0.CO;2-A).
- [29] A. Biedermann, M. Schmid, P. Varga, Nucleation of bcc iron in ultrathin fcc films, *Phys. Rev. Lett.* 86 (2001) 464–467. <https://doi.org/10.1103/PhysRevLett.86.464>.
- [30] C.D. Wagner, L.E. Davis, M.V. Zeller, J.A. Taylor, R.H. Raymond, L.H. Gale, Empirical Atomic Sensitivity Factors for Quantitative Analysis by Electron Spectroscopy for Chemical

2.8 References

- Analysis, Surf. Interface Anal. 3 (1981) 211–225. <https://doi.org/https://doi.org/10.1002/sia.740030506>.
- [31] J.E. Castle, A.M. Salvi, Interpretation of the Shirley background in x-ray photoelectron spectroscopy analysis, *J. Vac. Sci. Technol. A Vacuum, Surfaces, Film.* 19 (2001) 1170–1175. <https://doi.org/10.1116/1.1378074>.
- [32] A.V. Shchukarev, D.V. Korolkov, XPS study of Group IA carbonates, *Cent Eur J Chem.* 2 (2004) 347–362. <https://doi.org/https://doi.org/10.2478/BF02475578>.
- [33] C. Linsmeier, Auger electron spectroscopy, *Vacuum.* 45 (1994) 673–690. [https://doi.org/10.1016/0042-207X\(94\)90108-2](https://doi.org/10.1016/0042-207X(94)90108-2).
- [34] J.C. Rivière, Auger electron spectroscopy, *Contemp.Phys.* 14 (1973) 513–559.
- [35] L.E. Davis, N.C. MacDonald, P.W. Palmberg, G.E. Riach, R.E. Weber, *Handbook of Auger electron spectroscopy*, Second, Edina, MN, 1972. <https://doi.org/10.16309/j.cnki.issn.1007-1776.2003.03.004>.
- [36] C. Argile, G.E. Rhead, Calibration in Auger electron spectroscopy by means of coadsorption, *Surf. Sci.* 53 (1975) 659–674. [https://doi.org/10.1016/0039-6028\(75\)90162-4](https://doi.org/10.1016/0039-6028(75)90162-4).
- [37] P. Palmberg, Quantitative Auger Electron Spectroscopy Using Elemental Sensitivity Factors., *J Vac Sci Technol.* 13 (1975) 214–218. <https://doi.org/10.1116/1.568853>.
- [38] P.M. Hall, J.M. Morabito, D.K. Conley, Relative sensitivity factors for quantitative Auger analysis of binary alloys, *Surf. Sci.* 62 (1977) 1–20. [https://doi.org/10.1016/0039-6028\(77\)90424-1](https://doi.org/10.1016/0039-6028(77)90424-1).
- [39] R.N. Lee, H.E. Farnsworth, LEED studies of adsorption on clean (100) copper surfaces, *Surf. Sci.* 3 (1965) 461–479. [https://doi.org/10.1016/0039-6028\(65\)90026-9](https://doi.org/10.1016/0039-6028(65)90026-9).
- [40] J.H. Onuferko, D.P. Woodruff, LEED structural study of the adsorption of oxygen on Cu {100} surfaces, *Surf. Sci.* 95 (1980) 555–570. [https://doi.org/10.1016/0039-6028\(80\)90195-8](https://doi.org/10.1016/0039-6028(80)90195-8).
- [41] M. Wuttig, R. Franchy, H. Ibach, Oxygen on Cu(100) - a case of an adsorbate induced reconstruction, *Surf. Sci.* 213 (1989) 103–136. [https://doi.org/10.1016/0039-6028\(89\)90254-9](https://doi.org/10.1016/0039-6028(89)90254-9).
- [42] J.W. Niemantsverdriet, *Spectroscopy in Catalysis*, 3rd ed., Weinheim, 2007.
- [43] J.L. Falconer, J.A. Schwarz, Temperature-Programmed Desorption and Reaction: Applications to Supported Catalysts, *Catal.Rev.* 25 (1983) 141–227. <https://doi.org/10.1080/01614948308079666>.
- [44] J. Pritchard, On the structure of CO adlayers on Cu(100) and Cu(111), *Surf. Sci.* 79 (1979) 231–244. [https://doi.org/10.1016/0039-6028\(79\)90039-6](https://doi.org/10.1016/0039-6028(79)90039-6).
- [45] I. Chorkendorff, P.B. Rasmussen, Reconstruction of Cu(100) by adsorption of atomic hydrogen, *Surf. Sci.* 248 (1991) 35–44. [https://doi.org/10.1016/0039-6028\(91\)90059-2](https://doi.org/10.1016/0039-6028(91)90059-2).
- [46] C. Egawa, E.M. McCash, R.F. Willis, Adsorption of hydrogen on thin fcc-iron films grown on Cu(100), *Surf. Sci.* 215 (1989). [https://doi.org/10.1016/0039-6028\(89\)90691-2](https://doi.org/10.1016/0039-6028(89)90691-2).

- [47] I. Chorkendorff, P.B. Rasmussen, The p4g or pgg reconstruction on Cu(100), *J. Phys. Condens. Matter.* 3 (1991). <https://doi.org/10.1088/0953-8984/3/S/017>.
- [48] M.D. Marcinkowski, M.T. Darby, J. Liu, J.M. Wimple, F.R. Lucci, S. Lee, A. Michaelides, M. Flytzani-Stephanopoulos, M. Stamatakis, E.C.H. Sykes, Pt/Cu single-atom alloys as coke-resistant catalysts for efficient C-H activation, *Nat. Chem.* 10 (2018) 325–332. <https://doi.org/10.1038/NCHEM.2915>.
- [49] T. Detzel, Th., Memmel, N., and Fauster, Growth of ultrathin iron films on Cu(001): an ion-scattering spectroscopy study, *Surf. Sci.* 293 (1993) 227–238. [https://doi.org/10.1016/0039-6028\(93\)90316-C](https://doi.org/10.1016/0039-6028(93)90316-C).

03

**FABRICATION OF IRON
CARBIDE FILMS ON
Cu(100)**

ABSTRACT: Iron carbide (Fe_xC_y) thin films were prepared via iron evaporation on Cu(100) followed by ethylene adsorption and heating to 500K. Epitaxial growth of iron on Cu(100) led to the coexistence of FCC(100) and strained BCC(110) iron, whereby superstructure spots appear in the Low Energy Electron Diffraction (LEED) patterns at almost every coverage. Synchrotron X-ray photoelectron spectroscopy (SR-XPS) and Auger electron spectroscopy (AES) confirm that a pure carbide is formed after ethylene dissociation, showing a single peak at 282.6 eV in the C1s spectrum, and three characteristic Auger transitions in the C_{KLL} Auger spectrum. Quantification of H_2 produced during ethylene decomposition shows that a maximum of 0.5 ML carbon can be deposited for films that cover the substrate completely (2-12 ML). Carbon atoms enforce a tetracoordinate square planar arrangement of the surrounding iron atoms, creating a $\text{p}4\text{g}(2\times 2)$ clock reconstruction with coverage of 0.5 ML, forming a Fe_2C surface composition. The electron diffraction does not show any spots related to BCC-Fe(110), indicating that the structure of the underlying Fe layers transforms into the FCC structure when the outermost layer reconstructs into the $\text{p}4\text{g}(2\times 2)$ clock reconstruction. The formation of bulk carbide with a $\text{p}4\text{g}(2\times 2)$ surface structure was found after evaporating Fe in an ethylene atmosphere.

This chapter was published as: D.Garcia Rodriguez, M.A. Gleeson, J.V. Lauritsen, Z.Li, X.Yu, J.W. Niemantsverdriet, C.J. Weststrate. Iron Carbide Formation on Thin Iron Films Grown on Cu(100): FCC Iron Stabilized by a Stable Surface Carbide. Appl.Surf.Sci. 585 (2022) 152684. <https://doi.org/10.1016/j.apsusc.2022.152684>

3.1 Introduction

Fe_xC_y finds application in various fields due to its magnetic properties, such as in biomedicine, which can be used for drug delivery or magnetic hyperthermia [1,2]. Iron oxides have also been tested for oxygen reduction reactions as a negative electrode for application in energy storage [3], and they are also used in the chemical industry where iron catalysts are being used for Fischer-Tropsch Synthesis (FTS), among others, due to high selectivity manipulation and low price [4,5]. Although the bulk structure of catalytically active Fe_xC_y particles has been studied extensively through the years with many different techniques like HRTEM, EXAFS, and Mössbauer spectroscopy [6–8], very few experimental studies discuss the structure and reactivity of Fe_xC_y surfaces, where the catalytic action happens. Most articles

where well-defined Fe_xC_y surfaces are studied take a computational approach [9–14], while experimental work is much more difficult since iron carbide crystal surfaces are not commercially available. Although iron carbide films can be formed on single-crystal surfaces of Fe, e.g., Fe(100), Fe(110), and Fe(111) [14–17], Fe single-crystal surfaces are generally hard to clean due to the presence of bulk contaminants such as sulfur and carbon. In practice, multiple cycles of Ar^+ sputtering combined with prolonged heating in a H_2 atmosphere are often needed to remove these persistent impurities [18,19]. Another approach is to evaporate metallic Fe onto a single crystal substrate of, e.g., Au, an approach that has been used often to study thin film Fe oxides [20–22] but hardly in the formation of Fe_xC_y model systems. A recent study about Fe deposited on Au(111) used atomic carbon and ethylene as carbon sources in the carburizing process and highlighted the influence of Fe thickness on the carburization process [23]. The Fe film on top of Au(111) shows a structural evolution from a close-packed FCC-like structure for sub-ML Fe film thicknesses to a BCC [23,24]. Bulk Fe carbide formation was only found to occur for $\geq 3\text{ML}$ films, but the resulting carbide is not pure as the XPS spectrum shows sp^3 and sp^2 carbon peaks along with the carbide peak.

We used a Cu(100) crystal to investigate the influence of the substrate on Fe_xC_y formation. The complexity of the binary system Fe+Cu has been studied due to its interesting magnetic properties, which vary with Fe thickness and have inspired detailed LEED and STM studies [25–31]. We refer to the work of Biedermann et al. for an in-depth discussion about the morphology of thin Fe films on Cu surfaces [25,32–35].

Carbon monoxide is used as the carbon source for Fe_xC_y formation in applied catalysis, where the oxygen is removed as either CO_2 or H_2O when CO/H_2 mixtures are used [4]. As oxygen removal is difficult in our model system, ethylene was instead used as a carbon source.

After outlining the experimental details, we start with a brief discussion of the coverage-dependent Fe film morphology prior to exposure to ethylene. The intermediate and final stages of Fe_xC_y formation via ethylene decomposition on the evaporated Fe film are discussed in more detail. We then show how the Fe film thickness influences the morphology of the carbide layer, followed by an

investigation of the thermal stability. In the last part, we step away from ethylene post-treatment of Fe films and briefly study how Fe bulk phases can be produced by modifying the experimental procedure.

3.2 Experimental

Temperature programmed desorption (TPD), low energy electron diffraction (LEED) experiments, and Auger electron spectroscopy (AES), with a primary energy of 2000 eV, were carried out in a home-built UHV chamber with a base pressure below 2×10^{-10} mbar. It is equipped with two quadrupole mass spectrometers, LEED/Auger optics, and a dual pocket e⁻ beam evaporator. TPD experiments were performed using a QMS located inside a separately pumped compartment with a 5mm wide aperture connecting the main chamber. During a desorption experiment, the sample is placed 2mm from the aperture to eliminate desorption signals from other parts of the sample holder. Quantitative evaluation was cross-checked with the simultaneously measured signal from a second QMS located in the main chamber to eliminate potential errors that arise from directional desorption [36].

Synchrotron radiation x-ray photoelectron spectroscopy (SR-XPS) was performed at the Matline beamline at the ASTRID2 synchrotron light source (Aarhus, Denmark). Fe3p and Cu3p, C1s, and O1s core level spectra were recorded in normal emission using photon energies of 150eV, 380eV, and 650eV, respectively. The Fermi edge measured at each photon energy was used to calibrate the binding energy (BE) scale. STM was measured using a home-built Aarhus STM at the Interdisciplinary Nanoscience Center (iNANO).

For TPD and LEED/Auger experiments, a disc-shaped Cu(100) single crystal was mounted using a U-shape 0.5mm (diameter) tungsten (W) wire placed in a couple of slits at the side of the sample. The W wire was in thermal contact with a liquid nitrogen reservoir to reach sample temperatures of ~90K. The temperature was measured using a K-type thermocouple fixed in a small hole on the side of the Cu sample. Heating was achieved by passing a direct current through the support wires. For the SR-XPS and STM measurements, a hat-shaped Cu(100) single crystal was mounted in a Ta sample holder. The sample is heated using a filament placed at the

backside of the sample. e^- beam heating was employed for high-temperature annealing, while only radiative heating was used during in-situ photoemission experiments to minimize the influence of the heater on the position of the photoemission peaks. The temperature was measured using a type K (chromel-alumel) thermocouple tightly clamped to the backside of the sample. The Cu(100) substrates (8mm diameter) were cleaned by cycles of Ar^+ ion bombardment (10 minutes, 1keV and 300K), followed by flash annealing to 1000K, and this resulted in a sharp (1x1) LEED pattern. Surface impurities, including carbon and oxygen, were below the AES and SR-XPS detection limit, although small amounts of residual Fe were occasionally detected by SR-XPS after cleaning.

Fe was evaporated at 300K by electron beam evaporation from a 99.999% purity rod. The new evaporated Fe film remains up to around 500K, after which alloying between Fe and Cu becomes significant, particularly for very thin films [37]. Our studies were, therefore, in most cases limited to <500K to avoid Cu segregation [38]. An evaporation rate of around 0.5ML/min was typically used, and it was calibrated using the attenuation of Cu_{LMM} Auger electrons.

3.3 Iron thin film structure and morphology

The thickness-dependent iron morphology on a Cu(100) substrate after evaporation at room temperature was studied using a combination of LEED, STM, TPD, and AES, where the latter was used to determine film thickness based on Auger electron attenuation as explained in detail in Chapter 2.

The initial stages of iron growth on Cu(100) were studied using STM, as shown in Figure 3.1. Height measurements of a 0.6 ML iron film show that the smaller islands have a height of 0.2 nm, that is, a thickness of 1 ML, with a square-like structure. The larger islands have a typical height of 0.4 nm (2 ML), while a height of 0.6 nm (3 ML) is seen occasionally. We can see, in these Fe islands, how some of the edges follow the Cu substrate (direction indicated in (b)), whereas other island edges form angles of 75° - 78° , close to the 70.5° bond angles of relaxed BCC Fe [39]. Thus, the STM images show a tendency for bilayer island growth in the sub-ML regime, as

reported elsewhere [34,35,40]. Moreover, the LEED and STM images highlight that the BCC-Fe forms already for a local Fe thickness of 2 ML.

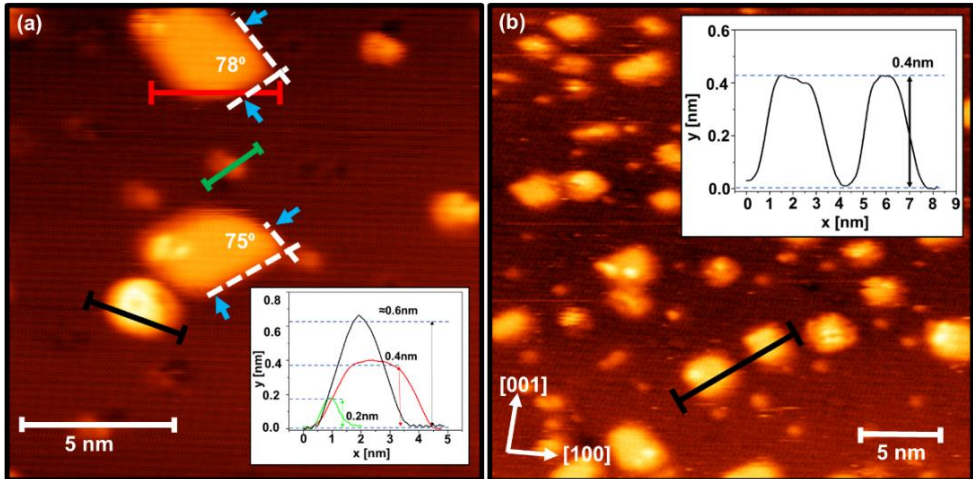


Figure 3.1. 0.6 ML of Fe deposited and imaged at RT. **(a)** An STM image shows some Fe clusters with bond angles of 75°-78°, close to the BCC (110) bond angle of 70.5°. ($V_t=0.15V$ $I_t=0.31$ (15nm x 15nm)) **(b)** STM image showing two monoatomic step islands and as bright spots, the third layer nucleates before the Cu substrate is completely covered ($V_t=0.22V$ $I_t=0.36V$ (30nm x 30nm)).

LEED provides information about the surface structure of the iron film before and after carbon deposition. After the iron is deposited at room temperature, in Figure 3.2, superstructure beams can be observed at 1/4-order positions for coverage of 2 ML, at 1/5-order positions for coverage of 4 ML, and at 1/2-order positions for coverage of 5 to 12 ML. The superstructure beams are shown as extra spots with discernible intensities and can only be observed near substrate spots, such as satellites of the substrate spots.

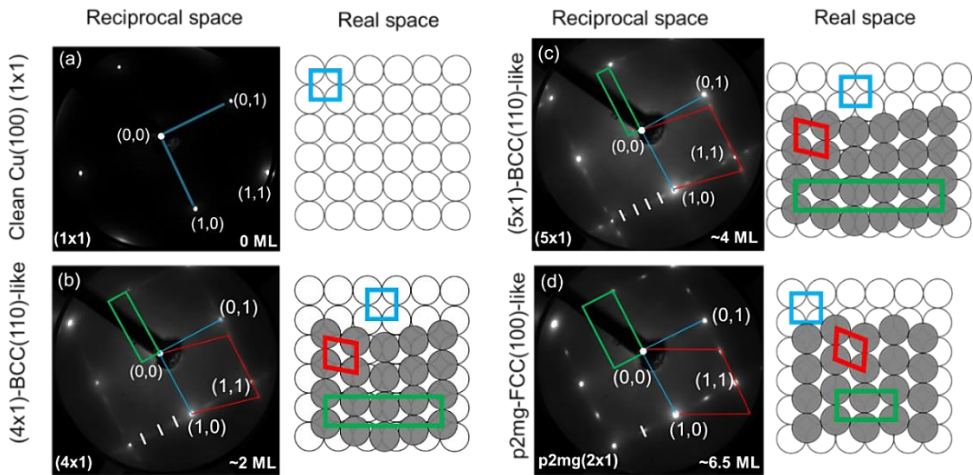


Figure 3.2. **(a)** (1×1) pattern from the $\text{Cu}(100)$ substrate after Ar^+ sputtering and flash anneal cycle. **(b-d)** Coexistence of Fe BCC(110) and Fe FCC(100) forming the superstructures (4×1) , (5×1) and (2×1) . Colored in green is the FCC(100) unit cell due to $\text{Cu}(100)$ and Fe FCC(100). The unit cell of the BCC-like structure is colored red. LEED were taken at 100 K and with 100 eV electron energy.

On the on-top view (real space schemes), only the top substrate layer (open circles) and the top iron layer (grey) are displayed for simplicity. The order positions correspond to the inverse of the distance in real space. In other words, an order of $1/4$ in reciprocal space corresponds to a distance of 4 atoms in real space. The direction of the unit cell in the diffraction pattern needs to be rotated by 90° to create the real space diagram. With our current techniques, we cannot determine the atomic distribution of atoms in space, although many studies in IV-LEED and STM can confirm the distribution of atoms [30,34]. More information on how to extract information from a diffraction pattern can be found in Chapter 2.

The (5×1) unit cell is characteristic of a ~ 4 ML iron film on $\text{Cu}(100)$, as shown in several articles [28,31,32,41]. The model of the corresponding surface structure included in Figure 3.2 (c) is based on the IV-LEED studies by Müller et al. [42], who propose that the (5×1) pattern is caused by a BCC-like distortion that affects all Fe layers in the film where the outermost layer has a strained BCC-(110) surface. This was confirmed later in STM studies performed by Biedermann et al. [32,33], who

show that the surface of iron films below 6 ML consists of a regular arrangement of 2–4 atoms wide strained BCC twins. STM furthermore revealed that a few per cent of the FCC-(100) structure [25,34] coexists alongside the strained BCC layer for films thinner than 4 ML. The amount of FCC-(100) can vary significantly as a function of experimental parameters such as iron deposition rate and temperature but generally becomes more abundant for layer thicknesses above 4 ML. A $p2mg(2 \times 1)$ found between ~ 5 ML and ~ 12 ML is attributed to an FCC Fe film with a reconstructed surface. The corresponding real space structure was determined elsewhere [43] and is displayed schematically in Figure 3.2 (d).

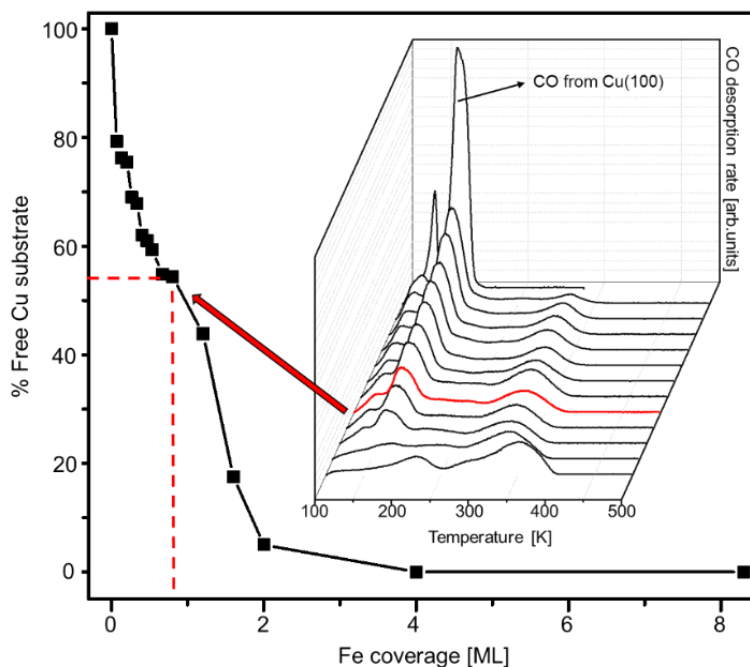


Figure 3.3. The figure shows the decrease in the contribution of the CO desorption on Cu when the Fe coverage increases. In the inset, the CO-titration technique where the CO TPD series is plotted. For 1 ML of evaporated Fe, there is 50% of free Cu, equivalent to bilayer island growth. The heating rate of the TPD was 2 K/s.

CO desorption from Cu(100) occurs below 200 K and can be distinguished from CO desorbing from the Fe-covered part [44], thus providing additional information about the Fe growth mode on Cu(100). The main panel of Figure 3.3 shows the available

Cu surface area as a function of the quantity of Fe deposited as derived from the CO desorption spectra provided in the inset. The data show that 1 ML of Fe deposition leads to ~50% suppression of the Cu-related CO desorption peaks, consistent with the growth of bilayer islands observed in STM. This is further corroborated by the observation that the Cu-related desorption peaks have disappeared after depositing 2 ML. The nature of the peaks at temperatures higher than 200 K will be discussed in more detail in Chapter 4, related to the reactivity of CO on iron and iron carbide films.

3.4 Ethylene dissociation on a 4 ML iron film

The 4 ML thick iron layer that appears as a (5x1) overlayer pattern in LEED was selected for a detailed investigation of carbide formation via ethylene decomposition. Figure 3.4 (a) shows the H₂ ($m/z=2$) and ethylene ($m/z=26$) desorption spectra after dosing ethylene to saturation (~3 L) at 100 K. H₂ desorption is seen in two stages and occurs up to ~425 K. A second ethylene adsorption step at 100 K followed by heating to 500 K showed only a small quantity of additional H₂ produced, whereas a third cycle did not show any additional H₂ production. This indicates that one cycle is sufficient to saturate the surface with carbon.

Figure 3.4 (a) also shows the H₂ desorption spectrum from the Cu(100) substrate (dotted line), which served as a reference to determine the quantity of carbon deposited via ethylene decomposition, as explained in more detail in Chapter 2.

Figure 3.4 (b) shows the XP spectra obtained for two subsequent ethylene adsorption and heating cycles. The intensity of C1s after the second dose of ethylene hardly changes, confirming that two doses are sufficient to saturate the iron surface with carbon. The C1s spectrum contains only a single peak in the carbide region around 282.6 eV, attributed to a carbide of high purity [23,45–49]. This is different from the Fe_xC_y/Au(111) system, where sp² and sp³ forms of carbon were reported alongside carbidic carbon after decomposing ethylene, as shown by the dashed line in Figure 3.4 (b). A minor shift of 0.3 eV towards higher BE can be attributed to strain effects [50]. The shape of the Auger spectrum recorded immediately after the TPD experiments is shown in the inset of Figure 3.4 and confirms that a carbide layer is

formed, as it clearly shows the Auger transitions at 254.2 eV, 261.5 eV, and 271.3 eV characteristic of carbide [45,50].

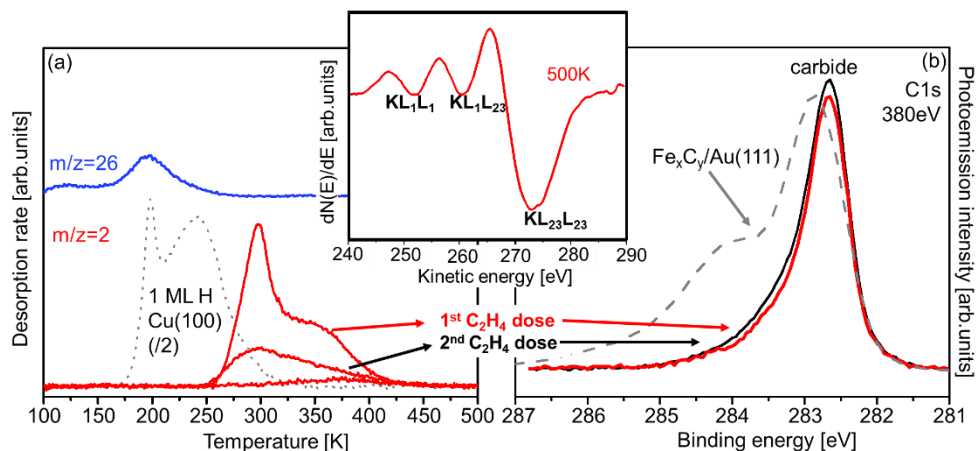


Figure 3.4. (a) As red, the hydrogen desorption for three consecutive ethylene dosing-heating cycles (2 K/s) on ~ 4 ML Fe/Cu(100). The desorption of molecular ethylene ($m/z=26$) for the first cycle is also provided, along with the desorption of 1 ML H_{ad} from the clean Cu(100) substrate used to quantify the carbon content. Note that its intensity is divided by 2 to match the scale of the other spectra. (b) C1s after dissociating ethylene two times on the ~ 4 ML Fe (5x1) film (the red spectrum was recorded after the first ethylene dissociation reaction, black after the second).

For comparison, we include the C1s spectrum of a ~ 6 ML Fe/Au(111) film after exposure to ethylene and heating from [23], shown as a dotted line. The C1 spectrum contains sp^2 , sp^3 , and carbide contributions. XPS spectra were taken with 380 eV photon energy and at 100 K. The inset shows the C_{KLL} Auger spectrum of the 4 ML Fe/Cu(100) film after heating in ethylene, confirming the presence of carbidic carbon.

SR-XPS was also used to identify the intermediates formed during the heating of an ethylene-covered ~ 4 ML Fe/Cu(100) sample. Figure 3.5(a) shows a heat map of the C1s spectral region recorded during a slow heating of the sample, while individual spectra at key temperatures are shown in Figure 3.5(b). At 100 K, the peak at a BE of 284 eV is attributed to ethylene molecules adsorbed intact on the Fe surface. The spectrum between 210-280 K shows two components, at 283.2 eV and 282.7 eV, respectively, associated with the first ethylene decomposition product. Ethylene decomposition on Fe(110) gives acetylene (C_2H_2) as a product [15]; however, the

presence of two peaks at 250 K suggests a species with two inequivalent carbons or a mixture of products. Ethylene decomposition on Ni(100) was studied by high-resolution XPS, and in this study, vinyl ($\text{CH}_2\text{-CH}$), as well as acetylene and acetylide (CCH), were identified as the intermediates formed during ethylene decomposition [51]. Due to the presence of two peaks at 250 K, we suggest that the species involved in ethylene decomposition on Fe/Cu(100) are either vinyl or vinylidene ($\text{CH}_2\text{-C}$), where the 283.2 eV peak would then be attributed to the $\text{H}_2\text{C-}$ end and the 282.7 eV peak to the -C(-H) end, respectively. The spectral shape changes again at 300 K, and together with the H_2 TPD from the ethylene dissociation, we can say that 50% of the hydrogen atoms desorbed from the surface at this temperature leaving acetylene or vinylidene as possible species. Further heating causes the remaining hydrogen to desorb until 400 K, most likely involving acetylide (CCH or $\text{C}\equiv\text{C}$) intermediates. All carbon atoms in these species have a BE close to 282.5 eV, characteristic for carbidic carbon and it is difficult to identify the exact composition from the XP spectrum alone. An additional change of intensity occurs around 425K. It is important to clarify that the C1s intensity of the C_xH_y adsorbates is often affected by photoelectron diffraction effects, especially for the low kinetic energy used here (100 eV) [52]. This increase in the C1s intensity is then not related to an increase in the surface carbon concentration but instead to a change in the chemical nature of the carbon, and because at 425 K there is no hydrogen adsorbed on the surface, we attribute this change in intensity to the scission of the C-C to yield atomic carbon. In summary, we conclude that ethylene decomposition occurs in three steps and involves similar intermediates to those found on Ni(100), as reported by Neubauer et al. [51]. Ethylene decomposes around 200 K to form vinyl or vinylidene while the two hydrogen atoms produced remain co-adsorbed. They desorb around 300 K while the C_2H_x adsorbates dehydrogenate further via acetylide intermediates. At 425 K, the C-C bond breaks to form atomic carbon.

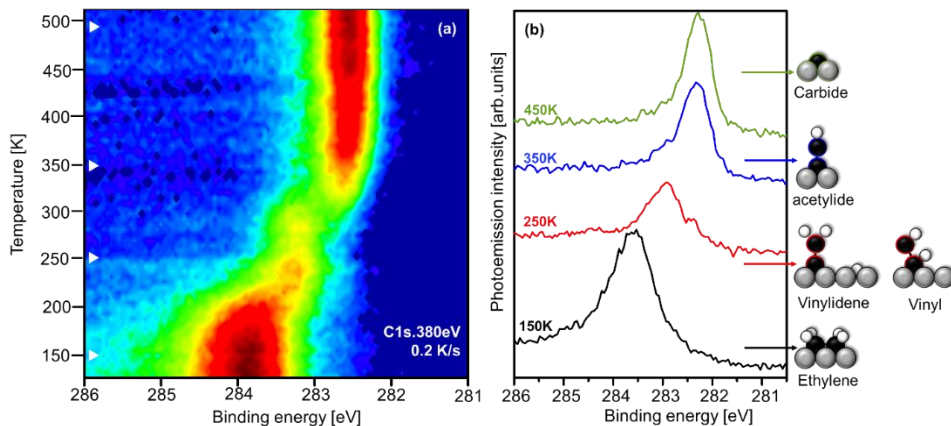


Figure 3.5. (a) C1s spectra were recorded while heating an ethylene-covered 4 ML Fe film in vacuum ($h\nu=380\text{eV}$, 6K per spectrum, low intensity=dark blue, high intensity=red/black, heating rate 0.2 K/s). (b) Individual C1s spectra [average of 3-5 scans from (a)] representative of the temperatures indicated in the figure as white symbols.

3.5 Carbon-induced “clock” reconstruction on iron thin films

Figure 3.6 (b) shows the sharp LEED pattern found after three cycles of ethylene adsorption at 100 K and heating to 500K on a ~ 4 ML thick Fe film. The diffraction pattern shows a $p4g(2\times 2)$ with missing spots at $(h+\frac{1}{2}, 0)$ and $(0, k+\frac{1}{2})$ due to the presence of two glide planes that arise from a clock-anti-clock-wise rotation of the substrate atoms [53–55]. The carbon coverage of 0.5 ML for this structure matches the experimentally determined carbon coverage of ~ 0.5 ML. This so-called ‘clock’ reconstruction is known to form due to carbon on FCC(100) surfaces of Ni(100) [54] and FCC-Co(100) [56], while it occurs under the influence of oxygen on Rh(100) [57]. It should be noted that the LEED diffraction pattern shows no traces of diffraction spots other than those that come from an FCC lattice. This implies that the whole ~ 4 ML thick Fe layer, which exposed a BCC(110)-like surface before carbon deposition as evident from the (5×1) pattern [Figure 3.6(a)], changes to the FCC structure after transforming only the outermost Fe layer into clock-reconstructed Fe_2C . Thus, the combined characterisation shows that carbon causes a $\sim 4\text{ML}$ thick Fe film on

Cu(100) with a distorted BCC(110) structure to reconstruct into an FCC-Fe film terminated by a clock'-reconstructed Fe₂C surface layer, as summarized schematically in Figure 3.6.

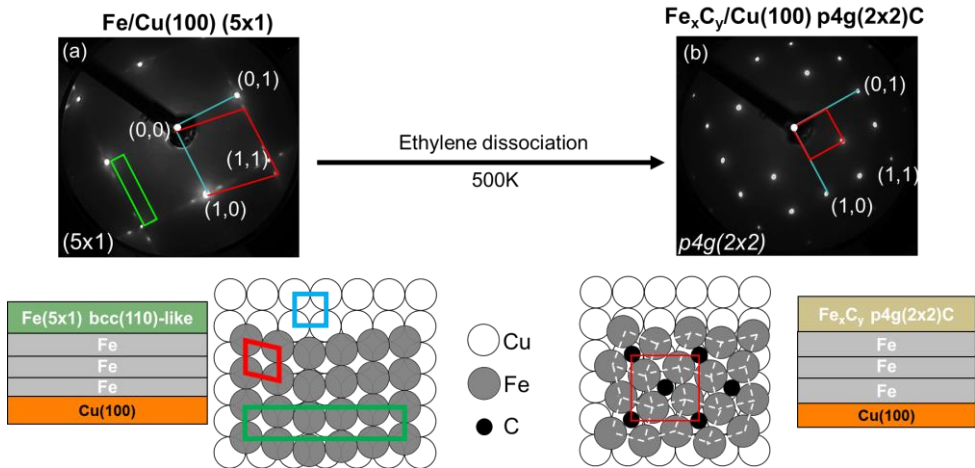


Figure 3.6. **(a)** A ~4 ML substrate was used for the carburization reaction. **(b)** The LEED pattern obtained after carbon reconstructed the (5x1) Fe surface shows a p4g(2x2), the carbon unit cell is colored red. The systematic absences $(h+1/2,0)$ and $(0,k+1/2)$ confirm the glide planes in the structure. LEED patterns were taken at 100K and 100 eV electron energy

3.6 Film-thickness dependence

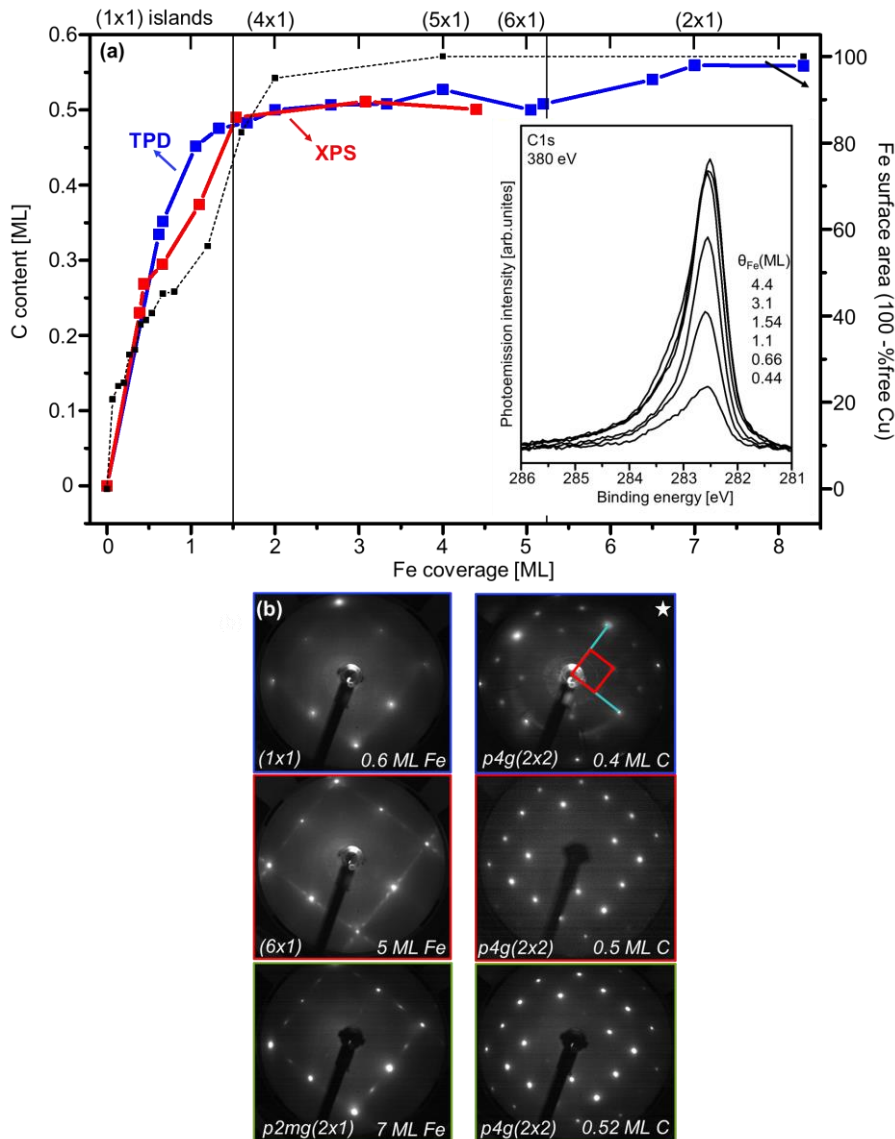


Figure 3.7 (a) Carbon content as a function of iron coverage, derived from TPD and XPS analysis after three consecutive cycles of ethylene adsorption at 100 K and heating to 500 K. The dotted line shows the total iron surface area derived from CO-titration. The C1s spectra confirm the carbide formation in all cases in the inset. (b) The LEED patterns after carbon reconstruct the iron film confirm the $p4g(2 \times 2)$ formation at all ranges. LEED were taken at 100K and electron energy of 100 eV.

The likelihood of subsurface carbon formation was further explored in a systematic study of how the Fe film thickness affects the carburization process. Figure 3.7 shows the H₂-TPD-based quantification of carbon deposited as a function of Fe film thickness. Multiple ethylene dissociation cycles were applied for each thickness to ensure that the value derived corresponds to the carbon-saturated state in all cases. Also, the carbon coverage was cross-checked with the XP spectra provided in the inset, confirming that carbide is formed at all Fe coverages, including the sub-ML regime. The fraction of surface that consists of Fe is included in the figure and was derived from the CO titration experiment shown in Figure 3.3. Starting at the low Fe coverage, the carbon content increases along with the fraction of Fe exposed on the surface but levels off at ~0.5 ML as soon as the Fe film is entirely closed (around 1.5 ML), indicating that the carbon resides only on the surface for the thicker Fe films and diffusion to the bulk does not occur. The LEED patterns after ethylene treatment show a very clear and sharp ‘clock’ reconstruction pattern for coverages >2 ML, whereas thicknesses <2 ML show the same spots but are significantly weaker and somewhat broader than thicker films, as shown in Figure 3.7 (b). Also, the (1x1) intensity spots are higher for films that do not cover the substrate completely. The LEED pattern marked with a white star shows a higher intensity for the (1x1) substrate spots. The difference in intensity may be associated with the high influence of the substrate on the diffraction pattern. Additionally, some broadening of the spots indicates island growth and disorder; however, this disorder does not influence the purity of the carbide formed.

3.7 Iron carbide thermal stability

The Fe/Cu(100) system is unstable when heated to higher temperatures [58]. For this reason, the maximum temperature used was limited to 500 K. Iron carbides also have limited stability as they are known to decompose and form graphitic forms of carbon, a property used for the growth of carbon nanotubes [57]. The thermal stability of the Fe_xC_y/Cu(100) model system was investigated for an 8 ML thick carburized Fe film using a combination of AES and LEED, summarized in Figure 3.8. After heating the Fe_xC_y/Cu(100) sample to 700 K, the spectrum shows decreased

C_{KLL} peak intensity and a different shape than 500 K. This is attributed to the partial decomposition of the carbide into graphitic carbon. It can also be seen that the Fe_{LMM} intensity decreases while the Cu_{LMM} signal increases, an indication that Fe starts to diffuse into the Cu bulk. The LEED pattern shows that the spots due to the $p4g(2 \times 2)$ structure become slightly less intense. The shape of the C_{KLL} peak after heating to 900 K has changed, where the three carbide transitions are no longer there. Instead, the shape now corresponds to that of graphitic carbon [45]. In addition to this, the Fe peaks have reduced significantly while the Cu peaks have grown larger. The LEED pattern shows only very weak spots due to $p4g(2 \times 2)$, and it is clear that the surface carbide has disintegrated. We find that the $Fe_xC_y/Cu(100)$ model system is stable up to 600 K. At higher temperatures, both Fe diffusion into the Cu bulk and Fe_xC_y decomposition destroy the structure of the surface carbide.

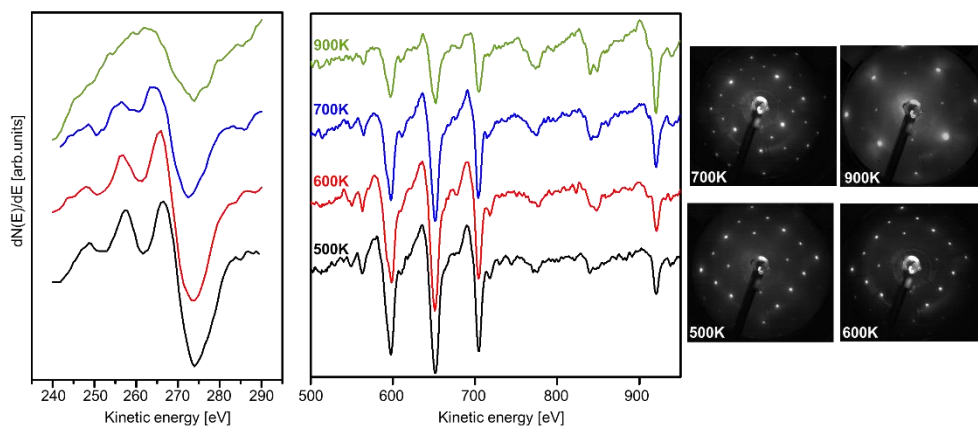


Figure 3.8. AES and LEED were recorded after heating Fe_xC_y film to the temperatures indicated in the figure. The LEED patterns were recorded at 100 K with 100 eV electron energy.

3.8 Bulk carbide formation and decomposition

The thermal stability tests show that the surface carbide decomposes to graphite rather than forming subsurface carbon after heating to around 700 K, which also causes significant Fe diffusion into the Cu crystal, making this approach less suited

for fabricating bulk Fe_xC_y phases. A different method for bulk carbide formation was explored in an experiment in which an ethylene pressure of 5×10^{-7} mbar was introduced *during* a 1.5 ML Fe evaporation at room temperature. After evaporation, the sample was slowly heated in vacuum to study the thermal stability, as shown in the heat map of Figure 3.9 (a). The C1s TP-XPS heat map shows the result of heating the surface after iron evaporation in an ethylene atmosphere. Individual spectra for selected temperatures from the heat map are provided in Figure 3.9 (b), providing further information about the chemical identity of the C1s species on the surface at each stage. The C1s spectrum at 340 K shows a broad peak between 285.5 eV and 282 eV, which is attributed to a mixture of C_xH_y species that form during evaporation in ethylene. The BE of the peak shifts towards lower values, and it becomes sharper during heating to 550 K, suggesting a transition to the formation of pure carbide. However, at approximately 640 K, a new peak develops at ~ 284.8 eV related to graphite formation [45]. LEED patterns recorded for a slightly thicker film are provided in Figure. 3.9(b).

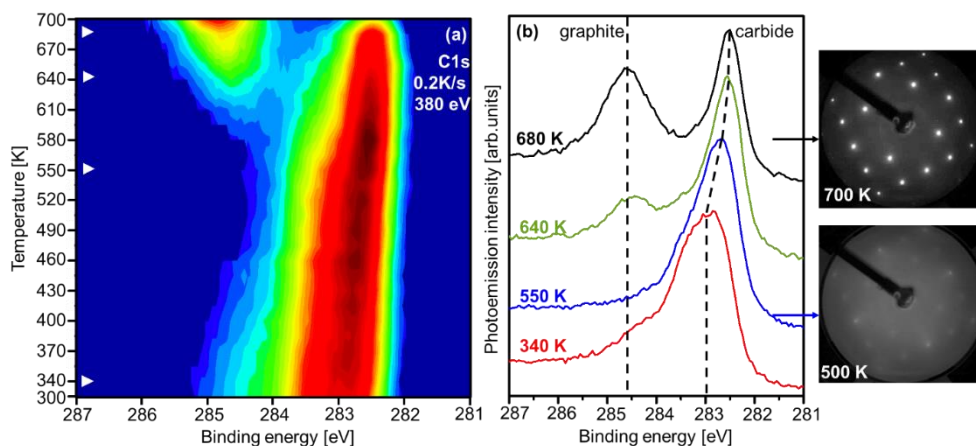


Figure 3.9. **(a)** C1s spectra after evaporating 1.5 ML of iron in an ethylene atmosphere (5×10^{-7} mbar) at 300 K followed by heating (0.2 K/s) to 700 K. **(b)** Individual C1s representative of the temperatures indicated in the figure as white symbols. LEED patterns were recorded at 100 K and 100 eV electron energy.

A blurry pattern is found at 500 K, suggesting high disorder on the surface, whereas after heating to 700 K, the pattern becomes sharper, forming a $p4g(2 \times 2)$, confirming the high stability of this structure. The C1s spectrum shows that graphite carbon has formed, however, the diffraction pattern does not show extra spots related to graphite formation.

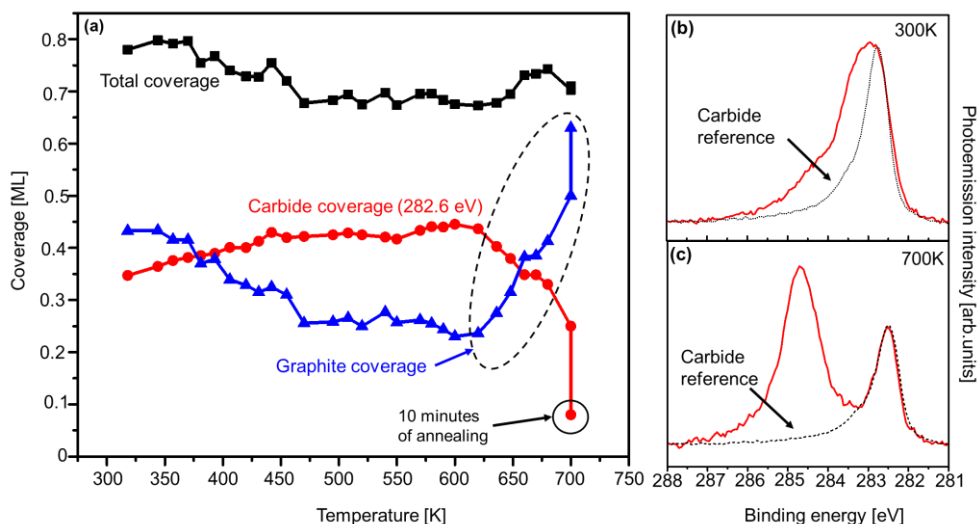


Figure 3.10 (a) Graph depicting the extent of coverage of different carbon types versus temperature after evaporating 1.5 ML of iron in an ethylene atmosphere (5×10^{-7} mbar), followed by heating to 700 K at 0.2 K/s. (b) and (c) Individual C1s spectrum with the carbide reference used for quantification.

Figure 3.10 (a) shows the coverage of various species present during heating, as derived from the series of XPS spectra shown as a heat map in Figure 3.9(a). To deconvolute the C1s spectra, we used the surface carbide for an equally thick Fe film as a carbide reference. After subtracting the known quantity of carbide, the intensity left is given as a single component and corresponds to the peaks present between 284.8-283.5 eV. It is attributed to a mixture of species at low temperatures and to graphite above 600 K. Figure 3.10 (b) and (c) show a couple of C1s spectra to illustrate how the quantitative evaluation of the spectra during heating was done. The data clearly show that the carbon coverage is significantly higher than 0.5 ML (the maximum C coverage found when ethylene is dosed *after* iron evaporation),

3.9 Iron carbide thick films (>12 ML)

meaning that carbon, in this case, is also located in the subsurface region of the sample.

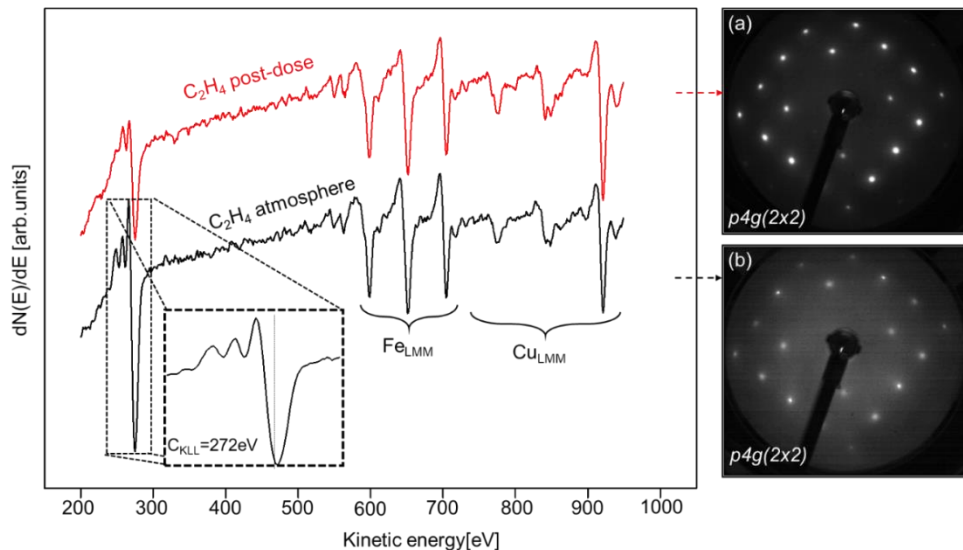


Figure 3.11. Auger survey spectra of a ~ 4 ML Fe film after (a) post-dosing ethylene (b) evaporation in 1×10^{-7} mbar ethylene, respectively. The increased C_{KLL} peak height and the peak shape indicate bulk carbide formation after evaporation in ethylene. LEED was taken at 100eV.

3.9 Iron carbide thick films (>12ML)

After evaporating ~ 20 ML of Fe, ethylene decomposition was used to deposit carbon as described before. Quantitative analysis of the amount of carbon deposited in each cycle, provided in Figure 3.13 (a), shows that the first dose of ethylene is enough to deposit 0.4 ML of carbon on the surface, very similar to what happened with thin films < 12 ML. However, hydrogen desorption continues during further ethylene deposition cycles, unlike the thin films where saturation was found after two cycles. The prolonged dissociation of ethylene indicates that there continues to be space on the surface to accommodate more ethylene decomposition products. The integral of the amount of carbon deposited reaches a value of 0.82 ML after eight cycles, but this does not appear to be a saturation point. Figure 3.13 (b) shows a slight increase

of the C_{KLL} peak with respect to a saturated thin iron carbide surface with the three characteristic carbide transitions, which excludes the possibility that the carbon beyond 0.5 ML forms graphitic types of carbon, something that has been found to happen on Co(0001) after multiple ethylene decomposition cycles [55]. The electron diffraction pattern after one ethylene cycle does not show signs of surface reconstruction, and thus no change in the “(3x1)” structure.

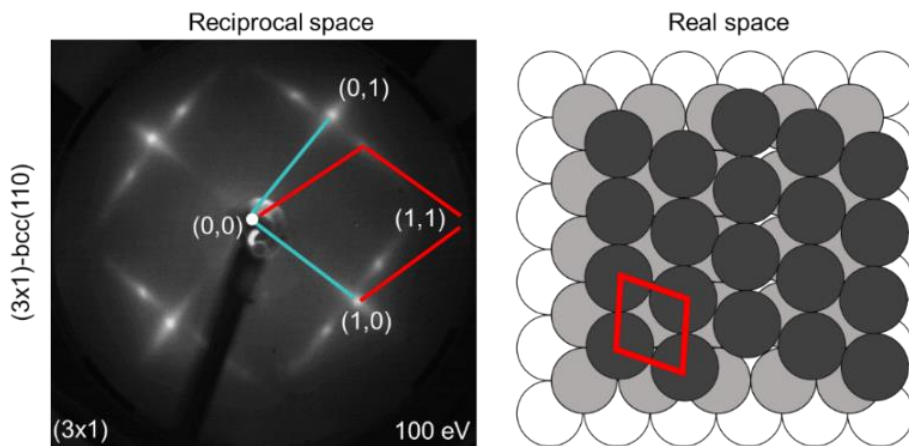


Figure 3.12. LEED picture and real space diagram for BCC(110) iron film. LEED was taken at 100 K and 100 eV electron energy.

Our explanation of the differences in carbon types between thin and thick films is related to the $p4g(2x2)$ structure. We said before that the $p4g(2x2)$ structure acts as a carbon trap, and its high stability makes the structure on the surface stable until 700 K, thus creating a constant carbon concentration on the surface. The lack of $p4g(2x2)$ makes the thick iron carbide film more dynamic. The diffusion of surface carbon into the bulk after each TPD experiment releases space for the dissociation products of ethylene to find space to accommodate. The inelastic mean free path (IMFP) of C_{KLL} electrons is 0.67nm (3.5 ML), so some of the carbon on the bulk for films thicker than 12 ML will not be detected; this is the reason why after the equivalent of 0.82 ML of carbon, quantified with H_2 TPD, we see only a small intensity increase of the C_{KLL} peaks.

In conclusion, the difference between thin and thick iron films on Cu(100) is related to the formation of a $p4g(2 \times 2)$ on the surface of films below 12 ML. The diffusion of carbon into the bulk on thick films creates *different types of carbon* (bulk carbide).

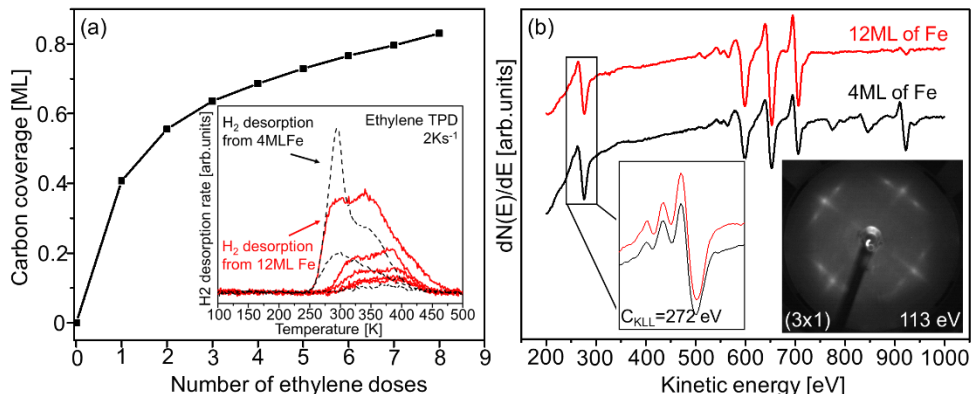


Figure 3.13. (a) Uptake curve of the carbon coverage against ethylene dose derived from the H₂TPD from the inset. (b) The Auger spectra of a Fe_xC_y surface after eight ethylene cycles, compared to a 4 ML Fe film after three ethylene cycles. In the inset, the C_{KLL} region compares the carbide reference from a 4 ML with the carbide deposited on 12 ML of iron. The LEED recorded shows a (3x1) after ethylene dissociation.

3.10 General discussion

While the structure of Fe films on top of metallic single crystal surfaces and their oxidation to form FeO_x has received considerable attention [14–17], much less is known about their reactivity towards Fe_xC_y formation. Li et al. discussed Fe_xC_y formation on a Au(111) substrate, and we here show that a change in the chemical identity and the surface structure of the substrate, from Au to Cu and from FCC(111) to FCC(100), profoundly influences the reactivity of the Fe films towards carbide formation. Thin iron films on Au(111) were unreactive for carbide formation using ethylene as a precursor, and this could only be achieved on thicker Fe films, while the formation of other types of carbon could not be avoided.

On the other hand, in Fe/Cu(100), we find that ethylene readily decomposes on Fe films of all thicknesses studied, and a pure surface carbide is formed with a very different structure compared to Fe/Au(111). For Fe/Au(111), the carbide was proposed to consist of a BCC-Fe lattice where carbon occupies every second interstitial site. The strong tendency to form a clock-reconstructed Fe₂C surface carbide on Cu(100) is most likely due to the presence of FCC-Fe(100) up to a coverage of 12 ML on this substrate, while BCC-Fe forms already for 3 ML Fe on Au(111). The formation of the carbon-induced FCC-p4g(2x2) structure is apparently only favourable on an FCC surface, as it does not form on the BCC-Fe(110) surface. This is also evident from our experiment on thick Fe films with a BCC structure that does not show carbon-induced clock reconstruction.

The carbon-induced 'clock' reconstruction structure is known to occur on Ni(100) as well as on Co(100) [54,56,59]. Recent calculations show that it is remarkably stable because the carbon atoms reconstruct the metal surface to create a local tetracoordinate square planar arrangement that introduces aromaticity due to overlapping d-orbitals. The resulting bond energy is between 743 and 791 kJmol⁻¹, higher than the bond energies in graphite and diamond [60,61]. The calculations did not explicitly consider the Fe(100) surface but indicated that the carbon bond strength increases with decreasing number of d-electrons. Very high stability is therefore expected for clock-reconstructed Fe(100). Consequently, it acts as a thermodynamic trap that keeps carbon at the surface and prevents carbon migration to the subsurface regions. This can explain the absence of bulk carbide formation on thin Fe films on Cu(100), as the stable surface carbon layer inhibits ethylene decomposition so that no further carbon can be deposited. This is different on BCC-Fe films that form only for a thickness of more than 12 ML on Cu(100) and already for ~3 ML on Au(111). In both these cases, carbon diffused into the subsurface during heating to 500 K while a different structure forms at the surface.

3.11 Summary and conclusions

Motivated by the lack of experiments in the fabrication and characterisation of well-defined iron carbide films on Cu(100) and by the results of other groups using

Au(111) as a substrate, we have performed an experimental study on the morphology and structure of iron carbide on Cu(100) using LEED, AES, SR-XPS and TPD. Fe grows predominantly in bi-layer islands and forms a closed film around 2 ML. The Fe films adopt a (strained) BCC-like structure coexisting with FCC-Fe(100). In-situ SR-XPS shows that decomposition of adsorbed ethylene occurs in three steps, around 200 K, where species such as CCH₂ and HCCH₂ are most likely formed. The next step occurs around 300 K and forms acetylene and CCH species which gradually lose their hydrogen. C-C bond scission around 450 K leads to the formation of a pure carbide after heating to 500 K, as confirmed by SR-XPS and Auger spectroscopy. Further cycles of ethylene adsorption and heating did not increase the carbon concentration much further, and TPD-based quantification shows that the carbon concentration reaches a saturation point of 0.5 ML for all films ≥ 2 ML.

Carbon deposition causes the surface to reconstruct, as evident from the very sharp p4g(2x2) electron diffraction pattern seen for all films thinner than 12 ML. The absence of BCC-related diffraction spots in all cases after carburization suggests that the Fe film converts to FCC-Fe after modifying the surface with carbon. The Fe₂C surface carbide thermally stable structure up to 600K after which decomposition to graphitic carbon occurs while iron dissolves into the copper substrate.

The particularly strong bond between Fe-C in the square-planar structure p4g-(2x2) acts as a thermodynamic trap preventing carbon diffusion into the subsurface region, inhibiting the formation of bulk carbide. The bulk iron carbide formation on thin films could be brought about by evaporating Fe in an ethylene atmosphere. For a 1.5 ML Fe film, a carbon content of ~0.75 ML was derived from SR-XPS. LEED shows that the surface of the carbon-rich film still shows the 'clock' reconstructed Fe₂C surface. Heating above 600 K causes the decomposition of the carbide into graphitic carbon. The comparison with a previous carbiding study performed on Fe/Au(111) shows significant structural and compositional differences. Carbide forms much more easily on thin Fe films on Cu(100) and has higher purity than the carbide formed on Au(111). The carbide structure found is also very different: on Au(111), Fe maintains the BCC structure with carbon occupying interstitial sites, whereas on Cu(100), thin

Fe film becomes FCC-Fe terminated by a Fe₂C surface carbide. Thick films on Cu(100) grow as BCC iron, and for such films, the 'clock' reconstruction does not occur, and carbon diffusion into the bulk occurs. [62]

3.12 References

- [1] J. Yu, F. Chen, W. Gao, Y. Ju, X. Chu, S. Che, F. Sheng, Y. Hou, Iron carbide nanoparticles: An innovative nanopatform for biomedical applications, *Nanoscale Horizons*. 2 (2017) 81–88. <https://doi.org/10.1039/c6nh00173d>.
- [2] E. Borowiak-Palen, C. Tripisciano, M. Rummeli, S. Costa, X. Chen, R.J. Kalenczuk, Filling of carbon nanotubes: Containers for magnetic probes and drug delivery, *Carbon Nanostructures*. 0 (2011) 67–82. https://doi.org/10.1007/978-3-642-14802-6_4.
- [3] A.R. Paulraj, Y. Kiros, B. Skarman, H. Vidarsson, Core/Shell Structure Nano-Iron/Iron Carbide Electrodes for Rechargeable Alkaline Iron Batteries, *J. Electrochem. Soc.* 164 (2017) A1665–A1672. <https://doi.org/10.1149/2.1431707jes>.
- [4] J. Van de Loosdrecht, F.G. Botes, I.M. Ciobica, A. Ferreira, P. Gibson, D.J. Moodley, A.M. Saib, J.L. Visagie, C.J. Weststrate, J.W. Niemantsverdriet, *Fischer-Tropsch Synthesis: Catalysts and Chemistry*, Elsevier Ltd., 2013. <https://doi.org/10.1016/B978-0-08-097774-4.00729-4>.
- [5] H. Mahmoudi, M. Mahmoudi, O. Doustdar, H. Jahangiri, A. Tsolakis, S. Gu, M. Wyszynski, A review of Fischer Tropsch synthesis process, mechanism, surface chemistry and catalyst formulation, *Biofuels Eng.* 2 (2018) 11–31. <https://doi.org/10.1515/bfuel-2017-0002>.
- [6] J.W. Niemantsverdriet, A.M. van der Kraan, W.L. van Dijk, H.S. van der Baan, Behavior of Metallic Iron Catalysts during Fischer-Tropsch Synthesis Studied with Mossbauer Spectroscopy , X-ray Diffraction , Carbon Content Determination , and Reaction Kinetic Measurements, *J.Phys.Chem.* 25 (1980) 3363–3370. <https://doi.org/10.1021/j100462a011>.
- [7] J. Xu, C.H. Bartholomew, Temperature-Programmed Hydrogenation (TPH) and in Situ Mossbauer Spectroscopy Studies of Carbonaceous Species on Silica-Supported Iron Fischer - Tropsch Catalysts, *J.Phys.Chem B.* (2005) 2392–2403. <https://doi.org/10.1021/jp048808j>.
- [8] P. Thune, P. Moodley, F. Scheijen, H. Fredriksson, R. Lancee, J. Kropf, J. Miller, J.W. (Hans) Niemantsverdriet, The Effect of Water on the Stability of Iron Oxide and Iron Carbide Nanoparticles in Hydrogen and Syngas Followed by in Situ X-ray Absorption Spectroscopy, *J. Phys. Chem. C.* 116 (2012) 7367–7373. <https://doi.org/10.1021/jp210754k>.
- [9] M.O. Ozbek, J.W. Niemantsverdriet, Elementary reactions of CO and H₂ on C-terminated X-Fe₅C₂(001) surfaces, *J. Catal.* 317 (2014) 158–166. <https://doi.org/10.1016/j.jcat.2014.06.009>.

- [10] J.M. Gracia, F.F. Prinsloo, J.W. Niemantsverdriet, Mars-van Krevelen-like Mechanism of CO Hydrogenation on an Iron Carbide Surface, *Catal. Letters*. (2009) 257–261. <https://doi.org/10.1007/s10562-009-0179-5>.
- [11] M.O. Ozbek, J.W. Niemantsverdriet, Methane, formaldehyde and methanol formation pathways from carbon monoxide and hydrogen on the (001) surface of the iron carbide X-Fe₅C₂, *J. Catal.* 325 (2015) 9–18. <https://doi.org/10.1016/j.jcat.2015.01.018>.
- [12] R.J.P. Broos, B. Zijlstra, I.A.W. Filot, E.J.M. Hensen, Quantum-Chemical DFT Study of Direct and H- and C-Assisted CO Dissociation on the χ -Fe₅C₂ Hägg Carbide, *J. Phys. Chem. C*. 122 (2018) 9929–9938. <https://doi.org/10.1021/acs.jpcc.8b01064>.
- [13] X.W. Liu, S. Zhao, Y. Meng, Q. Peng, A.K. Dearden, C.F. Huo, Y. Yang, Y.W. Li, X.D. Wen, Mossbauer Spectroscopy of Iron Carbides: From Prediction to Experimental Confirmation, *Sci. Rep.* 6 (2016). <https://doi.org/doi.org/10.1038/srep26184>.
- [14] F.J.E. Scheijen, D. Curulla Ferré, J.W. Niemantsverdriet, Adsorption and dissociation of CO on body-centered cubic transition metals and alloys: effect of coverage and scaling relations, *J. Phys. Chem. C*. 113 (2009) 11041–11049. <https://doi.org/10.1021/jp811130k>.
- [15] W. Erley, A.M. Baro, H. Ibach, Vibrational spectra of acetylene and ethylene adsorbed on Fe(110), *Surf. Sci.* 120 (1982) 273–290. [https://doi.org/10.1016/0039-6028\(82\)90151-0](https://doi.org/10.1016/0039-6028(82)90151-0).
- [16] S. Booyens, M. Bowker, D.J. Willock, The adsorption and dissociation of CO on Fe(111), *Surf. Sci.* 625 (2014) 69–83. <https://doi.org/10.1016/j.susc.2014.02.019>.
- [17] S. Booyens, L. Gilbert, D. Willock, M. Bowker, The adsorption of ethene on Fe(111) and surface carbide formation, *Catal. Today*. 244 (2015) 122–129. <https://doi.org/10.1016/j.cattod.2014.06.025>.
- [18] D.W. Moon, D.J. Dwyer, S.L. Bernasek, Adsorption of CO on the clean and sulfur modified Fe(100) surface, *Surf. Sci.* 163 (1985) 215–229. [https://doi.org/10.1016/0039-6028\(85\)90859-3](https://doi.org/10.1016/0039-6028(85)90859-3).
- [19] C. Brucker, T. Rhodin, Chemisorption and reaction of acetylene and ethylene on the α -Fe(100) clean iron surface, *J. Catal.* 47 (1977) 214–231. [https://doi.org/10.1016/0021-9517\(77\)90169-5](https://doi.org/10.1016/0021-9517(77)90169-5).
- [20] W. Weiss, W. Ranke, Surface chemistry and catalysis on well-defined epitaxial iron-oxide layers, *Prog. Surf. Sci.* 70 (2002) 1–151. [https://doi.org/10.1016/S0079-6816\(01\)00056-9](https://doi.org/10.1016/S0079-6816(01)00056-9).
- [21] Y. Li, K.C. Adamsen, L. Lammich, J. V Lauritsen, S. Wendt, Atomic-Scale View of the Oxidation and Reduction of Supported Ultrathin FeO Islands, *ACS Nano*. 13 (2019) 11632–11641. <https://doi.org/10.1021/acsnano.9b05470>.
- [22] H.-J. Freund, The Surface Science of Catalysis and More, Using Ultrathin Oxide Films as Templates: A Perspective, *J. Am. Chem. Soc.* 138 (2016) 8985–8996. <https://doi.org/10.1021/jacs.6b05565>.
- [23] Y. Li, Z. Li, A. Ahsen, L. Lammich, G.J.A. Mannie, J.W. Niemantsverdriet, J. V. Lauritsen, Atomically Defined Iron Carbide Surface for Fischer-Tropsch Synthesis Catalysis, *ACS Catal.* 9 (2019) 1264–1273. <https://doi.org/10.1021/acscatal.8b03684>.

- [24] G.J.A. Mannie, L. Lammich, Y.W. Li, J.W. Niemantsverdriet, J. V. Lauritsen, Monolayer iron carbide films on Au(111) as a Fischer-Tropsch model catalyst, *ACS Catal.* 4 (2014) 3255–3260. <https://doi.org/10.1021/cs500902z>.
- [25] A. Biedermann, R. Tscheliessnig, M. Schmid, P. Varga, Local atomic structure of ultra-thin Fe films grown on Cu(100), *Appl. Phys. A Mater. Sci. Process.* 78 (2004) 807–816. <https://doi.org/10.1007/s00339-003-2435-7>.
- [26] P. Schmailzl, K. Schmidt, P. Bayer, R. Döll, K. Heinz, The structure of thin epitaxial Fe films on Cu(100) in the transition range fcc ~ bcc, *Surf. Sci.* 312 (1994) 73–81. [https://doi.org/10.1016/0039-6028\(94\)90804-4](https://doi.org/10.1016/0039-6028(94)90804-4).
- [27] D.A. Steigerwald, I. Jacob, W.F. Egelhoff, Structural study of the epitaxial growth of fcc-Fe films, sandwiches, and superlattices on Cu(100), *Surf. Sci.* 202 (1988) 472–492. [https://doi.org/10.1016/0039-6028\(88\)90048-9](https://doi.org/10.1016/0039-6028(88)90048-9).
- [28] M. Wuttig, B. Feldmann, J. Thomassen, F. May, H. Zillgen, A. Brodde, H. Hannemann, H. Neddermeyer, Structural transformations of fcc iron films on Cu(100), *Surf. Sci.* 291 (1993) 14–28. [https://doi.org/10.1016/0039-6028\(93\)91472-2](https://doi.org/10.1016/0039-6028(93)91472-2).
- [29] T. Bernhard, M. Baron, M. Gruyters, H. Winter, Surface structure of ultrathin Fe films on Cu(001) revisited, *Phys. Rev. Lett.* 95 (2005) 5–8. <https://doi.org/10.1103/PhysRevLett.95.087601>.
- [30] Y. Darici, J. Marcano, H. Min, LEED measurements of Fe epitaxially grown on Cu(100), *Surf. Sci.* 182 (1987) 477–488. [https://doi.org/10.1016/0039-6028\(87\)90014-8](https://doi.org/10.1016/0039-6028(87)90014-8).
- [31] K. Heinz, S. Müller, P. Bayer, Iron multilayers on Cu(100) - A case of complex reconstruction investigated by quantitative LEED, *Surf. Sci.* 352–354 (1996) 942–950. [https://doi.org/10.1016/0039-6028\(95\)01306-7](https://doi.org/10.1016/0039-6028(95)01306-7).
- [32] A. Biedermann, R. Tscheliessnig, M. Schmid, P. Varga, Crystallographic structure of ultrathin Fe films on Cu(100), *Phys. Rev. Lett.* 87 (2001) 86103-1-86103-4. <https://doi.org/10.1103/PhysRevLett.87.086103>.
- [33] A. Biedermann, Stability of the nanomartensitic phase in ultrathin Fe films on Cu(100), *Phys. Rev. B - Condens. Matter Mater. Phys.* 80 (2009) 1–11. <https://doi.org/10.1103/PhysRevB.80.235403>.
- [34] A. Biedermann, M. Schmid, P. Varga, Nucleation of bcc iron in ultrathin fcc films, *Phys. Rev. Lett.* 86 (2001) 464–467. <https://doi.org/10.1103/PhysRevLett.86.464>.
- [35] A. Biedermann, R. Tscheliessnig, C. Klein, M. Schmid, P. Varga, Reconstruction of the clean and H covered 'magnetic live surface layer' of Fe films grown on Cu(1 0 0), *Surf. Sci.* 563 (2004) 110–126. <https://doi.org/10.1016/j.susc.2004.06.150>.
- [36] J. Harris, On the adsorption and desorption of H₂ at metal surfaces, *Appl. Phys. A Solids Surfaces.* 47 (1988) 63–71. <https://doi.org/10.1007/BF00619699>.
- [37] W. Arnot, M., McCash, E.M., Allison, Growth and thermal properties of fcc iron films on Cu(100), *Surf. Sci.* 270 (1992) 724–730. [https://doi.org/10.1016/0039-6028\(92\)91340-H](https://doi.org/10.1016/0039-6028(92)91340-H).

- [38] M. Arnott, W. Allison, Thermal diffusion of iron into a copper(100) crystal studied by Auger Electron Spectroscopy (AES), *Phys. B Phys. Condens. Matter.* 161 (1990) 289–293. [https://doi.org/10.1016/0921-4526\(89\)90151-8](https://doi.org/10.1016/0921-4526(89)90151-8).
- [39] F. Dulot, B. Kierren, D. Malterre, Influence of the initial step density on the growth mechanisms of the Fe/Cu(100) interface, *Surf. Sci.* 494 (2001) 229–237. [https://doi.org/10.1016/S0039-6028\(01\)01450-9](https://doi.org/10.1016/S0039-6028(01)01450-9).
- [40] J. Shen, C. Schmidhals, J. Woltersdorf, J. Kirschner, Structural phase transformation under reversed strain: A comparative study of iron ultrathin film growth on nickel and copper (100), *Surf. Sci.* 407 (1998) 90–103. [https://doi.org/10.1016/S0039-6028\(98\)00153-8](https://doi.org/10.1016/S0039-6028(98)00153-8).
- [41] J. Thomassen, B. Feldmann, M. Wuttig, Growth, structure and morphology of ultrathin iron films on Cu(100), *Surf. Sci.* 264 (1992) 406–418. [https://doi.org/10.1016/0039-6028\(92\)90195-C](https://doi.org/10.1016/0039-6028(92)90195-C).
- [42] S. Müller, P. Bayer, A. Kinne, P. Schmailzl, K. Heinz, High precision LEED structure analysis of ultra-thin epitaxial fcc Fe films on Cu(100), *Surf. Sci.* 322 (1995) 21–33. [https://doi.org/10.1016/0039-6028\(95\)90013-6](https://doi.org/10.1016/0039-6028(95)90013-6).
- [43] H. Landskron, G. Schmidt, K. Heinz, K. Muller, Low-temperature p2mg(2x1) structure of ultrathin epitaxial films Fe/Cu(100), *Surf. Sci.* 256 (1991) 115–122. [https://doi.org/https://doi.org/10.1016/0039-6028\(91\)91206-D](https://doi.org/https://doi.org/10.1016/0039-6028(91)91206-D).
- [44] J. Pritchard, On the structure of CO adlayers on Cu(100) and Cu(111), *Surf. Sci.* 79 (1979) 231–244. [https://doi.org/10.1016/0039-6028\(79\)90039-6](https://doi.org/10.1016/0039-6028(79)90039-6).
- [45] W. Panzner, G., and Diekmann, The bonding state of carbon segregated to α -iron surfaces and on iron carbide surfaces studied by electron spectroscopy, *Surf. Sci.* 160 (1985) 253–270. [https://doi.org/10.1016/0039-6028\(85\)91040-4](https://doi.org/10.1016/0039-6028(85)91040-4).
- [46] C. Wiltner, A., and Linsmeier, Formation of endothermic carbides on iron and nickel, *Phys.Stat.Sol.* 201 (2004) 881–887. <https://doi.org/10.1002/pssa.200304362>.
- [47] J.B. Butt, Carbide phases on iron-based Fischer-Tropsch synthesis catalysts part I: Characterization studies, *Catal. Letters.* 7 (1990) 61–81. <https://doi.org/10.1007/BF00764492>.
- [48] N. Måtensson, A. Nilsson, On the origin of core-level binding energy shifts, *J. Electron Spectros. Relat. Phenomena.* 75 (1995) 209–223. [https://doi.org/10.1016/0368-2048\(95\)02532-4](https://doi.org/10.1016/0368-2048(95)02532-4).
- [49] S. Jackson, R. Nuzzo, Determining hybridization differences for amorphous carbon from the XPS C1s envelope, *Appl. Surf. Sci.* 90 (1995) 195–203. [https://doi.org/10.1016/0169-4332\(95\)00079-8](https://doi.org/10.1016/0169-4332(95)00079-8).
- [50] M. Salmerón, A.M. Baró, J.M. Rojo, Interatomic transitions and relaxation effects in Auger spectra of several gas adsorbates on transition metals, *Phys. Rev. B.* 13 (1976) 4348–4363. <https://doi.org/10.1103/PhysRevB.13.4348>.
- [51] R. Neubauer, C.M. Whelan, R. Denecke, H.P. Steinrück, The thermal chemistry of saturated layers of acetylene and ethylene on Ni(100) studied by in situ synchrotron x-ray photoelectron spectroscopy, *J. Chem. Phys.* 119 (2003) 1710–1718. <https://doi.org/10.1063/1.1582432>.

- [52] J.N. Andersen, A. Beutler, S.L. Sorensen, R. Nyholm, B. Setlik, D. Heskett, Vibrational fine structure in the C 1s core level photoemission of chemisorbed molecules: Ethylene and ethylidyne on Rh(111), *Chem. Phys. Lett.* 269 (1997) 371–377. [https://doi.org/10.1016/S0009-2614\(97\)00288-1](https://doi.org/10.1016/S0009-2614(97)00288-1).
- [53] Y. Gauthier, R. Baudoing-Savois, K. Heinz, H. Landskron, Structure determination of p4g Ni(100)-(2×2)C by LEED, *Surf. Sci.* 251–252 (1991) 493–497. [https://doi.org/10.1016/0039-6028\(91\)91041-U](https://doi.org/10.1016/0039-6028(91)91041-U).
- [54] C. Klink, L. Olesen, F. Besenbacher, I. Stensgaard, E. Laegsgaard, Interaction of C with Ni(100): Atom-Resolved Studies of the ‘Clock’ Reconstruction, *Phys. Rev.Lett.* 71 (1993) 4350–4353. <https://doi.org/10.1103/PhysRevLett.71.4350>.
- [55] J.H. Onuferko, D.P. Woodruff, B.W. Holland, Leed structure analysis of the Ni{100} (2 × 2)C (p4g) structure; A case of adsorbate-induced substrate distortion, *Surf. Sci.* 87 (1979) 357–374. [https://doi.org/10.1016/0039-6028\(79\)90535-1](https://doi.org/10.1016/0039-6028(79)90535-1).
- [56] I.M. Ciobîcă, R.A. van Santen, P.J. van Berge, J. van de Loosdrecht, Adsorbate induced reconstruction of cobalt surfaces, *Surf. Sci.* 602 (2008) 17–27. <https://doi.org/10.1016/j.susc.2007.09.060>.
- [57] J.R. Mercer, P. Finetti, F.M. Leibsle, R. McGrath, V.R. Dhanak, A. Baraldi, K.C. Prince, R. Rosei, STM and SPA-LEED studies of O-induced structures on Rh(100) surfaces, *Surf. Sci.* 352–354 (1996) 173–178. [https://doi.org/10.1016/0039-6028\(95\)01126-9](https://doi.org/10.1016/0039-6028(95)01126-9).
- [58] M.T. Kief, W.F. Egelhoff, Growth and structure of Fe and Co thin films on Cu(111), Cu(100), and Cu(110): A comprehensive study of metastable film growth, *Phys.Rev.B.* 47 (1993) 10785–10814. <https://doi.org/10.1103/PhysRevB.47.10785>.
- [59] C.J. Weststrate, A.C. Kazalkaya, E.T.R. Rossen, M.W.G.M. Verhoeven, I.M. Ciobîcă, A.M. Saib, J.W. Niemantsverdriet, Atomic and polymeric carbon on Co(0001): Surface reconstruction, graphene formation, and catalyst poisoning, *J. Phys. Chem. C.* 116 (2012) 11575–11583. <https://doi.org/10.1021/jp301706q>.
- [60] A. Nandula, Q.T. Trinh, M. Saeys, A.N. Alexandrova, Origin of extraordinary stability of square-planar carbon atoms in surface carbides of cobalt and nickel, *Angew. Chemie - Int. Ed.* 54 (2015) 5312–5316. <https://doi.org/10.1002/anie.201501049>.
- [61] K. Fei Tan, J. Xu, J. Chang, A. Borgna, M. Saeys, Carbon deposition on Co catalysts during Fischer-Tropsch synthesis: A computational and experimental study, *J. Catal.* 274 (2010) 121–129. <https://doi.org/10.1016/j.jcat.2010.06.008>.
- [62] D. García Rodríguez, M.A. Gleeson, J. V. Lauritsen, Z. Li, X. Yu, J.W. Hans Niemantsverdriet, C.J. Kees-Jan Weststrate, Iron carbide formation on thin iron films grown on Cu(100): FCC iron stabilized by a stable surface carbide, *Appl. Surf. Sci.* 585 (2022) 152684. <https://doi.org/10.1016/j.apsusc.2022.152684>.



04

**CO AND H₂ REACTIVITY ON
IRON AND IRON CARBIDE
FILMS ON Cu(100)**

ABSTRACT: The adsorption, desorption and dissociation of carbon monoxide and hydrogen on iron and iron carbide films supported on Cu(100) were investigated using SR-XPS, AES, TPD, RAIRS and LEED.

When the iron film covers the copper substrate completely, all the CO molecules pre-adsorbed at 100 K dissociate between 275-300 K up to a maximum of 0.5 ML of products (0.25 ML O_{ad} + 0.25 ML C_{ad}). CO_{ad} in excess of 0.25ML desorbs molecularly between ~200 K–400 K.

The pre-adsorbed CO on Fe_2C desorbs molecularly since the presence of the atomic carbon inhibits dissociation. The molecular desorption temperature of CO decreases by more than 100 K with respect to the non-carburized iron film. Dissociative adsorption of hydrogen only occurs on the pure Fe film but is inhibited on iron films passivated by a well-ordered Fe_2C layer. It is possible to populate the carbide-terminated surface using hydrogen atoms produced on the surface of a hot W filament. The two distinct H_2 desorption peaks can be attributed to a second-order recombination peak from hydrogen adsorbed on iron sites and a first-order, reaction-limited peak attributed to the decomposition of CH species formed during exposure to highly reactive hydrogen atoms. Both desorption peaks occur around or below ~250 K, a temperature of ~100 K lower than on pure iron films of comparable thickness.

4.1 Introduction

Carbon monoxide dissociation is a key step in Fischer-Tropsch synthesis, and it is often considered a slow reaction due to the high strength of the triple bond between carbon and oxygen and the fact that it is iso-electronic with the highly stable N_2 molecule. In the carbide mechanism [1], chain growth proceeds via polymerization of C_1H_x intermediates that are either formed by direct CO dissociation into $C_{ad}+O_{ad}$ followed by hydrogenation or via a hydrogen-assisted scission mechanism, in which a hydrogen atom binds to the CO molecule to form a CH_xOH_y species and scission of the weakened C-O bond into $C(H)_x + O(H)_y$ subsequently occurs [2,3]. In a CO-insertion mechanism, CO dissociation is not needed for every step, but it is still required to produce the first C_1H_x species that initiates chain growth. In this alternative mechanism, chain growth proceeds via the insertion of CO into the carbon-metal bond to form an H_xC_y-CO intermediate followed by (R-)C-O bond scission. [4,5].

Although carbon monoxide has often been used as a probe molecule on model catalyst surfaces, there are only a few studies that discuss carbon monoxide

adsorption on evaporated iron films and carburized iron films [6–8], while several experimental studies use iron single-crystal surfaces. For this reason, we compared our results with the literature on CO on Fe(110) and polycrystalline iron. In a study by Sieben et al. [9] on Fe(110), CO shows two desorption maxima, one at 420-440 K due to molecular desorption and the other at 750 K due to associative desorption. The latter peak confirms the CO dissociation on the surface. Scheijen [10] demonstrated that the molecular desorption of CO from polycrystalline iron occurs at 100 K lower than on BCC Fe(110). An additional desorption maximum associated with recombination at 750-800 K confirms the dissociation of CO on these surfaces. Similar to what occurs with CO and H₂ on evaporated films, there is also a dearth of experimental studies of CO and H₂ on iron carbide surfaces. We compared our results to those of DFT studies done elsewhere on different types of iron carbide surfaces. Several computational studies of CO on iron carbide surfaces can be found in the literature [3,11–16]. Ozbek et al. [11] report that the CO dissociation reaction on a carbon-terminated Fe₅C₂(001) surface only occurs on carbon vacancies in the lattice, while CO dissociation on a carbon-saturated surface is strongly endothermic, and the desorption is preferred. Similar findings were reported by Gracia et al. [3] on a Fe₅C₂ surface, where they did not see any CO dissociation on a surface saturated with carbon atoms.

Egawa et al. [17] studied the H₂ adsorption on evaporated iron films, where they found the heat of adsorption of hydrogen on the thickest film (8ML) is -71 kJ/mol, which is low compared to that on BCC Fe single crystals -(88-109 kJ/mol).

According to theory, on BCC Fe(100) single crystal surfaces with different concentrations of pre-adsorbed carbon, the dissociation barrier of hydrogen increases as the carbon coverage increases. The calculated barrier for H₂ dissociation on clean and pre-covered 0.5 ML carbon on Fe(100) is 23 kJ/mol and 94 kJ/mol, respectively [18].

Once hydrogen has overcome the dissociation barrier, the adsorption energy predicted with DFT is -74.4 kJ/mol, -144.7 kJ/mol, and -143.7 kJ/mol for non-carburized Fe(100), Fe₅C₂(100)(3-Fold), and Fe₃C(100)(3-Fold/CH) respectively

[18–20], meaning that hydrogen prefers to adsorb on the carbon-rich Fe₃C(100) surface (3-fold hydrogen adsorption on carbon atoms and forming a surface CH fragment).

The present chapter describes our findings on the adsorption and dissociation of CO and H₂ on different iron and iron carbide films and film thicknesses. Similar to the previous chapter, we use a combination of SR-XPS, TPD, RAIRS, and AES to determine the nature and concentration of the various adsorbates, while LEED informs us about the surface structure.

4.2 Experimental

Temperature-programmed desorption (TPD), low energy electron diffraction (LEED) experiments, and Auger electron spectroscopy (AES) were carried out in a home-built UHV chamber with a base pressure below 2×10^{-10} mbar. The chamber was equipped with two quadrupole mass spectrometers, LEED/Auger optics, and a dual pocket e⁻ beam evaporator. TPD experiments were performed using a QMS located inside a separately pumped compartment with a 5 mm-wide aperture connecting to the main chamber. During a desorption experiment, the sample is placed 2 mm from the aperture to eliminate desorption signals from other parts of the sample holder. Quantitative evaluation was cross-checked with the simultaneously measured signal from a second QMS located in the main chamber to eliminate potential errors that could arise from directional desorption [21].

Synchrotron radiation x-ray photoelectron spectroscopy (SR-XPS) was performed at the Matline beamline of the ASTRID2 synchrotron light source (Aarhus, Denmark). Fe3p and Cu3p, C1s, and O1s core level spectra were recorded in normal emission using photon energies of 150 eV, 380 eV, and 650 eV, respectively. The position of the fermi-edge was measured after each change of the monochromator settings and was used to calibrate the binding energy (BE) scale.

Fe was evaporated at 300 K by electron beam evaporation from a 99.999% purity Fe rod. A freshly evaporated Fe film remains stable up to around 500K, after which alloying between Fe and Cu becomes significant, particularly for the thin films [22]. Therefore, our studies were usually limited to temperatures below 500 K to avoid

mixing [23]. An evaporation rate of around 0.5 ML/min was typically used, a value derived from film thickness estimations based on the attenuation of Cu_{LMM} Auger electrons.

4.3 Results and discussion

In this section, we study the reactivity of carbon monoxide and hydrogen on iron films of different thicknesses using TP- XPS, TPD, AES and LEED.

4.3.1 Reactivity of CO on 4 ML of Fe/Cu(100)

A heat map of the C1s region during slow heating of a 4 ML Fe film exposed to 5 L CO (saturation) at 130 K is shown in Figure 4.1(a) and in the selected spectra at key temperatures to facilitate closer inspection of Figure 4.1(b).

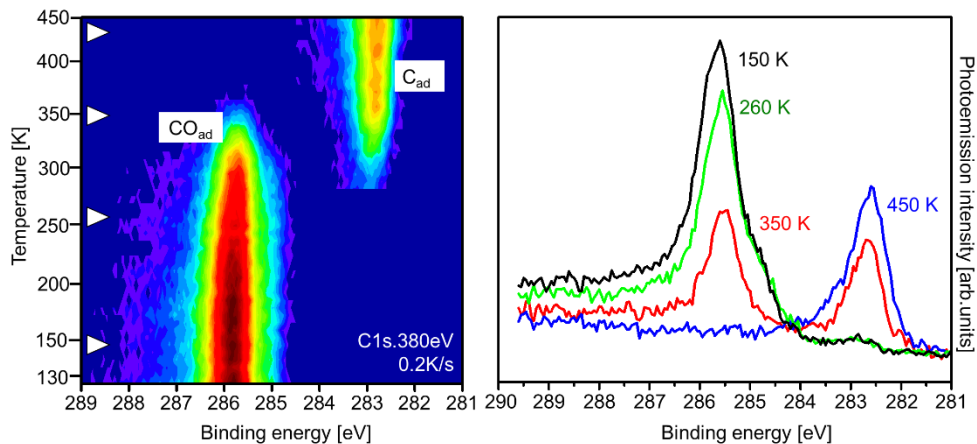


Figure 4.1. (a) Intensity map of C1s spectra recorded during heating of a pre-saturated CO on 4 ML Fe/Cu(100) surface in vacuum ($h\nu=380$ eV), 6 K per spectra, low intensity=dark blue, high intensity=red/black, heating rate 0.2 K/s. (b) Individual C1s spectra correspond to the white symbols in the intensity map.

At low temperatures, the C1s spectra contain a single peak at 285.8 eV, attributed to molecularly adsorbed CO on top sites [24]. This adsorption site is confirmed by IR absorption experiments discussed in more detail in section (4.3.3). The intensity of

the CO peak decreases gradually during heating in vacuum due to the desorption of CO. At 275 K, a new peak appears at 282.6 eV, a binding energy identical to that found after the ethylene decomposition (see Chapter 3), attributed to atomic carbon [25] formed by CO decomposition. In Chapter 3, it was found that ethylene decomposition produces a carbon coverage of 0.5 ML, and the corresponding C1s spectrum on a Fe film of similar thickness was used to quantify both the molecularly adsorbed CO and carbon and plotted in Figure 4.2 (a). The coverages found show excellent agreement with an independent determination of the molecular CO coverage from a TPD experiment (Figure. 4.2, inset), where the CO-saturated Cu(100) surface with $\theta_{\text{CO}}=0.57$ ML served as a quantitative reference. [26]

The quantitative analysis shows that the coverage of the CO-saturated surface is 0.58 ML, somewhat higher than the 6.9×10^{14} atoms of CO/cm² (0.4ML) reported on BCC Fe(110) but lower than the 1.2×10^{15} atoms of CO/cm²(1ML) of CO adsorbed on BCC Fe(100) (atomic density of Fe(110) is 1.7×10^{15} atoms/cm² and Fe(100) is 1.2×10^{15} atoms/cm²) [27–29]. Comparing the CO coverage of different single crystals with our surface requires establishing the fraction of Fe(100) and BCC(110) present on the surface at each thickness. As such, it is not possible to perform the coverage comparison without conducting an STM analysis at each thickness to determine the surface composition.

After CO adsorption at low temperature, a single O1s peak is seen at 531 eV in Figure 4.2 (b), which is attributed to molecularly adsorbed CO. This peak, according to quantitative evaluation of the C1s spectra, corresponds to $\theta_{\text{CO}}=0.58$ ML used as a reference to quantify the oxygen coverage after CO dissociation. The C1s data shows that this happens below 400 K, and the single peak at 528 eV after heating to 450 K is attributed to atomic oxygen [30]. Quantitative analysis of the peak area yields an O_{ad} coverage of 0.25 ML, a value that agrees well with the 0.25 ML found in the quantitative evaluation of the C1s spectra. The O1s spectrum after a second CO dosing (at 100 K) and heating (to 500 K) is identical to that after the first cycle and thus shows that one CO dissociation cycle already saturates the surface with 0.25 ML C_{ad} and 0.25 ML O_{ad} .

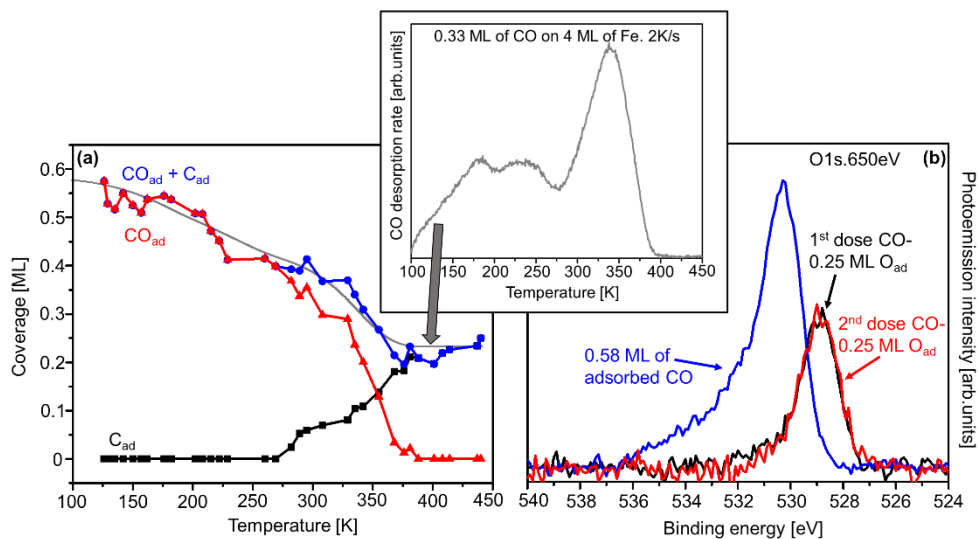


Figure 4.2. **(a)** The CO and carbon coverages during heating a CO-covered 4 ML Fe film. The black, red, and blue curves in **(a)** represent the coverage of the C1s intensity of the atomic carbon, the adsorbed carbon monoxide and the total carbon content on the surface, either in the form of CO or atomic carbon, respectively. The integral of the CO TPD spectrum in the inset is shown as a grey curve, representing the CO species desorbed from the surface. **(b)** The O1s spectra after dissociation of CO and after a second dose of CO show no change in intensity (recorded at 100 K), which indicates no additional O_{ad} was absorbed after the second dose.

Figure 4.3 shows a collection of LEED patterns taken at different stages of the CO interaction with the iron film. The pattern obtained prior to CO exposure [shown in (a)] shows a (5×1) structure typical for a ~ 4 ML iron film. The pattern after CO adsorption at 100 K [provided in (b)] shows a blurry and broad $c(2 \times 2)$ pattern and almost indistinguishable $p(2 \times 2)$ spots. This $c(2 \times 2)$ pattern matches our findings in Chapter 2, where 0.5 ML of CO was adsorbed on Cu(100) and used as a reference for quantification. The diffraction pattern after heating the CO-covered iron film is provided in Figure 4.3 (c) and shows a sharp $c(2 \times 2)$ structure along with a much weaker $p(2 \times 2)$ pattern with missing spots characteristic of $p4g$ symmetry. The pattern is difficult to understand since we do not know whether carbon and oxygen form an atomically mixed layer or if they instead segregate into pure carbon and pure oxygen islands. The pattern may suggest the latter, where the weak $p4g(2 \times 2)$ spots

come from clock-reconstructed C-only islands with a local carbon coverage of 0.5 ML and covering 50% of the surface, whereas the strong $c(2 \times 2)$ spots come from the combined contribution of the carbon-covered part and pure oxygen islands with a $c(2 \times 2)$ structure and a local coverage of 0.5 ML O_{ad}. However, further information, e.g. an STM image, would be needed to obtain more details about the morphology of the surface after CO dissociation.

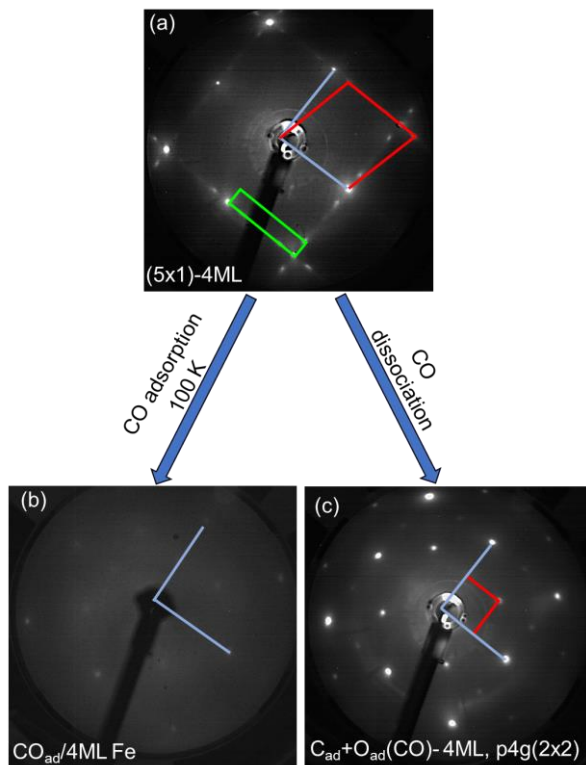


Figure 4.3. LEED images of (a) (5x1) 4 ML iron film on Cu(100) (b) CO adsorbed to saturation on the (5x1) at 100 K (c) $p(2 \times 2)+c(2 \times 2)/0.25$ ML C_{ad}+ 0.25 ML O_{ad} after CO dissociation. Images were taken at 100 K and 100 eV.

As shown in Figure 4.4 (a), TPD was used to study CO reactivity as a function of the CO coverage. It should be noted that a fresh Fe film was deposited for each CO coverage studied since the TPD involves heating to a high temperature which destroys the Fe layer. Apart from CO ($m/z=28$), only a small amount of H₂ desorption

(~0.05 ML) was found, while the absence of CO_2 ($m/z=44$) desorption excludes that CO reacts with surface oxygen. For the smallest CO dose (0.1 L), only a single desorption peak is visible at around 775 K, attributed to the recombination of C_{ad} and O_{ad} produced by CO dissociation. Additional desorption peaks develop around 675 K as the CO coverage increases and are also attributed to the $\text{C}_{(\text{ad})} + \text{O}_{(\text{ad})}$ recombination reaction. Molecular desorption (at 375 K) only starts to be seen for the highest CO coverages when the recombination peaks are fully developed, which is as expected, in line with the TP-XPS data shown in Figure 4.1 and has been reported elsewhere on a polycrystalline surface [29], Fe(110) single crystals [23,24,28], and stepped iron Fe(310) and Fe(710) [31,32].

The desorbed amount of CO [ML] from both the low- and high-temperature desorption features in Figure 4.4 (a) is plotted against the total dosed amounts of CO [ML] in Figure 4.4. (b). The maximum amount of carbon and oxygen recombined extracted from the TPD is 0.15 ML, 0.1 ML less than the values obtained in the XPS; the discrepancy may be attributed to the high temperature needed for the recombination of C_{ad} and O_{ad} . Stability tests presented in Chapter 3 show that iron diffuses into the Cu bulk above 600 K, while carbon tends to form unreactive graphitic carbon.

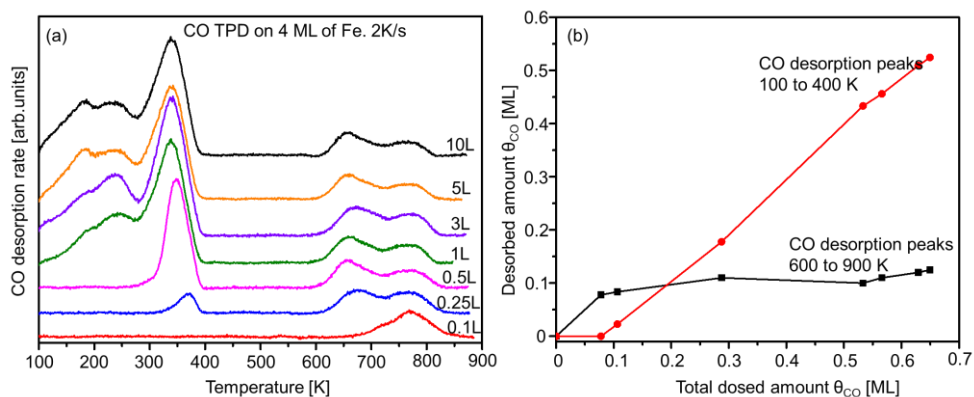


Figure 4.4. (a) TPD spectra of CO were obtained after exposing 4 ML iron films on Cu(100) to various doses of CO at 100 K. The heating rate was 2K/s. (b) The amount of CO desorbing from 4 ML iron film either molecularly (100 to 400 K) or by recombination (600 K to 900 K) against the total dosed amount of CO.

One of the main differences between the desorption spectra of our evaporated iron film, both (BCC-)Fe(110) and polycrystalline (BCC)-Fe, is the presence of what appears to be two recombination peaks at 675 K and 775 K for coverages higher than 0.1 ML (Figure 4.4). These recombination peaks are probably related to the presence of FCC Fe(100) and BCC Fe(110) on films of between 2-10 ML, and thus the dissociation products could be accommodated on different adsorption sites. Unfortunately, no CO dissociation experiments can be carried out on FCC Fe(100), and no DFT papers are related to this topic. However, the difference in desorption energy on polycrystalline iron at 775 K is 177 kJ/mol [10], and on BCC Fe(110), it is 152-188 kJ/mol [14], which suggests different desorption temperatures, and thus the two desorption peaks at 675 K and 775 K could be the consequence of the recombination of C_{ad} and O_{ad} adsorbed on different sites. It should be noted that from 500 K, the iron and iron carbide films begin to intermix, diffuse and segregate, complicating any hypothesis related to recombination peaks.

4.3.2 CO reactivity: influence of Fe film thickness

In addition to the 4 ML film thickness discussed in the previous paragraphs, SR-XPS was also used to study CO adsorption and dissociation on Fe films with a nominal thickness of 1 ML and 8 ML to determine the effect of thickness on CO molecular desorption and dissociation. An iron film with a nominal thickness of ~1 ML typically contains regions with one and two iron layers so that a part of the copper surface is still available [31,32] while intermixing of copper atoms in the Fe may also occur [33]. Figure 4.5 (a) shows a heat map of the C1s region recorded while slowly heating a CO-covered 1 ML Fe film, while individual spectra at key temperatures are shown in the inset. The complex shape of CO photoemission peaks on coinage metals, e.g. Cu, Ag and Au [29,34,35], is attributed to low energy electron-hole pair excitations and shows three characteristic peaks on Cu(100) at 285.5, 288.5 and 293 eV. This sets the CO-on-Cu peak apart from CO-on-Fe, which shows only a single peak. Using the C1s spectrum of CO-saturated Cu(100), the spectrum of CO on 1 ML Fe/Cu(100) could be deconvoluted into the two contributions and evaluated

quantitatively. At 115 K, a CO coverage of 0.6 ML is found, with 0.4 ML CO adsorbed on Cu and 0.2 ML on Fe.

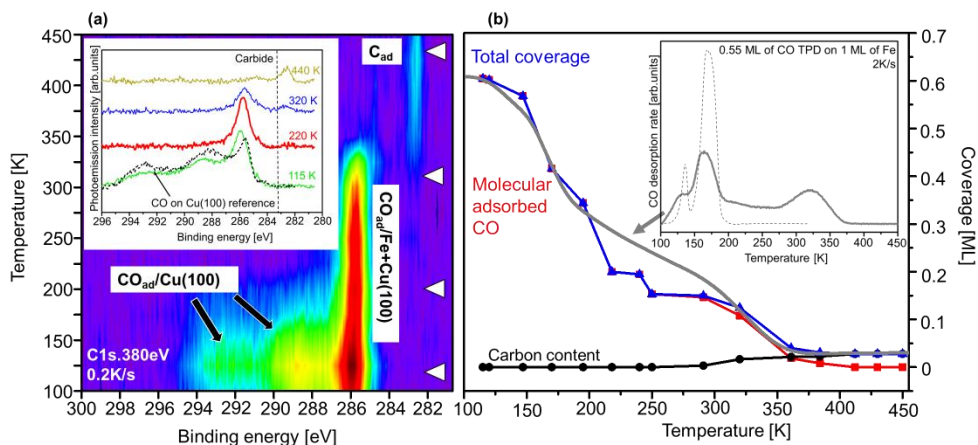


Figure 4.5. **(a)** Intensity map of C1s spectra recorded during heating of a pre-saturated CO on 1 ML Fe/Cu(100) surface in vacuum ($h\nu=380\text{eV}$, 6K per spectra, low intensity=dark blue, high intensity=red/black, heating rate 0.2K/s). **Inset** Individual spectra corresponding to the white symbols on the intensity map. **(b)** The black, red, and blue curves in **(b)** represent the coverage of the C1s intensity of the atomic carbon, the adsorbed carbon monoxide and the total carbon content on the surface, either in the form of CO or atomic carbon, respectively. The integral of the CO TPD spectrum in the inset is shown as a grey curve, representing the CO species desorbed from the surface. The heating rate was 2K/s.

All CO adsorbed on copper desorbs molecularly below 200 K, leaving only 0.2 ML of CO adsorbed on iron. At 300 K, the appearance of a peak at 282.6 eV due to atomic carbon indicates that some CO dissociates and forms carbide. Figure 4.5(b) shows that the adsorbed CO coverage calculated from the quantitative evaluation of the C1s intensity is very similar to the TPD-based quantification of the CO fraction that desorbs molecularly.

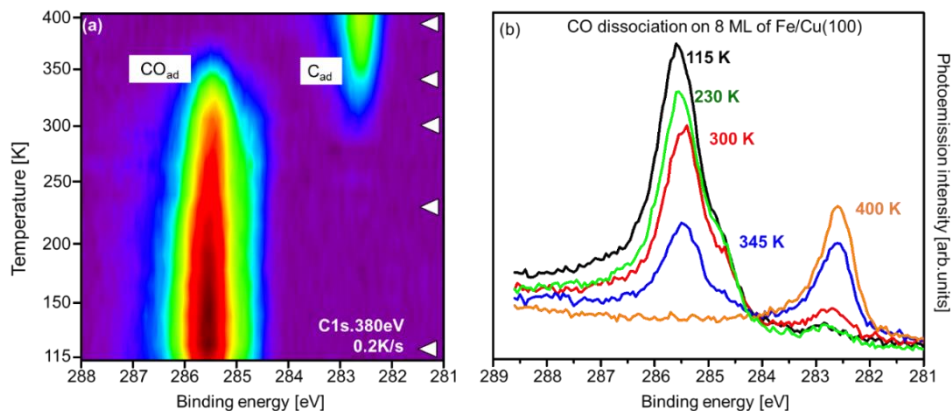


Figure 4.6. (a) Intensity map of C1s spectra recorded during heating of a pre-saturated CO on 8 ML of Fe on Cu(100) surface in vacuum ($h\nu=380\text{eV}$, 6K per spectra, low intensity=purple, high intensity=red/black, heating rate 0.2K/s. (b) Individual spectra corresponding to the white symbols on the intensity map.

The experiment shown in Figure 4.6 is similar to that in Figures 4.5 and 4.1, except that CO was adsorbed on 8 ML of iron instead.

The total CO coverage calculated from the C1s intensity plotted against the temperature in Figure 4.7 was again consistent with the quantification of the CO desorption spectra. The total CO coverage calculated was 0.75 ML, a value within the range of coverages on polycrystalline iron films (0.73 ML) [36]. Approximately 0.25 ML of CO can be dissociated, the same amount as in 4 ML of iron films, leaving 0.5 ML of dissociation products on the surface. The desorption spectrum shown in the inset of Figure 4.7 is similar to the TPD spectra found by others on Fe BCC(110) [9,37] and for polycrystalline surfaces [38]. However, the CO desorption temperature from the 8 ML iron film is 50 K lower than BCC(110) and polycrystalline iron.

Using SIMS, XPS, UPS, and EELS, different groups have shown that CO dissociates at a temperature of roughly 300 K on polycrystalline iron surfaces, with a rate constant ten times higher than the desorption constant at a temperature of 390 K [34], where no more molecular CO remains on the surface [39,40].

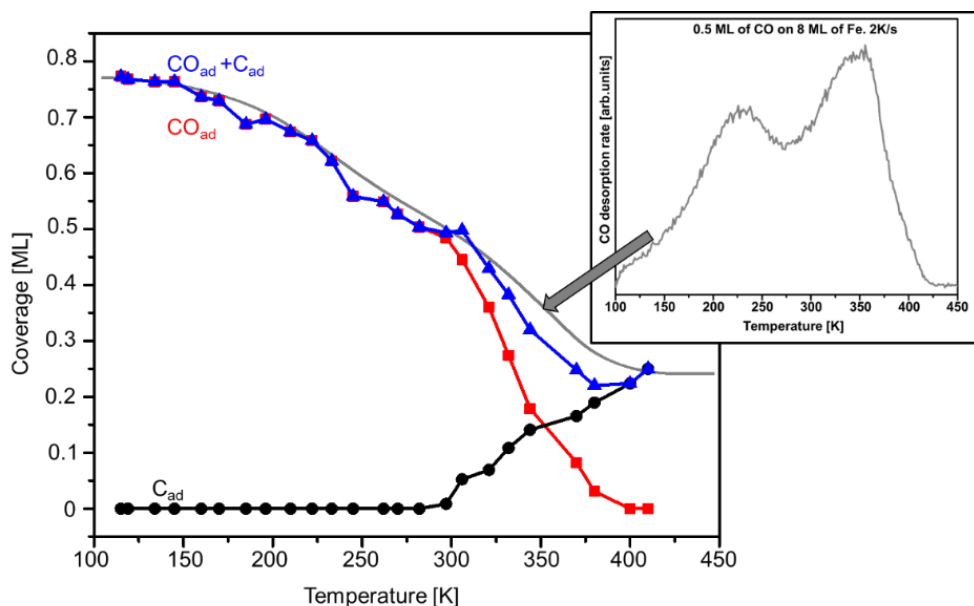


Figure 4.7 The evolution of the molecular coverage of CO on 8 ML of Fe and the amount of carbide formed derived from the individual spectra from the heat map vs. temperature. The black, red, and blue curves represent the coverage of the C1s intensity of the atomic carbon, the adsorbed carbon monoxide and the total carbon content on the surface, either in the form of CO or atomic carbon, respectively. The integral of the CO TPD spectrum in the inset is shown as a grey curve, representing the CO species desorbed from the surface. In the *inset*, a TPD spectra that was obtained after exposing an 8 ML film with CO at 100 K to saturation. Heating rate 2K/s.

On BCC Fe(110), Gonzalez et al. [37] reported that the maximum amount of CO able to dissociate corresponds to 1/8 of a monolayer, similar to the findings on polycrystalline iron [10] and 0.1 ML lower than those found for Fe BCC(100), 0.25 ML (0.25 C_{ad} + 0.25 O_{ad}) [41,42]. Thus, the total dissociation products on evaporated iron films up to 10 ML is higher than in single crystals, probably related to the open structure of the FCC Fe(100) influence of the film, which can accommodate more products on the surface.

Figure 4.8 summarises the XPS and TPD results presented in this section. In (a), the CO TPD spectra from different thicknesses show how the desorption and dissociation temperature shifts towards higher temperatures with increased

thickness, also confirmed by XPS measurements summarized in (b). At 4 ML and 8 ML, the reactivity is almost identical, meaning a similar surface structure. However, at 4 ML, the surface is a mixture between FCC Fe(100) and BCC Fe(110), and at 8 ML, the surface is mostly BCC Fe(110). From these graphs, we can also extract the ratios between adsorbed CO and dissociated CO: For 1, 4, and 8 ML, the ratio between the total adsorbed CO on iron and the quantity of CO that dissociates is 3:1 (0.15/0.025), 2.2:1 (0.55/0.25), and 3:1 (0.75/0.25), respectively.

We propose that CO reacts as follows on films between 2-10 ML (close film): CO adsorbs molecularly at low temperatures (100 K) and dissociates into carbon and oxygen on the surface at temperatures between 275-300 K. Similar values of dissociation are found on polycrystalline iron or Fe BCC(110) (300 K – 350 K) [10,24].

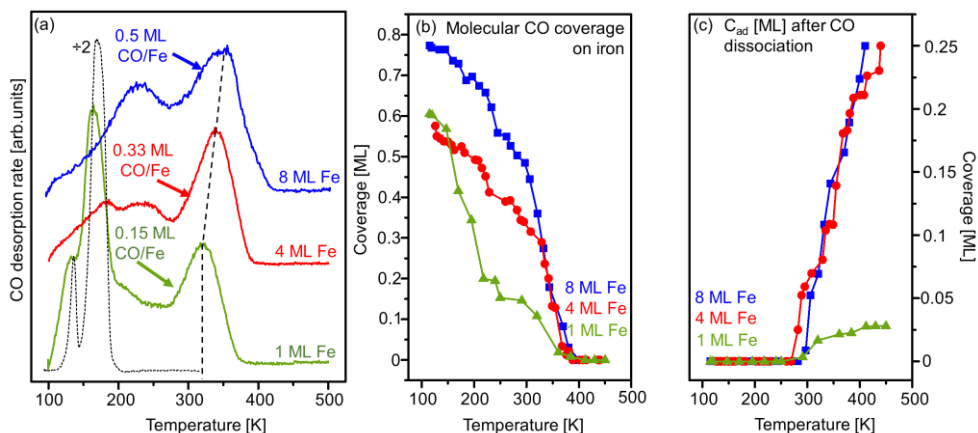


Figure 4.8 (a) CO TPD from iron films of different thicknesses (2K/s) (b) Uptake curve of the molecular CO coverage extracted from the TP-XPS C1s area. (c) The uptake curve of the carbon content after CO dissociation was extracted from the C1s intensity in the TP-XPS

4.3.3 CO on Fe_xC: molecular adsorption, desorption and dissociation

In this section, we examine the results of the interaction of CO with the Fe₂C p4g(2x2) surface carbide, named Fe₂C/Fe/Cu(100), for simplicity, which was studied

using a combination of SR-XPS, TPD, RAIRS and Auger electron spectroscopy. Chapter 3 describes in detail that the Fe₂C structure formed by ethylene decomposition on Fe films is very stable and acts as a carbon trap, which prevents carbon diffusion into the bulk so that the surface remains carbon-rich and inactive for further ethylene dissociation.

Figure 4.9 (a) compares CO desorption spectra from clean copper, a pure (4 ML) Fe film and a Fe₂C/Fe/Cu(100), respectively. The CO desorption from CO-saturated Fe₂C/Fe/Cu(100) shows two desorption peaks (dark blue) corresponding to ~0.25 ML CO_{ad} with a ratio of ~1:2. The most strongly bound CO desorbs ~300 K (~0.17ML), around 50 K lower than the most strongly bound molecular desorption peak from the pure Fe film (red), implying that CO adsorbs more weakly on the Fe₂C surface than on the pure Fe film. The same effect has been observed to a lesser extent in polycrystalline iron films. It has been demonstrated in the PhD thesis by Dr F.J.E. Scheijen [36] that carbon on the surface can decrease the desorption barrier by 10 kJ/mol, attributed to repulsion between pre-adsorbed carbon and CO_{ad}.

A small desorption peak is observed at 650 K on Fe₂C, whose origin is difficult to determine due to the high temperature. However, there are reports on non-carburized Fe(100), Fe(111) and polycrystalline iron films that these peaks are related to the recombination of C_{ad} and O_{ad} [38,43,44]. It was shown in the previous chapter that saturated iron carbide films are inactive toward ethylene dissociation due to the presence of atomic carbon, which blocks the sites at which dissociation products are accommodated. We attribute this peak to contamination during iron evaporation; if we take the area under the curve, between 600 K and 700 K, the coverage calculated results in 0.01 ML of C_{ad}+O_{ad}.

Figure 4.9 (b) shows the C1s spectra after adsorbing CO on Fe₂C/Fe/Cu(100) at 100 K. The two peaks at 286 eV and 282.5 eV are attributed to CO_{ad} and have the same binding energy as CO_{ad} on pure Fe films, while 282.5 eV is attributed to surface carbide. The decrease of the signal intensity, as well as the shift to higher binding energy, is attributed to the effect of co-adsorbed CO on the position and intensity of the C_{ad} peak, as previously reported on cobalt by Weststrate et al. [45] and gold by Yi et al. [30]. Upon desorption of CO from the carburized surface, the process is completely reversed; a comparison with the spectrum prior to CO dosing indicates

that neither the intensity nor the binding energy of the atomic carbon/carbide peak has changed, and no significant CO dissociation took place. This is confirmed by the absence of an O_{ad} peak in the O1s region following desorption of CO, as shown in the inset of Figure 4.9.

CO thus adsorbs intact and does not dissociate on the stoichiometric Fe_2C surface, and IR absorption spectroscopy was used to further characterize molecularly adsorbed CO on Cu(100), Fe/Cu(100) and $Fe_2C/Fe/Cu(100)$. As shown in the inset of Figure 4.9, the frequency of the C-O stretching band ranges from 2088 cm^{-1} for CO on Cu(100) to 2030 cm^{-1} for CO on 2 ML Fe/Cu, that is, all in the region for CO bound on top sites [7,40,46–48]. We note that the spectra of the 2 ML Fe show two peaks, one for CO adsorbed on Fe and a second for CO on Cu, indicating that the iron film had not yet fully closed for this small quantity of iron. A sharp peak with a shoulder at lower wavenumbers can be seen at 4 ML of CO adsorbed on $Fe_2C/Fe/Cu(100)$. According to Tanabe et al. [49], this shoulder could be related to CO adsorption on an equivalent bridge adsorption site ($1942\text{--}1970\text{ cm}^{-1}$). They used IR to study the different adsorption sites of CO at 90 K on polycrystalline Fe foil and 8 ML Fe film on Cu(100), using different CO doses [7,49]. At low doses (0.2 L), CO adsorbs predominantly on bridge sites with a band at 1960 cm^{-1} . The bridge band remains unchanged at high doses (1.2 L), but a new band representing adsorption on top sites can be seen, $2032\text{--}2055\text{ cm}^{-1}$.

At this point, there are two hypotheses as to why CO can not dissociate on Fe_2C films. The first is related to electrostatic repulsion between the pre-adsorbed carbon and the adsorbed CO molecules, making molecular desorption the more favourable reaction. An alternative explanation is that CO cannot dissociate since the preferred location for the dissociation products is already occupied [16,41,50]. For ethylene decomposition, depositing more than 0.5 ML on the surface was found unfavourable, and we found the same value when adding the C + O dissociation products for the maximum amount of CO dissociation.

4.3 Results and discussion

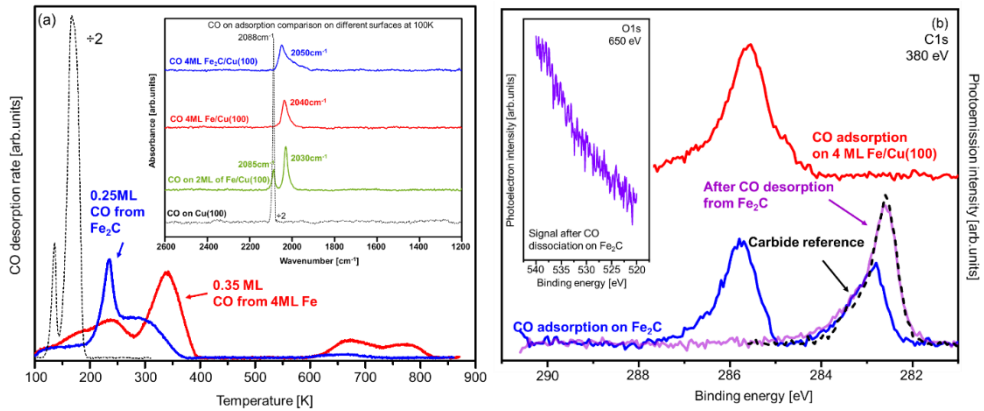


Figure 4.9. (a) TPD spectra of CO on 4 ML iron and iron carbide film at a heating rate of 2 K/s. In the *inset* RAIRS spectra of CO for saturated adsorption at 100 K on 2 ML and 4 ML of iron and Fe₂C/Fe/Cu(100). (b) C1s spectrum of CO adsorbed on 4 ML of Fe₂C at 100 K, and after CO desorbed the surface at 500 K. The Black dotted line is the 0.5 ML carbide reference. In the *inset*, the O1s intensity after trying to dissociate CO on the iron carbide overlayer.

Figure 4.10 shows the LEED pattern before and after adsorbing CO at 100 K on a Fe₂C surface carbide, which shows a pattern with p4g(2x2) symmetry prior to and after CO dosing. This is similar to the results reported by Nieskens et al. [51], who found that CO adsorption on carbon-covered c(2x2)C/Rh(100) did not create extra spots in the LEED pattern.

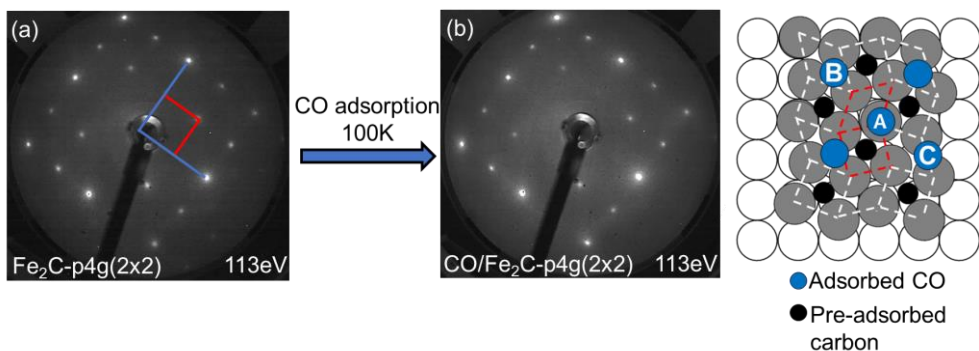


Figure 4.10 LEED pictures of (a) A p4g(2x2) before and (b) after adsorbing CO at 100 K. A proposed model for CO adsorption on Fe₂C/Fe/Cu(100). LEED were taken at 113 eV and 100 K.

Proposing a CO adsorption model on Fe₂C only based on our IR results is not enough. In our case, the wavenumber after adsorbing CO at 100 K on iron and iron carbide is the same, corresponding to a top site on iron. In Figure 4.10. we draw a model based on this finding, where (A) is an adsorption site where the CO is surrounded by pre-adsorbed carbon atoms where electrostatic repulsion makes this scenario the least likely. However, the threefold (B) or bridge sites (C) are more plausible adsorption options. More experiments with IR, together with DFT, are required in this system to propose a valid model.

CO dissociation on a sub-saturated iron carbide surface was explored by dosing the equivalent of 0.3 ML of carbon (=1 L ethylene) onto a 4 ML thick Fe film. Figure 4.11 shows the XPS results obtained before and after CO dosing and heating to 450 K. The C1s spectrum afterwards shows a slight increase in the atomic carbon signal, from 0.25 to 0.33 ML, but the O1s spectra provide much clearer proof for CO dissociation. The O1s spectrum, after preparation of the sub-saturated Fe_xC_y, contains only a tiny amount of oxygen, but it shows a peak equivalent to 0.1 ML O after CO adsorption and heating. An attempt was made to dissociate additional CO by performing another adsorption + heating cycle, but as we did not find an increase of either the C1s or O1s, we concluded that one cycle of CO adsorption and heating created a surface that is inactive for CO dissociation. With the initial carbon concentration of 0.25 ML, a gain of 0.08 ML C_{ad} and 0.1 ML O_{ad}, the sum of C and O becomes 0.43 ML, reasonably close to the value of 0.5 ML that we find at the saturation point of ethylene decomposition as well as after CO dissociation on clean iron. Thus, this coverage seems to be the point where the reactivity of the surface shows a pronounced change, irrespective of the exact chemical identity of the adsorbate.

Concerning the FTS mechanism, our results demonstrate that non-carburized and partially-carburized iron surfaces contain sites that enable CO dissociation. Since CO dissociation cannot be rate-determining, as no carbon build-up would occur if it were, these sites might be necessary to form the iron carbides, which are believed, as noted earlier, to be active species in the FTS [3].

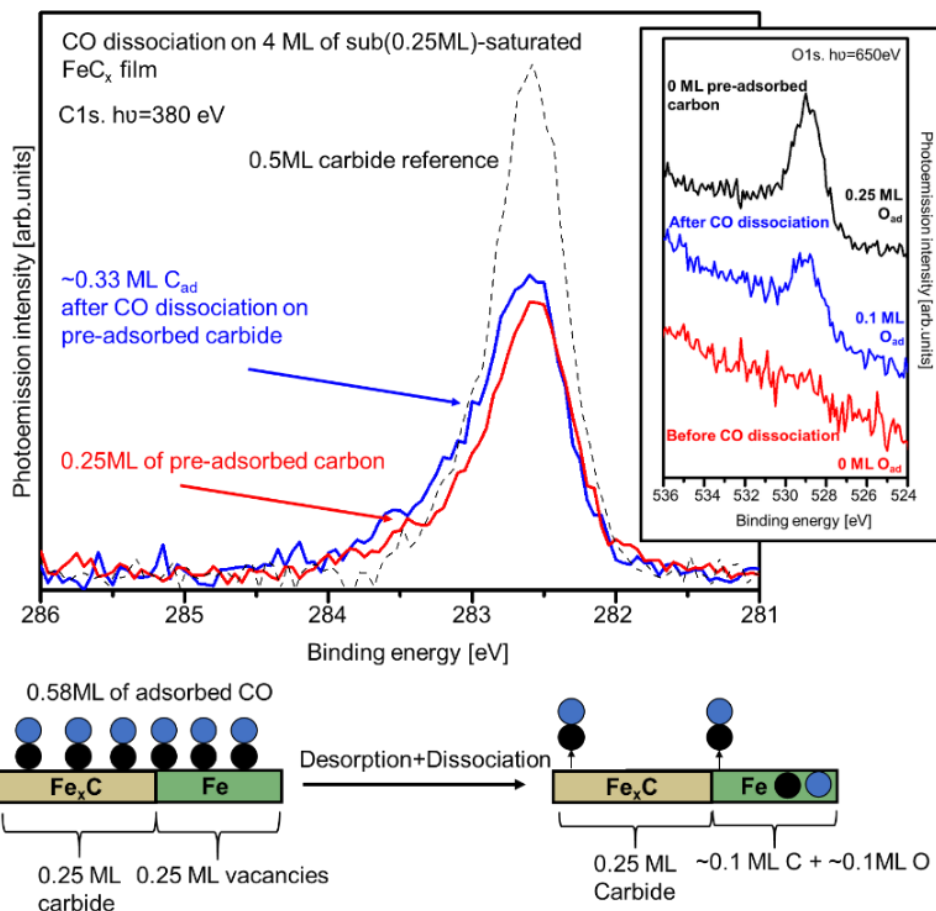


Figure 4.11. XPS spectra of the C1s region after CO dissociation on a pre-covered iron carbide surface with 0.3 ML of carbon taken at 160 K. As a black dotted line, the 0.5 ML carbide reference after ethylene dissociation. In the inset, the O1s before and after CO dissociation on a pre-adsorbed 0.3 ML carbon surface.

4.3.4 H₂ adsorption and desorption on Fe and Fe₂C films on Cu(100)

Dissociative adsorption of hydrogen on both pure iron films and Fe₂C/Fe/Cu(100) was investigated using thermal desorption spectroscopy. Figure 4.12 (a) shows a series of H₂ desorption spectra for different Fe film thicknesses using the same hydrogen dose of 10 L, which was found to be sufficient to saturate the different iron

films. For an iron coverage of 0.5 ML, only a relatively small single peak at 375 K can be seen. The shape and temperature of the desorption peaks remain the same when the Fe coverage is increased from 1 to 6 ML of iron, and only the amount of desorbed H_2 increases.

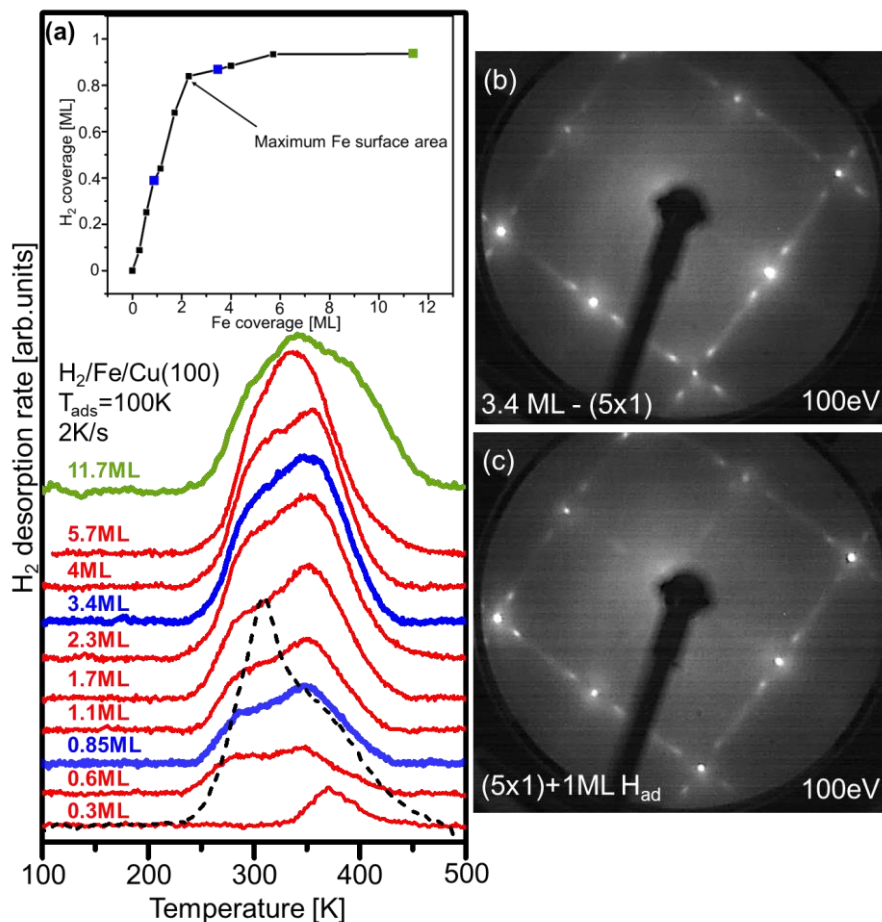


Figure 4.12 (a) Hydrogen thermal desorption spectra from iron films on Cu(100) as a function of iron coverage. Hydrogen exposure 10L (saturated). In the *inset*, the coverage calculation is extracted from the desorption areas of the TPD. The green line corresponds to the desorption from a BCC(110) surface. As a black dotted line, the H_2 reference from ethylene dissociation. (b) (5×1) LEED pattern after evaporating 3.4 ML of iron. (c) $(5 \times 1) + 1 ML H_{ad}$ LEED pattern after adsorbing at 100 K 1 ML of H_{ad} . LEED images were taken at 100 K and 100 eV.

The morphology of the iron film changes from FCC-Fe(100) to BCC-Fe(110) around 12 ML (see Chapter 3). The H₂ desorption temperature and shape match the previous experiments on Cu(100)-supported Fe films reported by Egawa et al. [17,52]. As in their case, we found that the hydrogen desorption temperature shifts towards higher temperatures with increased thickness.

We tentatively attribute the new high-temperature shoulder that appears for $\theta_{\text{Fe}} \sim 12$ ML to hydrogen adsorbed on BCC-Fe(110) and note that the spectral shape converges to the desorption temperature found for polycrystalline pure BCC-Fe films reported in [53]. The maximum temperature of desorption on iron single crystals, BCC Fe(100) [44] and BCC Fe(110) [9], vary from 400 K to 450 K, respectively. Polycrystalline iron [36] and evaporated iron films on Cu(100) [17] are 350 K and 325 K, respectively. The heating rates for these experiments vary from 2 K/s to 10 K/s, so the desorption temperature difference could be related to this.

The hydrogen coverage is reported relative to a 1 ML Had-on-Cu(100) reference. The area under the H₂ desorption peaks was plotted against iron film thickness and is shown in the inset of figure 4.12 (a). At a thickness of 2 ML, the area underneath the H₂ desorption reaches a constant value, indicating that the Fe film closes at a film thickness of 2 ML, as discussed previously in Chapter 3.

Figure 4.12 (c) shows the LEED pattern after 1 ML of hydrogen adsorption on 3.4 ML of iron, where a vague $p(2 \times 1)\text{-H}$ is observed. Biedermann et al. [54] observed an iron surface reconstruction to $p4g(2 \times 2)$ without adsorbants between 5 K and 80 K on 6-7 ML. On this $p4g(2 \times 2)$, hydrogen is adsorbed, resulting in a $p(2 \times 1)$ with hydrogen sitting on the threefold sites. In Chapter 3, we found that the $p4g(2 \times 2)$ reconstruction of the (5×1) iron surface can only occur when carbon is adsorbed on the surface. Hydrogen or temperature changes cannot lead to $p4g(2 \times 2)$ symmetry. Therefore, we can exclude the possibility of $p4g(2 \times 2)$ formation due to H adsorption. Some articles related to the appearance of additional LEED spots due to H_{ad} can be found in the literature: H_{ad} on W(100) [55], Pd [56], and H_{ad} on Co(0001) [57]. Boszo et al. [58] studied hydrogen adsorption on BCC Fe(110) single crystals where ordered overlayers were observed on coverages between 0.5 ML and 1 ML. Therefore, we may tentatively interpret this diffraction as an ordered structure in the evaporated iron films.

The hydrogen desorption temperature from our experiments was much lower than the 450 K obtained from the Fe(110) crystal and resembles the BCC Fe(100), confirming the complexity of this system when interpreting the adsorption and desorption of hydrogen from iron films.

After adsorbing hydrogen on different thicknesses of iron, we investigated the adsorption and desorption of hydrogen on fully saturated iron carbide films ($\text{Fe}_2\text{C}/\text{Fe}/\text{Cu}(100)$).

Similar to the case of Cu(100), we found that H_2 does not dissociatively adsorb on saturated iron carbide surfaces ($\text{Fe}_2\text{C}/\text{Fe}/\text{Cu}(100)$) even with high doses of H_2 , 1000 L at 100 K. Therefore, we used a hot W filament to generate atomic H, which we found to adsorb on the iron carbide film as well.

Figure 4.13 shows a H_2 TPD series after dosing different quantities of H_2 on a $\text{Fe}_2\text{C}/4\text{MLFe}/\text{Cu}(100)$. Apart from H_2 , no other traces, such as CO ($m/z=28$) or CO_2 ($m/z=44$), were observed. At 0.1 ML of H_{ad} , only one desorption feature is visible at a temperature of 240 K. At higher coverages of H_{ad} , a shoulder develops from the main peak following second-order kinetics (shift towards lower temperatures with an increase in coverage). In contrast, the temperature of the main peak remains constant irrespective of the coverage of H_2 , characteristic of first-order desorption kinetics. The desorption spectra from Fe_2C and non-carburized iron films demonstrate that the desorption temperature is almost 100 K lower. As there is no previous literature related to hydrogen desorption from iron carbide films on Cu(100), the interpretation of these peaks and the possible adsorption sites must be derived from DFT results.

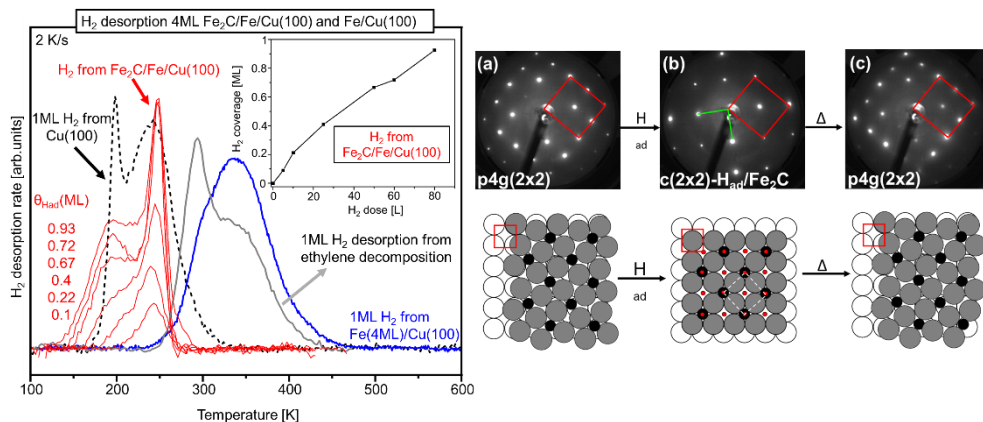


Figure 4.13. TPD spectra of H_2 from 4ML of iron (blue) and the TPD spectra of H_2 desorption (2 K/s) after different dosages on $Fe_2C/Fe/Cu(100)$ at 100K as red. H_2 was adsorbed onto the Fe_2C film using a W filament at 100 K. The dotted spectrum is from H_2 desorption from $Cu(100)$ used as a reference, together with H_2 desorption from ethylene dissociation shown as grey. In the **inset**, the uptake curve in which the areas of the H_2 desorption from $Fe_2C/Fe/Cu(100)$ have been converted to coverage. The LEED pictures were taken before **(a)** and after **(b)** adsorption of hydrogen (W filament), and **(c)** pattern after desorbing all the H_{ad} . LEED were taken at 100K and 100 eV.

An uptake curve is shown in the inset derived from the area under the curve of the TPD spectra. The total content we adsorbed on the saturated iron carbide film is 0.93 ML; we decided to stop the experiment when we reached almost 1 ML of H_{ad} , where the ratio between desorption peaks from a $Fe_2C / 4 MLFe/Cu(100)$ is approximately 1:1.

A possible explanation for the 1st order behaviour would be that hydrogen atoms are reactive enough to create a C-H bond. The 1st order behaviour would be caused by C-H bond breaking, a 1st order reaction, as the rate-limiting step. This hypothesis aligns with the size of the 1st order peak in TPD, 0.5 ML H_{ad} , which matches the carbon concentration. The low desorption temperature, on the other hand, speaks against the formation of C-H bonds: ethylene decomposition on our Fe films proceeds in steps, where the first C-H bond is broken around 250 K, but the last C-H bond in the C-CH species persists up to 400 K. As CH is most similar to the latter species, it appears unlikely that it would decompose already at 250 K. This also

could explain the formation of the $c(2 \times 2)$ pattern, where, according to DFT calculations made elsewhere [18,19], H_{ad} sit on the fourfold site between iron atoms following second-order desorption, while the other 50% of adsorbed atoms (TPD peak ratio is 1:1) is bonded to C. Note how we suggest a model, in 4.13 (c) where no $p4g(2 \times 2)$ can be seen. Instead, an FCC Fe(100) dominates the surface now. The reasoning for drawing such a model is the following: When H is adsorbed, a C-H bond is formed, and thus, this weakens the bonding between C and the surrounding Fe atoms, making the surface slightly reconstructed until all the H is desorbed, after this, the lack of the fourth bond in C, creates a driving force where the $p4g(2 \times 2)$ is formed again.

However, without spectroscopic information from, e.g., XPS or EELS, the origin of the 1st order H_2 desorption peak at 250 K remains undetermined.

In their study, Benziger et al. [24] adsorbed H_2 on a carbon-contaminated iron single-crystal surface without using a W filament. It was found that the H_2 desorption temperature shifted toward lower temperatures compared to the non-contaminated surface, and after heating, the carbon diffused into the bulk, similar to what we observed in our thick films (>12 ML, as discussed in Chapter 3). They also claim, together with Brucker and Rodin [59], that the adsorption of hydrogen on a carburized BCC Fe(100) surface at 98 K leads to the formation of methylene, so the desorption of hydrogen from the surface could be a combination of hydrogen desorption and methylene decomposition.

4.4 Conclusions

This chapter describes the interaction of CO and H_2 on 1,4 and 8 ML of iron and iron carbide surfaces with different pre-adsorbed carbon concentrations.

Carbon monoxide dissociation on evaporated iron films on Cu(100) is the preferred reaction over molecular desorption. This is concluded since the desorption peak from TPD, at 750 K, due to recombination saturates before molecular desorption is seen. The CO dissociation reaction always occurs independently of the thickness, between 275-300 K, leaving 0.5 ML of products on the surface when the iron films cover the

substrate entirely. The BE of the C1s after CO dissociation is 282.6 eV, confirming that CO is a precursor for the carbide phase.

Molecular desorption of CO from a Fe₂C surface occurs at a 100 K lower temperature than uncarbided films, indicating that the pre-adsorbed carbon and CO interact in an electrostatically repulsive manner, leading to a weakening of the bond between CO and the surface. Also, the presence of pre-adsorbed carbon inhibits CO dissociation primarily because carbon atoms occupy the preferred adsorption sites of the dissociation products. When the iron film becomes thicker, the molecular desorption temperature of CO increases from 325 K (1 ML of Fe) to 350 K (8 ML of Fe) until the surface reaches a relaxed BCC Fe(110) structure, where the desorption temperature is similar to the single crystals.

We found that H₂ desorption temperature is also affected by the iron thickness, showing a shift towards higher temperatures when the film behaves BCC Fe(110), increasing the similarities with the BCC Fe(110) single crystal and total coverage of ~1 ML H_{ad}.

The carbon on the surface inhibits dissociative adsorption of H₂, thus exciting the H₂ molecule to overcome the dissociation barrier is required for adsorption. The H₂ desorption temperature on iron carbides is 100 K lower than on non-carburized films, suggesting a weakening of the Fe-H and C-H bonds when carbon is present on the surface. The desorption temperatures of H₂ from Fe₂C/Fe/Cu(100) show a mixed behaviour between second- and first-order desorption. We suggest C-H and Fe-H bonding, being the latter related to second-order and the 1st order behaviour, would be caused by C-H bond breaking, a 1st order reaction, as the rate-limiting step. We wish to conclude this chapter by highlighting the objective of this thesis, which is to create an iron carbide model catalyst for FTS.

The use of near ambient pressure (NAP)- XPS may prove helpful to push the surface to higher H₂ and H radical pressures in order to evaluate, i.e., whether the carbon in the p4g(2x2) structure can be removed or/and act as an initiator for chain growth. Nonetheless, the Fe₂C films may have potential applications in the study of catalyst deactivation or the investigation of the importance of defects on surfaces.

Surfaces with lower amounts of carbon exhibit reactivity towards CO and H₂ dissociation. In order to explore the feasibility of iron carbide as a model catalyst,

lower carbon concentration experiments are necessary to determine if it can be used as a model catalyst.

4.5 References

- [1] S.R. Craxford, E.K. Rideal, The mechanism of the synthesis of hydrocarbons from water gas, *J. Chem. Soc.* 338 (1939) 1604. <https://doi.org/10.1039/jr9390001604>.
- [2] S. Shetty, A.P.J. Jansen, R.A. Van Santen, Direct versus hydrogen-assisted CO dissociation, *J. Am. Chem. Soc.* 131 (2009) 12874–12875. <https://doi.org/10.1021/ja9044482>.
- [3] J.M. Gracia, F.F. Prinsloo, J.W. Niemantsverdriet, Mars-van krevelen-like mechanism of CO hydrogenation on an iron carbide surface, *Catal. Letters.* 133 (2009) 257–261. <https://doi.org/10.1007/s10562-009-0179-5>.
- [4] R. a. VanSanten, A.J. Markvoort, Chain growth by CO insertion in the Fischer-Tropsch reaction, *ChemCatChem.* 5 (2013) 3384–3397. <https://doi.org/10.1002/cctc.201300173>.
- [5] R.A. van Santen, A.J. Markvoort, I.A.W. Filot, M.M. Ghouri, E.J.M. Hensen, Mechanism and microkinetics of the Fischer-Tropsch reaction., *Phys. Chem. Chem. Phys.* 15 (2013) 17038–63. <https://doi.org/10.1039/c3cp52506f>.
- [6] K. Jagannathan, A. Srinivasan, M.S. Hegde, C.N.R. Rao, Interaction of carbon monoxide with transition metal surfaces, *Surf. Sci.* 99 (1980) 309–319. [https://doi.org/10.1016/0039-6028\(80\)90395-7](https://doi.org/10.1016/0039-6028(80)90395-7).
- [7] T. Tanabe, T. Shibahara, R. Buckmaster, T. Ishibashi, T. Wadayama, A. Hatta, Infrared spectral study of CO adsorption on molecular-beam epitaxially grown, fcc iron films on Cu(100), *Surf. Sci.* 466 (2000) 1–10. [https://doi.org/10.1016/S0039-6028\(00\)00772-X](https://doi.org/10.1016/S0039-6028(00)00772-X).
- [8] J. Radnik, E. Chopovskaya, M. Grüne, K. Wandelt, Interaction of CO with heteroepitaxial fcc-and bcc-Fe films on Cu(100), *Surf. Sci.* 352–354 (1996) 268–273. [https://doi.org/10.1016/0039-6028\(95\)01145-5](https://doi.org/10.1016/0039-6028(95)01145-5).
- [9] B. Sieben, H.P. Bonzel, Adsorption of H₂ and CO on Mn/Fe(110) surfaces, *Surf. Sci.* 282 (1993) 246–254. [https://doi.org/10.1016/0039-6028\(93\)90930-I](https://doi.org/10.1016/0039-6028(93)90930-I).
- [10] F.J.E. Scheijen, The surface chemistry of CO on iron and other bcc metals, Technische Universiteit Eindhoven, 2010. <https://doi.org/10.6100/IR657952>.
- [11] M.O. Ozbek, J.W. Niemantsverdriet, Elementary reactions of CO and H₂ on C-terminated χ -Fe 5C₂(0 0 1) surfaces, *J. Catal.* 317 (2014) 158–166. <https://doi.org/10.1016/j.jcat.2014.06.009>.
- [12] A. Chakrabarty, O. Bouhali, N. Mousseau, C.S. Becquart, F. El-Mellouhi, Influence of surface vacancy defects on the carburization of Fe 110 surface by carbon monoxide, *J. Chem. Phys.* 145 (2016). <https://doi.org/10.1063/1.4958966>.

- [13] A. Chakrabarty, O. Bouhali, N. Mousseau, C.S. Becquart, F. El-Mellouhi, Insights on finite size effects in ab initio study of CO adsorption and dissociation on Fe 110 surface, *J. Appl. Phys.* 120 (2016). <https://doi.org/10.1063/1.4959990>.
- [14] D.E.Jiang, E.A.Carter, Adsorption and dissociation of CO on Fe(110) from first principles, *Surf. Sci.* 570 (2004) 167–177. <https://doi.org/10.1016/j.susc.2004.07.035>.
- [15] D.E. Jiang, E.A. Carter, Diffusion of interstitial hydrogen into and through bcc Fe from first principles, *Phys. Rev. B.* 70 (2004) 064102-1-064102–9. <https://doi.org/10.1103/PhysRevB.70.064102>.
- [16] T.C. Bromfield, D.C. Ferré, J.W. Niemantsverdriet, A DFT study of the adsorption and dissociation of CO on Fe(100): Influence of surface coverage on the nature of accessible adsorption states, *ChemPhysChem.* 6 (2005) 254–260. <https://doi.org/10.1002/cphc.200400452>.
- [17] C. Egawa, E.M. McCash, R.F. Willis, Adsorption of hydrogen on thin fcc-iron films grown on Cu(100), *Surf. Sci.* 215 (1989). [https://doi.org/10.1016/0039-6028\(89\)90691-2](https://doi.org/10.1016/0039-6028(89)90691-2).
- [18] E. Van Steen, P. Van Helden, A DFT study of hydrogen dissociation on CO- and C-precovered Fe(100) surfaces, *J.Phys.Chem C.* 114 (2010) 5932–5940. <https://doi.org/10.1021/jp909689a>.
- [19] X.Y. Liao, S.G. Wang, Z.Y. Ma, J. Wang, Y.W. Li, H. Jiao, Density functional theory study of H₂ adsorption on the (100), (001) and (010) surfaces of Fe₃C, *J. Mol. Catal. A Chem.* 292 (2008) 14–20. <https://doi.org/10.1016/j.molcata.2008.06.007>.
- [20] D.B. Cao, F.Q. Zhang, Y.W. Li, J. Wang, H. Jiao, Density functional theory study of hydrogen adsorption on Fe 5C₂(001), Fe₅C₂(110), and Fe₅C₂(100), *J. Phys. Chem. B.* 109 (2005) 833–844. <https://doi.org/10.1021/jp046239>.
- [21] J. Harris, On the adsorption and desorption of H₂ at metal surfaces, *Appl. Phys. A Solids Surfaces.* 47 (1988) 63–71. <https://doi.org/10.1007/BF00619699>.
- [22] E.M.M. and W.A. M.Arnott, Growth and thermal properties of fcc iron films on Cu(100), *Surf. Sci.* 270 (1992) 724–730.
- [23] M. Arnott, W. Allison, Thermal diffusion of iron into a copper(1 0 0) crystal studied by Auger Electron Spectroscopy (AES), *Phys. B Phys. Condens. Matter.* 161 (1990) 289–293. [https://doi.org/10.1016/0921-4526\(89\)90151-8](https://doi.org/10.1016/0921-4526(89)90151-8).
- [24] J. Benziger, R.J. Madix, The effects of carbon, oxygen, sulfur and potassium adlayers on CO and H₂ adsorption on Fe(100), *Surf. Sci.* 94 (1980) 119–153. [https://doi.org/10.1016/0039-6028\(80\)90160-0](https://doi.org/10.1016/0039-6028(80)90160-0).
- [25] C. Wiltner, A., and Linsmeier, Formation of endothermic carbides on iron and nickel, *Phys.Stat.Sol.* 201 (2004) 881–887. <https://doi.org/10.1002/psa.200304362>.
- [26] J. Pritchard, On the structure of CO adlayers on Cu(100) and Cu(111), *Surf. Sci.* 79 (1979) 231–244. [https://doi.org/10.1016/0039-6028\(79\)90039-6](https://doi.org/10.1016/0039-6028(79)90039-6).
- [27] M. Nassir, D.J. Dwyer, P. Kleban, Dissociation-stimulated desorption: A new mechanism for CO/Fe(100), *Surf. Sci.* 356 (1996) 9–12. [https://doi.org/10.1016/0039-6028\(96\)00671-1](https://doi.org/10.1016/0039-6028(96)00671-1).

- [28] G. Brodén, G. Gafner, H.P. Bonzel, CO adsorption on potassium promoted Fe(110), *Surf. Sci.* 84 (1979) 295–314. [https://doi.org/10.1016/0039-6028\(79\)90139-0](https://doi.org/10.1016/0039-6028(79)90139-0).
- [29] A. Sandell, P. Bennich, A. Nilsson, B. Hernnäs, O. Björneholm, N. Mårtensson, Chemisorption of CO on Cu(100), Ag(110) and Au(110), *Surf. Sci.* 310 (1994) 16–26. [https://doi.org/10.1016/0039-6028\(94\)91366-8](https://doi.org/10.1016/0039-6028(94)91366-8).
- [30] Y. Li, Z. Li, A. Ahsen, L. Lammich, G.J.A. Mannie, J.W. Niemantsverdriet, J. V. Lauritsen, Atomically Defined Iron Carbide Surface for Fischer-Tropsch Synthesis Catalysis, *ACS Catal.* 9 (2019) 1264–1273. <https://doi.org/10.1021/acscatal.8b03684>.
- [31] T. Bernhard, M. Baron, M. Gruyters, H. Winter, Surface structure of ultrathin Fe films on Cu(001) revisited, *Phys. Rev. Lett.* 95 (2005) 5–8. <https://doi.org/10.1103/PhysRevLett.95.087601>.
- [32] A. Biedermann, Stability of the nanomartensitic phase in ultrathin Fe films on Cu(100), *Phys. Rev. B - Condens. Matter Mater. Phys.* 80 (2009) 1–11. <https://doi.org/10.1103/PhysRevB.80.235403>.
- [33] A. Biedermann, R. Tscheliessnig, M. Schmid, P. Varga, Local atomic structure of ultra-thin Fe films grown on Cu(100), *Appl. Phys. A Mater. Sci. Process.* 78 (2004) 807–816. <https://doi.org/10.1007/s00339-003-2435-7>.
- [34] C.J. Weststrate, E. Lundgren, J.N. Andersen, E.D.L. Rienks, A.C. Gluhoi, J.W. Bakker, I.M.N. Groot, B.E. Nieuwenhuys, CO adsorption on Au(3 1 0) and Au(3 2 1): 6-Fold coordinated gold atoms, *Surf. Sci.* 603 (2009) 2152–2157. <https://doi.org/10.1016/j.susc.2009.04.026>.
- [35] S.A. Isa, R.W. Joyner, M.W. Roberts, Adsorption of carbon monoxide on copper (100) studied by photoelectron spectroscopy and low energy electron diffraction, *J. Chem. Soc. Faraday Trans. 1 Phys. Chem. Condens. Phases.* 74 (1978) 546–554. <https://doi.org/10.1039/F19787400546>.
- [36] G. Wedler, K.G. Colb, W. Heinrich, G. McElhiney, The interaction of hydrogen and carbon monoxide on polycrystalline iron films, *Appl. Surf. Sci.* 2 (1978) 85–101. [https://doi.org/10.1016/0378-5963\(78\)90008-9](https://doi.org/10.1016/0378-5963(78)90008-9).
- [37] L. Gonzalez, R. Miranda, S. Ferrer, A thermal desorption study of the adsorption of CO on Fe(110); enhancement of dissociation by surface defects, *Surf. Sci.* 119 (1982) 61–70. [https://doi.org/10.1016/0039-6028\(82\)90187-X](https://doi.org/10.1016/0039-6028(82)90187-X).
- [38] G. Wedler, K.G. Colb, G. McElhiney, W. Heinrich, An investigation of the interaction of CO with polycrystalline iron films, *Appl. Surf. Sci.* 2 (1978) 30–42. [https://doi.org/10.1016/0378-5963\(78\)90004-1](https://doi.org/10.1016/0378-5963(78)90004-1).
- [39] K.Y. Yu, W.E. Spicer, I. Lindau, P. Pianetta, S.F. Lin, UPS studies of the bonding of H₂, O₂, CO, C₂H₄ and C₂H₂ on Fe and Cu, *Surf. Sci.* 57 (1976) 157–183. [https://doi.org/https://doi.org/10.1016/0039-6028\(76\)90175-8](https://doi.org/https://doi.org/10.1016/0039-6028(76)90175-8).
- [40] M. Barber, J.C. Vickerman, J. Wolstenholme, The application of SIMS to the study of CO adsorption on polycrystalline metal surfaces, *Surf. Sci.* 68 (1977) 130–137. [https://doi.org/10.1016/0039-6028\(77\)90197-2](https://doi.org/10.1016/0039-6028(77)90197-2).

- [41] G. Blyholder, M. Lawless, A theoretical study of the site of CO dissociation on Fe(100), *Surf. Sci.* 290 (1993) 155–162. [https://doi.org/10.1016/0039-6028\(93\)90597-D](https://doi.org/10.1016/0039-6028(93)90597-D).
- [42] M.H. Nassir, B. Frühberger, D.J. Dwyer, Coverage dependence of CO dissociation on clean and hydrogen presaturated Fe(100) surface, *Surf. Sci.* 312 (1994) 115–123. [https://doi.org/10.1016/0039-6028\(94\)90808-7](https://doi.org/10.1016/0039-6028(94)90808-7).
- [43] L.J. Whitman, L.J. Richter, B.A. Gurney, J.S. Villarrubia, W. Ho, CO adsorption site occupations on Fe(111) vs coverage and temperature: The kinetics of adsorption and reaction, *J. Chem. Phys.* 90 (1989) 2050–2062. <https://doi.org/10.1063/1.455996>.
- [44] M.L. Burke, R.J. Madix, Effect of CO on hydrogen thermal desorption from Fe(100), *Surf. Sci.* 237 (1990) 20–34. [https://doi.org/10.1016/0039-6028\(90\)90516-B](https://doi.org/10.1016/0039-6028(90)90516-B).
- [45] C.J. (Kee. J. Weststrate, D. Sharma, D. Garcia Rodriguez, M.A. Gleeson, H.O.A. Fredriksson, J.W. (Hans. Niemantsverdriet, Mechanistic insight into carbon-carbon bond formation on cobalt under simulated Fischer-Tropsch synthesis conditions, *Nat. Commun.* 11 (2020) 1–10. <https://doi.org/10.1038/s41467-020-14613-5>.
- [46] C.E. Bartosch, L.J. Whitman, W. Ho, The adsorption, interconversion, and dissociation of CO on Fe(111), *J. Chem. Phys.* 85 (1986) 1052–1060. <https://doi.org/10.1063/1.451298>.
- [47] J.Hulva, Z.Jakub, Z. Novotny, N. Johansson, J.Knudsen, J. Schnadt, M. Schmid, U. Diebold, G.S. Parkinson, Adsorption of CO on the Fe₃O₄(001) surface, *Electrochem. Commun.* 55 (2019) 1164–1176. <https://doi.org/10.1134/s0424857019100049>.
- [48] T. Tanabe, R. Buckmaster, T. Ishibashi, T. Wadayama, A. Hatta, Infrared reflection absorption spectroscopic study for CO adsorption on molecular beam epitaxially grown Fe films on Cu(1 1 1), *Surf. Sci.* 472 (2001) 1–8. [https://doi.org/10.1016/S0039-6028\(00\)00931-6](https://doi.org/10.1016/S0039-6028(00)00931-6).
- [49] T. Tanabe, Y. Suzuki, T. Wadayama, A. Hatta, Carbon monoxide adsorption on ultra-thin Fe film deposited on Cu(100), *Surf. Sci.* 427–428 (1999) 414–418. [https://doi.org/10.1016/S0039-6028\(99\)00313-1](https://doi.org/10.1016/S0039-6028(99)00313-1).
- [50] T.E. Meehan, J.D. Head, A theoretical comparison of CO bonding on the Fe(100) surface, *Surf. Sci.* 243 (1991) 55–62. [https://doi.org/10.1016/0039-6028\(91\)90334-O](https://doi.org/10.1016/0039-6028(91)90334-O).
- [51] D.L.S. Nieskens, M.M.M. Jansen, A.P. Van Bavel, D. Curulla-Ferré, J.W. Niemantsverdriet, The influence of carbon on the adsorption of CO on a Rh(100) single crystal, *Phys. Chem. Chem. Phys.* 8 (2006) 624–632. <https://doi.org/10.1039/b513233a>.
- [52] C. Egawa, E.M. McCash, Reactivity of hydrogen on ultra-thin FCC iron films, *J. Phys. Condens. Matter.* 1 (1989) 3–7. <https://doi.org/10.1088/0953-8984/1/SB/027>.
- [53] G. Wedler, K.-. Geuss, K.G. Colb, G. McElhiney, Heats of adsorption of hydrogen on polycrystalline iron films, *Appl. Surf. Sci.* 1 (1978) 471–478. [https://doi.org/10.1016/0378-5963\(78\)90025-9](https://doi.org/10.1016/0378-5963(78)90025-9).
- [54] A. Biedermann, R. Tscheliessnig, C. Klein, M. Schmid, P. Varga, Reconstruction of the clean and H covered 'magnetic live surface layer' of Fe films grown on Cu(1 0 0), *Surf. Sci.* 563 (2004) 110–126. <https://doi.org/10.1016/j.susc.2004.06.150>.

- [55] P.J. Estrup, J. Anderson, Chemisorption of hydrogen on tungsten (100), *J. Chem. Phys.* 45 (1966) 2254–2260. <https://doi.org/10.1063/1.1727919>.
- [56] H. Conrad, G. Ertl, E.E. Latta, Adsorption of hydrogen on palladium single crystal surfaces, *Surf. Sci.* 41 (1974) 435–446. [https://doi.org/10.1016/0039-6028\(74\)90060-0](https://doi.org/10.1016/0039-6028(74)90060-0).
- [57] C.J. Weststrate, D. Garcia Rodriguez, D. Sharma, J.W. Niemantsverdriet, Structure-dependent adsorption and desorption of hydrogen on FCC and HCP cobalt surfaces, *J. Catal.* 405 (2022) 303–312. <https://doi.org/https://doi.org/10.1016/j.jcat.2021.12.016>.
- [58] F. Bozso, G. Ertl, M. Grunze, M. Weiss, Chemisorption of hydrogen on iron surfaces, *Appl. Surf. Sci.* 1 (1977) 103–119. [https://doi.org/10.1016/0378-5963\(77\)90009-5](https://doi.org/10.1016/0378-5963(77)90009-5).
- [59] C. Brucker, T. Rhodin, Chemisorption and reaction of acetylene and ethylene on the α -Fe(100) clean iron surface, *J. Catal.* 47 (1977) 214–231. [https://doi.org/10.1016/0021-9517\(77\)90169-5](https://doi.org/10.1016/0021-9517(77)90169-5).

05

**IRON CARBIDE
FABRICATION ON
Cu(111)**

ABSTRACT: In this chapter, the fabrication of iron carbide films on Cu(111) via ethylene post-treatment of pre-deposited iron films of various thicknesses are explored. The thin film morphology and composition were characterized using a combination of AES, TPD, and LEED. The first part describes the iron film thickness regime below 2.6 ML, where the iron film prior to ethylene exposure consists of multilayer islands with an FCC-Fe structure. After dissociating ethylene on such islands, the shape of the C_{KLL} peak in AES corresponds to graphitic rather than carbidic carbon. Between 2.6 and 16 ML, Fe forms a mixed BCC-FCC film. AES after ethylene decomposition indicates that a pure carbide is formed after ethylene dissociation, while a complex LEED pattern suggests the formation of a mixture of structures, where the FCC-Fe parts appear to form a clock-reconstructed surface ($p4g(2 \times 2)$). This structure acts as a carbon trap, preventing further ethylene dissociation on the surface. The behaviour changes for films thicker than 16 ML: the LEED pattern shows that the BCC(110) surface is formed, but after dissociating ethylene on this surface, the presence of both on-surface and bulk carbide are identified from quantification of the carbon content and spectroscopically by means of AES.

5.1 Introduction

The previous chapters describe the fabrication, characterization and reactivity of the $p4g\text{-Fe}_2\text{C}$ surface iron carbide on iron grown on a Cu(100) substrate. The present chapter expands on this work by investigating how a change from the Cu(100) to the Cu(111) substrate affects the structure, composition and morphology of the iron carbide phase formed after ethylene post-treatment of the iron film.

The literature contains several studies of the structure of Fe films on Cu(111), where earlier work made use of low-energy electron diffraction [1–3] and Auger spectroscopy while Scanning Tunneling microscopy [4–8] was used in more recent studies. These studies show that iron on Cu(111) grows in small multilayer islands, unlike iron on Cu(100), where the initial bilayer island growth is followed by layer-by-layer growth. The Fe/Cu(111) film contains a mixture of relatively flat FCC-Fe islands and ridgelike BCC-Fe structures, which expose the (110) surface, where the BCC parts become increasingly dominant with increasing thickness. The in-plane nearest neighbour distance of 2.54 \AA for FCC Fe(111) is very close to the value of 2.55 \AA for the Cu(111) substrate, so little strain is expected. Due to the different shape of

the BCC-Fe(110) unit cell, only one of the lattice vectors aligns with the FCC(111) lattice of the substrate so that six differently oriented domains are formed in the so-called Kurdjumov-Sachs orientation [9–11].

Currently, studies that describe iron carbide formation on Cu(111) are unavailable in the literature. Li et al. [12] studied iron carbide formation on iron films grown on a Au(111) substrate. They report that “Fe films with a thickness less than two atomic layers showed no tendency to form Fe carbide in XPS studies irrespective of the C source used, while Fe films thicker than three atomic layers readily incorporated C, either via exposure to ethylene at 500 K or by using atomic carbon as carbon precursor at 300 K”. Carbon was found to populate both surface and subsurface sites, but XPS showed that other types of carbon were formed alongside the carbide. This is different from the findings on Cu(100) described in Chapter 3, where it was found that a pure surface carbide forms upon ethylene decomposition, even on thin films, while carbon diffusion into the subsurface region does not occur unless the initial film is thick and has adopted the BCC form. The present study of iron carbide formation on Cu(111) was undertaken to understand better the influence of the substrate on iron carbide formation: Cu(111) has a structure that is similar to Au(111) but lacks the herringbone reconstruction typical for Au(111). In addition, the lattice mismatch with FCC-Fe(111) is much smaller, and iron growth on both substrates is expected to be different.

This chapter starts by providing some experimental details, after which the coverage-dependent Fe film morphology before exposure to ethylene is discussed in detail. Afterwards, we demonstrate how the initial structure of the Fe film, which varies with film thickness, influences the composition and morphology of the carbide layer.

5.2 Experimental

Temperature-programmed desorption (TPD), low energy electron diffraction (LEED), and Auger electron spectroscopy (AES), with a primary energy of 2000 eV, were conducted in a UHV chamber with a base pressure below 2×10^{-10} mbar. The vacuum chamber has two quadrupole mass spectrometers, LEED/Auger optics, and a dual pocket e- beam evaporator. The QMS used for the TPD experiments was placed

inside a compartment with a 5 mm wide hole connecting it to the main chamber. Desorption experiments typically involve placing the sample 2 mm away from the aperture to eliminate signals generated by other areas of the sample holder. To prevent errors that may arise from directional desorption, the quantitative evaluation was cross-checked against the signal measured by a second QMS located in the main chamber [13].

For TPD and LEED/Auger experiments, a disc-shaped Cu(111) single crystal was mounted using a U-shaped 0.5 mm (diameter) tungsten (W) wire placed in the slits at the side of the sample. The W wire was in thermal contact with a liquid nitrogen reservoir to reach sample temperatures of ~90K. The temperature was measured using a K-type thermocouple fixed in a small hole in the side of the Cu sample. Heating was achieved by passing a direct current through the support wires. The temperature was measured using a type K (chromel- alumel) thermocouple fixed in a hole in the side of the sample. The Cu(111) substrate (8mm diameter) was cleaned by cycles of Ar⁺ ion bombardment (10 minutes, 1 keV and 300 K), followed by flash annealing to 1000K, and this resulted in a sharp (1x1) LEED pattern. Surface impurities, including carbon and oxygen, were below the AES detection limit.

The carbon content was quantified from the amount of H₂ desorption deriving from ethylene decomposition, where the hydrogen-saturated Cu(111) surface, with coverage equal to 0.7 ML H_{ad} [14], was used as a reference. The nominal thickness of the deposited iron was determined by AES following the approach of Tian et al. [3], who used equation 5.1:

$$R = R_{\infty} \frac{1 - e^{-\frac{d}{\lambda_{651 \text{ eV}}}}}{e^{-\frac{d}{\lambda_{920 \text{ eV}}}}} \quad \text{Eq. (5.1)}$$

The ratio $R = I_{\text{Fe}(651 \text{ eV})} / I_{\text{Cu}(920 \text{ eV})}$, that is, the peak-to-peak intensities of the Fe AES line at 651 eV and the Cu AES line at 920 eV, respectively, while $R_{\infty} = I_{\text{Fe}(651 \text{ eV})}^{\infty} / I_{\text{Cu}(920 \text{ eV})}^{\infty} = 0.84$ corresponds to the signal ratio of a very thick Fe film and a clean copper sample, respectively. The values of λ correspond to the inelastic mean free paths in iron. Following ref. [15] these values were taken as $\lambda_{651 \text{ eV}} = 13.8 \text{ \AA}$ and $\lambda_{920 \text{ eV}} = 16.4 \text{ \AA}$. The thickness of the film, d , was derived iteratively from this

equation. It should be noted that this approach assumes a film of *uniform* thickness over the Cu(111) substrate, but since iron forms 3D island structures, this nominal thickness is expected to deviate somewhat from the absolute quantity of iron deposited [7,8,16,17]]. The iron surface structure also changes with thickness, similarly as in the case of Fe/Cu(100) [18]. These changes in surface structure give different diffraction patterns, which are well-documented in the literature and were used to verify the thickness of the evaporated iron film [3,8].

The diffusion barrier of iron into Cu(111) is even lower than on Cu(100) [8], which makes the experiments sensitive to the loss of iron to the bulk of the copper substrate during heating. To minimise this effect, the temperature used for the experiments discussed here was kept below 500 K. For some experiments, an annealing step to 600 K was required to improve the crystallinity of the structure and thus obtain a better quality LEED pattern.

5.3 Iron thin film structure and morphology

The present section describes the thickness-dependent iron morphology on a Cu(111) substrate after evaporation at room temperature up to a nominal thickness of ~16 ML before ethylene decomposition using a combination of LEED, AES and TPD. Figure 5.1. (a) shows the LEED pattern typical of the thickness regime between ~1 ML and ~2.6 ML. The threefold symmetric $p(1 \times 1)$ pattern with respect to the clean copper substrate indicates pseudomorphic growth, meaning that the iron atoms follow the structure of the FCC-Cu(111) substrate.

For films between ~2.6 and ~16 ML (Fig.5.1 (b)), five satellite spots are seen around each substrate spot, with three in the inner circle and two in the outer circle. They arise because of the formation of BCC-Fe, which forms six different domains on the hexagonal Cu(111) substrate, often referred to as Kurdjumov-Sachs orientations (KS) [4,10,19,20]. These correspond to the alignment of FCC(111) dense-packed $\langle -110 \rangle$ rows of atoms with the BCC(110) troughs along the $\langle -111 \rangle$ ($\langle 001 \rangle$) directions [10], as schematically depicted for four different domains in Figure 5.1. These orientations are also found in Fe on Ni(111) [21], Mn on Pd(111) [22], and Fe on Ru(0001) [23]. The angular separation of 8° calculated in the LEED pattern in

Figure 5.1 (b) is related to the differences in lattice between BCC α -Fe(110) and FCC Cu(111) and agrees well with the literature [8]. The reader is referred to the studies by van der Merwe [20,24,25] for a detailed discussion on the structures of metallic overlayers.

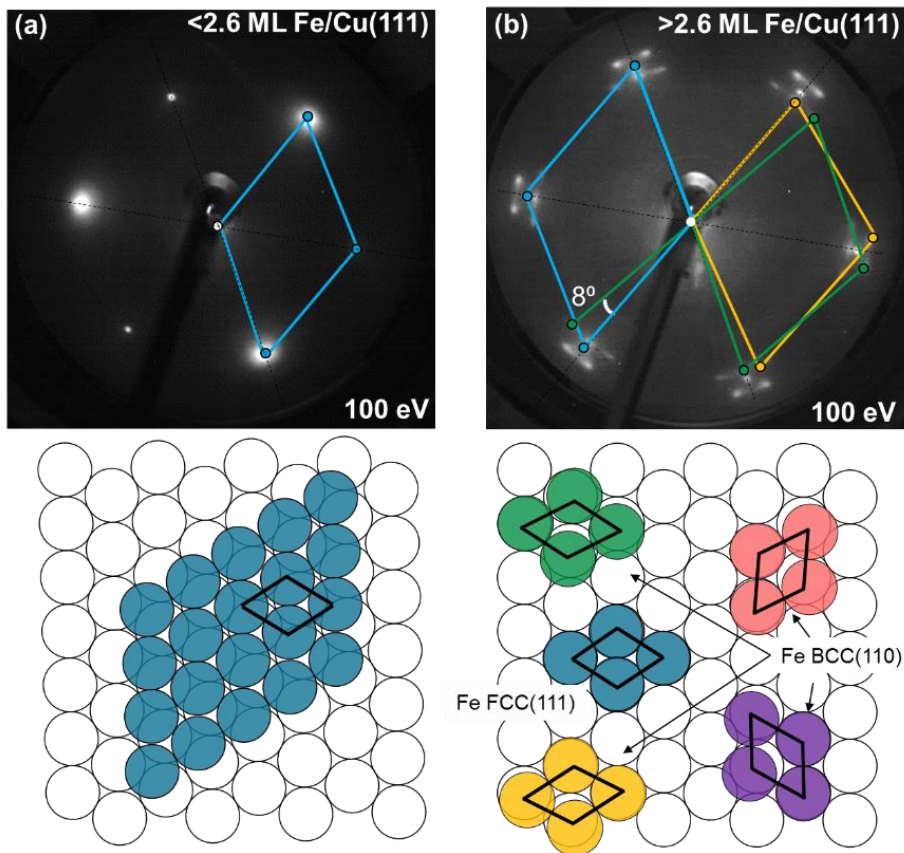


Figure 5.1 (a) LEED pattern of 1 ML Fe/Cu(111) film showing a $p(1 \times 1)$ pattern indicative of FCC-Fe(111). (b) For iron film thicknesses of 3 ML and higher, satellite spots start to appear around the substrate spots. These satellite spots are caused by BCC(110) domains with Kurdjumov-Sachs orientations (KS), two of which are explicitly shown (yellow and green unit cells). The corresponding atomic models are shown in the lower half, where only four out of the six possible orientations of BCC Fe(110) have been drawn for simplicity. Also, the Fe FCC(111) phase, represented in blue, appears in the thickness range between ~ 2.6 and ~ 16 ML together with Fe BCC(110). The LEED patterns were recorded at 100 K.

The diffraction spots of FCC-Fe(111) overlap with those of the Cu(111) substrate, so LEED alone cannot determine whether FCC-Fe(111) is still present alongside BCC-Fe. STM studies reported by other authors [16,17] indicate that both phases coexist on the surface between 2.6 ML and 16 ML. For example, the ~2.6 ML Fe image in Figure 5.2 contains relatively large, flat islands attributed to patches with an FCC structure. The ridgelike structures (white arrows in the STM image) are attributed to the onset of BCC(110) domain formation, which, in LEED, gives rise to additional spots with a KS orientation [6].

CO desorption from Cu(111) occurs below 200 K and can be distinguished from CO that is adsorbed on the Fe-covered part, which desorbs between 300-450 K [26–29]. This was used to deduce the wetting of the copper surface as a function of nominal iron film thickness. The main panel in Figure 5.2. shows the available copper surface area as a function of the quantity of iron deposited, as derived from the CO desorption spectra provided in the inset. The data shows that the available copper surface area in Fe/Cu(111) decreases much slower with iron thickness than in Cu(100). For example, the deposition of ~2.8 ML of iron leads to ~60% suppression of the Cu(111)-related CO desorption peaks, while the same amount of Fe practically covers the surface of Cu(100). This suggests that Fe grows in the form of multilayer islands on Cu(111), a conclusion that agrees with STM images of Fe on Cu(111) [adapted from ref. [17], plotted in the inset of Figure 5.2], which shows multilayer islands of approximately 5 ML in height after depositing ~2.6 ML Fe. The CO desorption peaks from the iron-covered parts show that the peak maximum shifts towards lower temperatures with Fe thickness. At ~9 ML, the iron film completely covers the substrate, implying that CO desorption from the copper substrate no longer occurs at these iron coverages.

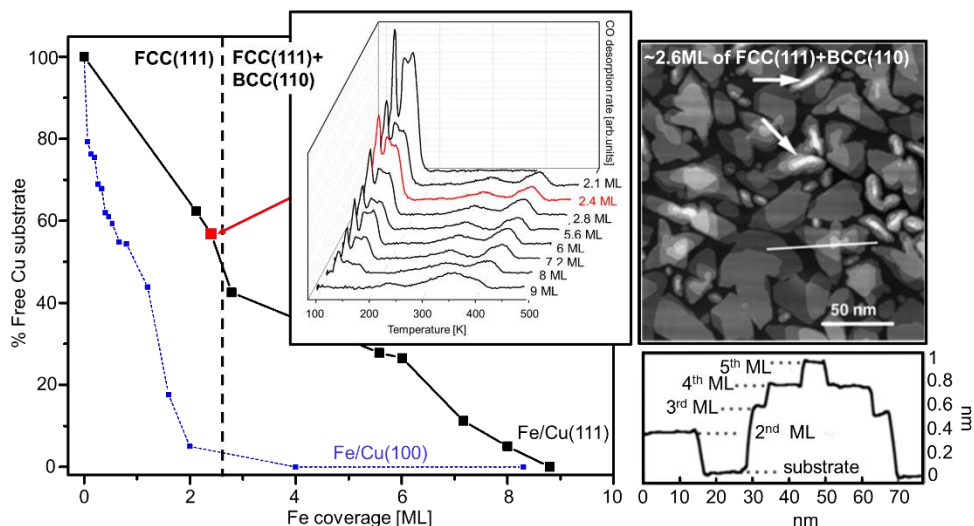


Figure 5.2. Two CO titration experiments from iron on Cu(100) and Cu(111). In the inset, the CO TPD series from different iron thicknesses. STM image of a 2.6 ML iron on Cu(111) film. The marked line profile is shown below the STM image, which indicates that there are five layers exposed on the surface before iron completely covers the substrate. Ridgelike structures are known to be BCC(110) domains indicated by white arrows. STM image adapted from [17].

5.4 Ethylene dissociation for Fe coverages below 2.6 ML

Our experiments, combined with insights from the literature, indicate that iron films with thicknesses below ~ 2.6 ML form multilayer islands. In the LEED pattern of figure 5.3, no extra spots apart from the (1×1) of the substrate are seen, indicating that the predominant phase at this stage is Fe FCC(111). Figure 5.3 shows that a large amount of H_2 ($m/z=2$) desorbs in a TPD experiment after dosing 3 L of ethylene at 100 K onto a ~ 2.6 ML Fe film. A second ethylene adsorption step at 100 K followed by heating showed only a small quantity of additional H_2 produced. Since additional ethylene exposure steps do not produce significant hydrogen desorption, it is clear that a single ethylene decomposition cycle already saturates the surface with carbon. The carbon quantity was indirectly determined by using a reference experiment where H_2 was dosed onto Cu(111) in the presence of a hot filament, such that part

of the H_2 dissociates, and atomic H adsorbs directly on the surface. The (3×3) LEED pattern afterwards corresponds to 0.7 ML H_{ad} [14], and from this quantitative reference, the maximum carbon content on ~ 2.6 ML Fe after ethylene decomposition was determined as ~ 0.2 ML. The CO titration experiment for 2.6 ML Fe showed that only 40% of the surface is covered by iron. Assuming ethylene decomposition only occurs on Fe, the local carbon surface coverage on the iron island surface is 0.5 ML, the same coverage found on Cu(100) for saturated pure carbide. More information about the chemical identity of carbon was obtained by Auger electron spectroscopy. The shape of the C_{KLL} spectrum after two ethylene cycles (shown in the inset of Figure 5.3) differs from that of a pure carbide reference. It contains features similar to the spectrum of graphitic carbon - for which a reference spectrum is included - and thus shows that a mixture of these different forms of carbon is present instead of a pure carbide, in contrast to the Fe/Cu(100) case. The LEED image after two ethylene cycles shows no differences with the $p(1 \times 1)$ of the clean iron surface.

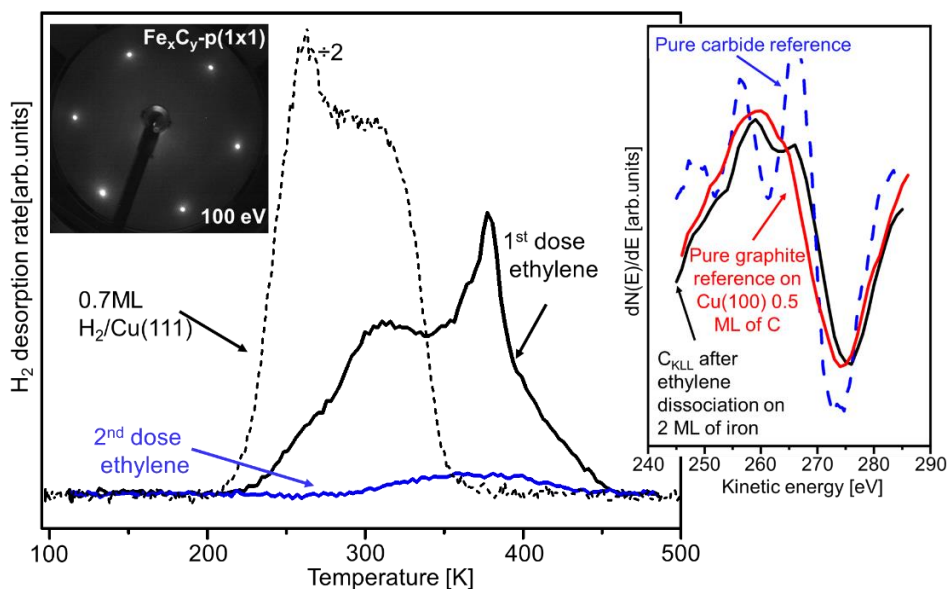


Figure 5.3 H_2 desorption spectrum from the first and second dose of ethylene (2K/s) on 2 ML of iron. The desorption of 0.7 ML H_{ad} from the clean Cu(111) substrate was used to quantify the carbon content. Note that its intensity has been divided by 2 to match the scale of the other spectrum. The $p(1 \times 1)$ LEED and C_{KLL} Auger spectra were taken after two ethylene decomposition cycles at 100K/100eV and 300K, respectively.

5.5 Ethylene dissociation on iron for film thicknesses between 2.6 ML and 16 ML. Carburization on BCC Fe(110) + FCC(111) mixtures.

5.5 Ethylene dissociation on iron for film thicknesses between 2.6 ML and 16 ML. Carburization on BCC Fe(110) + FCC(111) mixtures.

The carburization of the BCC-rich iron film that forms above 2.6 ML of Fe on Cu(111) is markedly different from that of the thinner films. Figure 5.4 shows the hydrogen ($m/z=2$) desorption spectrum after dosing ethylene to saturation (~ 3 L) at 100 K on 3 ML of Fe (which covers 60% of the surface). Three doses are enough to saturate the surface. For a ~ 3 ML iron film, the maximum amount of carbon that can be reached is $\sim 0.3(\pm 0.05)$ ML, where the error margin stems from the uncertainty about the amount of hydrogen adsorbed during Fe evaporation prior to ethylene dosing. In contrast to the thinner films, the C_{KLL} Auger spectrum shows the three characteristic carbide features confirming that a relatively pure carbide is formed.

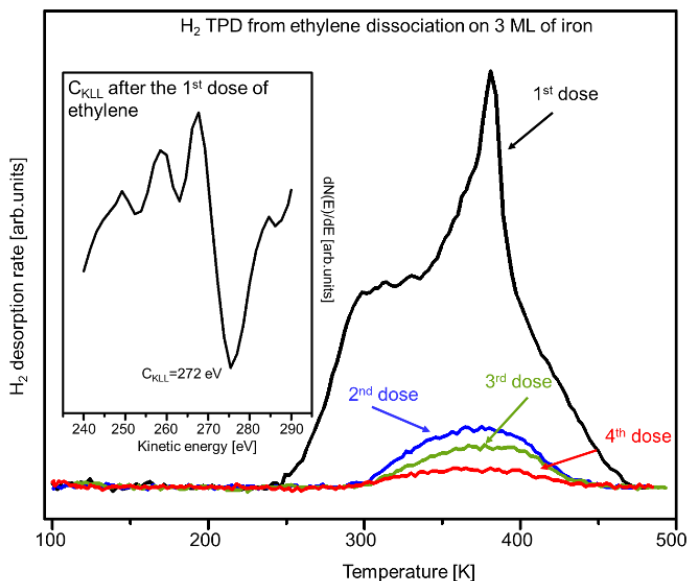


Figure 5.4. H_2 desorption from ethylene dissociation from a 3 ML Fe film on Cu(111). In the inset, the C_{KLL} Auger spectra after the fourth dose of ethylene show the three carbide transitions. The Auger spectrum was taken at 300 K.

The LEED patterns recorded before and after ethylene dissociation on a 3 ML Fe film are provided in Figures 5.5 (a) and (b), respectively. The pattern before ethylene

5.5 Ethylene dissociation on iron for film thicknesses between 2.6 ML and 16 ML. Carburation on BCC Fe(110) + FCC(111) mixtures.

treatment shows the weak KS spots related to the BCC(110) phase alongside the more intense (1x1) spots due to FCC-Fe and the substrate. In the pattern recorded after ethylene decomposition, shown in Figure 5.5 (b), the BCC(110)-related spots have become very weak, while very faint spots in between the (1x1) substrate spots suggest that a disordered structure is formed. A flash anneal to 600 K increases the order of the surface structure and shows a complex pattern. The same pattern was also found on thicker films up to a thickness of 16 ML after ethylene treatment and annealing. The three carbide transitions in the C_{KLL} Auger spectrum provided in the inset of Figure 5.5 confirm that a pure carbide structure is present after annealing. The pattern is tentatively attributed to a complex mixture of carbide-terminated FCC-Fe and BCC-Fe phases, where a p4g(2x2) clock reconstruction forms on top of the FCC-(111) parts, in a similar manner as earlier reported for carbon on Co(0001) [30] and Ni(111) [31,32]. A more detailed discussion of the possible structure responsible for this complex pattern will be provided later.

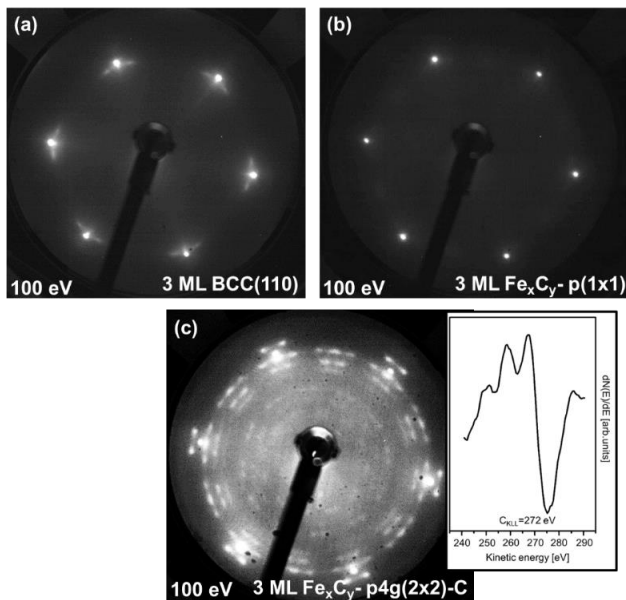


Figure 5.5 (a) LEED taken after evaporating ~ 3 ML of iron. (b) LEED taken at 100 K after four cycles of ethylene decomposition (c) Sharp LEED pattern found after annealing to 600 K. The inset shows the C_{KLL} spectrum, which indicates that carbidic carbon is present (three transitions in the C_{KLL} spectrum) after annealing to 600 K. LEED were recorded at 100 K

Iron thickness vs. carbon content

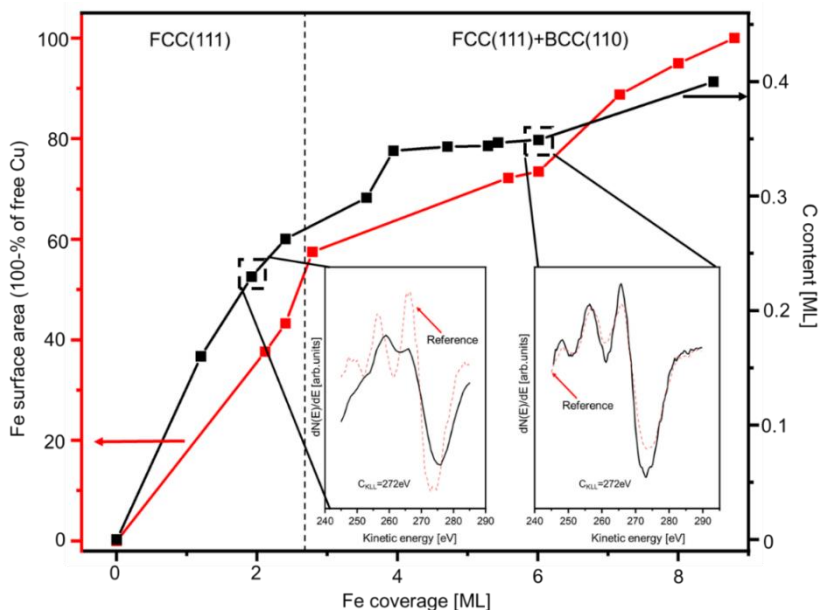


Figure 5.6. The black curve shows the maximum amount of carbon that can be added to different Fe coverages. The curve flattens at approximately 4 ML, and the maximum amount of deposited carbon is 0.35 ML. The red line shows the total iron surface area derived from CO-titration. Each inset shows two C_{KLL} spectra, where the dotted red spectrum is a pure carbide reference from Fe_2C on $Cu(100)$.

Figure 5.6 shows the H_2 -TPD-based quantification of the amount of carbon deposited (black line) as a function of the exposed iron surface area derived from the CO titration experiment in Figure 5.2. In all cases, multiple ethylene dissociation cycles were applied for each sample to ensure that the value derived corresponds to the carbon-saturated state. One sees that the carbon content increases in approximately the same way as the exposed amount of surface Fe and reaches a value of 0.4 ML of carbon when the substrate is completely covered ($\rightarrow 7$ ML). This indicates that carbon does not diffuse into the bulk but stays on the surface. In all cases, the same complex LEED pattern was found after annealing. On $Cu(100)$, the stable clock reconstruction was found to act as a carbon trap that prevents carbon from diffusing into the bulk and thereby limits the carbon uptake of the sample. The

complex structure found on Cu(111) likely has the same role: it is highly stable and traps the carbon in the surface region. With carbon trapped there, the formation of the bulk carbide is not possible.

5.6 Ethylene dissociation on a thick iron film on Cu(111), with ~16 ML of iron

In this coverage regime, around 16 ML, a pure BCC(110) film forms through which the C_{LMM} signal is no longer visible. The Fe coverage was estimated by extrapolation based on the evaporation time, using the same filament power as for the thinner films. The TPD desorption series for ethylene dissociation in Figure 5.7 shows that the first ethylene decomposition cycle deposits ~0.4 ML of carbon on the surface. Subsequent ethylene decomposition cycles continue to produce significant H_2 desorption in contrast to the case for the thin films, which saturate after a few ethylene cycles. In the experiment, up to eight ethylene cycles were applied, but for clarity, only four of the desorption spectra are provided in Figure 5.7. The fourth, fifth and sixth doses show the same amount of desorbed H_2 , suggesting that ethylene can always dissociate on the surface, similar to what happened on thick films of Fe on Cu(100). The constant hydrogen desorption after ethylene dissociation confirms that the surface cannot be saturated with carbon, implying carbon diffusion into the bulk, which only happens in our experiments for pure BCC iron. A comparison of the C_{KLL} shape for 16 ML $Fe_xC_y/Cu(111)$ and 16ML $Fe_xC_y/Cu(100)$ in Figure 5.7 (b) shows the three transitions typical of a pure carbide. The subtly different shape of the peaks compared to the surface carbide reference indicates that a large amount of carbon deposited occupies a combination of surface and bulk sites, as discussed in Chapter 3.

5.6 Ethylene dissociation on a thick iron film on Cu(111), with ~16 ML of iron

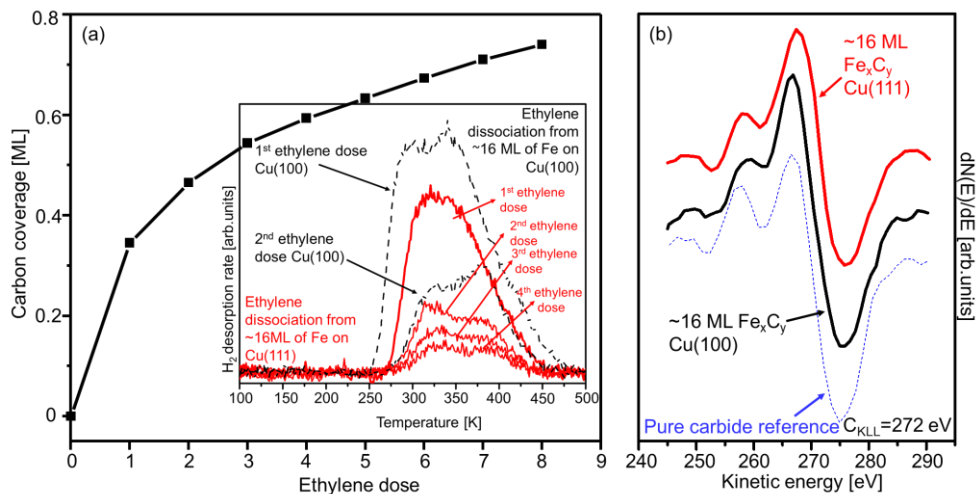


Figure 5.7. **(a)** Uptake curve of the carbon coverage against ethylene dose on a 16 ML iron film on Cu(111), derived from the H_2 TPD from the inset. **(b)** The Auger spectra of a Fe_xC_y surface after four ethylene cycles, compared to Fe_xC_y with a 16 ML nominal thickness on Cu(100) for comparison.

Figure 5.8 shows the diffraction patterns before and after two ethylene dissociation cycles. The pattern of the pristine iron film right after evaporation corresponds to the different domains of BCC(110), which become somewhat weaker after ethylene treatment. The pattern sharpens after a short annealing step at 600 K [shown in (c)], and very vague spots are seen at the (2x2) positions after enhancing the image contrast. On BCC Fe(110) on Au(111), a (2x2) structure was found by STM after carbon. We, therefore, tentatively suggest that the faint extra spots at the (2x2) positions seen in the present LEED study are due to the same Fe BCC(110)/Au(111) structure [33].

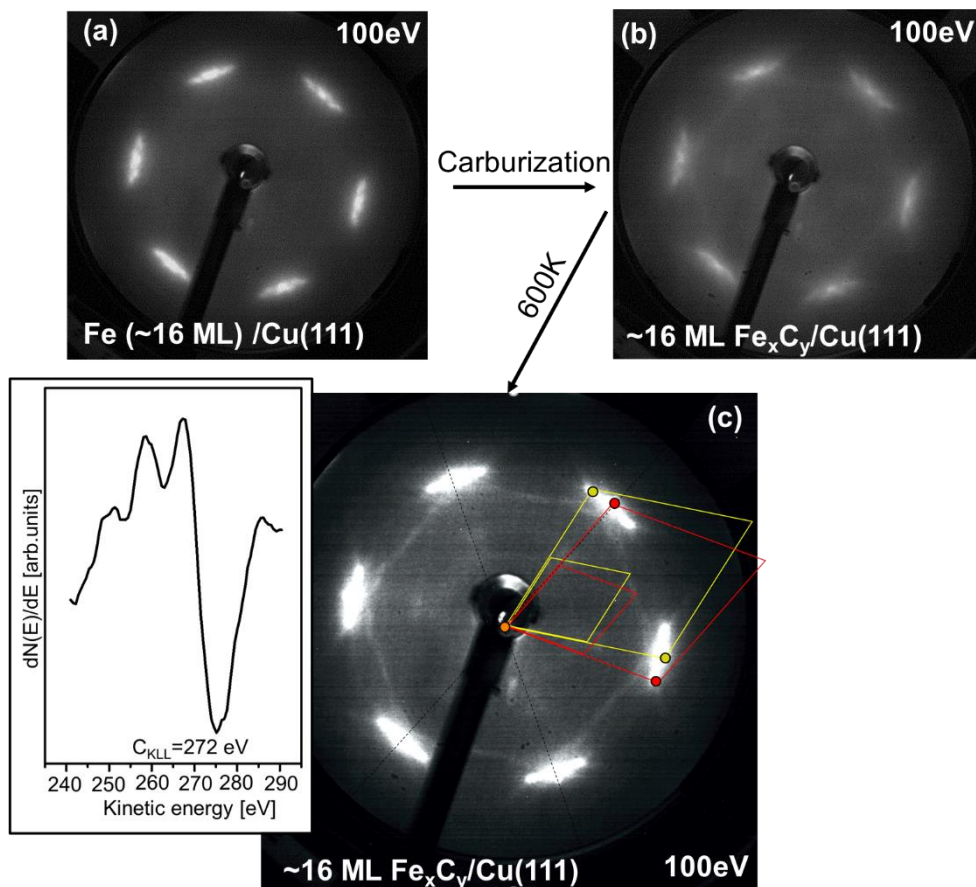


Figure 5.8 The evolution of the diffraction patterns from a thick iron film before (a) and after ethylene dissociation (b). The blurriness in pattern (b) suggests that the iron carbide film is disordered, and after annealing (c), the spots become sharper and reveal what appears to be a (2x2) unit cell. In the inset: The AES spectrum after annealing the surface, where the three carbide transitions and the shape resemble bulk carbide. LEED images were taken at 113 eV and 100 K.

Thick Fe films with a pure BCC bulk structure thus react in a fundamentally different manner compared to the FCC-Fe and mixed FCC-BCC films formed for thin iron layers, which tend to form stable surface carbide that traps carbon at the surface and prevents carbon diffusion to the bulk. For thick iron films, the absence of such a 'carbon trap' causes the carbon to diffuse into the bulk so that a much higher carbon

content can be reached and bulk carbide formation occurs. We note that this is similar to the behaviour found on Cu(100) and described in Chapter 3, where bulk carbide formation was only found for thick Fe films.

5.7 General discussion

The fabrication and structures of iron carbide on Cu(111) were studied using AES, LEED, and temperature-programmed desorption. Three different coverage regimes can be distinguished for the carburization process. For thicknesses below 2.6 ML, only the FCC(111) iron phase is present in the form of multilayer islands that cover part of the substrate. The total carbon that can be adsorbed is 0.25 ML, and AES indicates the presence of graphitic carbon instead of the carbide, as it was seen for Cu(100) for similar coverages. For coverages above 2.6 ML, BCC Fe(110) starts to form alongside FCC Fe(111). After dissociating ethylene on top of this surface, AES shows only carbidic carbon. A sharp LEED pattern is only seen after heating to 600 K and is tentatively interpreted as a mixture of different phases: the FCC-Fe part appears to form the 'clock' reconstruction, while on the BCC-Fe parts, a different structure appears to be formed. The structures formed act as a carbon trap, preventing carbon from diffusing into the sub-surface and bulk. Only BCC-Fe is present for coverages higher than ~16 ML in multiple domains. Repeated ethylene decomposition cycles continue to deposit carbon on the sample, which indicates that carbon can diffuse into the bulk.

The C_{KLL} peaks show that ethylene decomposes to carbidic carbon except for the thinnest films, where a significant amount of graphitic carbon was found instead. This coincides with the regime where LEED shows only FCC(111) spots, and we attribute the different nature of the carbon found to this difference. Single crystal studies on Ni(111) and Co(0001) show that ethylene decomposes initially to acetylene [30,34]. The acetylene intermediates can decompose via C-C bond scission to atomic carbon but may instead also polymerize into graphitic-type structures, as found by Weststrate et al. [30] on Co(0001). We propose that both mechanisms are active on the thin FCC-Fe(111) film so that a mixture of atomic and graphitic carbon is formed afterwards. Thicker films expose BCC-Fe(110), and while single crystal studies on

this surface show that ethylene also decomposes to acetylene, the decomposition of the C_2H_2 intermediate to CH_x was instead found to be dominant [35]. The lower tendency for graphene formation may be related to the poor match of the BCC-(110) lattice with graphene, unlike FCC-Fe(111), the lattice of which fits very well with that of graphene. In Chapter 3, the decomposition of ethylene was found to proceed via vinyl (CH_2-CH-) or vinylidene (CH_2-C-), followed by acetylide ($CCH-$), and finally carbide, not via acetylene. Here, the absence of acetylene intermediates rationalizes why no graphene was found.

The LEED pattern found after annealing the carburized iron layers, between 3-16 ML, shows many spots belonging to multiple domains and possibly different iron phases, making the interpretation complex. Figure 5.9 shows the LEED pattern after ethylene dissociation on a 3 ML iron film, where different markers are used to indicate the various families of spots attributed to a specific structure along with the corresponding unit cells.

The pristine iron film consists of a mixture of BCC and FCC-Fe, and in analogy to Ni(111) and Co(0001) [30,34], it is possible that a clock-reconstructed $p4g(2 \times 2)$ surface carbide forms on top of the hexagonal FCC-Fe(111) lattice. This overlayer has a square-shaped unit cell that can exist in six orientations relative to the (111) pattern. The resulting spots, marked with a circle, are located on rings (f,d) and (c,b) and account for the most prominent spots in the observed pattern. Focusing on the spots that surround the substrate spots, it can be seen that the weak spots in ring (a) cannot be accounted for by the clock reconstruction. Instead, we attribute the spots in ring (a) to the different domains of BCC-Fe(110), a structure that also gives rise to spots in ring (b) that overlap with those of the clock-reconstruction. In addition to these, weak spots are seen on a ring labelled as (e) and also on a ring labelled as (X). While some of these spots may be associated with a (2×2) structure on the BCC-(110) surface, their exact origin remains unclear. We, therefore, emphasize that the interpretation of the LEED pattern is tentative, and further structural characterization is needed to unravel the details of the structure formed. Atomic-resolved STM has proven to be a good technique for determining different phases on surfaces, as Biedermann et al. [36] did to confirm that FCC Fe(111) and BCC Fe(110) can coexist.

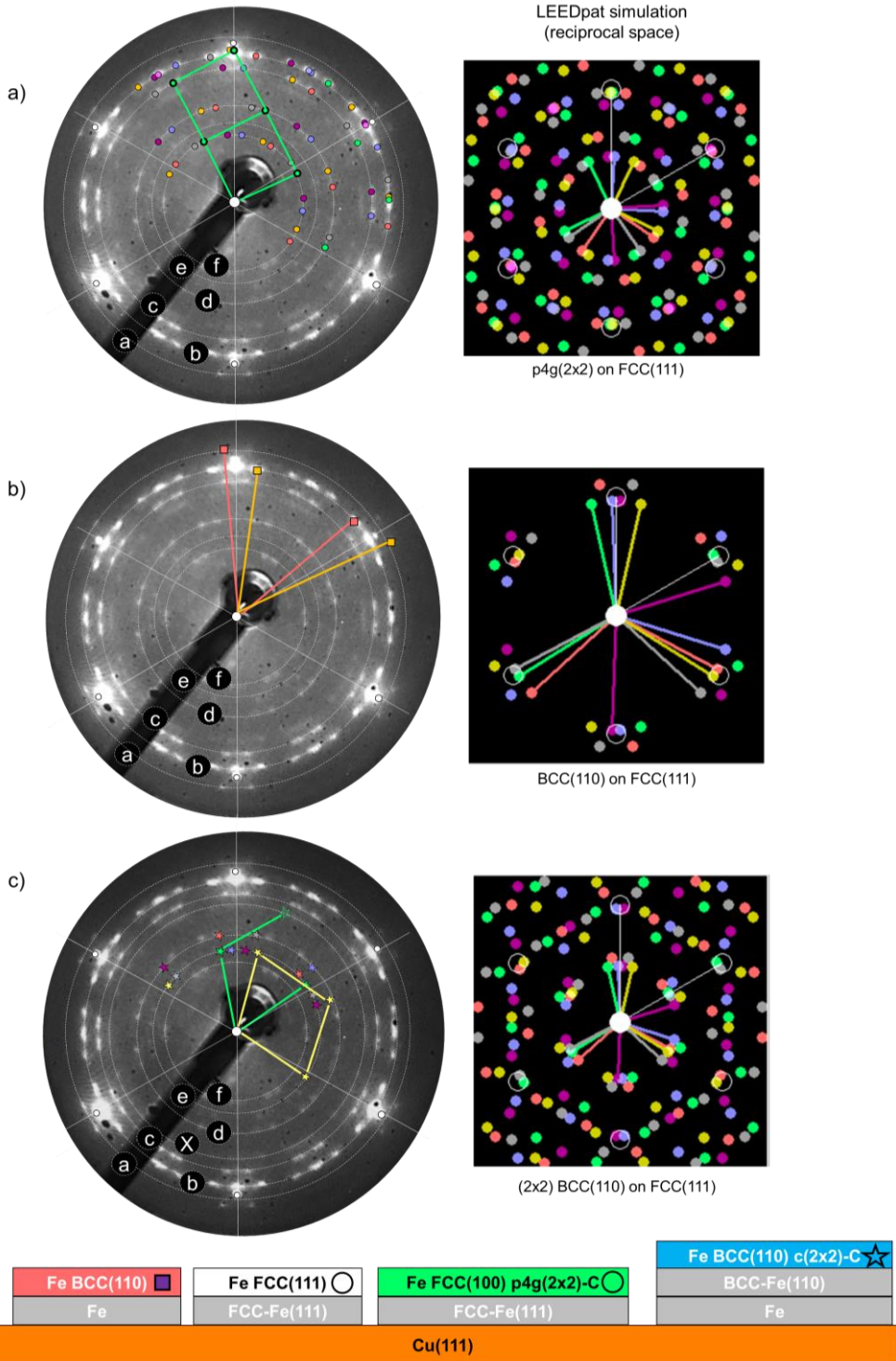


Figure 5.9. The same LEED pattern is shown, for simplicity, three times after evaporating 3 ML of iron at 300 K on a Cu(111) surface, followed by carburization using ethylene as a carbon precursor and annealing to 600 K. Different phases can be distinguished from the pattern and are represented by different symbols. In (a), the square-shaped unit cell from the $p4g(2 \times 2)$ on top of the Fe FCC(111). (b) The non-carburized Fe BCC(110) (Kurdjumov-Sachs). (c) Possible (2×2) unit cell on the Fe BCC(110) on top of the Fe FCC(111). The white dotted circles were painted as a guide to assign the different spots. Not all the unit cells were drawn, nor all the spots were assigned for clarity. Next to the LEED patterns, a simulation was generated using LEEDpat42 software for each one of the scenarios. LEED pattern was taken at 100 eV and 100 K

In conclusion, the iron carbide fabrication process on the Cu(111) substrate produces a heterogeneous structure for thicknesses <16 ML and the mixture of phases formed after carbon deposition makes this substrate less ideal for fabricating well-defined iron carbide model samples. The techniques used here, AES and LEED, were – although informative – inconclusive. Further experiments using SR-XPS and STM are suggested to study the chemical nature of the carbon layer formed on FCC-Fe(111) and to obtain more information on the ordered structure formed after annealing on Cu(111).

5.8 References

- [1] U. Gradmann, P. Tillmanns, Supersaturation and mode of growth for Fe films on Cu(111). An experimental study using LEED and AES, Phys. Status Solidi. 44 (1977) 539–547. <https://doi.org/10.1002/pssa.2210440217>.
- [2] H. Pontkees, F., Neddermeyer, Electronic and structural properties of thin films of Fe on Cu(111) and of the system Cu/Fe/Cu(111), Phys. B Phys. Condens. Matter. 161 (1989) 276–280. [https://doi.org/https://doi.org/10.1016/0921-4526\(89\)90148-8](https://doi.org/https://doi.org/10.1016/0921-4526(89)90148-8).
- [3] D. Tian, F. Jona, Structure of ultrathin films of Fe on Cu{111} and Cu{110}, Phys.Rev.B. 45 (1992) 11216–11221. <https://doi.org/10.1103/physrevb.45.11216>.
- [4] M. Klaua, J. Shen, P. Ohresser, H. Jenniches, J. Barthel, C. V. Mohan, J. Kirsckner, Changes of morphology, structure, and magnetism of Fe on stepped Cu(111), IEEE Trans. Magn. 34 (1998) 1216–1218. <https://doi.org/10.1109/20.706500>.
- [5] M.T. Kief, W.F. Egelhoff, Face-centered-cubic (111) to body-centered-cubic (110) transition in epitaxial Fe on Cu(111), J. Vac. Sci. Technol. A. 11 (1993) 1661–1666. <https://doi.org/10.1116/1.578475>.

- [6] J. Shen, M. Klaua, P. Ohresser, H. Jenniches, J. Barthel, C. V. Mohan, J. Kirschner, Structural and magnetic phase transitions of Fe on stepped Cu(111), *Phys. Rev. B - Condens. Matter Mater. Phys.* 56 (1997) 11134–11143. <https://doi.org/10.1103/PhysRevB.56.11134>.
- [7] A. Brodde, H. Neddermeyer, Nucleation and growth of Fe on Cu(111) in the monolayer range, *Ultramicroscopy.* 42–44 (1992) 556–561. [https://doi.org/10.1016/0304-3991\(92\)90323-C](https://doi.org/10.1016/0304-3991(92)90323-C).
- [8] M.T. Kief, W.F. Egelhoff, Growth and structure of Fe and Co thin films on Cu(111), Cu(100), and Cu(110): A comprehensive study of metastable film growth, *Phys.Rev.B.* 47 (1993) 10785–10814. <https://doi.org/10.1103/PhysRevB.47.10785>.
- [9] K. Rahman, A., Schuller, Epitaxy and superlattice growth, *Phys.Rev.B.* 30 (1984) 6208–6210. <https://doi.org/https://doi.org/10.1103/PhysRevB.30.6208>.
- [10] E. Bauer, J.H. van der Merwe, Structure and growth of crystalline superlattices: From monolayer to superlattice, *Phys. Rev. B.* 33 (1986) 3657–3672. <https://doi.org/https://doi.org/10.1103/PhysRevB.33.3657>.
- [11] G. Kurdjumow, G. Sachs, Der Mechanismus der Stahlhärtung, *Naturwissenschaften.* 18 (1930) 534. <https://doi.org/10.1007/BF01513427>.
- [12] Y. Li, Z. Li, A. Ahsen, L. Lammich, G.J.A. Mannie, J.W. Niemantsverdriet, J. V. Lauritsen, Atomically Defined Iron Carbide Surface for Fischer-Tropsch Synthesis Catalysis, *ACS Catal.* 9 (2019) 1264–1273. <https://doi.org/10.1021/acscatal.8b03684>.
- [13] J. Harris, On the adsorption and desorption of H₂ at metal surfaces, *Appl. Phys. A Solids Surfaces.* 47 (1988) 63–71. <https://doi.org/10.1007/BF00619699>.
- [14] E.M. Mccash, S.F. Parker, J. Pritchard, M.A. Chesters, The adsorption of atomic hydrogen on Cu(111) investigated by reflection-absorption infrared spectroscopy, electron energy loss spectroscopy and low energy electron diffraction, *Surf. Sci.* 215 (1989) 363–377. [https://doi.org/10.1016/0039-6028\(89\)90266-5](https://doi.org/10.1016/0039-6028(89)90266-5).
- [15] M.P. Seah, W.A. Dench, Quantitative Electron Spectroscopy of Surfaces : A Standard Data Base for Electron Inelastic Mean Free Paths in Solids, *Surf. Interface Anal.* 1 (1979) 2–11. <https://doi.org/https://doi.org/10.1002/sia.740010103>.
- [16] Y.K. Kim, J.Y. Maeng, S.Y. Lee, S. Kim, Growth properties of ultrathin Fe overlayers grown on a highly stepped Cu(111) surface, *Appl. Surf. Sci.* 174 (2001) 316–323. [https://doi.org/10.1016/S0169-4332\(01\)00194-5](https://doi.org/10.1016/S0169-4332(01)00194-5).
- [17] P. Ohresser, J. Shen, J. Barthel, M. Zheng, C. V. Mohan, M. Klaua, J. Kirschner, Growth, structure, and magnetism of fcc Fe ultrathin films on Cu(111) by pulsed laser deposition, *Phys. Rev. B - Condens. Matter Mater. Phys.* 59 (1999) 3696–3706. <https://doi.org/10.1103/PhysRevB.59.3696>.
- [18] D.Garcia Rodríguez, M.A. Gleeson, J. V. Lauritsen, Z. Li, X. Yu, J.W. Hans Niemantsverdriet, C.J. Kees-Jan Weststrate, Iron carbide formation on thin iron films grown on Cu(100): FCC iron stabilized by a stable surface carbide, *Appl. Surf. Sci.* 585 (2022) 152684. <https://doi.org/10.1016/j.apsusc.2022.152684>.

- [19] L. Sandoval, H.M. Urbassek, P. Entel, The Bain versus Nishiyama-Wassermann path in the martensitic transformation of Fe, *New J. Phys.* 11 (2009). <https://doi.org/10.1088/1367-2630/11/10/103027>.
- [20] J.H. van der Merwe, Analytical selection of ideal epitaxial configurations and some speculations on the occurrence of epitaxy III. Epitaxy of thin (111) f.c.c. films on (110) b.c.c. substrates by coherence, *Philos.Mag.Lett.* 45 (1982) 159–170. <https://doi.org/10.1080/01418618208243909>.
- [21] B. An, L. Zhang, S. Fukuyama, K. Yokogawa, Growth and structural transition of Fe ultrathin films on Ni(111) investigated by LEED and STM, *Phys. Rev. B - Condens. Matter Mater. Phys.* 79 (2009) 1–7. <https://doi.org/10.1103/PhysRevB.79.085406>.
- [22] D. Tian, H. Li, S.C. Wu, F. Jona, P.M. Marcus, Atomic and electronic structure of thin films of Mn on Pd{111}, *Phys. Rev. B.* 45 (1992) 3749–3754. <https://doi.org/10.1103/PhysRevB.45.3749>.
- [23] J. Korecki, M. Przybylski, J. Prokop, K. Krop, P. Auric, CEMS studies of ultrathin Fe films grown on Ru, *J. Magn. Mater.* 140–144 (1995) 673–674. [https://doi.org/10.1016/0304-8853\(94\)00824-8](https://doi.org/10.1016/0304-8853(94)00824-8).
- [24] J.H. van der Merwe, Analytical selection of ideal epitaxial configurations and some speculations on the occurrence of epitaxy II. Epitaxy of (111) f.c.c. overlayers on (110) b.c.c. substrates, *Philos.Mag.Lett.* 45 (1982) 145–157. <https://doi.org/10.1080/01418618208243908>.
- [25] J.H. van der Merwe, Analytical selection of ideal epitaxial configurations and some speculations on the occurrence of epitaxy I. Epitaxy with rectangular interfacial atomic meshes, *Philos.Mag.Lett.* 45 (1982) 127–143. <https://doi.org/10.1080/01418618208243907>.
- [26] D.E.Jiang, E.A.Carter, Adsorption and dissociation of CO on Fe(110) from first principles, *Surf. Sci.* 570 (2004) 167–177. <https://doi.org/10.1016/j.susc.2004.07.035>.
- [27] L.J. Whitman, L.J. Richter, B.A. Gurney, J.S. Villarrubia, W. Ho, CO adsorption site occupations on Fe(111) vs coverage and temperature: The kinetics of adsorption and reaction, *J. Chem. Phys.* 90 (1989) 2050–2062. <https://doi.org/10.1063/1.455996>.
- [28] M.H. Nassir, B. Frühberger, D.J. Dwyer, Coverage dependence of CO dissociation on clean and hydrogen presaturated Fe(100) surface, *Surf. Sci.* 312 (1994) 115–123. [https://doi.org/10.1016/0039-6028\(94\)90808-7](https://doi.org/10.1016/0039-6028(94)90808-7).
- [29] C.N.R. Rao, P.V. Kamath, K. Prabhakaran, M.S. Hegde, Adsorption of carbon monoxide on the surfaces of polycrystalline transition metals and alloys: electron energy loss and ultraviolet photoelectron spectral studies, *Can. J. Chem.* 63 (1985) 1780–1787. <https://doi.org/10.1139/v85-298>.
- [30] C.J. Weststrate, A.C. Kizalkaya, E.T.R. Rossen, M.W.G.M. Verhoeven, I.M. Ciobîcă, A.M. Saib, J.W. Niemantsverdriet, Atomic and polymeric carbon on Co(0001): Surface reconstruction, graphene formation, and catalyst poisoning, *J. Phys. Chem. C.* 116 (2012) 11575–11583. <https://doi.org/10.1021/jp301706q>.

- [31] C. Klink, I. Stensgaard, F. Besenbacher, E. Lægsgaard, An STM study of carbon-induced structures on Ni(111): evidence for a carbide-phase reconstruction, *Surf. Sci.* 342 (1995) 250–260. [https://doi.org/10.1016/0039-6028\(95\)00697-4](https://doi.org/10.1016/0039-6028(95)00697-4).
- [32] J. McCarroll, T. Edmonds, R. Pitkethly, Interpretation of a Complex Low Energy Electron Diffraction Pattern: Carbonaceous and Sulphur-containing Structures on Ni(111), *Group. 223* (1969) 1260–1262. <https://doi.org/10.1038/2231260a0>.
- [33] Y. Li, Atomic-scale study of iron-based Fischer-Tropsch catalysts. A combined STM and XPS study, iNANO (Interdisciplinary Nanoscience Center), 2018.
- [34] M.E. Lam, R.J. Boyd, H.J. Kreuzer, Mechanism of C₂H₄ dehydrogenation to C₂H₂ on the Ni(111) surface, *Chem. Phys. Lett.* 253 (1996) 129–134. [https://doi.org/10.1016/0009-2614\(96\)00214-X](https://doi.org/10.1016/0009-2614(96)00214-X).
- [35] J.C. Bertolini, B. Tardy, Vibrational EELS studies of CO chemisorption on clean and carbided (111), (100) and (110) nickel surfaces, *Surf. Sci.* 102 (1981) 131–150. [https://doi.org/10.1016/0039-6028\(81\)90312-5](https://doi.org/10.1016/0039-6028(81)90312-5).
- [36] A. Biedermann, W. Rupp, M. Schmid, P. Varga, Coexistence of fcc- and bcc-like crystal structures in ultrathin Fe films grown on Cu(111), *Phys. Rev. B - Condens. Matter Mater. Phys.* 73 (2006) 1–16. <https://doi.org/10.1103/PhysRevB.73.165418>.



06

CO REACTIVITY ON
IRON AND IRON
CARBIDE FILMS ON
Cu(111)

ABSTRACT: Auger spectroscopy, TPD, RAIRS, and LEED were used to investigate molecular desorption and dissociation of carbon monoxide on iron and iron carbide films supported on Cu(111). The formation of a closed iron film on Cu(111) requires ~8.6 ML of Fe, and on such pure iron films, the maximum amount of CO that can be dissociated is 0.2 ML, leaving a maximum of 0.4 ML of dissociated products on the surface. A pure BCC-Fe phase is formed for films with only the BCC(110) phase, above ~16 ML, which exposes the (110) surface. On such films, a maximum of 0.3 ML CO can dissociate. Like Fe₂C/Cu(100) described in Chapter 4, carbon monoxide cannot dissociate on a fully saturated iron carbide film. The desorption temperature of carbon monoxide on the iron carbide film decreases by 50 K with respect to the desorption from the non-carburized iron film, which is attributed to weaker bonding of CO in the presence of surface carbon. The carbon monoxide dissociation reaction has been examined on an 8 ML iron film surface with different concentrations of pre-adsorbed carbon. The dissociated amount decreases linearly with increasing carbon coverage, and the sum of dissociation products (C_{ad}+O_{ad}) remains constant at 0.4 ML. After saturating the surface with carbon and oxygen, the surface becomes unreactive toward any dissociation reaction.

6.1 Introduction

Heterogeneous catalysts used in the chemical industry are highly complex materials. The active component is often dispersed on supporting materials, while additives (promoters) are typically used to improve the catalyst activity and durability. This high complexity makes commercial catalysts poorly accessible for atomic-level studies, mainly because the active phase of the catalyst is hard to identify. For this reason, we aim to develop simple, well-defined model systems for the iron carbide Fischer-Tropsch synthesis (FTS) catalyst to facilitate such atomic-level studies.

In Chapter 5, we discussed the fabrication and structure of iron and iron carbide thin films on Cu(111), in which three distinct structural regimes were identified: below 2.6 ML, iron follows the FCC(111) substrate, between 2.6 and 16 ML, the iron film exposes a mixture of FCC(111) and BCC(110) surfaces, and for thicker films, a pure BCC(110) surface is formed.

The interaction of CO with the iron and iron carbide surfaces is of great importance for understanding the catalytic processes in FTS. In general, CO dissociation

produces carbon atoms required for hydrocarbon formation [1]. References [2–6] provide an in-depth analysis of CO dissociation and hydrogenation at the metallic Fe surface. Furthermore, references [1,7,8] show DFT calculations on the catalytic properties of iron carbides towards CO in FTS. Due to the considerable challenges in synthesis, mechanistic studies based on experiments are limited [9–11]. Besides our findings on Cu(100) in Chapter 4, there are no fundamental studies of CO adsorption on iron carbide surfaces to our knowledge. The successful synthesis of iron carbide films on Cu(111) allows us to study CO adsorption and dissociation on the carbide surface.

A comparison of the results obtained by Li et al. [12] on an Au(111) substrate and our own on a Cu(100) substrate revealed substantial differences: on Cu(100), pure surface carbides were formed between 0.5 ML and 8 ML of iron, while on Au(111), pure carbides were impossible to make at any studied iron thickness. To better understand the origin of the reactivity, we decided to investigate how changing from Cu(100) to Cu(111) affects carbide formation, as discussed in Chapter 5. In the present chapter, we investigate reactivity differences of CO on different thicknesses of iron and iron carbide on Cu(111) in comparison to Cu(100).

An important factor that contributes to reactivity differences between $\text{Fe}_x\text{C}_y/\text{Au}(111)$, $\text{Fe}_2\text{C}/\text{Cu}(100)$ and $\text{Fe}_x\text{C}_y/\text{Cu}(111)$ are the differences in iron growth mode during deposition at room temperature. The iron film evaporated on Cu(111) exhibits different phases from ~2.6 ML to ~16 ML. We tentatively proposed in Chapter 5 that these phases are: Uncarburized BCC(110) and Fe FCC(111), carburized Fe_xC_y p4g(2x2)-C + Fe_xC_y BCC(110). The p4g(2x2) formation on Cu(100) and Cu(111) acts as a carbon trap inhibiting further ethylene dissociation, and as in Chapter 4, it is expected that it also inhibits CO dissociation.

In this chapter, we show the CO results on iron and iron carbide films, and in the discussion section, we compare the results from these films with those from Cu(100) and Au(111).

6.2 Experimental

The Reflection Adsorption Infrared Spectroscopy (RAIRS), temperature-programmed desorption (TPD), low energy electron diffraction (LEED), and Auger electron spectroscopy (AES) results described in this chapter were obtained using the home-built UHV chamber with a base pressure of around 2×10^{-10} mbar as described in Chapter 2.

RAIRS experiments were performed in a compartment with a base pressure of $< 1 \times 10^{-10}$ mbar using a Perkin Elmer Frontier spectrometer equipped with a liquid nitrogen-cooled MCT detector. After passing through a KBr window, the infrared beam is specularly reflected from the front face of the single crystal and then exits via a second KBr window to the detector. The spectra were recorded at 100 K with a resolution of 4 cm^{-1} .

The chamber was equipped with two quadrupole mass spectrometers, LEED/Auger optics, and a dual pocket e- beam evaporator. TPD experiments were performed using a QMS inside a separately pumped compartment with a 5 mm-wide aperture connecting to the main chamber. During a desorption experiment, the sample is placed 2 mm from the aperture to eliminate desorption signals from other parts of the sample holder. Quantitative evaluation was cross-checked with the simultaneously measured signal from a second QMS located in the main chamber to eliminate potential errors that arise from directional desorption [13].

The surface free energy of Cu(111) is lower than iron, which causes copper atoms to segregate on the surface, reducing the surface energy of the system [14]. Moreover, the surface free energy of Cu(111) is lower than for Cu(100); therefore, the experiments should not be performed the same way when using different substrates, i.e., with different maximum sample temperatures. It should be noted that some of the experiments presented here require temperatures similar to those in Chapter 4, where the sample was heated to 500 K. At this temperature, molecularly adsorbed carbon monoxide and ethylene will fully desorb from the surface. However, some iron will be lost and diffuse into the bulk of the single crystal during the heating process. A further discussion of this topic is provided in the results section.

Iron was evaporated at 300 K by electron beam evaporation from a 99.999% purity rod. An evaporation rate of around 0.5 ML/min was typically used, and it was calibrated using the attenuation of Cu_{LMM} Auger electrons, as described in Chapter 5 (Equation 5.1).

6.3 Results

6.3.1 CO dissociation on different iron thicknesses on Cu(111)

In Chapter 5, the decrease in CO desorption from the copper substrate was used to infer the iron growth mode and the iron and copper surface areas after different quantities of iron were evaporated. We found in Chapter 5 that the evaporated iron does not grow layer-by-layer and is not a flat film, on the contrary, it is a rough layer with 5 ML height islands, and it takes ~ 9 ML for the iron film to close up completely. In this chapter, we use the same data set as in Chapter 5 but now focus on the desorption peaks from the iron-covered parts to investigate CO reactivity on the iron-thin film in more detail.

Iron films with six different thicknesses were exposed to carbon monoxide at 100 K until saturation (3 L). The TPD spectra recorded afterwards are shown in Figure 6.1 (a). On films between 2.5 and 7.5 ML, the desorption peaks below 200 K are caused by CO desorption from the Cu(111) substrate, and their presence confirms that the film is not yet fully closed [15].

Molecular desorption of CO from iron occurs up to 450 K and shows a complex desorption peak shape that varies with Fe film thickness. For films between 2.5 ML and 3 ML, a high-temperature desorption peak is seen around 400 K. This desorption feature is only visible in the Fe thickness regime where only FCC Fe(111) is formed [16]. The intensity of this peak decreases with increasing film thickness while the intensity of the desorption peaks at 220 K and 320 K increases, indicating a marked difference in the interaction of CO as a function of film thickness on Cu(111). The broadening of the desorption peaks indicates some disorder, as discussed in Chapter 5 (some indications of this disorder are the broadening of the LEED spots right after evaporation).

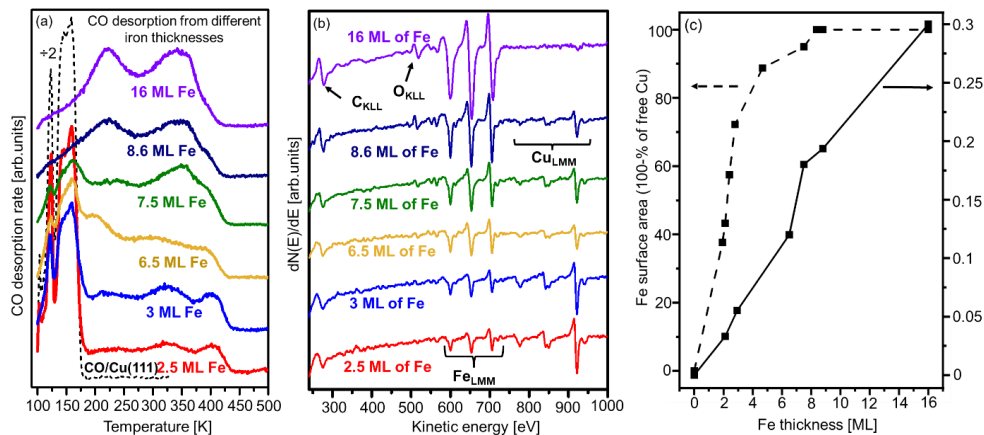


Figure 6.1. (a) CO desorption spectra (2 K/s) as a function of Fe thickness after dosing CO to saturation (3 L) onto six different iron films at 100 K followed by heating to 500 K. (b) AES spectra taken at 300 K after heating CO-covered Fe/Cu(111). (c) Uptake curve in which the intensities of FeLMM, CuLMM, CKLL and OKLL have been normalized and converted into iron thickness and carbon coverage. The iron thickness is plotted against the iron surface area and the oxygen coverage after CO dissociation. The dashed line indicates the surface area of Fe obtained from the desorption of CO from Cu(111) (Chapter 5).

During heating, some CO dissociates, leaving behind carbon and oxygen adsorbates. The dissociation of CO was investigated with AES as a function of iron film thickness after heating a CO-covered Fe/Cu(111) to 500 K, above the desorption temperature of molecularly adsorbed CO. The AES spectra in Figure 6.1 (b) show that carbon and oxygen are present after heating, confirming that CO dissociation occurs for all Fe film thicknesses. The oxygen found afterwards was quantified based on the absolute O_{KLL} signal intensity, where the well-defined ($\sqrt{2} \times \sqrt{2}$)R45°-O structure on Cu(100) with $\theta_{\text{O}} = 0.5$ ML was used as a quantitative reference (see Chapter 2 and references [17,18]). It should be noted that the copper surface atom density of Cu(111) is 1.15 times larger than in Cu(100), so the AES signal intensity from 0.5 ML O_{ad} on Cu(100) is equivalent to 0.43 ML O_{ad} on Cu(111), and this value was used for quantitative evaluation of the oxygen coverage in the present work. We note that although the C_{KLL} intensity is larger than the O_{KLL}, the

latter was used to quantify the amount of dissociated CO as this approach can also be applied to (partly) carbided films where the carbon signal is already high, making it more challenging to determine the increase in the carbon signal after dissociation. In Figure 6.1 (c), the oxygen coverage and iron surface area are plotted against the iron thickness on Cu(111).

The oxygen content follows a linear behaviour until ~6.5 ML, close to the maximum iron surface area extrapolated from the CO titration experiment. A marked difference is seen between the iron surface area, and the amount of CO dissociated, mainly related to the morphology and structure of the iron film on the Cu(111) (this is discussed more in detail in the discussion section).

6.3.1.1 CO dissociation on (~16 ML) Fe BCC(110) films

The CO dissociation reaction was studied in more detail for a nominal thickness of 16 ML, where the iron exposes a BCC(110) surface [14,16]. Figure 6.2 shows the CO desorption spectra for two different iron films with the same thickness, evaporated at 300 K and subsequently exposed to different amounts of CO at 100 K. The surface was first saturated with 3 L of carbon monoxide and heated to 500 K to ensure complete molecular desorption. Afterwards, Auger spectra were recorded at 500 K to determine the surface composition after all the molecular desorption. Once the spectra were recorded, we resumed the heating process to 800 K to record the recombination peaks. In the second experiment, a fresh film was prepared after adsorbing on the surface a smaller dose of CO (0.1 L).

After dosing 0.1 L of CO, the desorption spectrum shows a small desorption peak at 375 K, ascribed to molecularly desorbed CO from the iron surface, while another, much larger desorption peak is found around 700 K, attributed to the recombination of atomic carbon and oxygen on the surface [19]. The presence of oxygen and carbon in the AES measurements during a pause in the desorption experiment at 500 K confirmed the dissociation of CO. The shape of the CKLL spectra shown in the inset displays the three characteristic carbide transitions while their intensity corresponds to a carbon coverage of 0.3 ML. This coverage is approximately 0.1 ML more than for films <16 ML. The carbon and oxygen produced by CO dissociation

recombine and desorb around 700 K. The area under the recombination peak seen corresponds to a coverage of only 0.18 ML, a smaller value than the 0.3 ML calculated with AES. This difference may be attributed to the temperature at which the system was heated. It is known that oxygen can dissolve into the copper crystal [20], which consumes a part of the oxygen from CO dissociation so that less recombination can occur.

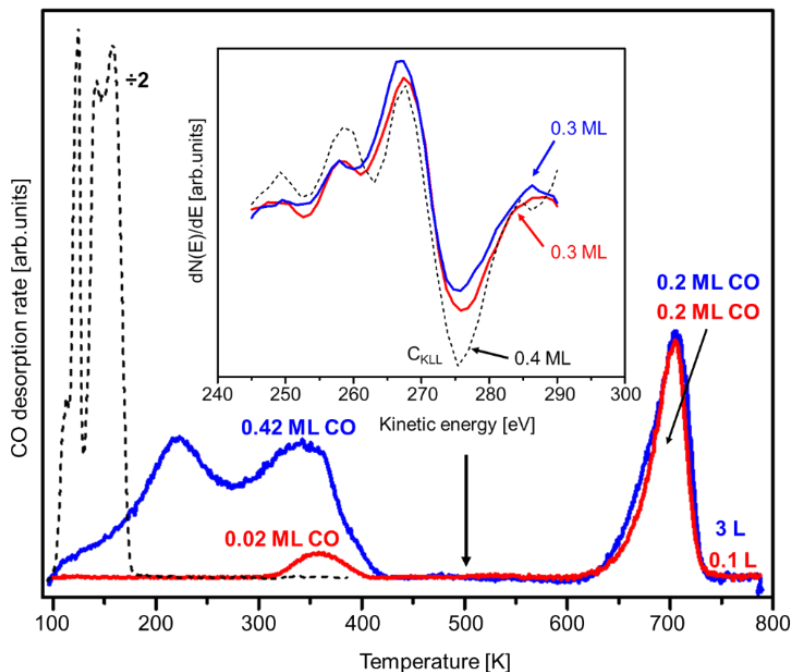


Figure 6.2. TPD spectra (2 K/s) of CO were obtained after exposing two different ~ 16 ML Fe films to a low and a high CO dose at 100 K. In the inset, the C_{KLL} Auger spectra after all the molecular CO desorbed from the surface. The dashed lines are the CO desorption from the Cu(111) surface and a C_{KLL} spectrum from pure carbide as a reference. $E=2000$ eV.

6.3.1.2 Morphological changes upon CO dissociation

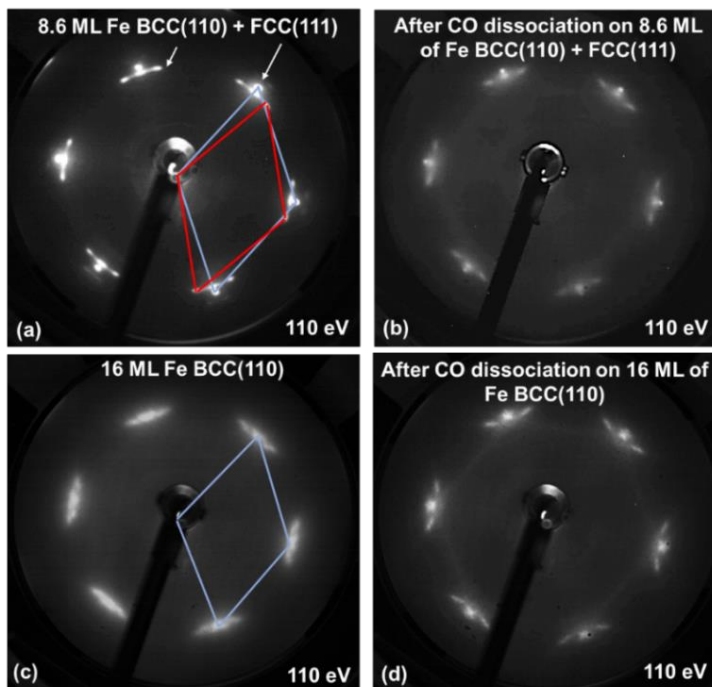


Figure 6.3 The LEED images of (a) 8.6 ML iron film right after evaporation. (b) After CO desorption from an 8.6 ML iron film. (c) After evaporating ~16 ML of iron. (d) After CO dissociation on ~16 ML of iron. Images were taken at 100 K and 110 eV.

Figure 6.3 shows a series of LEED patterns taken before and after CO adsorption and desorption on different iron thicknesses, 8.6 and 16 ML (when the substrate is fully covered and the film behaves mostly BCC(110)). In Figure 6.3. (a) the LEED pattern of a pure 8.6 ML iron film where the Kurdjumov-Sachs (KS) spots or BCC(110) features and the FCC(111) substrate spots can be seen [14,16]. Figure 6.3 (b) shows the same film after exposure to CO followed by heating to 500 K. This results in the BCC(110) spots getting blurrier and weaker, indicating an increase in surface disorder probably due to the atomic carbon and oxygen left behind after heating. For pattern (c), only the KS spots are seen due to the different domains of BCC(110), while the FCC(111) spots from the substrate and FCC Fe(111) are no longer visible. Figure 6.3 (d) shows the pattern after CO dissociation on a ~16 ML

iron film. It is similar to that found in (b), where the blurriness and the extra features between the substrate spots suggest that carbon and oxygen influence the structure, but the details cannot be resolved from LEED. In summary, we do not find clear morphology differences induced by CO dissociation and heating to 500 K in LEED. For further study, we recommend STM, which could bring valuable morphology information to resolve the reconstruction, as has been seen previously in other studies like carbon reconstruction on Ni(100) [21] or on Fe(100) single crystals [22].

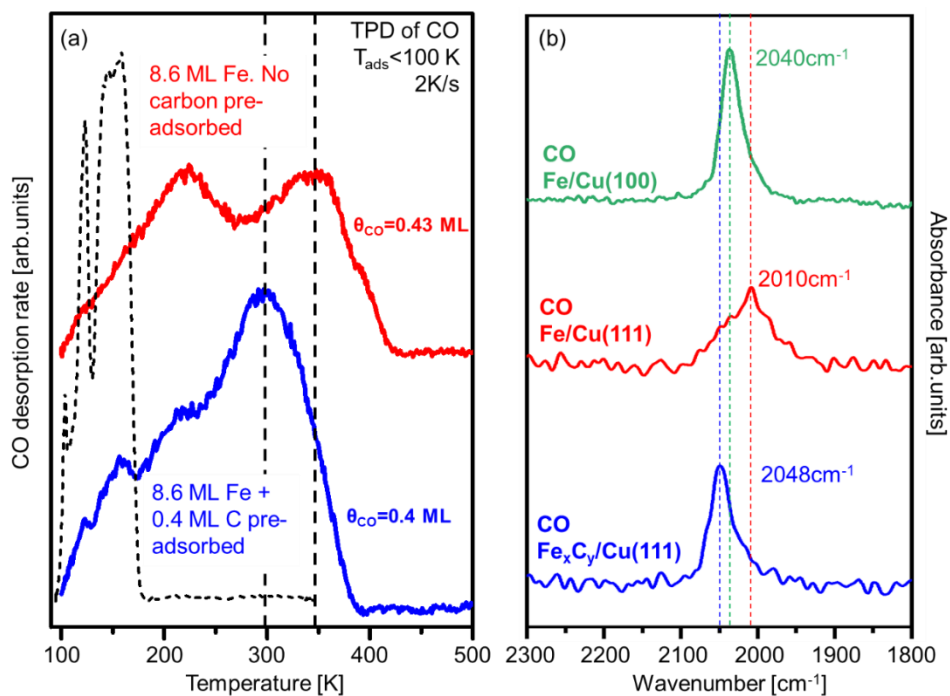


Figure 6.4 (a) TPD spectra of CO obtained after exposing a freshly evaporated iron film and a saturated iron carbide film (3 ethylene cycles). (b) RAIRS results after adsorbing CO on an 8.6 ML iron and 8.6 ML pre-adsorbed saturated iron carbide film. CO was adsorbed at 100 K, and the heating rate was 2 K/s.

6.3.1.3 CO desorption from iron carbide films

Ethylene can be used as a carbon precursor to create an iron carbide surface on the Fe/Cu(111) system, as described in Chapter 5. We here use a combination of IR absorption spectroscopy, TPD and AES to investigate the interaction of CO with the iron carbide surface formed on Fe/Cu(111). We first look at the carbide surface obtained after three ethylene dosing cycles on an 8.6 ML Fe film, which produces a carbon coverage of 0.4 ML, hereafter referred to as the 'saturated surface carbide' for short. Figure 6.4 (a) compares the CO desorption spectra from 8.6 ML Fe/Cu(111) and Fe_xC_y/Cu(111), while Figure 6.4 (b) shows the IR absorption spectra after adsorbing CO at 100 K onto Fe/Cu(111), Fe_xC_y/Cu(111) and CO on Fe/Cu(100) that will be discussed later. A comparison of the desorption peaks of CO from Fe/Cu(111) and Fe_xC_y/Cu(111) shows that the high-temperature CO desorption peak from the saturated iron carbide occurs at around ~50 K lower with respect to the non-carburized iron film. Also, like in Cu(100) systems, the CO desorbs at a lower temperature in carburized films than in non-carburized films. The presence of carbon on the surface weakens the surface-CO bond mainly due to the electrostatic repulsion [7,23], thus decreasing the CO desorption temperature with respect to the non-carburized film.

The minor desorption feature seen at 150 K for the carbon-covered sample is related to CO desorbing from the substrate, which originates from how the experiments were done. To make the iron carbide, we need first to dissociate ethylene by heating the surface to 500 K, followed by adsorption and desorption of CO. These multiple heating steps cause copper segregation and iron diffusion into the copper, thus losing material in the process and exposing the copper substrate, hence changing the surface area respect to the freshly evaporated iron film.

The IR spectrum of CO adsorbed at 100 K, shown in Figure 6.4 (b), confirms that the adsorption of CO on Fe_xC_y vs pure Fe is different. CO adsorbed on Fe/Cu(111) shows one broad absorption band at 2010 cm⁻¹, indicating that the surface is not atomically smooth due to the presence of BCC(110) and FCC(111) features. As a result of this mixture of phases, the CO wavenumber will differ from that found in BCC(110) single crystals, which is 2036 cm⁻¹, and CO on Fe BCC(110) films grown

on Cu(100) [24]. Tanabe et al. investigated the CO adsorption on different iron film surfaces with different thicknesses, from 1 ML to 21 ML. Their findings show a wavenumber change from 2000 cm^{-1} to 2032 cm^{-1} with respect to the thickness, the first value corresponding to top sites on 1 ML FCC Fe(111) and the other to a mixture on 21 ML BCC Fe(110), respectively. According to Tanabe's findings, at 8.6 ML, FCC iron is still on the surface and a substantial amount of BCC(110), as we saw in the LEED patterns of Chapter 5.

In summary, the wavenumber of adsorbed carbon monoxide on carburized and non-carburized iron differs by $\sim 38\text{ cm}^{-1}$. This difference in wavenumber could be attributed to numerous things, but mainly due to the difference between surface composition and morphology (binding sites, lateral interactions). Also, the desorption temperature of carbon monoxide is different for carburized and non-carburized films, the latter being higher than carburized films, suggesting that carbon plays a role in the desorption energy.

6.3.1.4 Carbon influence on CO dissociation Fe FCC(111)+BCC(110)

The influence of carbon on the dissociation of carbon monoxide was investigated in more detail on 8 ML films by dosing CO to saturation (3 L) using five different 8 ML iron carbide films with various amounts of pre-adsorbed carbon. To create iron-carbide surfaces with different carbon concentrations, we need different ethylene doses at 100 K, followed by heating to 500 K.

Figure 6.5 shows the C_{KLL} and the O_{KLL} Auger spectra after CO dissociation for five samples with different quantities of pre-adsorbed carbon. First, on the film without pre-adsorbed carbon (**green**), 0.18 ML of carbon monoxide was dissociated, leaving 0.36 ML of dissociation products on the surface (0.18 ML C_{ad} + 0.18 ML O_{ad}). After pre-adsorbing 0.15 ML of carbon (**pink**) on the surface, the total C_{KLL} intensity after dissociating CO corresponds to 0.25 ML (0.15 ML of pre-adsorbed carbon + 0.1 ML of C_{ad} from CO dissociation), leaving on the surface a total of 0.35 ML of products. After pre-adsorbing 0.22 ML of carbon, the total CO dissociated is 0.1 ML, and the total adsorbants on the surface is 0.32 ML. Figure 6.5 (black) is the iron film pre-

saturated with carbon after CO dissociation where no OKLL signal is present, meaning no CO was dissociated on the surface.

Figure 6.5 (b) shows the oxygen coverage [ML] against pre-adsorbed carbon [ML] for the different experiments. The amount of CO dissociation decreases linearly with carbon pre-coverage, where the total amount of dissociation products remains approximately constant at around 0.4 ML.

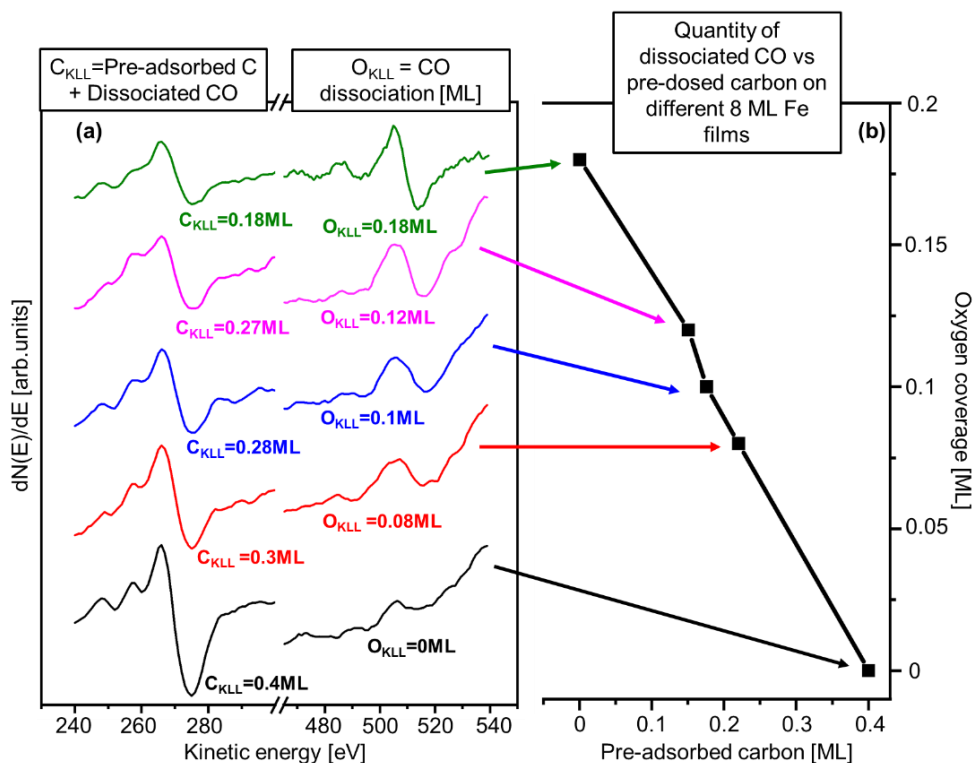


Figure 6.5. (a) CKLL and OKLL spectra taken after CO dissociation at 500 K. (b) Uptake curve of the total CO dissociated against the total pre-adsorbed carbon from ethylene dissociation decomposition on different ~ 8 ML iron films.

6.4 Discussion

This section discusses the adsorption and dissociation of CO on iron and iron carbide films on Cu(111) and compares them to the results on Cu(100). An important

underlying complexity for the Cu(111) substrate is that the growth mode of iron is 3D instead of 2D as in the case of iron on Cu(100), and the structure varies with layer thickness [14]: films below 2.6 ML are coherent with the substrate, and only when the islands are larger, and the iron thickness is higher than 2.6 ML, the Fe relaxes into the BCC phase. Also, 8 ML of evaporated iron at 300 K is required to cover the substrate completely due to 3D growth. The structure of these films, according to Biedermann et al. [16], has a pyramidal shape (“ridgelike”), and a mixed FCC(111) + BCC(110) film is present until 16 ML of iron, after which a pure BCC(110) structure forms. The heterogeneity of these films makes detailed interpretation of the carbon monoxide desorption spectra difficult, but comparing the adsorption and desorption of CO on these films with iron single crystals can yield some useful insights.

6.4.1 CO desorption and dissociation on Fe/Cu(111) and comparison with Fe/Cu(100)

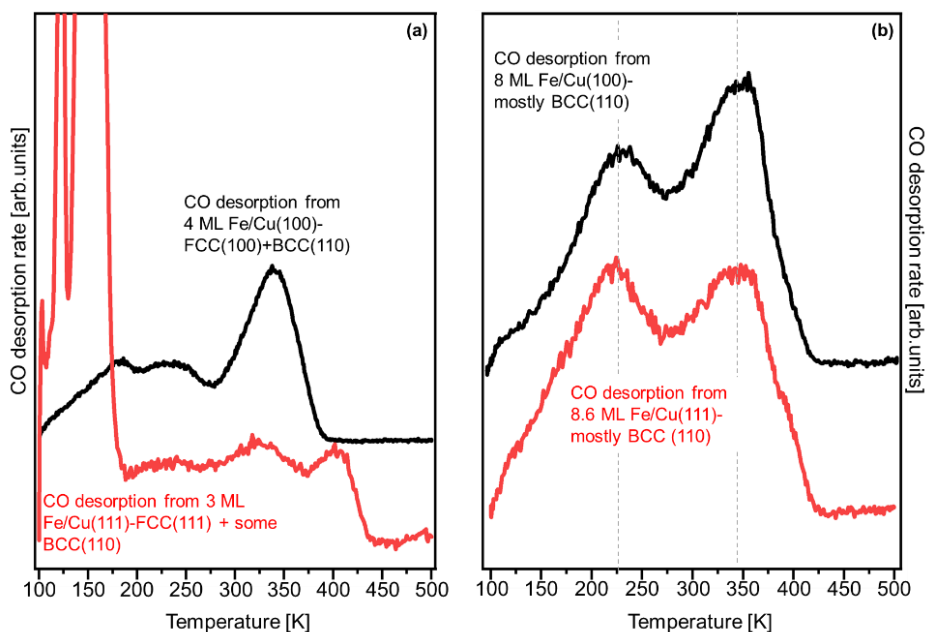


Figure 6.6. CO TPD from two different iron surfaces exposing different phases. In (a), 3 and 4 ML of iron on Cu(111) and Cu(100), exposing FCC(111) and FCC(100)+BCC(110), respectively. In (b), mostly BCC(110) is exposed. Spectra recorded at 2 K/s.

Figure 6.6 (a) compares the desorption of carbon monoxide from 3-4 ML iron films supported on Cu(100) and Cu(111). At least three different desorption temperatures in Fe/Cu(111) can be seen, 225 K, 325 K and 400 K, alongside the peaks from bare copper below 200 K. The absence of the desorption peak at 400 K from the Fe/Cu(100) film shows that it is inherent to the Fe/Cu(111) system. However, the peak at 325 K is present in both systems. The iron on 4 ML Fe/Cu(100) forms a (4x1) BCC-like structure, and we, therefore, attribute this peak to desorption from the BCC(110) phase. On Cu(111), the film instead exposes a mixture of FCC and BCC. We attribute the peak at 400 K, only seen on Cu(111), to CO adsorbed on FCC-Fe(111). In Figure 6.1. it can be seen how this peak at 400 K gets smaller with iron thickness until it is not present anymore, which suggests that the phase FCC(111) disappears with increasing thickness (Chapter 5). These desorption peaks are no longer visible for thicker iron films, 8 ML Fe, where the BCC(110) phase is dominant on both surfaces.

This explains why the CO desorption spectra for both the Cu(100) and Cu(111) substrates [shown in Figure 6.6. (b)] look very similar. Note how in Figure 6.6. (b) these peaks are shifted slightly towards higher desorption temperatures and are sharper compared to the BCC-related peaks for the thin films. This is probably because, at this thickness, the BCC(110) phase is the predominant one on the surface, making it more relaxed and, thus, smoother and more homogeneous.

Figure 6.7 shows the total oxygen concentration after CO dissociation on Fe/Cu(100) and Fe/Cu(111) together with the total iron surface area against iron thickness. The total oxygen content on Fe films that fully covered the substrate is 0.05 ML lower for Fe/Cu(111). Furthermore, the oxygen on Fe film on Cu(100) saturates faster than Fe on Cu(111). This is seen by how fast the maximum oxygen coverage is reached at 2 ML Fe/Cu(100) and at 8 ML on Cu(111). This is taken as an indication that the FCC(100)+BCC(110) is more reactive than the FCC(111)+BCC(110) film, which is not surprising due to the open structure of the FCC(100), which can accommodate dissociation products much easier than FCC(111).

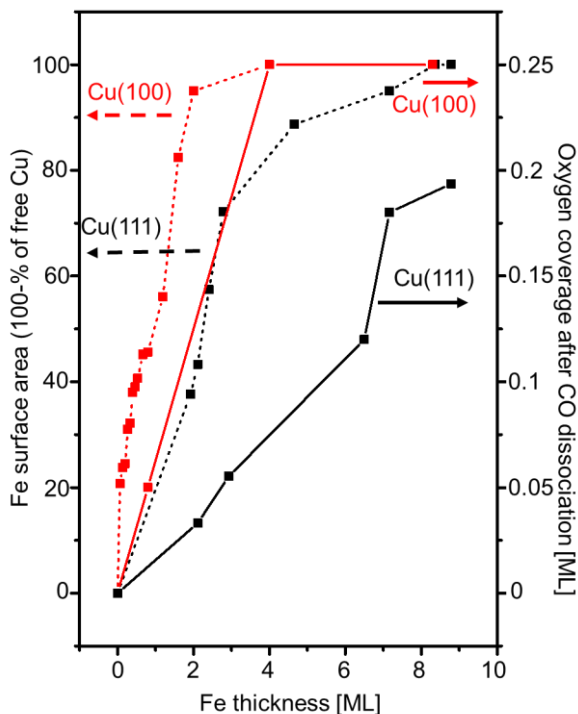


Figure 6.7. Oxygen content as a function of iron coverage derived from AES analysis after heating to 500 K a pre-adsorbed saturated carbon monoxide surface. The graph also shows the uptake curve of the oxygen content after CO dissociation extracted from the C1s intensity in the TP-XPS from Chapter 4.

A closer look at Figure 6.5 shows how the C_{KLL} carbidic nature decreases when we decrease the quantity of pre-adsorbed carbon or increase the quantity of adsorbed oxygen (the three carbidic transitions are less defined). However, this decrease in carbidic nature could also be related to carbon diffused into the bulk or the formation of graphitic carbon. In these cases, no $p4g(2 \times 2)$ symmetry is seen (no carbon trap), as we mentioned in the LEED patterns of Figure 6.3. In Chapter 4, XPS measurements on 8 ML of Fe on Cu(100) show a clear BE of 282.5 eV, confirming carbide formation after CO dissociation, contrary to what we see in the AES spectra of Figure 6.5 for a system without pre-adsorbed carbon. More experiments with SR-XPS are required to determine the exact nature of the carbon after CO dissociation on a non-carburized iron film and semi-saturated iron surface.

6.4.2 CO desorption and dissociation on $\text{Fe}_x\text{C}_y/\text{Cu}(111)$ and comparison with $\text{Fe}_2\text{C}/\text{Cu}(100)$

This section compares how the CO molecule interacts with iron carbide films on Cu(100) and Cu(111). Figure 6.8 compares two CO desorption spectra from iron carbide films on Cu(100) and Cu(111).

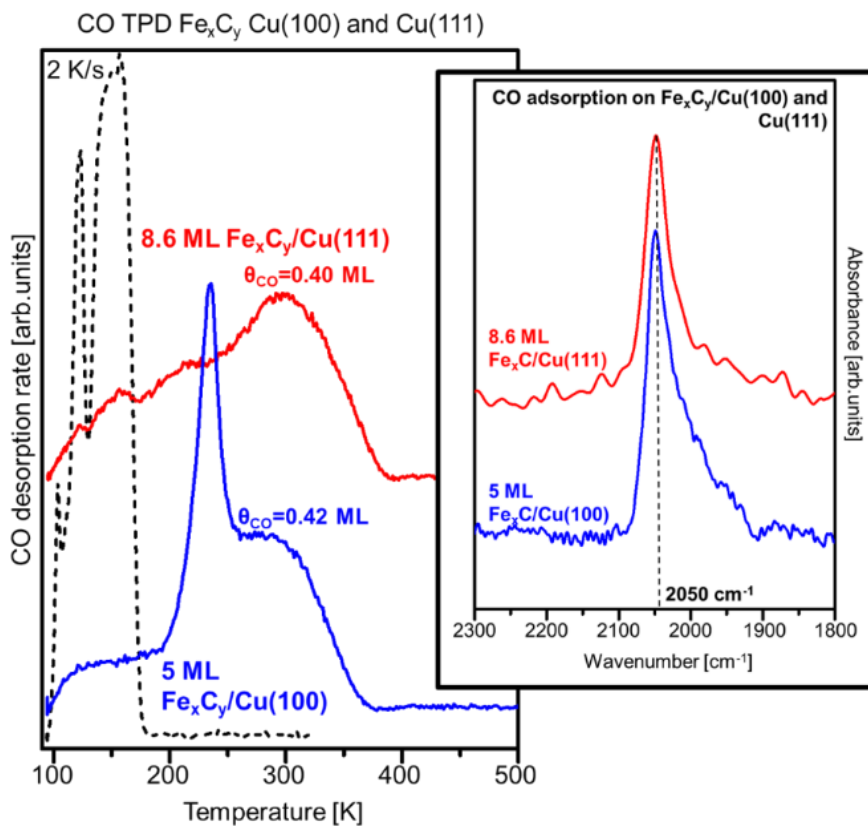


Figure 6.8. (a) TPD spectra of CO were obtained after exposing different thicknesses of iron carbide to CO on Cu(111) and Cu(100) at a temperature of 100 K and a heating rate of 2 K/s. (b) IR spectra after CO adsorption on different thicknesses of iron carbide on Cu(100) and Cu(111) at 100 K.

Both systems have the same high desorption temperature at ~ 300 K. However, the low-temperature desorption peak for the $\text{Fe}_x\text{C}_y/\text{Cu}(100)$ system is different than on

Cu(111). This difference could be attributed to the roughness of the $\text{Fe}_x\text{C}_y/\text{Cu}(111)$ system and the possible Cu segregation after carburizing the iron film. The copper segregation at 300 K is already high [14], so the non-carburized phase of the iron film could be covered with copper, reducing the iron surface area for the next experiment, i.e. CO adsorption on thin films on Cu(111). Figure 6.7 shows a feature of the aforementioned scenario at ~ 150 K (red spectrum).

RAIRS experiments were also done in conjunction with the TPD experiments after adsorbing CO on fully carburized iron films on Cu(100) and Cu(111), as shown in Figure 6.8. The C-O stretch band on both systems is the same, 2050 cm^{-1} , and corresponds to the adsorption of CO on top sites on the iron carbide surface [25,26]. A surface structure with $p4g(2 \times 2)$ symmetry is obtained after carburizing iron films on Cu(100) and Cu(111). An extremely highly stable structure that acts as a carbon trap and avoids any diffusion. Taking this into account, we can say that the results obtained of CO dissociation reaction on films that form the $p4g(2 \times 2)$, 2-12 ML and 2.6-16 ML, respectively, are very similar.

However, similar to Cu(100), the wavenumber difference between stretch bands of C-O adsorbed on iron and iron carbide is less than 10 cm^{-1} . Hence, no significant differences are expected in the adsorption of CO on Fe and Fe_xC_y on Cu(111). If the copper substrate was not entirely covered, a stretch band of C-O at $2078\text{-}2070\text{ cm}^{-1}$ is expected from CO/Cu(111) [27].

Saturated iron carbide surfaces on Cu(100) and Cu(111) show no reactivity towards CO dissociation. In the presence of carbon, the dissociation products cannot accommodate on the surface; hence there is a lack of reactivity toward dissociation. Molecular desorption of CO shifts to lower temperatures also due to the presence of carbon and the electrostatic repulsion it generates on the adsorbed CO, which weakens the Fe-CO bond.

6.5 Summary and Conclusions

We studied the CO dissociation reaction and molecular adsorption and desorption on iron and carburized iron films on Cu(111) through AES, TPD and RAIRS.

An increase in the O_{KLL} intensity confirmed CO dissociation on non-carburized iron films from FCC(111), FCC(111)+BCC(110) and finally, BCC(110). The quantity of CO that can be dissociated increases with iron thickness due to an increase in the projected iron surface area up to 0.4 ML of dissociation products on FCC(111)+BCC(110) (when the substrate is fully covered by iron). For films with a thickness where only pure BCC(110) is present, ~16 ML, the maximum amount of CO dissociation products measured was 0.6 ML ($C_{ad}+O_{ad}$).

The saturated $Fe_xC_y/Cu(111)$, like in $Fe_2C/Cu(100)$, is unreactive towards CO dissociation. The amount of CO that dissociates decreases linearly with the amount of pre-adsorbed carbon and reaches zero when the surface is fully saturated. The molecular desorption temperature of CO on iron carbide films decreases between 50 K and 100 K with respect to the non-carburized iron film, suggesting weaker bonding to the film due to repulsion between carbon and the adsorbed CO. Lower quantities of pre-adsorbed carbon on the surface show activity towards CO dissociation confirming that the responsible for inhibiting this reaction is the presence of carbon on the surface.

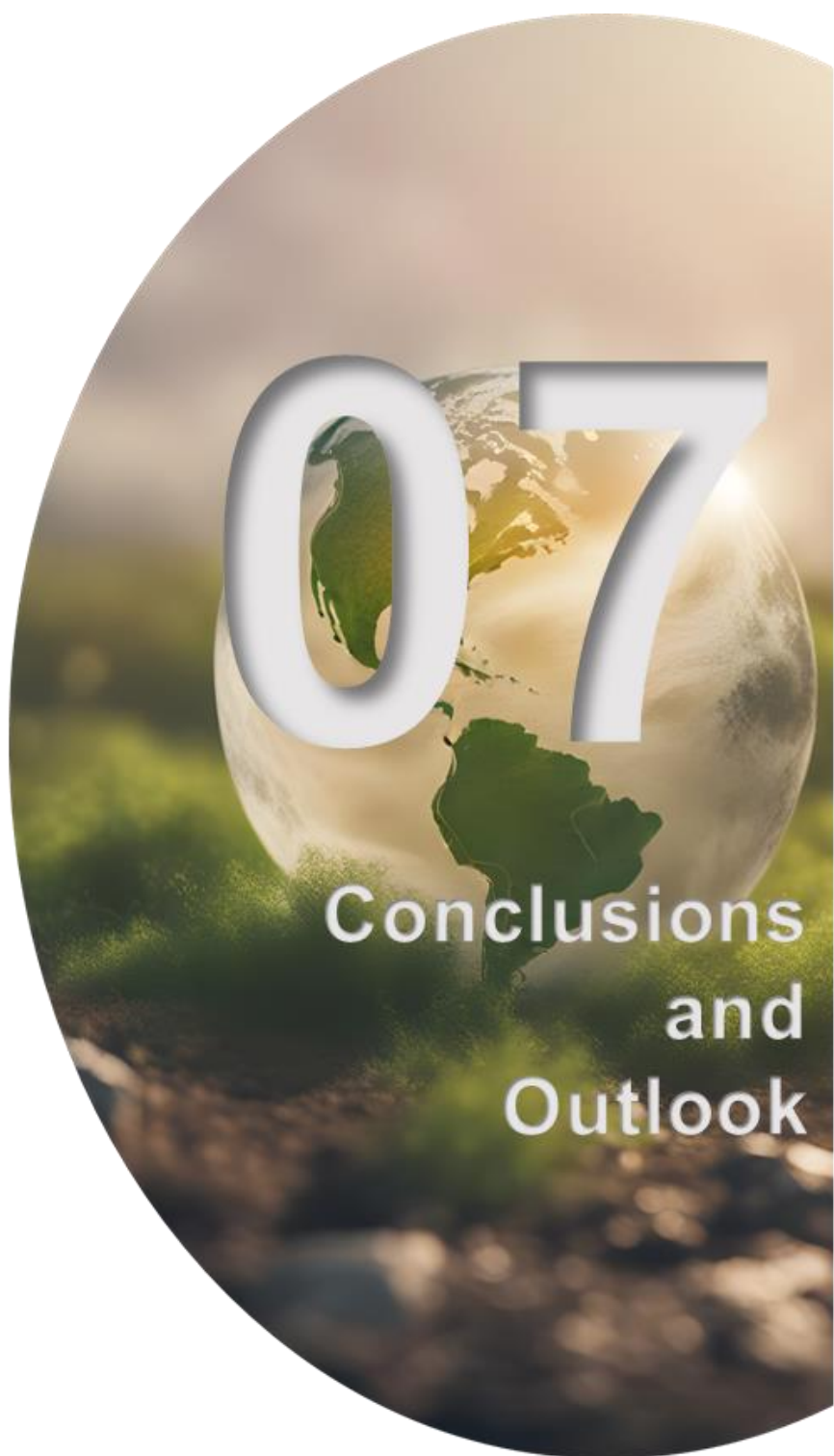
Overall, the CO reactivity on $Fe_xC_y/Cu(111)$ and $Fe_2C/Cu(100)$ are similar. After ethylene dissociation, both systems form a very stable and unreactive $p4g(2 \times 2)$ structure, which inhibits any dissociation reaction studied here, ethylene and CO dissociation.

6.6 References

- [1] M.O. Ozbek, J.W. Niemantsverdriet, Elementary reactions of CO and H₂ on C-terminated X-Fe₅C₂(001) surfaces, *J. Catal.* 317 (2014) 158–166. <https://doi.org/10.1016/j.jcat.2014.06.009>.
- [2] C.K. Kuei, M.D. Lee, Temperature-programmed reaction of pre-adsorbed CO on iron catalyst: new experimental evidence for competition model, *J. Mol. Catal.* 65 (1991) 293–305. [https://doi.org/10.1016/0304-5102\(91\)85066-B](https://doi.org/10.1016/0304-5102(91)85066-B).
- [3] C.F. Rhodin, T.N., Brucker, Effect of surface deactivation on molecular chemisorption: CO on alpha-Fe(100) surfaces, *Solid State Commun.* 23 (1977) 275–279. [https://doi.org/https://doi.org/10.1016/0038-1098\(77\)91328-X](https://doi.org/https://doi.org/10.1016/0038-1098(77)91328-X).
- [4] C. Zhang, G. Zhao, K. Liu, Y. Yang, H. Xiang, Y. Li, Adsorption and reaction of CO and hydrogen on iron-based Fischer-Tropsch synthesis catalysts, *J. Mol. Catal. A Chem.* 328 (2010) 35–43. <https://doi.org/10.1016/j.molcata.2010.05.020>.

- [5] W. Erley, P.H. McBreen, H. Ibach, Evidence for CH_x surface species after the hydrogenation of CO over an Fe(110) single crystal surface, *J. Catal.* 84 (1983) 229–234. [https://doi.org/10.1016/0021-9517\(83\)90100-8](https://doi.org/10.1016/0021-9517(83)90100-8).
- [6] H.J. Wan, B.S. Wu, C.H. Zhang, H.W. Xiang, Y.W. Li, B.F. Xu, F. Yi, Study on Fe-Al₂O₃ interaction over precipitated iron catalyst for Fischer-Tropsch synthesis, *Catal. Commun.* 8 (2007) 1538–1545. <https://doi.org/10.1016/j.catcom.2007.01.002>.
- [7] J. Gracia, F. Prinsloo, J.W. Niemantsverdriet, Mars-van Krevelen-like Mechanism of CO Hydrogenation on an Iron Carbide Surface, *Catal. Lett.* (2009) 257–261. <https://doi.org/10.1007/s10562-009-0179-5>.
- [8] M.O. Ozbek, J.W. Niemantsverdriet, Methane, formaldehyde and methanol formation pathways from carbon monoxide and hydrogen on the (001) surface of the iron carbide χ -Fe₅C₂, *J. Catal.* 325 (2015) 9–18. <https://doi.org/10.1016/j.jcat.2015.01.018>.
- [9] Y. Li, Atomic-scale study of iron-based Fischer-Tropsch catalysts. A combined STM and XPS study, iNANO (Interdisciplinary Nanoscience Center), 2018.
- [10] C. Yang, H. Zhao, Y. Hou, D. Ma, Fe₅C₂ nanoparticles: A facile bromide-induced synthesis and as an active phase for Fischer-Tropsch synthesis, *J. Am. Chem. Soc.* 134 (2012) 15814–15821. <https://doi.org/10.1021/ja305048p>.
- [11] M. Ding, Y. Yang, B. Wu, Y. Li, T. Wang, L. Ma, Study on reduction and carburization behaviors of iron phases for iron-based Fischer-Tropsch synthesis catalyst, *Appl. Energy.* 160 (2015) 982–989. <https://doi.org/10.1016/j.apenergy.2014.12.042>.
- [12] Y. Li, Z. Li, A. Ahsen, L. Lammich, G.J.A. Mannie, J.W. Niemantsverdriet, J. V. Lauritsen, Atomically Defined Iron Carbide Surface for Fischer-Tropsch Synthesis Catalysis, *ACS Catal.* 9 (2019) 1264–1273. <https://doi.org/10.1021/acscatal.8b03684>.
- [13] J. Harris, On the adsorption and desorption of H₂ at metal surfaces, *Appl. Phys. A Solids Surfaces.* 47 (1988) 63–71. <https://doi.org/10.1007/BF00619699>.
- [14] M.T. Kief, W.F. Egelhoff, Growth and structure of Fe and Co thin films on Cu(111), Cu(100), and Cu(110): A comprehensive study of metastable film growth, *Phys. Rev. B.* 47 (1993) 10785–10814. <https://doi.org/10.1103/PhysRevB.47.10785>.
- [15] W. Kirstein, B. Krüger, F. Thieme, CO adsorption studies on pure and Ni-covered Cu(111) surfaces, *Surf. Sci.* 176 (1986) 505–529. [https://doi.org/10.1016/0039-6028\(86\)90052-X](https://doi.org/10.1016/0039-6028(86)90052-X).
- [16] A. Biedermann, W. Rupp, M. Schmid, P. Varga, Coexistence of fcc- and bcc-like crystal structures in ultrathin Fe films grown on Cu(111), *Phys. Rev. B - Condens. Matter Mater. Phys.* 73 (2006) 1–16. <https://doi.org/10.1103/PhysRevB.73.165418>.
- [17] M. Wuttig, R. Franchy, H. Ibach, Oxygen on Cu(100) - a case of an adsorbate induced reconstruction, *Surf. Sci.* 213 (1989) 103–136. [https://doi.org/10.1016/0039-6028\(89\)90254-9](https://doi.org/10.1016/0039-6028(89)90254-9).
- [18] H. Hiehus, Surface reconstruction of Cu(111) upon oxygen adsorption, *Surf. Sci.* 130 (1983) 41–49. [https://doi.org/https://doi.org/10.1016/0039-6028\(83\)90258-3](https://doi.org/https://doi.org/10.1016/0039-6028(83)90258-3).
- [19] G. Wedler, K.G. Colb, W. Heinrich, G. McElhiney, The interaction of hydrogen and carbon monoxide on polycrystalline iron films, *Appl. Surf. Sci.* 2 (1978) 85–101. [https://doi.org/10.1016/0378-5963\(78\)90008-9](https://doi.org/10.1016/0378-5963(78)90008-9).

- [20] G. Li, X. Yu, C.J. Weststrate, P. Ren, J. Xu, Q. Xu, Y. Yang, Y. Li, J.W. Niemantsverdriet, X. Wen, J. Zhu, Role of Interfaces in the Thermal Reduction Process of the FeO/Cu₂O/Cu(100) Surface, *J. Phys. Chem. C* 125 (2021) 20863–20869. <https://doi.org/10.1021/acs.jpcc.1c05527>.
- [21] and E.L. C.Klink, L.Olesen, F. Besenbacher, I. Stensgaard, Interaction of C with Ni(100): Atom-Resolved Studies of the ‘Clock’ Reconstruction, *Phys. Rev. Lett.* 71 (1993) 4350–4353. <https://doi.org/10.1103/PhysRevLett.71.4350>.
- [22] G. Panaccione, J. Fujii, I. Vobornik, G. Trimarchi, N. Binggeli, A. Goldoni, R. Larciprete, G. Rossi, Local and long-range order of carbon impurities on Fe(100): Analysis of self-organization at a nanometer scale, *Phys. Rev. B - Condens. Matter Mater. Phys.* 73 (2006) 1–9. <https://doi.org/10.1103/PhysRevB.73.035431>.
- [23] F.J.E. Scheijen, The surface chemistry of CO on iron and other bcc metals, Technische Universiteit Eindhoven, 2010. <https://doi.org/10.6100/IR657952>.
- [24] T. Tanabe, T. Shibahara, R. Buckmaster, T. Ishibashi, T. Wadayama, A. Hatta, Infrared spectral study of CO adsorption on molecular-beam epitaxially grown, fcc iron films on Cu(100), *Surf. Sci.* 466 (2000) 1–10. [https://doi.org/10.1016/S0039-6028\(00\)00772-X](https://doi.org/10.1016/S0039-6028(00)00772-X).
- [25] T. Tanabe, Y. Suzuki, T. Wadayama, A. Hatta, Carbon monoxide adsorption on ultra-thin Fe film deposited on Cu(100), *Surf. Sci.* 427–428 (1999) 414–418. [https://doi.org/10.1016/S0039-6028\(99\)00313-1](https://doi.org/10.1016/S0039-6028(99)00313-1).
- [26] T. Wadayama, K. Kubo, T. Yamashita, T. Tanabe, A. Hatta, Infrared reflection absorption study of carbon monoxide adsorbed on submonolayer Fe-covered Cu(100), (110), and (111) bimetallic surfaces, *J. Phys. Chem. B* 107 (2003) 3768–3773. <https://doi.org/10.1021/jp026212v>.
- [27] B.E. Hayden, K. Kretzschmar, A.M. Bradshaw, An infrared spectroscopic study of CO on Cu(111): The linear, bridging and physisorbed species, *Surf. Sci.* 155 (1985) 553–566. [https://doi.org/10.1016/0039-6028\(85\)90013-5](https://doi.org/10.1016/0039-6028(85)90013-5).



The conclusions of the dissertation are presented in this chapter. The chapter contains several conclusions divided into different sections (structure versatility and usefulness as a model catalyst) where they are also compared with real-world conditions. The rationale for using new characterization techniques like STM and Near Ambient XPS is explained.

To achieve a more representative iron carbide model catalyst, we briefly explain how the evaporation of thick iron films on an ethylene atmosphere could shed some light on the fabrication of iron carbide model catalysts for FTS.

7.1 Chapter 3: Iron and iron carbide films on Cu(100)

This thesis presents a fundamental study on the fabrication of iron carbide thin films on FCC copper substrates and their reactivity towards CO and H₂. Cu(100) was chosen as the substrate, as its open structure was expected to yield an open FCC(100) iron film with a different reactivity than commercially available BCC iron single crystals. The similarity in atomic radii between iron and copper was also expected to result in a high level of epitaxy, which was observed mainly for films < ~3 ML. However, the formation of BCC(110) became more dominant as the iron thickness increased, and for films > ~12 ML, the films are purely BCC(110).

Structure versatility

Chapter 3 describes how iron and iron carbide thin films can be created on Cu(100) to be used as model catalysts. For iron, the thickness determines the surface structure. For films between 0 ML and ~3 ML, the iron films grow as bilayer islands following the FCC(100) substrate. From this point onwards, ~3 ML to ~12 ML, a mixture of FCC(100) and BCC(110) coexists on the surface, and the growth mode becomes layer-by-layer. The structure tends to become BCC(110) with an increase in iron thickness until no more FCC(100) can be seen using LEED. Full BCC(110) was found for films >12 ML.

An iron film saturated with ethylene at 100 K was heated to 500 K to complete the dissociation reaction of ethylene and create the iron carbide. However, this

fabrication process exhibited a drawback: From 500 K, the iron atoms begin to diffuse into the copper single crystal, meaning that the absolute iron film thickness might be lower than initially intended. This drawback is only evident after several cycles of ethylene, and depending on the thickness of the iron film, it might not affect the chemistry of the surface.

The carburization of iron films, < 12 ML, creates a surface structure with a p4g(2x2) symmetry, which is recurrent in this research. The p4g(2x2) structure acts as a carbon trap, limiting carbon diffusion due to its remarkable stability, limiting the formation of bulk iron carbide, and thus limiting the applications of these films. However, we can create subsurface and bulk iron carbides by evaporating iron in an ethylene atmosphere (5×10^{-7} mbar), and 300 K. The efficacy of this approach stems from the interaction between freshly deposited iron and atmospheric ethylene during the evaporation process. As iron undergoes evaporation, it reacts with ethylene, forming iron carbide. This sequential process continues, with iron continually evaporating atop the newly formed and deposited iron carbide. This method holds promise for synthesising bulk iron carbide and warrants further exploration in future investigations. Utilizing a more realistic model in subsequent studies could enhance our understanding of this process in real-life scenarios. Nonetheless, this method forms p4g(2x2) on the surface. In collaboration with Gubó et al. [2], bulk **Fe₄C** → **Fe₃C₂** (**Fe₄C₂**+**Fe₄**) was made (confirmed by XPS and STM) by evaporating iron on ethylene atmosphere, where they found on the uppermost layer, p4g(2x2). The formation of p4g(2x2), in the perspective of model catalysis, is an undesired structure, as we mentioned before. However, by evaporating larger quantities of iron, we could circumvent the formation of p4g(2x2), and achieve a more dynamic surface. For films >12 ML, an elongated (3x1) pattern is found using LEED attributed to multiple domains of BCC-Fe. Its reactivity towards carbon is markedly different since experiments show that carbon atoms (after ethylene dissociation on the surface) can now diffuse into the subsurface/bulk region of the sample (measured by the decrease in C_{KLL} intensity after a couple of heating cycles as shown in Chapter 6). By using thick iron films (>12 ML – full BCC(110)) we could create a model catalyst where the superficial carbon could be removed, i.e., by hydrogen and hence, try to mimic carbon removal as in FTS. However, it is important to take into account, that by

evaporating thick iron films we are replicating the behaviour from BCC(110) iron single crystals (this is discussed in 7.3.3.).

The versatility of these films, where different types of carbide structures can be formed depending on the fabrication method, is only limited by the presence of the FCC-Fe, which inhibits carbon diffusion, and forms p4g(2x2). By limiting the presence of FCC-Fe in our model catalysts, we could form a more reactive surface and tune the film at will and thus explore the model catalysts we want.

Usefulness as model catalysts

The evaporated iron films show a high activity towards CO, H₂ and ethylene dissociation. The iron films proved to be useful in investigating the reactivity of iron towards FT precursors, and hence, they give information about the reactions that occur during the formation of iron carbide in the initial stages of the FTS reaction.

The fully saturated carbon surface structure consists of a layer of Fe₂C with a p4g(2x2) symmetry and acts as a carbon trap, effectively impeding carbon diffusion and inhibiting the dissociation of CO, H₂, and ethylene. When the surface carbon concentration is lowered, the dissociation of both CO and ethylene is possible, where we observe an inverse proportionality between the dissociative ability and the carbon content. By tuning the carbon content, different model systems can be made. For example, a 3 ML thick iron film with 0.25 ML of carbon on the surface will present a pristine FCC Fe(100) and BCC Fe(110) + FCC Fe_xC_y(100)_{0.25}. This mixture of phases resembles real-life catalyst surfaces, where different carburized and not carburized species with different surface configurations coexist simultaneously.

As mentioned in the last section, the structures where Fe behaves BCC(110) (> 12 ML of Fe) can be a good candidate for further exploration as model catalysts due to its high carbon diffusion after ethylene dissociation and the lack of p4g(2x2) formation. Fabricating iron carbide structures by evaporating thick iron films (>12 ML) on an ethylene atmosphere is also a promising method of fabrication that forms bulk carbide structures with no p4g(2x2).

In an attempt to remove carbon from the surface of iron carbide and replicate C-H interaction in real-life catalysts, we adsorbed hydrogen using a W filament, as detailed in Chapter 2. However, the carbon content on the surface remained unchanged after the adsorption and desorption of hydrogen, indicating that no carbon was removed during these processes, confirmed by AES and XPS. After hydrogen desorption, the iron carbide structure remains unaltered as it was confirmed by the LEED pattern before and after adsorption.

7.2 Chapter 5 and Chapter 6: Iron and iron carbide films on Cu(111). Structure versatility and usefulness as a model catalyst

A Cu(111) single crystal was used to study the influence of the substrate on the iron carbide structure. In earlier work by Li et al. [1], an Au(111) substrate was used as a support for iron carbide structures, and unlike our Cu(100) results, these authors did not find pure carbide but mixtures of different carbon species at every thickness studied. Also, they found that thin FCC iron films on Au(111) were inert, and carbide could only be formed on thicker Fe films with a bulk BCC structure. The work on Cu(111) was therefore undertaken to investigate whether the role of these differences was due to the different chemical nature of the substrate or if it is instead due to the different surface termination, i.e. (111) vs (100).

Iron films on Cu(111) show a markedly different morphology than films on Cu(100). Iron deposition at room temperature leads to the formation of 3D islands up to a coverage of 5 ML, after which the film closes but remains rough/heterogeneous, making it interesting to study local differences for different film thicknesses. In this system, the iron structure depends on film thickness, where FCC-Fe forms at low thicknesses while BCC features start to appear around 3 ML. After 3 ML, a mixture of FCC and BCC coexist up to a coverage of ~16 ML, after which only BCC(110) is seen.

From the fabrication of iron carbide, we can say that the system Fe/Cu(111) is morphologically and structurally more complex compared to Fe/Cu(100) due to the higher Cu segregation at temperatures where the ethylene and CO dissociate (450 K), limiting the study to a small temperature window. Also, this finding makes the

quantification of iron and dissociation products complicated by averaging techniques.

Furthermore, the lack of superstructures (LEED) at each level of thickness makes the iron thickness quantification only reliable from the evaporation time.

After ethylene dissociation, iron carbide was found using AES. The expected product of the carburization of the morphologically heterogeneous iron film is also a heterogeneous iron carbide film. These iron films resemble real-life catalysts more than those found on Cu(100). Furthermore, after carburizing the iron film, we believe a mixture of structures was found: Fe BCC(110), Fe FCC(111), Fe_xC_y BCC(110) and Fe_xC_y FCC(111).

7.3 Outlook

Generally, research projects are never finished, which is not different for this thesis. In this section, we propose follow-up experiments and the usage of different characterization techniques to complement our findings.

7.3.1 Other characterization techniques

To gain more valuable information on the iron and iron carbide films on Cu(100) and Cu(111), pre and post-adsorption of CO and H₂, more characterization techniques could be used.

STM has been shown by others in the past to be an advantageous technique for characterizing the morphology of surfaces. With this extra information, we would be able to determine precisely what the proportion of BCC(110) and FCC(100)/FCC(111) is in iron films. Furthermore, and especially for iron carbide films on Cu(111), to gain extra depth on the phase distribution after carburization. We have shown, in Chapter 5, using LEED, to be at least five coexisting FCC and BCC phases that could be resolved with STM. As mentioned before, in collaboration with Gubó et al. [2] they characterized the surface of the iron carbide (p4g(2x2)) using STM.

SR-XPS (Synchrotron radiation X-ray photoelectron spectroscopy) in Cu(111) systems is crucial to level the data gathered in Cu(100) systems. Due to COVID-19,

the beamtime assigned to us in ASTRID2 was cancelled, and we never had the opportunity to recover the time. AES proved to be an extremely efficient and easy-to-use technique, but XPS gives a better resolution to determine the nature of the carbon. Replicating the SR-XPS experiments from Chapter 3 and Chapter 4, but in Cu(111), will be extremely valuable to understand CO and ethylene dissociation temperatures and the nature of carbon after dissociation.

Also, NAP-XPS (Near ambient pressure X-ray photoelectron spectroscopy) would help us to decrease the gap between real-life catalysts and our model catalysts. Of course, NAP-XPS is still far from real life, but it could bring light to: i.e. if the carbon from the p4g(2x2) can be removed with H₂ by applying more pressure onto the surface, as it usually occurs in real-life catalysts.

DFT calculations could also be interesting to learn about the energetics of catalytic systems on these surfaces. In this topic, other groups, like the group from Dr. Richárd Gubó et al. [2], are already working on STM and DFT calculations in Fe_xCy/Cu(100) systems. Some of their results are described in Chapter 3.

7.3.2 Improved measurements with present techniques

In the laboratory located at DIFFER, where most of this thesis was performed, there are some techniques with a lot of potential. RAIRS is one of these techniques that was not used as exhaustively as the others presented in this thesis, and it could teach us more about CO adsorption on pure and carburized iron films (interaction with the substrate, molecule orientation, coverage, and adsorption sites).

A Kelvin-Probe is also located in both systems used for this thesis. Work function measurements can potentially yield valuable information about adsorbate coverage, desorption, and surface reaction rates. However, it needs to be used together with other techniques in order to extract valuable information. By combining work function with other techniques, more information related to CO adsorption on iron and iron carbide films and its reactivity can be obtained.

7.3.3 Fe(110) single crystal comparison

A Fe(110) single crystal surface is to some extent similar to our thick iron films supported on Cu(100) or Cu(111), but the films on the copper substrate expose different (110) domains, and the iron films on these substrates, especially Cu(111), are not as flat and homogeneous as a single crystal. Hence, the binding sites are better defined on the single crystal.

One of the main drawbacks of using iron single crystals instead of evaporating iron films is related to the complexity of creating defined bulk carbide structures in single crystals. For thin films, the bulk is insignificant compared to the single crystal, making it easier to make more carbide-rich bulk structures. Also, this approach creates a structure which is closer to real-life catalysts. The present thesis presents limited results about bulk carbide fabrication, but follow-up work shows that different iron bulk carbides can be prepared on Cu(100) [2].

One could argue about the best choice between single crystals BCC Fe(110) and iron films as model catalysts. As mentioned in Chapter 2, contaminants in the iron single crystal make the cleaning process tedious and, thus, time-consuming. For evaporated films, the determining factor is the time spent in the fabrication and characterization of the films and the subsequent cleaning process to remove the contaminated iron film. Although it sounds like a lot of time, the preparation phase of these films, including the cleaning, usually does not take longer than two hours, against the time required to clean an iron single crystal which could be weeks.

7.4 Final Remarks

As highlighted in the introduction, the Surface Science approach creates a pressure disparity between the experimental system (typically maintained under vacuum conditions) and real-world catalysts. For example, a real-life iron catalyst for FT is usually used at 20 bar, which is a considerable pressure gap [3]. Also, temperature conditions in iron carbide catalysts for FTS are usually between 495-625 K, which is higher than we used in these experiments (100 K to 500 K for controlled conditions).

Despite all the possible differences between industrial catalysts and single crystals, the latter still delivers valuable information on the reaction kinetics and adsorbate-adsorbate interactions. It helps to gain fundamental insights into the structure-function relationships of catalysts under well-defined and controlled conditions. The insights from studying flat model catalysts can be used to design and optimize real-life industrial catalysts by tuning their structure and composition for better performance. Additionally, the flat model catalyst approach can be used to investigate the underlying principles of catalysis, which can lead to the development of novel catalytic materials and processes.

Gaining more insight into iron carbide structures and their interaction with CO and H₂ can help develop more active catalysts for FTS and study the deactivation mechanisms of these catalysts. Eventually, the focus of this research should be shifted to near-ambient pressures and try to bring the real-life catalysts and the results found in this thesis closer.

7.5 References

- [1] Y. Li, Z. Li, A. Ahsen, L. Lammich, G.J.A. Mannie, J.W. Niemantsverdriet, J.V. Lauritsen, Atomically Defined Iron Carbide Surface for Fischer-Tropsch Synthesis Catalysis, *ACS Catal.* 9 (2019) 1264–1273. <https://doi.org/10.1021/acscatal.8b03684>.
- [2] R. Gubo, P. Ren, D. Garcia Rodriguez, X. Yu, T. Zhang, X. Wen, Y. Yang, Y. Li, J.W. Niemantsverdriet, C.J. Weststrate, Atomistic Understanding of the Formation, Structure, and Decomposition of an Fe₄C Iron Carbide Phase on a Copper Substrate. *J.Phys.Chem.C.* 26 (2023) 12811–12820. <https://doi.org/10.1021/acs.jpcc.3c03134>.
- [3] J. van de Loosdrecht, F.G. Botes, I.M. Ciobica, A. Ferreira, P. Gibson, D.J. Moodley, A.M. Saib, J.L. Visagie, C.J. Weststrate, J.W. Niemantsverdriet, *Fischer-Tropsch Synthesis: Catalysts and Chemistry*, 2nd ed., Elsevier Ltd., 2013. <https://doi.org/10.1016/B978-0-08-097774-4.00729-4>.

Acknowledgements

Since 2017, when I started my PhD, many people have contributed either directly or indirectly to the development of this thesis. This section is for them:

First, I would like to thank my supervisor and mentor, Dr. C.J. (Kees-Jan) Weststrate, for his support and guidance. Your critical thinking taught me how to conduct research and how to find the bright side when the results are not as expected. Our countless hours in Synchrotrons taught me how to solve problems with a limited amount of time and learn to improvise, which are skills that made me the professional I am today.

Thanks to my first promotor, prof.dr.ir. Richard van Sanden for taking over after Hans, your help during the last months of the thesis was extremely valuable.

Second, to prof.dr. J.W. Niemantsverdriet. Hans, your guidance and support throughout this journey were extremely valuable to me. I will never forget your feedback during our presentations and, of course, your valuable comments in every single chapter.

I would like to thank prof.dr. Adriana Creatore, prof.dr.Guido Mul, prof.dr. Jeppe Vang Lauritsen, prof.dr.ir Marc Geers and Dr. Ludo Juurlink for accepting to be part of my committee and for taking the time to read my thesis.

Especial thanks to all members of Syngaschem B.V. Dr. Sapountzi, Dr. Fredriksson, Ir. Felderhof and Antonio Vaccaro, thank you for supporting me all these years, giving me amazing feedback during my presentations, and for the fantastic lunchtimes we spent together talking about mostly non-scientific topics (thanks for this).

Jeppe and Kræn (Dr. Adamsen), thank you for letting me be part of your group for three months in Aarhus, one of the nicest cities I have ever visited. Your technical help in ASTRID2 helped me immensely in creating this thesis. You also taught me the complexity that involves getting one good image in STM (it is very challenging).

Dr. Michael Gleeson, thank you for spending a week with me in Aarhus and helping me with the experiments. Your input and technical expertise were extremely important during the experiment's decision-making.

Devyani, my office and lab colleague, although we had very different projects, we always managed to talk a little bit about our projects, and in the end, we managed to share set-ups and support each other. We shared the burden of being unable to go to the lab during COVID and still trying to keep ourselves motivated. Good luck with your defence, and see you at the campus.

Gracias especiales a mis paranymphs Rafael Campos y Victor Bustos, primero decir que los quiero mucho, y siempre he sentido que una de las razones por las que hice un doctorado fue por vosotros dos, veros disfrutar haciendo ciencia y disfrutar la vida de doctorando, fue

sin duda una de las razones por las que decidí venir a Eindhoven. Gracias por apoyarme siempre y aconsejarme cuando fue necesario. Os quiero mucho.

James y Mochito, aunque no hayan apoyado nada, ni ayudado nada de nada en esta tesis, los quiero mucho y sin duda esas charlas off-topic, non-thesis related, son extremadamente importantes, aunque suene trillado. A Raúl y David, os quiero mucho, y espero poder seguir hablando de chorradas con vosotros dos por siempre.

To my DIFFER colleagues, Dr. Ong (Qin), Dr. Zafeiropoulos (Georgios), Dr. Kyriakou (Vassilis), and Dr. Belete (Tesfaye). To the Greek guys, I need to say: Thank you both, the DIFFER experience was much nicer with you guys around. The jokes and the non-related scientific topics were a way to think, for a bit, about other things besides writing and experiments. I really enjoyed my time with you two. Vasilis, our trip to China was a memory that will be very hard to forget. The memories of the Great Wall will be forever stuck in my brain (my favourite mongol).

To Qin, I will never forget our China trip and act as interpreter, for sure the trip was much easier with you on board. I am lucky to have you as a colleague and be able to hang out occasionally, where you have already given me support and amazing advice. Hope to see you soon. Dr. Belete, Tesfayito, in my first months at DIFFER, you were my role model, a knowledgeable person, always eager to help, always with a smile, and an extremely hard worker. I really hope I can see you again in the future.

I want to thank all DIFFER staff for their help. This thesis wouldn't have been possible without your continuous help and support.

También quiero agradecer a Jose, quizá esto no es lo convencional, pero siento que debo dejar registrado en algún lado la importancia que ejerciste durante este proceso. Tu forma de hacerme dar cuenta del proceso en el que estaba y como debía abordarlo me ayudaron muchísimo. Aún a día de hoy tu ayuda ha sido clave, no solo en mi vida personal, sino también en mi vida profesional. Espero poder seguir hablando contigo muchos años más.

Y por último, pero ciertamente no los últimos, a mi familia, ¿Quién se hubiese imaginado que yo terminaría un doctorado?, y esto solo fue posible por vuestro apoyo constante.

A mi madre, Pilar, mami, te quiero mucho, sin tu perseverancia como madre esto no hubiese sido posible, cada vez estoy más convencido que esta perseverancia que me caracteriza sale de ti. Tu capacidad de trabajo, tu organización con las cosas son cualidades que admiro e intento imitar. Te quiero muchísimo.

A mi, padre, Roberto, papito lindo, estoy convencido que el camino que seguí como científico es enteramente tu culpa, tu curiosidad por las cosas y por saber más, fue lo que me llevó a seguir este camino. Te quiero mucho. A mi hermana, Lara, Lá, L, un pilar fundamental en mi vida, tu capacidad de adaptarte a diferentes situaciones y tu valentía fueron siempre un

espejo en el que mirarme, a ti también tengo que achacarte parte de mi perseverancia. Este párrafo no representa ni el 1% de lo que me gustaría decir, pero ya llevo muchos años escribiendo esta tesis y me gustaria terminar este año. No quiero olvidarme de Amelia, mi ahijada, aún no lees, pero tu nacimiento fue el impulso extra que necesitaba, creo que desde que naciste empecé a levantarme a las 5am, ¡¡cada día!!, para terminar esta tesis. Aún es pronto para que leas esto, pero que sepas que tu tío favorito te ama mucho.

Maryori, suegrita amada, te quiero mucho, gracias por ayudarme a escribir la introducción, tu capacidad para organizarme las ideas fue clave en su desarrollo. Gracias también por apoyarme, y cuidarme tanto, cada vez que voy a tu casa ya la siento la mía, te quiero mucho. Naghi, amada mía, creo que podría escribir una tesis solo sobre todo lo que me has ayudado, apoyado,...Uno de los días más felices de mi vida, fue el día que viniste a vivir a tu casa en Eindhoven, ese día mi cabeza se calmó y la escritura de la tesis fue muchísimo más rápido. Tu apoyo constante en todo, no solo en la tesis, sino en el trabajo, en la vida, en situaciones familiares, etc fue clave para terminar esta tesis. Escribir una tesis doctoral no es sentarse y escribir, es estar en paz con uno mismo, y eso es lo que consigues tú conmigo. Y no quiero olvidarme de la portada, te fajaste hermosa esposita. Te amo infinito. →←

Thank you all, Bedankt, Gracias, ευχαριστώ!

List of publications

Publications within the scope of this thesis:

Chapter 3

- D.Garcia Rodriguez, M.A. Gleeson, J.V. Lauritsen, Z.Li, X.Yu, J.W. Niemantsverdriet, C.J. Weststrate. Iron Carbide Formation on Thin Iron Films Grown on Cu(100): FCC Iron Stabilized by a Stable Surface Carbide. *Appl.Surf.Sci.* 585 (2022) 152684. <https://doi.org/10.1016/j.apsusc.2022.152684>
- R. Gubo, P. Ren, D. Garcia Rodriguez, X. Yu, T. Zhang, X. Wen, Y. Yang, Y. Li, J.W. Niemantsverdriet, C.J. Weststrate, Atomistic Understanding of the Formation , Structure , and Decomposition of an Fe₄C Iron Carbide Phase on a Copper Substrate. *J.Phys.Chem.C.* 26 (2023) 12811–12820. <https://doi.org/10.1021/acs.jpcc.3c03134>.

Publications outside the scope of this thesis:

- C.J. Weststrate, D. Garcia Rodriguez, D. Sharma, J.W. Niemantsverdriet, Structure-Dependent Adsorption and Desorption of Hydrogen on FCC and HCP Cobalt Surfaces. *J.Catal.* 405 (2022) 303-312. <https://doi.org/10.1016/j.jcat.2021.12.016>.
- C.J. Weststrate, D.Sharma, D.Garcia Rodriguez, M.A. Gleeson, H.O.A. Fredriksson, J.W. Niemantsverdriet. Mechanistic Insight into Carbon-Carbon Bond Formation on Cobalt under Simulated Fischer-Tropsch Synthesis Conditions. *Nat.Commun.* 11 (2020) 1-9. <https://doi.org/10.1038/s41467-020-14613-5>
- C.J. Weststrate, D.Sharma, D.Garcia Rodriguez, H.O.A. Fredriksson, J.W. Niemantsverdriet Water Formation Kinetics on Co(0001) at Low and Near-Ambient Hydrogen Pressures in the Context of Fischer–Tropsch Synthesis. *J.Phys.Chem.C.* 127 (2023) 3452-3461. <https://doi.org/10.1021/acs.jpcc.2c08092>
- C.J. Weststrate, D.Sharma, D.Garcia Rodriguez, M.A. Gleeson, H.O.A. Fredriksson, J.W. Niemantsverdriet. Reactivity of C₃H_x Adsorbates in Presence of Co-adsorbed CO and Hydrogen: Testing Fischer–Tropsch Chain Growth Mechanisms. *Top Catal* 63 (2020) 1412-1423. <https://doi.org/10.1007/s11244-020-01306-y>.

Curriculum Vitae

Daniel García Rodríguez was born on July 17, 1986, in Barcelona. At the age of 5, he relocated to Bogotá, Colombia, where he pursued his high school education and completed one year of a biology bachelor's program at Universidad Javeriana. In 2005, at the age of 19, he returned to Barcelona. In 2007, he commenced his studies in Chemistry at Universitat Rovira i Virgili in Tarragona, completing his bachelor's degree in 2015 at Universitat de Barcelona.

Continuing his academic journey, he pursued a Master's in Nanoscience and Nanotechnology at Universitat de Barcelona, delving into research on the fabrication of carbon-encapsulated iron nanoparticles for potential use as carriers for cancer silencing molecules. After completing his Master's thesis, Daniel sought opportunities abroad. On March 1st, 2017, he embarked on his PhD journey at DIFFER, focusing on the fabrication of iron carbide model catalysts for Fischer-Tropsch synthesis, the results of which are presented in this dissertation.